

DISSERTATION

QUASI-STATIONARY, EXTREME-RAIN-PRODUCING  
CONVECTIVE SYSTEMS ASSOCIATED WITH MIDDLE  
CYCLONIC CIRCULATIONS

Submitted by

Russ Stanley Schumacher

Department of Atmospheric Science

In partial fulfillment of the requirements

For the Degree of Doctor of Philosophy

Colorado State University

Fort Collins, Colorado

Spring 2008

UMI Number: 3321309

### INFORMATION TO USERS

The quality of this reproduction is dependent upon the quality of the copy submitted. Broken or indistinct print, colored or poor quality illustrations and photographs, print bleed-through, substandard margins, and improper alignment can adversely affect reproduction.

In the unlikely event that the author did not send a complete manuscript and there are missing pages, these will be noted. Also, if unauthorized copyright material had to be removed, a note will indicate the deletion.

**UMI**<sup>®</sup>

---

UMI Microform 3321309

Copyright 2008 by ProQuest LLC.

All rights reserved. This microform edition is protected against unauthorized copying under Title 17, United States Code.

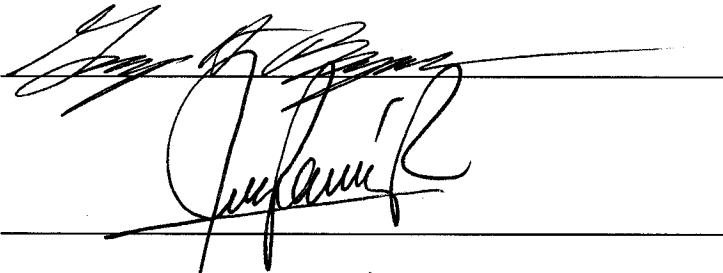
ProQuest LLC  
789 E. Eisenhower Parkway  
PO Box 1346  
Ann Arbor, MI 48106-1346

COLORADO STATE UNIVERSITY

31 March 2008

WE HEREBY RECOMMEND THAT THE DISSERTATION PREPARED UNDER OUR SUPERVISION BY RUSS STANLEY SCHUMACHER ENTITLED QUASI-STATIONARY, EXTREME-RAIN-PRODUCING CONVECTIVE SYSTEMS ASSOCIATED WITH MID-LEVEL CYCLONIC CIRCULATIONS BE ACCEPTED AS FULFILLING IN PART REQUIREMENTS FOR THE DEGREE OF DOCTOR OF PHILOSOPHY.

Committee on Graduate Work



Advisor



Department Head

## ABSTRACT OF DISSERTATION

### QUASI-STATIONARY, EXTREME-RAIN-PRODUCING CONVECTIVE SYSTEMS ASSOCIATED WITH MIDDLELEVEL CYCLONIC CIRCULATIONS

Observations and numerical simulations are used to investigate the atmospheric processes responsible for initiating, organizing, and maintaining quasi-stationary mesoscale convective systems (MCSs) that form in association with midlevel mesoscale convective vortices or cutoff lows. Six events were identified in which an MCS remained nearly stationary for 6-12 hours and produced excessive rainfall that led to significant flash flooding. Examination of individual events and composite analyses reveals that the MCSs formed in thermodynamic environments characterized by very high relative humidity at low levels, moderate convective available potential energy, and very little convective inhibition. In each case, the presence of a strong low-level jet (LLJ) led to a pronounced reversal of the wind shear vector with height. Convection was initiated by lifting associated with the interaction between the LLJ and the midlevel circulation.

One of these events was examined in detail using numerical simulations. This MCS, which occurred on 6-7 May 2000 in eastern Missouri, produced in excess of 300 mm of rain in 9 hours and led to destructive flash flooding. Simulations indicate that the MCS was long-lived despite the lack of a cold pool at the surface. Instead, a nearly stationary low-level gravity wave helped to organize the convection into a quasi-linear system that was conducive to extreme local rainfall amounts. Additionally, the convective system acted to reintensify the midlevel MCV and also caused a distinct surface low pressure center to develop in both the observed and simulated system.

To further understand the important processes in these MCSs, idealized simulations using a low-level lifting mechanism and a composite thermodynamic profile are employed. These simulations successfully replicate many of the features of the observed systems. The low-level environment is nearly saturated, which is not conducive to the production of a strong surface cold pool; yet the convection quickly organizes into a quasi-linear system that produces very heavy local rainfall. As in the May 2000 case, a low-level gravity wave was responsible for this organization. The upstream development of new convective cells is shown to result from the interaction of the reverse-shear flow with these waves.

Russ Stanley Schumacher  
Department of Atmospheric Science  
Colorado State University  
Fort Collins, Colorado 80523-1371  
Spring 2008

## ACKNOWLEDGMENTS

This research was supported by National Science Foundation Grant ATM-0500061. Computing resources were provided by the National Center for Atmospheric Research, which is sponsored by the National Science Foundation. NEXRAD and precipitation gauge data were provided by the National Climatic Data Center. RUC analyses were obtained from the Atmospheric Radiation Measurement (ARM) Program. Figures in this dissertation were created using a number of programs, including the Grid Analysis and Display System (GrADS), RIP (Read/Interpolate/Plot, provided by Mark Stoelinga), IDL, GEMPAK (provided by Unidata), and Vis5D, developed at the University of Wisconsin.

I would especially like to thank my graduate advisor, Prof. Richard Johnson, for all of his guidance during my years as a graduate student, for allowing me the freedom to follow my own research path, for giving me opportunities to present and discuss my work with the leaders in the field, and for encouraging me to learn and understand as much as I can about the atmosphere. I would also like to thank to the members of my graduate committee, Drs. George Bryan, Steven Rutledge, Chris Kummerow, and Jorge Ramirez, for reviewing my work and providing constructive suggestions for improving it. Dr. Bryan's willingness to provide the code to his cloud model and his unique insights about simulating convection have also been invaluable throughout the process of obtaining the results reported in this dissertation.

I would like to thank Prof. Matt Parker of North Carolina State University for many conversations about the workings of mesoscale convective systems and about atmospheric science generally. Thanks also go to Adrian Loftus of CSU for discussions regarding con-

vection within mesoscale convergence, and to Jason Knievel of NCAR, Gary Lackmann of North Carolina State, Robert Fovell of UCLA, Lance Bosart and Thomas Galarneau of the University at Albany, and Patrick Haertel of CSU for their assistance, guidance, and suggestions during the course of my research. I would also like to thank Gail Cordova, Rick Taft, Brian McNoldy, Dan Lindsey, Paul Ciesielski, and all of the other former and current members of the Johnson Research Group for providing help on countless occasions during my time at CSU and for contributing to a welcoming and scientifically stimulating work environment.

Finally, innumerable thanks go to my wife, Andrea, for supporting me unconditionally through my years of graduate school and for motivating me to think about science and life in new and exciting ways, and to my parents, who have supported and encouraged me in this and all of my endeavors.

## CONTENTS

<b>1 Introduction</b>	<b>1</b>
<b>2 Background and Motivation</b>	<b>4</b>
2.1 Past research on extreme rainfall . . . . .	4
2.2 The link between MCVs and heavy rainfall . . . . .	13
<b>3 Observations and Composite Analysis of Quasi-Stationary Convective Systems Associated with Midlevel Cyclonic Circulations</b>	<b>24</b>
3.1 Identification of events . . . . .	24
3.2 Data sources and analysis methods . . . . .	25
3.3 Description of the extreme rain events . . . . .	26
3.3.1 27–28 May 1998 . . . . .	27
3.3.2 5–6 May 2000 . . . . .	28
3.3.3 6–7 May 2000 . . . . .	29
3.3.4 3–4 June 2000 . . . . .	30
3.3.5 18 June 2007 . . . . .	31
3.3.6 20 August 2007 . . . . .	32
3.4 Similarities between the cases . . . . .	33
3.5 Composite analysis of synoptic and mesoscale conditions . . . . .	34
3.6 Summary . . . . .	44
<b>4 Observations and Numerical Simulations of the 6–7 May 2000 Eastern Missouri Flash-Flood-Producing Mesoscale Convective System</b>	<b>46</b>
4.1 Description of the event . . . . .	46
4.1.1 The mesoscale convective vortex . . . . .	47
4.1.2 Radar observations . . . . .	50
4.1.3 Surface observations . . . . .	52
4.2 Model configuration and experimental design . . . . .	53
4.3 Results . . . . .	56
4.3.1 Overall structure of convection and precipitation in convection-permitting simulations . . . . .	56
4.3.2 Initiation of convection . . . . .	59
4.3.3 Organization and maintenance of convective line . . . . .	62
4.3.4 Illustration of low-level waves in idealized simulations . . . . .	70
4.3.5 Development of surface low pressure and re-intensification of MCV . . . . .	75
4.4 Summary and conclusions . . . . .	79

<b>5 Idealized Simulations of Convective Updrafts in Varying Thermodynamic and Kinematic Environments</b>	<b>82</b>
5.1 Experimental design . . . . .	82
5.2 Results . . . . .	84
5.2.1 NOWIND . . . . .	84
5.2.2 FULL . . . . .	85
5.2.3 NOCOOL . . . . .	87
5.2.4 WK . . . . .	88
5.2.5 NOULSHEAR . . . . .	91
5.2.6 NOLLSHEAR . . . . .	93
5.2.7 NOLLSHEAR+5 . . . . .	94
5.2.8 NOLLSHEAR1KM . . . . .	98
5.2.9 HALFSHEAR . . . . .	98
5.2.10 NOULJET . . . . .	101
5.3 Summary and conclusions . . . . .	102
<b>6 Idealized Simulations of Quasi-Stationary Convective Systems</b>	<b>105</b>
6.1 Description of the numerical model and experimental design . . . . .	105
6.2 Results . . . . .	113
6.2.1 Development and organization of convective system . . . . .	113
6.2.2 Observational evidence for low-level gravity waves . . . . .	124
6.2.3 Evolution of simulated convective system at later times . . . . .	126
6.3 Sensitivity experiments . . . . .	130
6.3.1 Microphysical processes . . . . .	132
6.3.2 STOPFORCE . . . . .	138
6.3.3 CORIOLIS . . . . .	139
6.4 Summary and Conclusions . . . . .	141
<b>7 Conclusions and Future Work</b>	<b>144</b>
7.1 Conclusions . . . . .	144
7.2 Future Work . . . . .	147
<b>References</b>	<b>151</b>

## FIGURES

2.1	Schematic showing the near cancellation between cell motion and propagation, resulting in a quasi-stationary storm system. From Doswell et al. (1996). . . .	5
2.2	Schematic showing three stages in the evolution of a multicell thunderstorm system. From Doswell et al. (1996). . . . .	6
2.3	Surface, 850-hPa, and 500-hPa patterns for a typical frontal flash flood event. From Maddox et al. (1979) . . . . .	7
2.4	Surface, 850-hPa, and 500-hPa patterns for a typical mesohigh flash flood event. From Maddox et al. (1979) . . . . .	8
2.5	Conceptual model to highlight areas favorable for heavy convective rainfall. From Glass et al. (1995). . . . .	9
2.6	Schematic diagram of the radar-observed features of the TL/AS and BB patterns of extreme-rain-producing MCSs. From Schumacher and Johnson (2005). . . . .	11
2.7	Diurnal frequency distribution of heavy rain onset, peak rainfall, and rainfall end for MCS-related extreme rain events. From Schumacher and Johnson (2006). . . . .	12
2.8	Illustration of the displacement of isentropic surfaces after the sudden application of localized heating. Adapted from Haynes and McIntyre (1987). . . . .	14
2.9	Schematic diagram illustrating quasi-balanced lifting in the vicinity of a positive PV anomaly in ambient vertical shear. . . . .	16
2.10	(a) Locations of absolute thermodynamic instability. (b) 8-h change in CAPE and CIN associated with vortex-related ascent. From Trier et al. (2000a). . . . .	16
2.11	Conceptual diagram of the structure and redevelopment mechanism of the mesoscale warm core vortex. From Fritsch et al. (1994). . . . .	18
2.12	Schematic representation of the three regimes of low-level flow. From Crook and Moncrieff (1988). . . . .	20
2.13	Vertical $x$ - $z$ cross-sections in the zero-initial wind and control experiments. From Schmidt and Cotton (1990). . . . .	21
2.14	Schematic illustration of the height variation in the phase relations between the horizontal wind component in the direction of wave propagation and the wave-induced vertical motions for both an erect and tilted gravity wave. From Koch and Golus (1988). . . . .	22
3.1	(a) Absolute vorticity averaged over the 700–500-hPa layer, 600-hPa heights and winds from the RUC analysis at 0000 28 May 1998. (b) Base radar reflectivity from the Shreveport, Louisiana WSR-88D at 0956 UTC, surface observations and objective analysis of pressure corrected to sea level at 1000 UTC 28 May 1998. . . . .	27

3.2	(a) Absolute vorticity averaged over the 700–500-hPa layer, 600-hPa heights and winds from the RUC analysis at 0000 UTC 6 May 2000. (b) Base radar reflectivity from the Tulsa, Oklahoma WSR-88D at 0859 UTC, surface observations and objective analysis of pressure corrected to sea level at 0900 UTC 6 May 2000. . . . .	28
3.3	(a) Absolute vorticity averaged over the 700–500-hPa layer, 600-hPa heights and winds from the RUC analysis at 0000 UTC 7 May 2000. (b) Base radar reflectivity from the St. Louis, Missouri WSR-88D at 0659 UTC, surface observations and objective analysis of pressure corrected to sea level at 0700 UTC 7 May 2000. . . . .	29
3.4	(a) Absolute vorticity averaged over the 700–500-hPa layer, 600-hPa heights and winds from the RUC analysis at 0000 UTC 4 June 2000. (b) Base radar reflectivity from the Dallas–Fort Worth, Texas WSR-88D at 0759 UTC, surface observations and objective analysis of pressure corrected to sea level at 0800 UTC 4 June 2000. . . . .	30
3.5	(a) Absolute vorticity averaged over the 700–500-hPa layer, 600-hPa heights and winds from the RUC analysis at 0000 UTC 18 June 2007. (b) Base radar reflectivity from the Dallas–Fort Worth, Texas WSR-88D at 1056 UTC, surface observations and objective analysis of pressure corrected to sea level at 1100 UTC 18 June 2007. . . . .	31
3.6	(a) Absolute vorticity averaged over the 700–500-hPa layer, 600-hPa heights and winds from the RUC analysis at 0000 UTC 20 August 2007. (b) Base radar reflectivity from the Springfield, Missouri WSR-88D at 0959 UTC, surface observations and objective analysis of pressure corrected to sea level at 1000 UTC 20 August 2007. . . . .	32
3.7	Skew– $T$ log $p$ diagrams of three soundings representative of the inflow environments of extreme-rain-producing convective systems. . . . .	35
3.8	Composite of absolute vorticity averaged over the 700–500-hPa layer, 600-hPa heights, and winds for the six extreme rain events at the peak rainfall time. . .	36
3.9	Composite of 600-hPa absolute vorticity, 900-hPa winds and isotachs at (a) 12 h prior to peak rainfall; (b) 6 h prior to peak rainfall; (c) peak rainfall time; (d) 6 h after peak rainfall. . . . .	37
3.10	(a) Composite of 600-hPa absolute vorticity, surface-to-900-hPa wind shear vectors and shear magnitude at the peak rainfall time. (b) As in (a), except for 900–600-hPa shear vectors and shear magnitude. . . . .	38
3.11	Composite west-to-east vertical cross-sections through the vorticity maximum. . . . .	39
3.12	(a) Composite south-to-north vertical cross-section through the vorticity maximum. (b) Composite south-to-north vertical cross section showing divergence and pressure vertical velocity 6 h prior to peak rainfall. . . . .	40
3.13	Composite west-to-east vertical cross sections showing divergence and pressure vertical velocity at (a) 12 h prior to peak rainfall; (b) 6 h prior to peak rainfall; (c) peak rainfall time; (d) 6 h after peak rainfall. . . . .	40
3.14	Composite of 2-m virtual potential temperature, sea-level pressure, and 10-m winds at (a) 6 h prior to peak rainfall and (b) the peak rainfall time. . . . .	41
3.15	Composite of 900-hPa equivalent potential temperature, equivalent potential temperature advection, and winds at (a) 6 h prior to peak rainfall and (b) the peak rainfall time. . . . .	42

3.16	Composite of most-unstable convective available potential energy (MUCAPE) and convective inhibition (MUCIN) at (a) 12 h prior to peak rainfall; (b) 6 h prior to peak rainfall; (c) peak rainfall time; (d) 6 h after peak rainfall. . . . .	43
3.17	Composite skew- $T$ log $p$ diagram for the extreme rainfall environment. The parcel path for the parcel with the highest $\theta_e$ in the lowest 3 km is shown in the dotted line. . . . .	44
4.1	Objective analysis of National Weather Service/Cooperative rain gauge observations (mm) for the period 1200 UTC 6 May–1200 UTC 7 May 2000. . . . .	47
4.2	500-hPa heights, winds, and absolute vorticity from RUC analyses. Plots shown are for 1200 UTC (a) 3 May 2000, (b) 4 May 2000, (c) 5 May 2000, (d) 6 May 2000. . . . .	48
4.3	(a) 500-hPa heights, winds, and absolute vorticity from RUC analysis at 0000 UTC 7 May 2000. (b) West-east vertical cross-section of potential vorticity and potential temperature. . . . .	49
4.4	Most unstable CAPE and 850-hPa winds and isotachs from RUC analyses at (a) 0000 UTC and (b) 0600 UTC. . . . .	50
4.5	Observed composite radar reflectivity (dBZ) at (a) 0630 UTC and (b) 1100 UTC 7 May 2000. . . . .	51
4.6	Subjective analysis of surface observations at (a) 0000 UTC and (b) 0700 UTC 7 May 2000. . . . .	52
4.7	Location of model domains. The horizontal grid spacing is 9 km on domain 1, 3 km on domain 2, and 1 km on domain 3. . . . .	54
4.8	Model accumulated precipitation (mm) for the 15-h period ending at 1500 UTC 7 May 2000 from the run with 9-km grid spacing and Kain-Fritsch convection. The portion of the domain shown and the color scale is the same as that used in Fig. 4.1. The largest point rainfall total in this run was only 44 mm, compared with the observed maximum of 309 mm. . . . .	57
4.9	Simulated composite reflectivity (dBZ) at 0630 and 1100 7 May 2000 for (a–b) domain 3 in run 1KM and (c–d) domain 2 in run 3KM. . . . .	58
4.10	Model accumulated precipitation (mm) on domain 3 in run 1KM for the 15-h period ending at 1500 UTC 7 May 2000. . . . .	59
4.11	(a) 600-hPa geopotential height and absolute vorticity, and 900–600 hPa shear vectors. (b) Pressure, water vapor mixing ratio, and winds on the 300-K isentropic surface on domain 2 of run 3KM at 0100 UTC 7 May 2000. . . . .	60
4.12	Depth of moist absolutely-unstable layers (m, shaded) at 0600 UTC on domain 2 of run 3KM. . . . .	61
4.13	Approximately W-to-E section through development of several convective cells in run 1KM. . . . .	63
4.14	(a) 4-km vertical velocity and shear vectors in the 2–6-km layer at 0812 UTC on a portion of the domain in run 1KM. (b) Depth of moist absolutely-unstable layers at 0812 UTC on domain 3 of run 1KM. (c) Simulated radar reflectivity at 1 km AMSL at 0812 UTC showing the location of the rolls outlined in panel (a). (d) Observed base radar reflectivity from the St. Louis, MO radar (KLSX) at 0751 UTC. . . . .	64
4.15	(a) Simulated composite radar reflectivity at 1000 UTC on a portion of domain 3 of run 1KM. (b–c) Virtual potential temperature and winds at 1000 UTC for (b) the lowest model level and (c) 0.9 km AMSL (approximately 0.7 km AGL). . . . .	66

4.16	(a) North-south low-level vertical cross-section of potential temperature, CAPE for parcels lifted from each level, and flow vectors in the plane of the cross-section through line C-C' shown on Fig. 4.15c at 1000 UTC on domain 3 of run 1KM. (b) Average skew- $T$ log $p$ diagram for the immediate inflow region.	67
4.17	(a) Virtual potential temperature and winds at 1000 UTC at 0.9 km AMSL, except only values below 300 K are shaded. (b-c) Vertical sections showing potential temperature at 1000 UTC and representative parcel trajectories showing (b) airflow from south to north at low levels, rising and sinking over the gravity wave; and (c) air rising in deep updrafts.	68
4.18	Time-latitude plot of vertical velocity showing the relationship between low-level gravity waves and deep convection.	69
4.19	(a) Divergence and winds on the lowest model level and pressure adjusted to sea level on a portion of domain 3 of run 1KM at 0945 UTC. (b) Time series from 0800-1100 UTC showing pressure adjusted to sea level and wind speed in the direction of wave propagation in run 1KM at the point shown by the asterisk in panel (a).	71
4.20	(a) Simulated composite radar reflectivity at 1000 UTC on a portion of domain 2 of run NOEVAP. (b) Virtual potential temperature and winds at 1000 UTC at 0.9 km AMSL.	72
4.21	Skew- $T$ log $p$ diagram showing the thermodynamic and wind profile used in horizontally-homogeneous idealized simulations.	73
4.22	North-south vertical cross sections of potential temperature perturbation and vertical velocity for (a) simulation with no initial wind at $t = 30$ min; (b) simulation with wind profile shown in Fig. 4.21 at $t = 30$ min; (c) as in panel (b), but showing only the lowest 3 km and including streamlines; (d) as in panel (b) but at $t = 45$ min.	74
4.23	North-south vertical cross sections of potential temperature perturbation and vertical velocity for the simulation with all latent cooling processes removed at $t = 30$ min	76
4.24	(a) Composite radar reflectivity and pressure adjusted to sea level on domain 2 of run 3KM at 0945 UTC 7 May 2000. (b) Difference fields between run 3KM and run NOLATENT at 0945 UTC.	77
4.25	(Top row) 500-hPa potential vorticity, geopotential height, and winds at 1200 UTC 7 May 2000 in (a) NOLATENT and (b) 3KM. (Bottom row) West-to-east sections showing difference fields between 3KM and NOLATENT at (c) 1200 UTC and (d) 1500 UTC.	78
4.26	Three-dimensional picture highlighting the primary processes at work in the 6-7 May 2000 extreme-rain-producing MCS.	81
5.1	(a) Potential temperature perturbations at 1 km AGL for simulation NOWIND at $t=30$ min. (b) North-south vertical cross section through the convective cell.	84
5.2	(a) Initial wind profile in the lowest 6 km for simulation FULL. (b) Vertical velocity at 4 km AGL at $t=30$ min in FULL. (c) Potential temperature perturbations at 1 km AGL at $t=30$ min in FULL. (d) North-south vertical cross section through the convective cell at $t=30$ min in FULL.	86
5.3	(a) Vertical velocity at 4 km AGL at $t=1.25$ h in FULL. (b) North-south vertical cross section through the convective cell at $t=1.25$ h in FULL.	87

5.4	North-south vertical cross section through the convective cell at t=30 min in NOCOOL. . . . .	88
5.5	Skew-T log p diagram showing the analytic thermodynamic sounding from Weisman and Klemp (1982). . . . .	89
5.6	(a) Initial wind profile in the lowest 6 km for simulation WK. (b) Vertical velocity at 4 km AGL at t=30 min in WK. (c) Potential temperature perturbations at 1 km AGL at t=30 min in WK. (d) North-south vertical cross section through the convective cell at t=30 min in WK. . . . .	90
5.7	(a) Potential temperature perturbations at 1 km AGL for simulation WK at t=1.25 h. (b) North-south vertical cross section through the convective cell. . . . .	90
5.8	(a) Initial wind profile in the lowest 6 km for simulation NOULSHEAR. (b) Vertical velocity at 4 km AGL at t=30 min in NOULSHEAR. (c) Potential temperature perturbations at 1 km AGL at t=30 min in NOULSHEAR. (d) North-south vertical cross section through the convective cell at t=30 min in NOULSHEAR. . . . .	92
5.9	(a) Initial wind profile in the lowest 6 km for simulation NOLLSHEAR. (b) Vertical velocity at 4 km AGL at t=30 min in NOLLSHEAR. (c) Potential temperature perturbations at 1 km AGL at t=30 min in NOLLSHEAR. (d) North-south vertical cross section through the convective cell at t=30 min in NOLLSHEAR. . . . .	94
5.10	(a) Vertical velocity at 4 km AGL at t=1.25 h in NOLLSHEAR. (b) North-south vertical cross section through the convective cell at t=1.25 h in NOLLSHEAR. . . . .	95
5.11	(a) Initial wind profile in the lowest 6 km for simulation NOLLSHEAR+5. (b) Vertical velocity at 4 km AGL at t=30 min in NOLLSHEAR+5. (c) Potential temperature perturbations at 1 km AGL at t=30 min in NOLLSHEAR+5. (d) North-south vertical cross section through the convective cell at t=30 min in NOLLSHEAR+5. . . . .	96
5.12	(a) Vertical velocity at 4 km AGL at t=1.5 h in NOLLSHEAR+5. (b) North-south vertical cross section through the convective cell at t=1.5 h in NOLLSHEAR+5. . . . .	96
5.13	Potential temperature perturbations at 1 km AGL at t=1.5 h in (a) NOLLSHEAR and (b) NOLLSHEAR+5. . . . .	97
5.14	(a) Initial wind profile in the lowest 6 km for simulation NOLLSHEAR1KM. (b) Vertical velocity at 4 km AGL at t=30 min in NOLLSHEAR1KM. (c) Potential temperature perturbations at 1 km AGL at t=30 min in NOLLSHEAR1KM. (d) North-south vertical cross section through the convective cell at t=30 min in NOLLSHEAR1KM. . . . .	99
5.15	(a) Vertical velocity at 4 km AGL at t=1.5 h in NOLLSHEAR1KM. (b) North-south vertical cross section through the convective cell at t=1.5 h in NOLLSHEAR1KM. . . . .	99
5.16	(a) Initial wind profile in the lowest 6 km for simulation HALFSHEAR. (b) Vertical velocity at 4 km AGL at t=30 min in HALFSHEAR. (c) Potential temperature perturbations at 1 km AGL at t=30 min in HALFSHEAR. (d) North-south vertical cross section through the convective cell at t=30 min in HALFSHEAR. . . . .	100
5.17	(a) Vertical velocity at 4 km AGL at t=1.5 h in HALFSHEAR. (b) North-south vertical cross section through the convective cell at t=1.5 h in HALFSHEAR. . . . .	101

5.18	Comparison of initial wind profiles for simulations FULL and NOULJET. . . .	102
5.19	Vertical velocity at 4 km AGL at $t=2$ h in (a) FULL and (b) NOULJET. . . .	103
6.1	Composite skew- $T$ log $p$ diagram for the extreme rainfall environment. . . .	106
6.2	Vertical wind profile used for the horizontally-homogeneous initial state in the idealized simulations. . . . .	106
6.3	(a) Time series showing the maximum convergence and maximum upward vertical velocity (dashed line) in a dry simulation using the momentum forcing described in the text. (b) Divergence and wind perturbations at 1.5 km above the surface and vertical velocity at 2 km above the surface at $t=6$ h in the dry simulation. (c) North-south vertical section of potential temperature and vertical velocity in the lowest 4 km of the dry simulation. (d) Vertical profiles of divergence, averaged over a $150 \text{ km} \times 150 \text{ km}$ box centered on the maximum convergence. . . . .	110
6.4	(a) Skew- $T$ log $p$ diagram showing the effect of the lifting on the environment. (b) North-south vertical cross section through one of the first deep convective cells at $t=3$ h. . . . .	114
6.5	Simulated composite radar reflectivity from the 1-km simulation at (a) $t=3$ h, (b) $t=5$ h, (c) $t=7$ h, (d) $t=9$ h, and (e) $t=11.5$ h. . . . .	115
6.6	(a) Simulated composite radar reflectivity from the 500-m simulation at $t=5$ h. (b) Vertical velocity at 7 km AGL at $t=5$ h in the 500-m simulation. (c) Potential temperature perturbations on the lowest model level at the same time. (d) Potential temperature perturbations at 1 km AGL. . . . .	116
6.7	North-south vertical section through the convective line at $t=5$ h in the 500-m simulation. (b) A similar figure from Fovell and Tan (1998), showing a simulation of a cold-pool-driven squall line for comparison. . . . .	118
6.8	(a) Projection of selected 3-dimensional air parcel trajectories onto Cartesian planes. (b) North-south vertical section showing potential temperature, cloud outline, and low-level trajectories in the lowest 3 km to emphasize the low-level structure. . . . .	120
6.9	Series of southwest-to-northeast sections showing the development of several convective cells in the 500-m simulation. . . . .	122
6.10	(a,c) Observed composite radar reflectivity at (a) 0745 and (b) 0930 UTC 20 August 2007. (b,d) Time series showing station pressure and wind speed in the direction of (possible) wave propagation on 20 August 2007. . . . .	125
6.11	Potential temperature perturbations on the lowest model level and vertical velocity at 7 km AGL at $t=$ (a) 7 h, (b) 8 h, (c) 9 h, and (d) 11.5 h of the 1-km simulation. . . . .	127
6.12	North-south vertical section through the convective line at (a) $t=8$ h and (b) $t=8.58$ h in the 1-km simulation. . . . .	128
6.13	Comparison of accumulated rainfall between the idealized simulation and an accurate simulation of a real event. . . . .	130
6.14	Time series showing the maximum convergence and maximum upward vertical velocity (dashed line) in a dry version of STOPFORCE, where the momentum forcing is turned off after 2 h of integration. . . . .	132
6.15	Divergence and wind perturbations at 1.5 km above the surface and vertical velocity at 2 km above the surface at $t=6$ h in a dry version of CORIOLIS. . . . .	133
6.16	Time series comparing the sensitivity simulations. . . . .	134

6.17	Vertical velocity at 7 km AGL for (a) CTRL, (b) NOEVAP, (c) NOMELT, (d) STOPFORCE, and (e) CORIOLIS at t=7 h. . . . .	135
6.18	Vertical velocity at 7 km AGL for (a) CTRL, (b) NOEVAP, (c) NOMELT, (d) STOPFORCE, and (e) CORIOLIS at t=9 h. . . . .	136
6.19	North-south vertical section through the convective line at t=8.92 h in NOMELT.	137
6.20	Cross-sections showing instantaneous potential temperature tendency owing to microphysical effects and mixing ratio of graupel and snow. . . . .	138
6.21	Accumulated rainfall through t=9 h in CORIOLIS. . . . .	140

## TABLES

3.1	Details of the six MCV-related extreme rain events. . . . .	25
4.1	Design of WRF-ARW version 2.2 numerical model experiments. . . . .	54
5.1	Description of the simulations. . . . .	83
6.1	Parameters chosen for the convergence forcing in the idealized numerical simulations. . . . .	109
6.2	Descriptions of the sensitivity experiments. . . . .	131

## Chapter 1

### INTRODUCTION

Extreme rainfall is responsible for a variety of societal impacts, including flash flooding that can lead to damage, injury, and death. Over the past 30 years, flash flooding has been responsible for more fatalities in the United States than any other convective storm-related phenomenon, including tornadoes, hurricanes, and lightning (NOAA 2008). Despite the great need for accurate forecasts and warnings of extreme rainfall that can produce flash flooding, the prediction of warm-season heavy precipitation continues to be one of the most difficult challenges in operational forecasting (e.g., Fritsch and Carbone 2004). Flash-flood forecasting is made even more difficult because it requires information about the *hydrological* situation in addition to the meteorological environment. While this study will focus primarily on the meteorology of heavy rainstorms, the hydrological aspects and societal impacts will not be ignored.

In the warm season in the central and eastern United States, most heavy rainfall events are associated with mesoscale convective systems (MCSs; Schumacher and Johnson 2005, 2006). Most of these MCSs occur in “weakly forced” synoptic-scale environments, and a variety of mechanisms can initiate, organize, and maintain them. These forcings include surface fronts (e.g., Sanders 2000), convectively-generated outflow boundaries (e.g., Maddox et al. 1979), and orographic lifting (e.g., Pontrelli et al. 1999). In some cases, however, extreme-rain-producing MCSs develop when there are no apparent surface boundaries present prior to the initiation of convection. These systems can provide a particular challenge to forecasters, because there is no obvious focusing mechanism for the forecaster to

key in on. Regardless of the forcing, important factors for the production of extreme local rainfall by MCSs include slow system motion and the organization of convection such that deep convective cells repeatedly pass over a particular area (Doswell et al. 1996; Schumacher and Johnson 2005).

In some of the cases where pre-existing surface boundaries are absent, another prominent forcing mechanism is at work: the midlevel mesoscale convective vortex (MCV). A number of studies (Bosart and Sanders 1981; Fritsch et al. 1994; Trier and Davis 2002) have analyzed individual cases of flash-flood-producing rainfall occurring in conjunction with an MCV. Nielsen-Gammon et al. (2005) examined another event in which a convectively-reinforced midlevel potential vorticity (PV) anomaly, which originated from a cutoff low, contributed to the development of heavy rainfall. The work of Raymond and Jiang (1990) and Trier et al. (2000a) helped to elucidate why MCVs, which typically outlive the MCSs that spawned them, are often responsible for generating new convection on subsequent days. Raymond and Jiang showed that a midlevel vortex in a vertically sheared environment lifts air on its downshear side, and Trier et al. demonstrated that these motions also help to destabilize the environment by lifting moist and conditionally unstable air to saturation. When the direction of the shear vector opposes the direction of the (usually weak) ambient flow, the resulting convection tends to develop at the location of the vortex center and to move slowly (e.g., Fritsch et al. 1994; Trier and Davis 2002).

The synoptic and mesoscale environments in which MCVs typically develop have been well documented (e.g., Bartels and Maddox 1991), as have the characteristics of MCVs that go on to initiate subsequent convection (Trier et al. 2000b). However, motivated by the commonalities between some previously-studied events, as well as by several recent events of note, we will attempt herein to synthesize the characteristics of that subset of MCVs and other midlevel circulations that assist in initiating *extreme-rain-producing* convection and keeping it nearly stationary.

Additionally, the idealized findings of Raymond and Jiang (1990) and Trier et al.

(2000a) do not address another important component of extreme local rainfall production: the organization of the convective system. The organization is crucial in determining whether the MCS will produce smaller rainfall amounts over a large area or extremely large rainfall amounts over a local area that can lead to a flash flood threat. Schumacher and Johnson (2005) showed that most extreme-rain-producing MCSs have some degree of linear organization. However, MCV-related heavy rain events typically occur in environments with high relative humidity that are not conducive to the production of strong convectively-generated cold pools. Such cold pools (i.e., density currents) are typically the cause for linear organization in MCSs (e.g., Rotunno et al. 1988, Parker and Johnson 2004), but the fast propagation speeds of MCSs driven by strong cold pools make them less favorable for large rainfall amounts over a particular area. As such, understanding the mechanisms that lead to linear organization *and* slow system motion is an important research question. This study aims to bridge the gap between the more idealized studies of midlevel circulations in shear and the individual case study approach by examining the behavior of convection in an environment representative of such cases but without the unique attributes of each individual event.

In the chapters to follow, several extreme rain events that were associated with MCVs or other midlevel circulations will be examined to determine the processes responsible for initiating, organizing, and maintaining the heavy-rain-producing convection. Chapter 2 will provide a review of important past findings on the subjects of extreme rainfall, MCVs, and the organization and motion of MCSs. In chapter 3, six events will be introduced and their commonalities will be summarized through composite analysis. One of these events will be examined in detail in chapter 4 using observations and numerical simulations. In chapter 5, idealized simulations will be used to investigate the properties of deep convection that develops in the thermodynamic and kinematic environments typically observed in these events. Finally, chapter 6 will show the results of more complex simulations which are aimed at understanding the workings of quasi-stationary convective systems.

## Chapter 2

### BACKGROUND AND MOTIVATION

#### 2.1 Past research on extreme rainfall

As discussed by Doswell et al. (1996), certain atmospheric ingredients must be in place for extreme rainfall to occur. Doswell et al. describe these ingredients using a simple formula for any point on the earth:

$$P = \bar{R}D \tag{2.1}$$

where  $P$  is the total precipitation,  $\bar{R}$  is the average rainfall rate, and  $D$  is the duration of the rainfall. Thus, for large precipitation totals, either the rainfall rate or the rain duration (or both) must be large. Furthermore, since precipitation results from lifting moist air to condensation,

$$R = Ewq \tag{2.2}$$

where  $E$  is the precipitation efficiency,  $w$  the ascent rate in an updraft, and  $q$  the water vapor mixing ratio. This equation states that rapidly ascending air with large water vapor content is necessary to produce a significant rainfall rate. The rainfall rate is also limited by the precipitation efficiency, the proportion of water going into the system that actually falls out as precipitation. The rainfall duration is related to the system size and speed and the variations in rainfall intensity within a storm. A situation that is particularly conducive to extreme local rainfall is when deep convective cells (which typically have high rainfall rates) repeatedly pass over a given area, a process known as “echo training”. When the

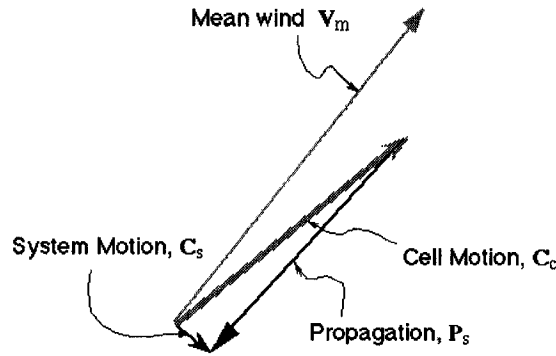


Figure 2.1: Schematic showing the near cancellation between cell motion and propagation, resulting in a quasi-stationary storm system. From Doswell et al. (1996).

motion of the convective system is slow, the rainfall duration at a given point increases, as does the total amount of rainfall.

Chappell (1986), Doswell et al. (1996), and Corfidi (2003) describe the motion of a convective system as the sum of two vectors: the velocity of the individual convective cells, and the propagation velocity resulting from the formation of new cells (Fig. 2.1). The cell motion is typically to the right of and slightly slower than the mean wind in the cloud layer (often calculated using the 850–300 hPa layer). The propagation velocity is defined by a variety of factors, including the direction of inflow to the storm, the location of preexisting boundaries and the location and motion of outflows produced by ongoing convective cells. When the cell motion and propagation vectors are nearly equal and they oppose each other, the motion of the overall system will be minimal (Fig. 2.1). An example of such a system is shown in Fig. 2.2. In this situation, new cells form upstream of the outflow boundary left behind by mature cells (i.e., a leftward-pointing propagation vector) and move from left to right (a rightward-pointing cell motion vector) over the same area, leading to large rainfall totals. Systems such as these with propagation vectors that oppose the cell motion are often described as “backward propagating” or “back-building” (e.g., Corfidi 2003).

In a study of 151 flash flood events in the United States, Maddox et al. (1979) listed four characteristics of the atmosphere that were common to almost all of the events they

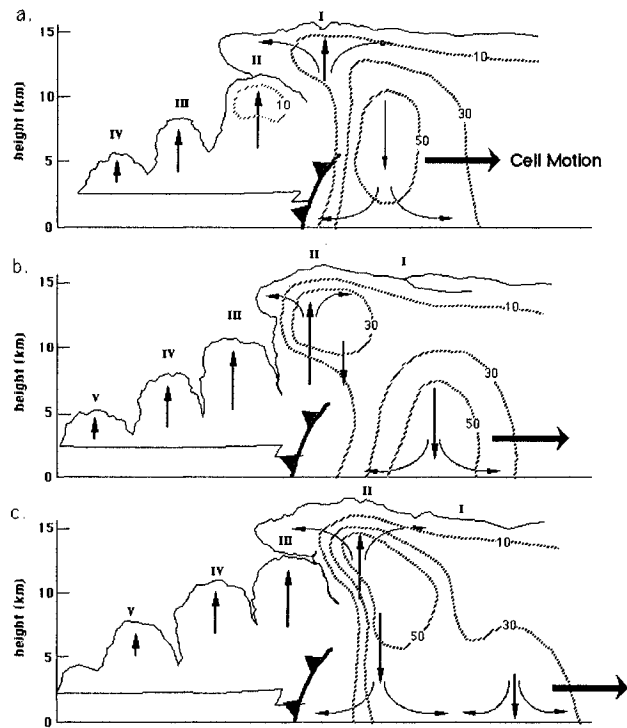


Figure 2.2: Schematic showing three stages in the evolution of a multicell thunderstorm system. Cells are labeled with Roman numerals (I, II, III, etc.); thin arrows indicate the updrafts, downdrafts, and divergence at the storm top and the surface associated with each cell; the frontal symbol indicates the low-level outflow boundary; the cell motion is indicated by the heavy arrow; and hatched lines show radar reflectivity and are labeled in dBZ. Note that the cells are moving left to right while the outflow boundary remains fixed in place. From Doswell et al. (1996)

studied, regardless of their location:

- (1) Heavy rains were produced by convective storms,
- (2) Surface dewpoint temperatures were very high,
- (3) Large moisture contents were present through a deep tropospheric layer,
- (4) Vertical wind shear was weak to moderate through the cloud depth,

In other words, satisfying (2.1) and (2.2), the necessary moisture and ascent were in place for large rainfall rates, and weak to moderate vertical shear allowed for organized but slow-moving storms.

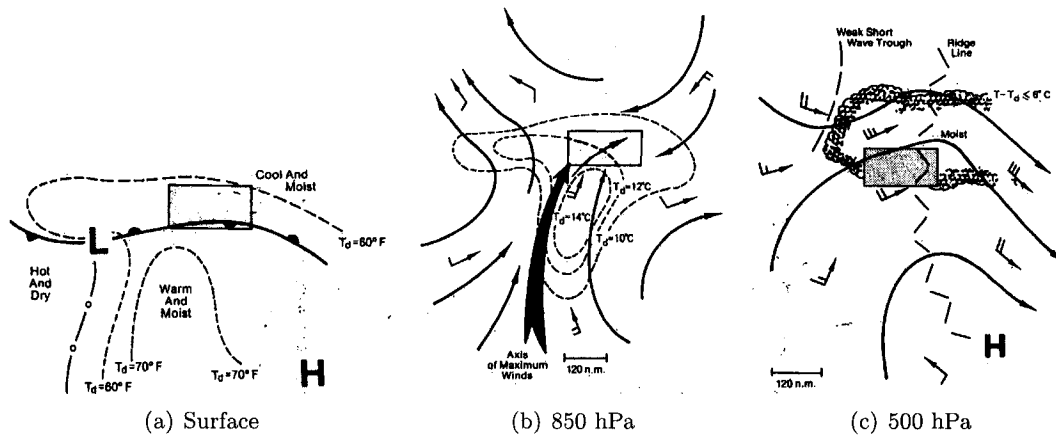


Figure 2.3: (a) Surface, (b) 850-hPa, and (c) 500-hPa patterns for a typical synoptic type flash flood event. Potential for heavy rains and flash flooding exists in the shaded rectangles. Winds are in knots with full barb representing 10 kt and flag representing 50 kt. From Maddox et al. (1979).

Davis (2001) also noted that moderate (as opposed to very large) values of convective available potential energy (CAPE) and high relative humidity (RH) through a deep layer are favorable for extreme rainfall production. Very large values of CAPE are usually associated with extremely intense updrafts, which limit the amount of time that water vapor spends at low levels. These circumstances are more conducive to large hail production than heavy rainfall. A deep moist layer is important because entrainment of dry air into the convective cloud (and thus reduction of precipitation efficiency) will be minimized. Deep moisture also limits evaporation of rainfall in the storm. Evaporation can lead to strong downdrafts and fast storm motion, which are not ideal for extreme local precipitation.

The ingredients discussed above are applicable to any situation, but several studies have examined the situations in which the atmospheric ingredients most often come together. The seminal study of this type is Maddox et al. (1979); their identification of the “synoptic,” “frontal,” and “mesohigh” flash-flood environments has guided much of the more recent research on the subject. Most relevant to the present study are the “frontal” (Fig. 2.3) and “mesohigh” (Fig. 2.4) types. In frontal events, warm, moist air from the south flows over a west-to-east-oriented surface boundary (Fig. 2.3a), leading to convection

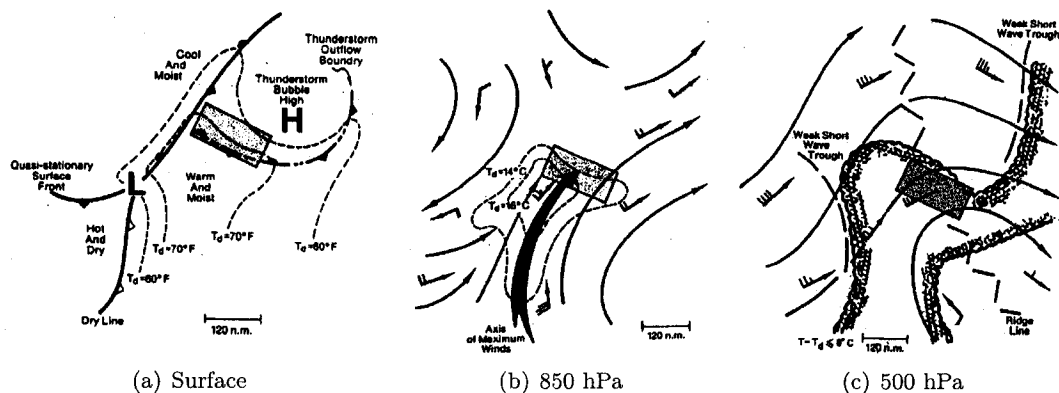


Figure 2.4: As in Fig. 2.3, except for a typical mesohigh event. From Maddox et al. (1979)

on the cool side (Fig. 2.3b). Winds aloft are approximately parallel to the boundary, and the heavy rains often occur near the large-scale ridge position (Fig. 2.3c) with a weak mid-level shortwave trough upstream. This arrangement leads to the development of new storms upstream, while mature cells are carried downstream by the upper-level winds. Mesohigh events are triggered by a quasi-stationary outflow boundary left behind by previous convection, with the heaviest rain falling on the cool side of the boundary and to the south or southwest of a convectively-generated mesohigh pressure center (Fig. 2.4a). The surface pattern is less defined for this type of event; Maddox et al. noted that some events occurred with a slow-moving surface front to the west, but for others there were no nearby fronts. As with the frontal type, the upper-level winds are approximately parallel to the outflow boundary (Fig. 2.4c), allowing storms to repeatedly develop and move over the same area.

Glass et al. (1995) and Junker et al. (1999) used composite analysis to further elucidate the synoptic and mesoscale conditions associated with extreme precipitation in the Midwest U. S. These studies emphasized the importance of strong low-level winds (often in the form of a low-level jet) advecting warm, moist air into the region where the heavy rainfall occurs. Glass et al.'s (1995) conceptual model (Fig. 2.5) applies to both the frontal and mesohigh-type events described by MCH79, as air with high equivalent potential temperature ( $\theta_e$ ) is advected over a quasi-stationary surface boundary by the low-level jet

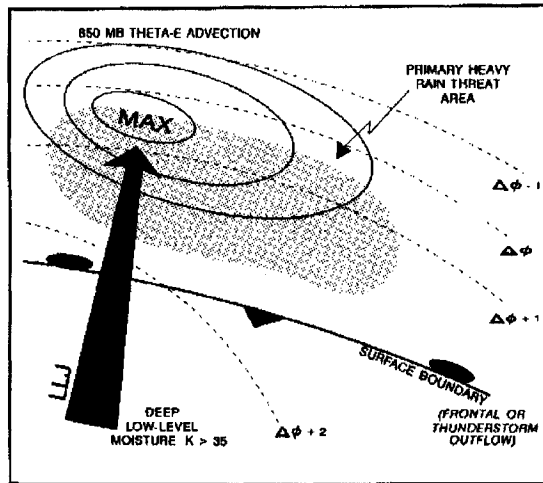


Figure 2.5: Conceptual model to highlight areas favorable for heavy convective rainfall. Dashed lines represent 850–300 hPa thickness contours. From Glass et al. (1995).

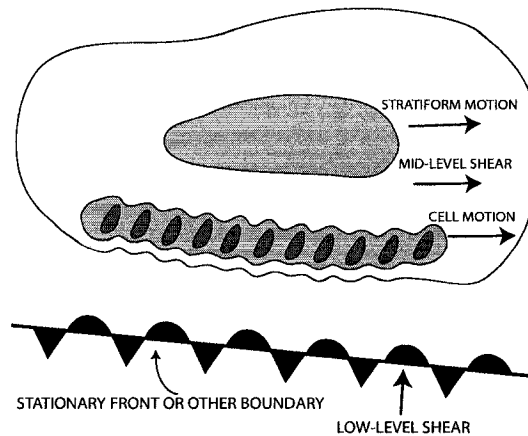
(LLJ). The highest potential for extreme rainfall is on the cool side of the boundary and coincides partially with the maximum of  $\theta_e$  advection. Junker et al. (1999) also noted that a maximum of positive  $\theta_e$  advection is typically located near the rainfall maximum and that extreme rain events often occur at the northern edge of the 850-hPa wind speed maximum. Trier and Parsons (1993) and Augustine and Caracena (1994) also showed that nocturnal MCSs often occur near the terminus of an LLJ, and LLJs were in place in all three types of flash floods described by Maddox et al. (1979). LLJs can be important to the development of extreme precipitation because they provide a source of moisture that replenishes the moisture falling out as rain in convective storms.

Moore et al. (2003) and Schumacher and Johnson (2005, 2006) added to the results of the aforementioned studies by considering the *organization* of deep convection in their analyses. In particular, these studies focused on extreme rain events that occurred in association with mesoscale convective systems (MCSs). Moore et al. (2003) examined MCS-related heavy rain events that occurred on the cool side of a surface boundary and confirmed the importance of moisture and temperature advection from an LLJ in these events. In addition to analyzing the environmental properties associated with extreme rain events,

Schumacher and Johnson (2005, 2006) showed how extreme-rain-producing convection is typically organized by examining radar data for 184 such events in the eastern two-thirds of the U. S. They found that 66% of all extreme rain events in this part of the country, and 74% of the warm-season events, were associated with MCSs. The radar-indicated organizational structures of many of these MCSs fit into previously-established patterns of organization (such as those found by Parker and Johnson (2000)), but two new patterns were identified. The first pattern, referred to as “training line/adjoining stratiform” (TL/AS; Fig. 2.6a), consists of a convective line, often oriented west-east, in which individual convective cells move in a line-parallel direction while there is very little motion in the line-perpendicular direction. TL/AS MCSs typically form on the cool side of a warm front or stationary front, consistent with Maddox et al.’s frontal type of flash flood. The second pattern, “back-building/quasi-stationary” (BB; Fig. 2.6b), occurs when convective cells repeatedly form upstream of their predecessors and pass over a particular area. These motion characteristics keep the system as a whole nearly stationary, and extreme local rainfall totals can result. Schumacher and Johnson (2006) showed that both of these MCS types occurred most commonly at night (Fig. 2.7), and nearly all of them were responsible for flash flooding.

Note that the schematic diagram for BB MCSs (Fig. 2.6b) reflects the presence of an outflow boundary, similar to that shown in Maddox et al.’s mesohigh type (Fig. 2.4a) and Doswell et al.’s schematic (Fig. 2.2). In many of the BB MCSs analyzed by Schumacher and Johnson (2005), an outflow boundary was evident in surface or radar observations, and the interaction between this boundary and low-level wind shear provided the lifting for repeated cell development. In other cases, however, it was difficult to identify any surface boundaries, yet the convection was still organized in a quasi-linear fashion and the system remained nearly stationary. In the very moist environments in which many BB MCSs form, cooling from the evaporation of raindrops—a major factor in the production of strong outflow boundaries and cold pools—is likely to be very limited. One of the primary questions this study intends to address is how long-lived, linearly-organized convection is

**A) TRAINING LINE -- ADJOINING STRATIFORM (TL/AS)**



**B) BACKBUILDING / QUASI-STATIONARY (BB)**

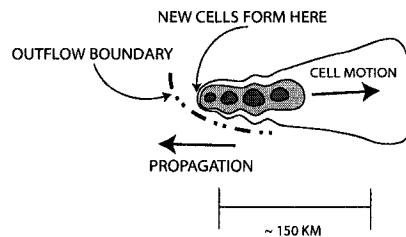


Figure 2.6: Schematic diagram of the radar-observed features of the (a) TL/AS and (b) BB patterns of extreme-rain-producing MCSs. Contours (and shading) represent approximate radar reflectivity values of 20, 40, and 50 dBZ. In (a), the low-level and mid-level shear arrows refer to the shear in the surface-to-925-hPa and 925–500-hPa layers, respectively, as discussed in section 4. The dash-dot line in (b) represents an outflow boundary; such boundaries were observed in many of the BB MCS cases. The length scale at the bottom is approximate and can vary substantially, especially for BB systems, depending on the number of mature convective cells present at a given time. From Schumacher and Johnson (2005).

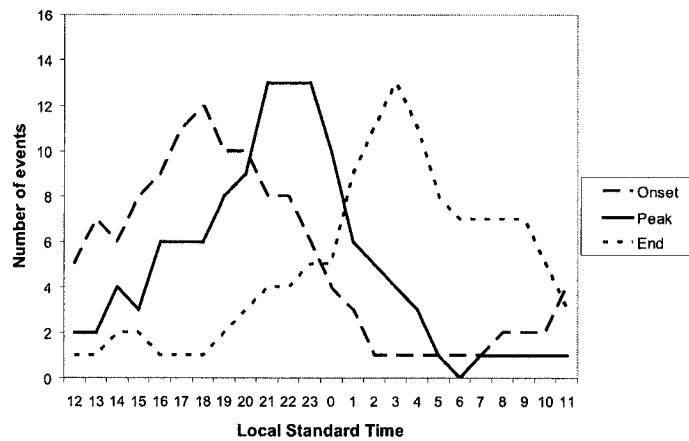


Figure 2.7: Diurnal frequency distribution for heavy rain onset, peak rainfall, and rainfall end for all 122 MCS-related extreme rain events, excluding the three classified as “multiple MCS” events. Number of events is smoothed with a 3-h running mean. From Schumacher and Johnson (2006).

maintained in environments that do not support the development of strong cold pools.

One particular BB MCS served as the initial motivation for the present study. This MCS, which occurred on 6–7 May 2000 in eastern Missouri, produced over 300 mm of rain in 9 h and led to destructive flash flooding that caused two fatalities and over \$100M in damage. This MCS was also of interest since it developed in an environment that provided few clues to indicate that such a large amount of rain would fall. Consistent with the past analyses of heavy rain environments discussed above, there were high values of precipitable water and relative humidity as well as a  $20 \text{ m s}^{-1}$  LLJ from the southwest. However, in contrast to the Maddox et al. (1979) flash flood types, there was relatively little conditional instability and no surface boundaries were apparent present prior to the onset of deep convection. The only midtropospheric feature evident was a mesoscale convective vortex (MCV) that developed in association with convection the previous night. Using observations and numerical simulations, this BB MCS will be studied in detail in chapter 4, with the goal of understanding the processes responsible for its initiation, organization, and maintenance.

## 2.2 The link between MCVs and heavy rainfall

Prior to discussing past studies that have examined the relationship between MCVs and extreme-rain-producing convection, some background on the dynamics of MCVs and their relationship to MCSs is warranted. The concept of “potential vorticity (PV) thinking,” reviewed by Hoskins et al. (1985), was extended to include diabatic heating effects (such as those produced in deep convection) by Haynes and McIntyre (1987). Haynes and McIntyre (1987) explained two important properties of PV, regardless of whether diabatic or frictional effects are present: first, that there can be no net transport of PV across an isentropic surface; and second, that PV can neither be created nor destroyed within a layer bounded by two isentropic surfaces. The Rossby-Ertel PV (denoted here by  $Q$ ) is defined as

$$\sigma Q = f + \zeta_\theta \quad (2.3)$$

where  $f$  is the Coriolis parameter,  $\zeta_\theta = \frac{\partial v}{\partial x} - \frac{\partial u}{\partial y}$  evaluated along an isentropic surface, and  $\sigma = -g^{-1}\partial p/\partial\theta$ , which is a positive number. Haynes and McIntyre put the PV equation into the conservation form

$$\frac{\partial(\sigma Q)}{\partial t} + \nabla \cdot \mathbf{J} = 0, \quad (2.4)$$

where

$$\mathbf{J} = \sigma Q \mathbf{u} + \mathbf{J}_\dot{\theta} + \mathbf{J}_\mathbf{F}. \quad (2.5)$$

The first term on the right hand side of (2.5) represents the advective flux of  $Q$ ,  $\mathbf{J}_\dot{\theta}$  is the nonadvective flux from diabatic heating, and  $\mathbf{J}_\mathbf{F}$  is the flux from frictional or other forces.  $\nabla$  represents the three-dimensional del operator.

These equations show that if there is no diabatic heating or friction, then the flux of PV is purely advective; in other words, PV is materially conserved. Of most concern when considering deep convection is the diabatic heating contribution  $\mathbf{J}_\dot{\theta} = \{\dot{\theta}\partial v/\partial\theta, -\dot{\theta}\partial u/\partial\theta, 0\}$ , where  $\dot{\theta}$  is the diabatic heating rate. Within a volume bounded by two isentropic surfaces, the amount of PV “substance” cannot change in time. How-

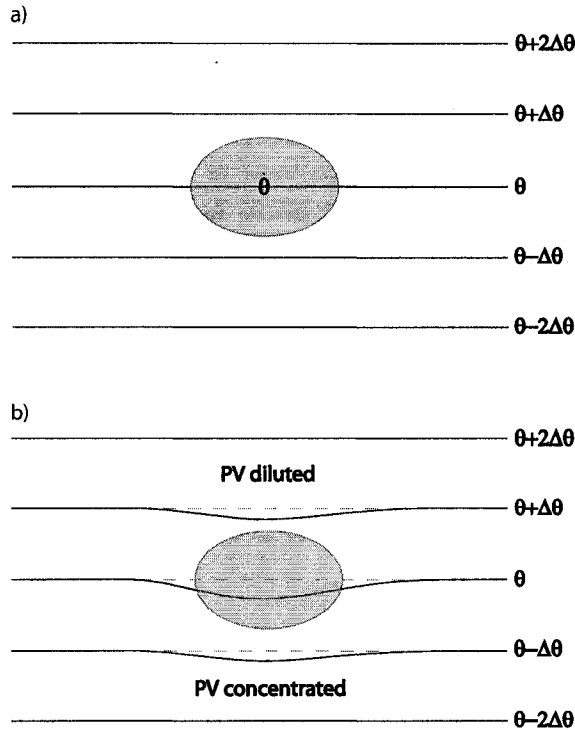


Figure 2.8: Vertical section showing the displacement of isentropic surfaces associated with the sudden application of localized heating. Panel (a) shows the undisturbed isentropes, and the location of the sudden heating is shown by the gray oval. Panel (b) shows the downward displacement of the isentropes after the heating is applied. The dashed gray lines show the initial position of the isentropes. Below the location of the heating, mass has been evacuated, and the PV is concentrated; whereas the mass has increased above the heating and the PV has been diluted. Adapted from Haynes and McIntyre (1987).

ever, diabatic processes, such as latent heating, can transport mass across isentropes, so that the mass within that volume can change. When the mass between the isentropic surfaces increases, the “PV substance” is diluted, whereas when the mass decreases, the PV becomes concentrated. This can be illustrated by a situation where an instantaneous diabatic heating is applied to a stably stratified, rotating fluid (Fig. 2.8a). Assuming this heating is applied much faster than the fluid can adjust to it, the result is that the isentropes are lowered in the region of the heating (Fig. 2.8b), and mass has been transported upward. Below the heating, the PV substance has been concentrated, and above the heating it has been diluted. As such, a positive PV anomaly (relative to the undisturbed state) exists below the maximum heating. This is analogous to what happens in deep convection:

latent heating and upward mass transport are maximized at midlevels, and a positive PV anomaly develops below the maximum heating.

Of course, in MCSs in the real atmosphere, other effects are also important. If the horizontal scale of the latent heating associated with the MCS is of the same order as the Rossby radius of deformation, as is often the case in midlatitudes, a non-negligible fraction of the potential energy will be converted into balanced flow (e.g., Schubert et al. 1980). Thus, the atmosphere will evolve toward a state in which the PV anomalies shown in Fig. 2.8b become balanced circulations with cyclonic flow around the positive anomaly and anticyclonic flow around the negative anomaly. Furthermore, the vertical profile of heating in an MCS is more complicated than shown in the simple thought experiment, particularly when a region of stratiform rainfall has developed. In an idealized modeling study, Hertenstein and Schubert (1991) showed that the combination of convective and stratiform heating is particularly conducive to the development of midlevel positive PV anomalies. Such midlevel anomalies are often observed to develop in association with MCSs, and they are generally referred to as MCVs.

Raymond and Jiang (1990) proposed a theoretical basis for how MCVs or other midlevel positive PV anomalies can assist in the initiation and maintenance of additional deep convection. They described how a steady-state vortex in a sheared environment promotes lifting on the downshear side of the vortex (Fig. 2.9). A balanced, warm-core vortex such as an MCV typically has a potential temperature structure where isentropes at low levels have been deformed upward as shown in Fig. 2.9a owing to the presence of a dome of cool air near the surface. With ambient westerly vertical shear, low-level air approaches the vortex from the east and rises along the upward-sloping isentropes. Furthermore, the presence of ambient shear implies the presence of background baroclinity if thermal wind balance is to be maintained. Fig. 2.9b shows how additional ascent can occur as the cyclonic flow associated with the vortex moves adiabatically along this baroclinic zone.

Trier et al. (2000a) extended Raymond and Jiang's results by showing that the ascent

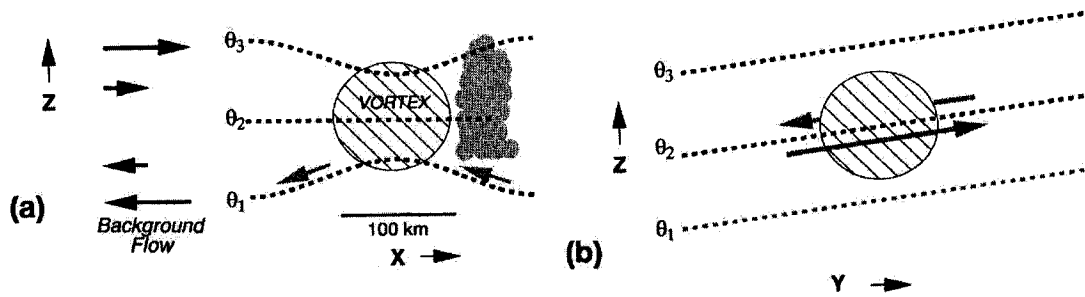


Figure 2.9: Schematic diagram illustrating quasi-balanced lifting in the vicinity of a positive PV anomaly (hatched region) in ambient vertical shear. (a) Upglide associated with the background vertical shear along isentropic surfaces deformed by the vortex, and (b) vortex-induced motion along the isentropic surfaces of the background baroclinic zone. From Trier et al. (2000b), adapted from Raymond and Jiang (1990).

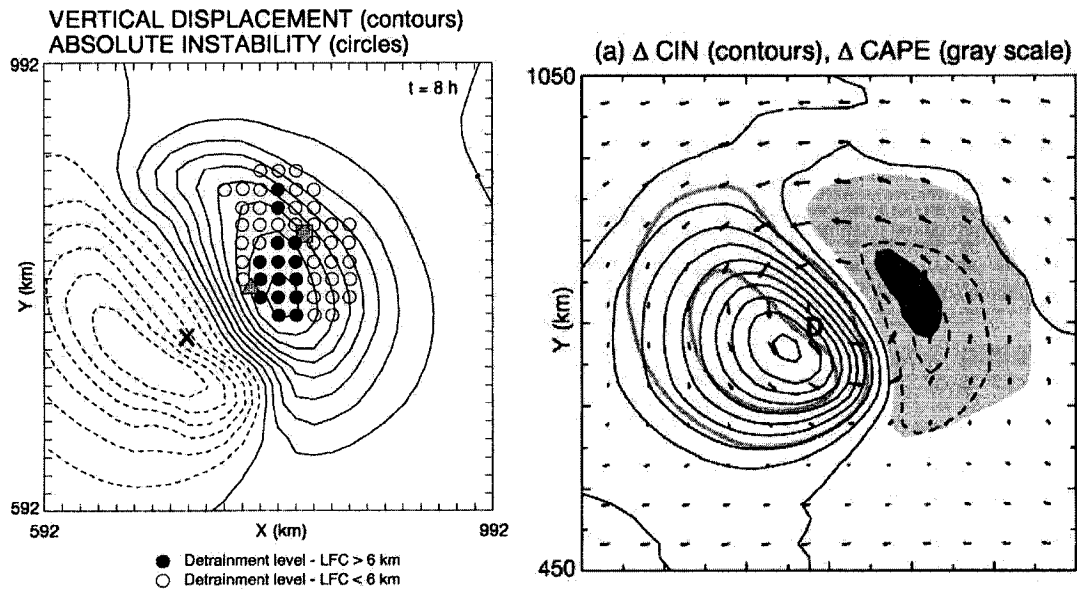


Figure 2.10: (a) Gridpoint locations of absolute thermodynamic instability in a saturated layer between 1.25 and 2.5 km AGL (circles) superposed on the vertical displacement field at 1.5 km AGL (100-m contour intervals, negative values dashed) for the control simulation at 8 h. Solid (open) circles represent locations of deep (shallow) convective instability of this layer according to predictions from parcel theory. The symbols represent the locations of the vertical vorticity centroid at 1.5 (X), 3.5 (triangle), and 5.5 (square) km AGL. (b) The 1.5-km AGL system-relative vectors at 8 h, with (a) 8-h change in the CIN for the lowest 500 m AGL ( $10 \text{ J kg}^{-1}$  contours, positive values solid, negative values dashed) and the 8-h change in CAPE for the lowest 500 m AGL [ $100\text{--}600 \text{ J kg}^{-1}$  (light shading),  $\geq 600 \text{ J kg}^{-1}$  (dark shading),  $-100$  and  $-600 \text{ J kg}^{-1}$  contoured in gray]. The annotations D and U denote the respective locations of the maximum downward and upward displacements. From Trier et al. (2000a).

caused by the vortex in shear can also help to destabilize the environment by lifting moist and conditionally unstable air to saturation. This can result in moist absolutely-unstable layers (MAULs; Bryan and Fritsch (2000); Fig. 2.10a). The vertical displacements associated with this lifting also lead to significant increases in convective available potential energy (CAPE) and reductions in convective inhibition (CIN; Fig. 2.10b). All of these factors make the environment more favorable for additional convective development on the downshear side of an MCV, and observations from the recent Bow Echo and MCV Experiment (BAMEX) have confirmed that these are important processes in midlatitude MCVs (Davis and Trier 2007; Trier and Davis 2007)

Much of the above discussion has considered the case of an eastward-moving MCV within westerly ambient *flow* and westerly *shear*. In that situation, the convective cell motion and propagation would be in the same direction, which is not particularly conducive to a slow-moving convective system (Fig. 2.1). However, if the direction of the shear vector *opposes* the direction of the ambient flow, the resulting convection is more likely to move slowly and produce excessive local rainfall. Several past studies have examined significant midlatitude flash flood events in which this occurred (e.g., Bosart and Sanders 1981; Fritsch et al. 1994; Trier and Davis 2002). These case studies provide ample insight into the processes by which MCVs can assist in the development and maintenance of slow-moving, heavy-rain-producing MCSs.

In the case studied by Fritsch et al. (1994), they observed that convection continuously developed near the center of the vortex—rather than at the outflow boundaries at the periphery—even though there was apparently very little convective available potential energy (CAPE) near the circulation’s center. In that event, an LLJ was also present, and Fritsch et. al. hypothesized that the horizontal vorticity associated with the reversed shear above the LLJ opposed the horizontal vorticity associated with the surface cold pool, allowing for the development of deep convection, but only once the air had been lifted *above the cold pool* (Fig. 2.11a). This contrasts with what would happen without an LLJ

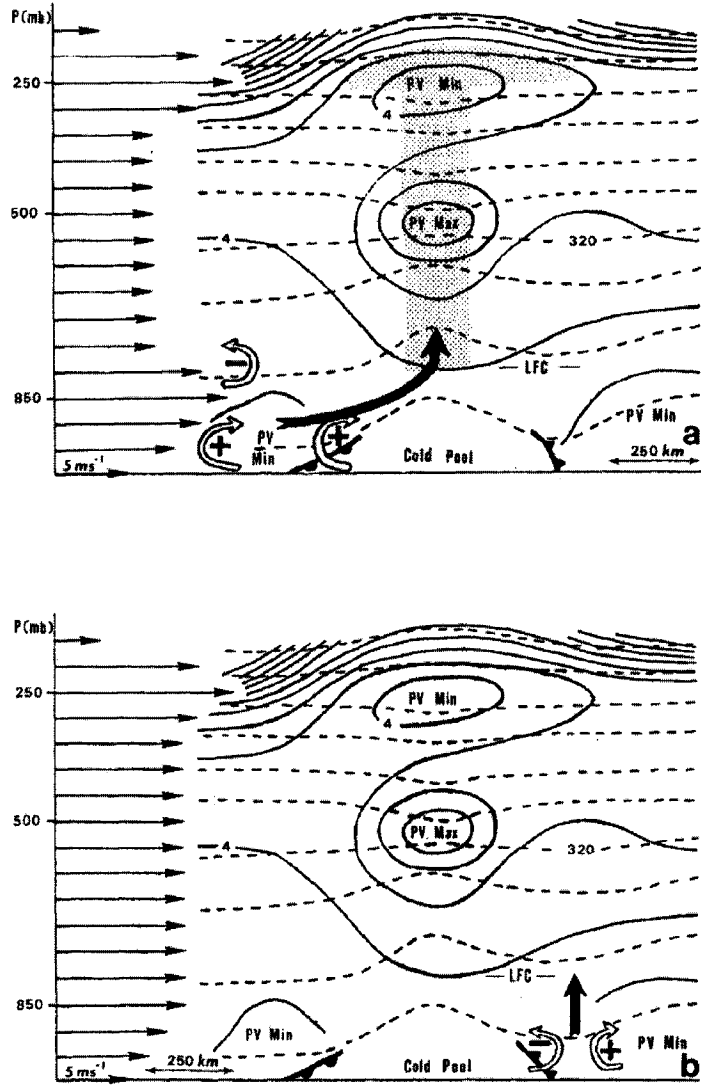


Figure 2.11: Conceptual diagram of the structure and redevelopment mechanism of the mesoscale warm core vortex. Thin arrows along ordinate indicated vertical profile of environmental wind. Open arrows with plus or minus signs indicated sense of vorticity produced by the cold pool and by the environmental wind shear. Thick solid arrow indicates updraft axis created by the vorticity distribution. Frontal symbols indicated outflow boundaries. Dashed lines are potential temperature (5-K intervals) and solid lines are potential vorticity ( $2 \times 10^{-7} \text{ m}^2 \text{ s}^{-1} \text{ K kg}^{-1}$  intervals). (a) System is propagating left to right at about 5–8  $\text{m s}^{-1}$  and is being overtaken by low-level high- $\theta_e$  air in the low-level jet. Air overtaking the vortex ascends isentropic surfaces, reaches its level of free convection (LFC), and thereby initiates deep convection. (b) As in (a) except that the vertical wind profile has been modified so that the vortex is overtaking the low-level high- $\theta_e$  air. From Fritsch et al. (1994).

(Fig. 2.11b), in which case convection is favored along the cold-pool edge on the eastern side of the vortex. Trier and Davis (2002) and Davis and Trier (2002) found that balanced uplift associated with an MCV played a similarly important role in the maintenance of the extreme-rain-producing MCS that they studied. The present study will attempt to synthesize the characteristics of such extreme rain events that occur near midlevel circulations. The results to be presented will establish that there are several characteristics common to midlevel vortex-related heavy rain events, including the reversal of the wind shear vector with height (such as in Fig. 2.11a).

Using relatively simple 2-dimensional simulations, Crook and Moncrieff (1988; hereafter CM88) presented several results that are relevant to the present study. They demonstrated a process for MCS maintenance that was different from the mechanism proposed by Rotunno et al. (1988): in a conditionally unstable environment with meso- to synoptic-scale convergence, convection can be long lived without the benefit of lifting by a convectively-generated cold pool. In a simulation of a heavy-rain-producing MCS associated with an MCV, Davis and Trier (2002) similarly found that convection was organized and long lived with only a very weak cold pool, and they concluded that “the simulated nocturnal cold pool helped localize the convection, but did not directly maintain its intensity through the mechanism advanced by Rotunno et al. (1988).” CM88 also showed that the low-level structure beneath their simulated convection progressed through three stages: first, a gravity wave without stagnation (Fig. 2.12a), next, a gravity wave with stagnation (Fig. 2.12b), and then a density current (i.e., cold pool) later on (Fig. 2.12c). Other studies (e.g., Dudhia et al. 1987; Schmidt and Cotton 1990; Parker 2008) have also shown the importance of low-level gravity waves, either instead of or in addition to density currents, to the structure of convective systems. Schmidt and Cotton (1990) simulated convection in a thermodynamic environment with stable low levels and near-neutral midlevels. They found that latent heating was responsible for exciting internal gravity waves near the surface as well as aloft. With no initial flow (Fig. 2.13a), symmetric low-level waves formed and propagated away,

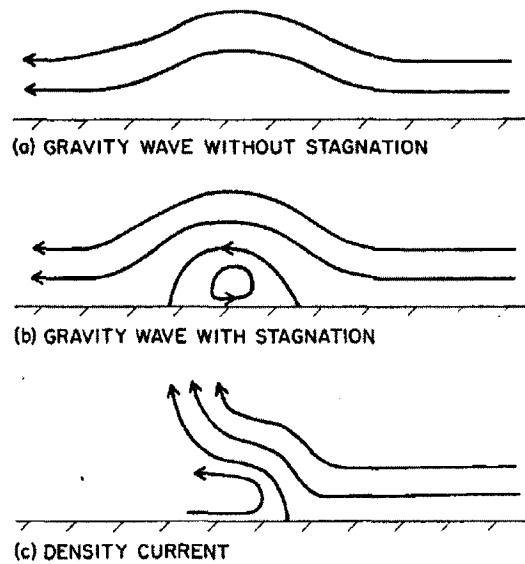


Figure 2.12: Schematic representation of the three regimes of low-level flow. In (c) the air ahead of the system is shown being lifted in the system's updraft, however at early stages of this regime some of this air is circulated into the cold pool. From Crook and Moncrieff (1988).

but when a sheared flow was included, a single wave developed, amplified, and helped to define the structure of a long-lived convective system (Fig. 2.13b).

Stensrud and Fritsch (1993) summarized the differences between gravity waves and density currents as propagation mechanisms for deep convection, and Koch and Golus (1988) illustrated the expected relationships between pressure, wind, and vertical motion in gravity waves versus those occurring solely from convective motions (Fig. 2.14). Namely, in a gravity wave, wind perturbations are in phase with pressure perturbations and out of phase with the strongest convergence and vertical motion.

To further investigate how long-lived, linearly-organized convection is maintained when the environment is not supportive of strong cold pools, an approach similar to that of Dudhia and Moncrieff (1987) and CM88 will be used in idealized simulations in chapter 6. They simulated the initiation and maintenance of squall lines that occur within large-scale lifting; they were not specifically concerned with MCVs, but MCVs represent another application of their ideas. Other studies that have simulated convection within environments

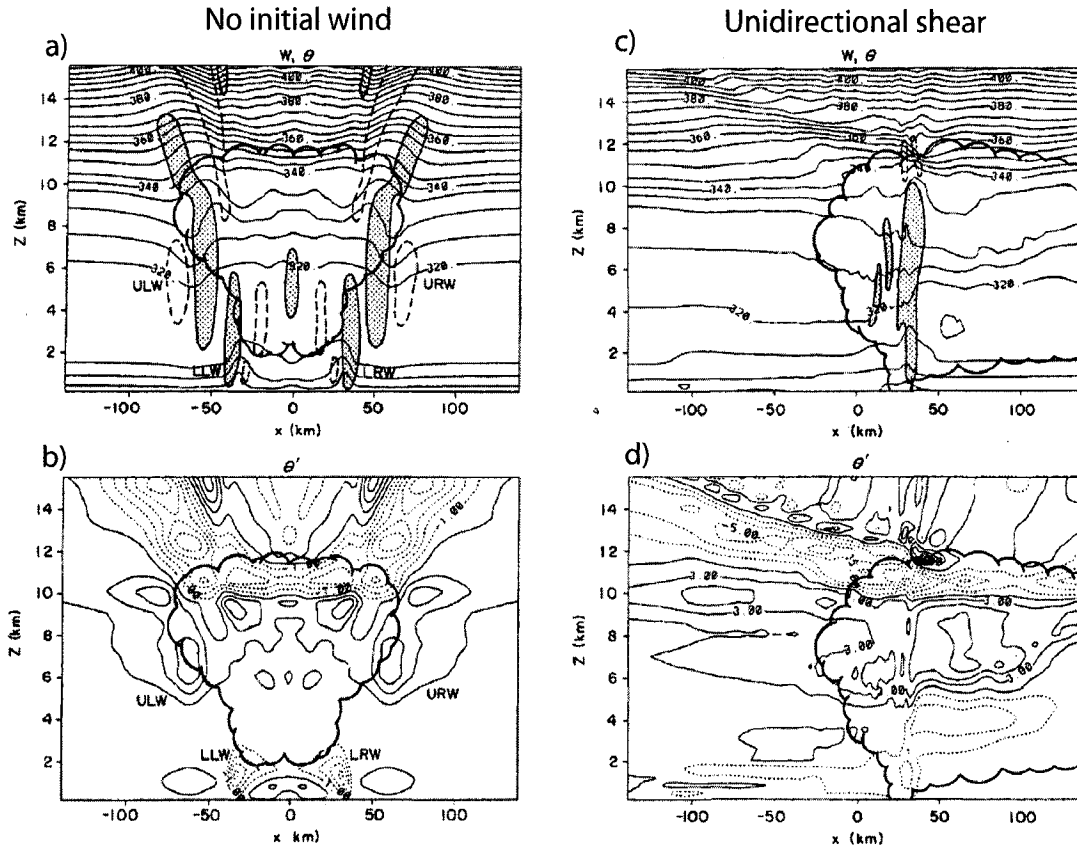


Figure 2.13: Vertical  $x$ - $z$  cross-sections of (a–b) the zero initial wind experiment at 3600 s and (c–d) the control experiment at 7200 s. (a, c) Potential temperature (contoured every 5 K) and vertical motion (updrafts greater than  $1 \text{ m s}^{-1}$  shaded, downdrafts less than  $-1 \text{ m s}^{-1}$  denoted by the dashed lines). (b, d) Perturbation potential temperature (contoured every 2 K). The annotations “LLW,” “LRW,” “ULW,” and “URW” in panel (a) denote gravity waves in the lower left, lower right, upper left, and upper right, respectively. Adapted from Schmidt and Cotton (1990).

with background lifting include Xin and Reuter (1996), Jewett and Wilhelmson (2006), and a recent study by Loftus et al. (2008) which was also used to design the idealized experiments in chapter 6.

Another important factor in the organization and motion of MCSs is the vertical wind shear. As discussed briefly above, extreme-rain-producing MCSs that occur in association with midlevel circulations typically develop in complex vertical wind profiles that include an LLJ. The combination of the LLJ and generally weak ambient midlevel flow results in a sharp reversal of the wind shear vector with height. As will be shown, the shear

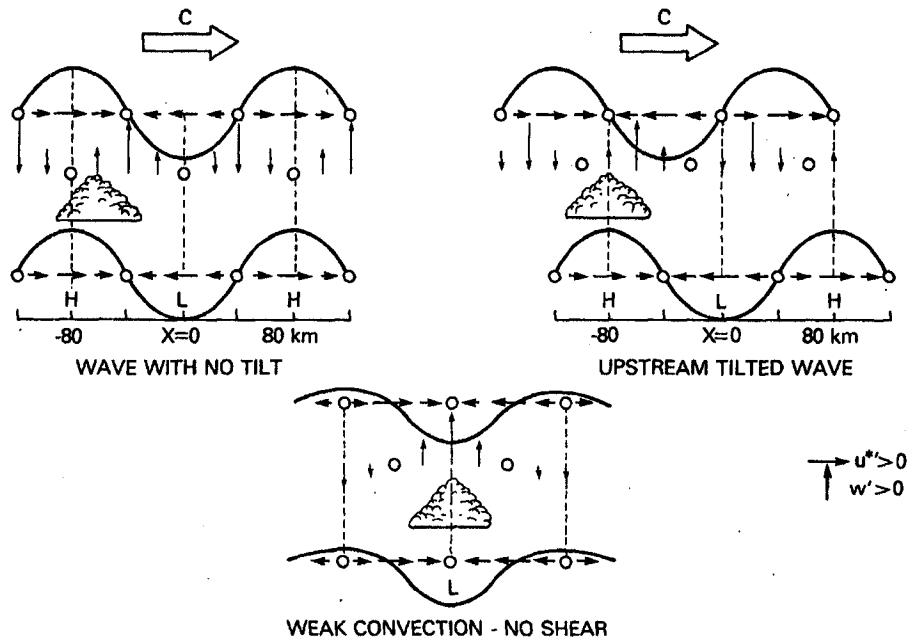


Figure 2.14: Schematic illustration of the height variation in the phase relations between the horizontal wind component in the direction of wave propagation ( $u^*$ ) and the wave-induced vertical motions ( $w'$ ) for both an erect (left panel) and tilted (right panel) gravity wave, which is propagating to the right with phase speed  $C$ . Bottom and top wave trains in each case refer to surface and 5 km altitude, respectively, whereas vertical motions are only for the latter height, as obtained from integrated mass divergence below that level. Also shown is location of strongest convection relative to gravity wave crest, assumed in both cases to be  $\pi/4$  behind maximum updraft. Bottom panel depicts phase relations for weak convection in an unsheared environment below level of nondivergence. “High” and “low” refer to pressure perturbations. From Koch and Golus (1988).

and the resulting convection are fundamentally three-dimensional. The majority of past modeling research on midlatitude squall lines has only included two-dimensional shear, however, there are a number of important studies that have considered 3D shear profiles, including shear that has a component parallel to the convective line (e.g., Dudhia and Moncrieff 1987; Trier et al. 1996; Parker 2007a, b). The two studies by Parker examined convective lines with parallel stratiform (PS) precipitation, which are closely related to the BB MCSs of interest in this study. Parker found that PS MCSs arise in strong along-line shear, although the convective line eventually tends to become perpendicular to the shear. Numerical investigations that include a strong reversal of shear at low levels are also

relatively few. Several studies have simulated squall lines that occur in association with the African easterly jet, which is usually located at approximately 700 hPa (e.g., Thorpe et al. 1982; Dudhia et al. 1987; Lafore and Moncrieff 1989). Robe and Emanuel (2001) simulated convective lines in a wide variety of shear profiles, including reverse-shear profiles with a jet at approximately 2 km AGL. However, the LLJs that are observed to occur with the MCSs of interest in this study are typically located much closer to the surface. The simulations to be presented in chapters 5 and 6 will investigate how a strong LLJ (such as those that are commonly observed in the central U. S.) affects the organization of convection and what role it may play in producing the back-building, quasi-stationary type of MCSs that often produce extreme rainfall.

## Chapter 3

### OBSERVATIONS AND COMPOSITE ANALYSIS OF QUASI-STATIONARY CONVECTIVE SYSTEMS ASSOCIATED WITH MIDDLELEVEL CYCLONIC CIRCULATIONS

#### 3.1 Identification of events

Six extreme rainfall events associated with midlevel circulations will be the focus of this chapter, and the events were identified in several ways. They are not intended to be a comprehensive list of events of this type, but they were identified by the authors as having many similarities such that some patterns began to emerge. Other similar events have likely occurred in the past, but it is unclear how frequently they occur. The details of the six events are shown in Table 3.1. One of the cases was described in the literature (27–28 May 1998, Trier and Davis 2002) and one (6–7 May 2000) will be examined in detail in chapter 4 of this dissertation. Two (5–6 May 2000 and 3–4 June 2000) were part of the investigation of extreme rain events in Schumacher and Johnson (2005). And two were very recent events (18 June 2007 and 20 August 2007), which occurred during the anomalously wet summer of 2007 in the southern Plains of the United States. Despite this subjective approach to choosing events, all have several similarities:

- Gauge-observed rainfall accumulation greater than 200 mm (7.9 in) in less than 12 h.
- Rainfall produced by an organized convective system that was nearly stationary.
- Heavy rainfall that was highly localized.

Table 3.1: Details of the six MCV-related extreme rain events. The states affected are shown in the “Location” column. The maximum rainfall shown below is the highest 24-h total reported at a NWS/Cooperative or hourly rain gauge.

Date	Location	Max. Rain (mm/in)	Reference
27–28 May 1998	Arkansas	254/10.0	Trier and Davis (2002)
5–6 May 2000	Oklahoma	206/8.1	
6–7 May 2000	Missouri	309/12.1	Chapter 4
3–4 June 2000	Texas	281/11.1	
18 June 2007	Texas	203/8.0	
20 August 2007	Missouri	266/10.5	

- The presence of a preexisting midlevel circulation near where the convective system developed.
- Significant flash flooding resulting from the rainfall.

These events have much more in common, which will be demonstrated in section 3.5.

### 3.2 Data sources and analysis methods

Observations and analyses from several sources will be shown in the following sections.

Among these datasets will be:

- Rain gauge observations from both the National Weather Service (NWS) Cooperative high-resolution 24-h gauge network and from the hourly precipitation dataset (HPD).
- Rapid Update Cycle (RUC; Benjamin et al. 2004) hourly analyses, which have horizontal grid spacing of approximately 40 km and have been interpolated to pressure levels with 25-hPa spacing between 1000–100 hPa.
- Level 2 and 3 base radar reflectivity data from WSR-88D radars.
- Representative radiosonde observations, when available. (The soundings taken at the 0000 and 1200 UTC observing times are often not representative of the envi-

ronment between observations, especially in cases such as these where a nocturnal low-level jet is present. Also, the combination of the sparse radiosonde network and the localized nature of the convective systems makes it difficult to find truly representative soundings.)

- Storm reports from the National Climatic Data Center's online Storm Events database at <http://www4.ncdc.noaa.gov/cgi-win/wwcgi.dll?wwEvent~Storms>

To show the important features in these events, data from individual events will be presented, as will the results of composite analysis on the RUC data. Though the RUC analyses are not without problems, they have been shown to be relatively accurate in capturing the thermodynamic environment near convection (Thompson et al. 2003) as well as MCV circulations (Davis et al. 2002). To perform the composite analysis, hourly precipitation observations were used to identify the location and time nearest to the heaviest rainfall in each event. Then, a  $41 \times 41$  grid point domain (approximately  $1640 \text{ km} \times 1640 \text{ km}$ ), centered at the RUC grid point nearest the heaviest rainfall location was created for each event, and these grids were averaged to create the composites shown in section 3.5. Composite grids for the hour of heaviest rainfall, as well as 12 and 6 hours prior to and 6 hours after the heaviest rainfall were created. This composite technique was generally the same as that used in Schumacher and Johnson (2005), except that the domain used in this study is larger, and there was no need to rotate any of the grids because the convective systems were all oriented generally west-to-east (section 3.3).

### **3.3 Description of the extreme rain events**

In this section, a very brief overview of each event is presented. For each event, an upper-level synoptic analysis at 0000 UTC (typically several hours before convection initiation) and a radar image at the time of peak rainfall will be shown, along with any other significant details as applicable. This will set the stage for the composite analysis that will be presented in the next section.

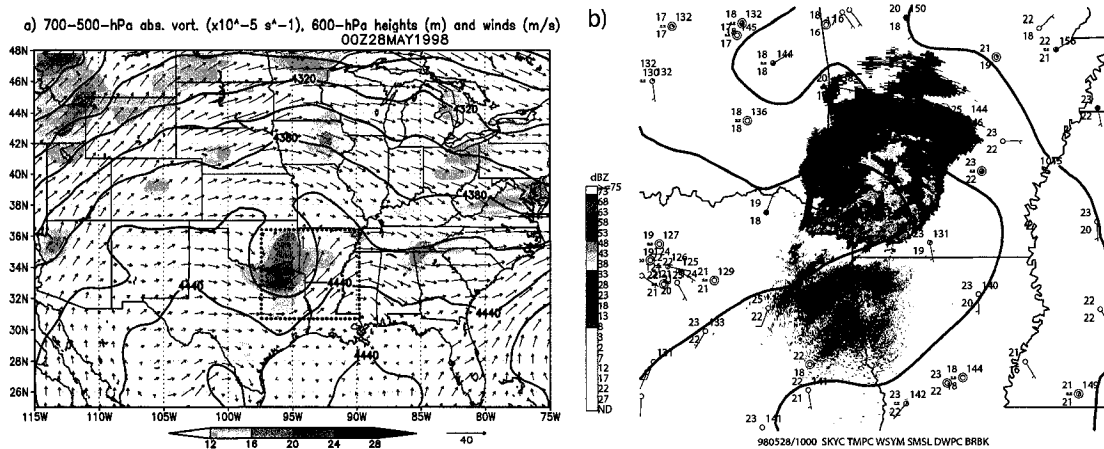


Figure 3.1: (a) Absolute vorticity averaged over the 700–500-hPa layer ( $\times 10^{-5} \text{ s}^{-1}$ , shaded every  $4 \times 10^{-5} \text{ s}^{-1}$  for values above  $12 \times 10^{-5} \text{ s}^{-1}$ ), 600-hPa heights (thick lines contoured every 30 m), and winds (vectors,  $\text{m s}^{-1}$ , with vector length scale indicated at bottom) from the Rapid Update Cycle analysis at 0000 28 May 1998. (b) Base radar reflectivity (dBZ) from the Shreveport, Louisiana WSR-88D at 0956 UTC, surface observations and objective analysis of pressure corrected to sea level (contoured every 1 hPa) at 1000 UTC 28 May 1998. The location of the map is shown by the dotted rectangle in panel (a).

### 3.3.1 27–28 May 1998

A thorough investigation of the 27–28 May 1998 event was presented in Trier and Davis (2002) and Davis and Trier (2002); we include it in this study because it fits the pattern of MCV-related extreme rain events and because it has been well documented in the literature. In this event, a strong MCV developed within the stratiform region of an MCS in central Texas early on 27 May 1998. This vortex drifted eastward through the day on the 27th, and by 0000 UTC<sup>1</sup> 28 May it was located over northeastern Texas (Fig. 3.1a). Around this time, new convection initiated near the vortex, and it eventually organized into a back-building, quasi-stationary MCS (Fig. 3.1b). (This was the MCS labeled “S2” by Trier and Davis (2002).) It produced very heavy rainfall in extreme northeastern Texas and southwestern Arkansas, with a maximum report of 262 mm (10.30 in) at Nashville, AR. Many homes, businesses, and roads in the Texarkana area were flooded, resulting in \$1.9M in damage. In animations of the radar reflectivity (not shown), the strong cyclonic

<sup>1</sup> For all of these cases, 0000 UTC corresponds to 1900 local daylight time.

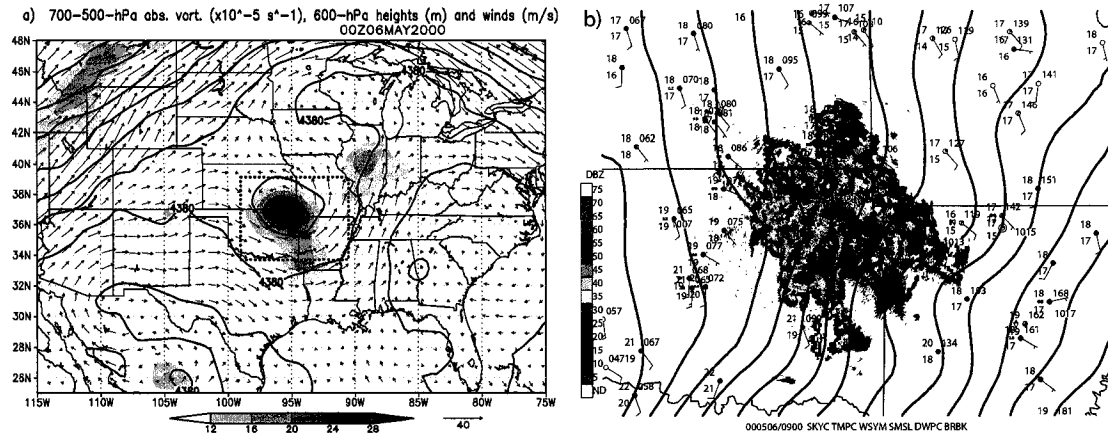


Figure 3.2: (a) As in Fig. 3.1a, except for 0000 UTC 6 May 2000. (b) As in Fig. 3.1b, except radar observations are from the Tulsa, Oklahoma radar at 0859 UTC and surface observations and analysis are from 0900 UTC 6 May 2000.

circulation of the MCV was evident in the stratiform precipitation region. At the surface (Fig. 3.1b), a weak low-pressure center was located just to the west of the convective line, and an associated mesoscale cyclonic circulation surrounded the MCS. This convective system in turn assisted in reintensifying the vortex, which went on to spawn additional convection on subsequent days.

### 3.3.2 5–6 May 2000

The 5–6 May 2000 heavy-rain-producing MCS occurred in conjunction with a strong MCV that had existed for several days prior to this event. It began as a cutoff low within a large-scale blocking pattern over the southern Plains, and was responsible for initiating convection each afternoon and evening, which then reinforced the vortex's circulation. (The full evolution of the MCV will be shown in the next chapter in Fig. 4.2.) By 0000 UTC 6 May 2000, the MCV was located over northeast Oklahoma (Fig. 3.2a), and it proceeded to assist in the initiation of convection in that area. Surface observations (Fig. 3.2b) showed nearly saturated conditions and moderate southeasterly flow. As the convection developed, it was scattered at first but then organized into several lines and clusters (Fig. 3.2b) that produced rainfall amounts exceeding 200 mm and flash flooding in several areas of northeast

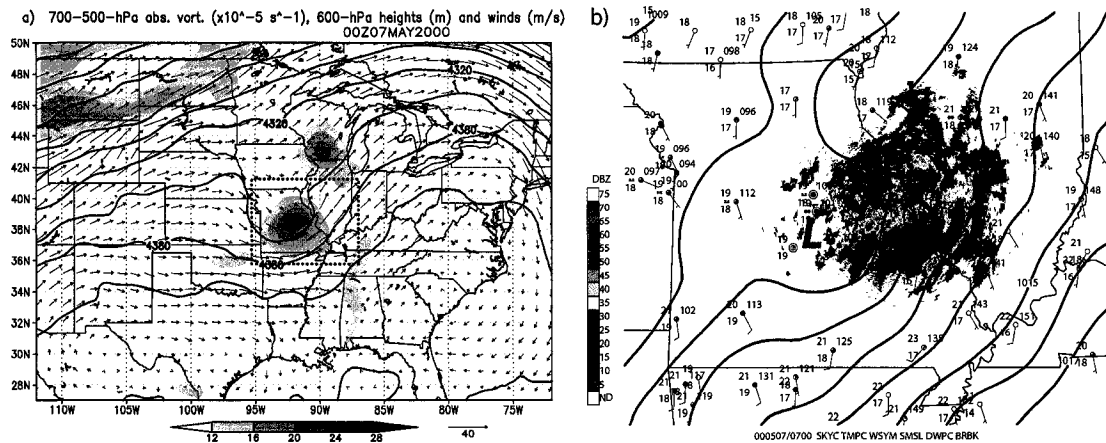


Figure 3.3: (a) As in Fig. 3.1a, except for 0000 UTC 7 May 2000. (b) As in Fig. 3.1b, except radar observations are from the St. Louis, Missouri radar at 0659 UTC and surface observations and analysis are from 0700 UTC 7 May 2000.

Oklahoma. The flooding caused over \$9M in damage and one fatality. The evolution of the MCS's organization was complex, with aspects of it resembling the LS and TS types of Parker and Johnson (2000), as well as the TL/AS and BB patterns described by Schumacher and Johnson (2005) at different stages of its life cycle.

### 3.3.3 6-7 May 2000

After assisting in the initiation of heavy rainfall and flash flooding in Oklahoma on the night of 5 May and the morning of 6 May, the MCV reintensified and moved eastward to central Missouri by the evening of 6 May. At 0000 UTC 7 May, the vortex was centered over Missouri (Fig. 3.3a) and again began to assist in the initiation of deep convection around 0300 UTC. This convection organized into a west-to-east oriented cluster of convection that remained nearly stationary through 1200 UTC (Fig. 3.3b). Associated with the development of the MCS was the appearance of a surface mesolow and pressure trough upstream of the deep convection (Fig. 3.3b). This and other processes involved in this quasi-stationary MCS were described in Glass et al. (2001) and will be explored in detail in chapter 4. Over 300 mm of rain fell between 0300 and 1200 UTC in east-central Missouri, which led to devastating flooding in the towns of Washington and Union, MO.

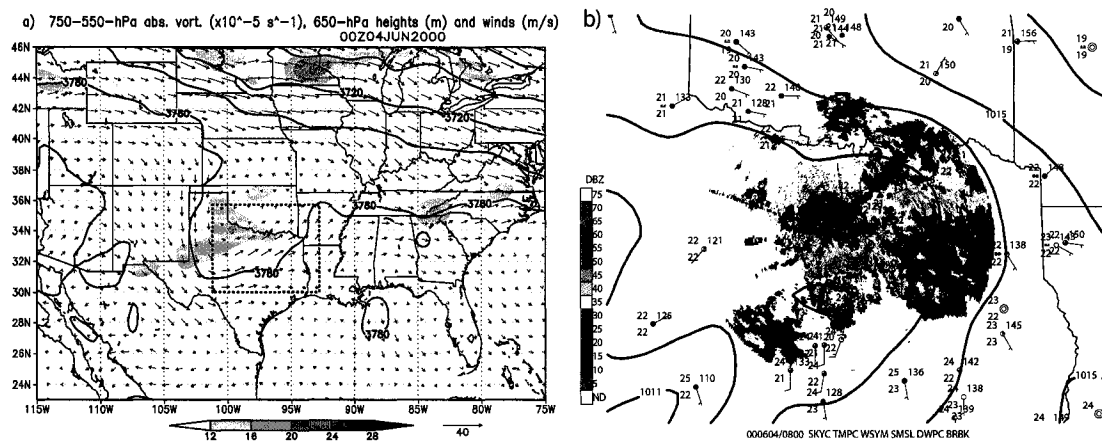


Figure 3.4: (a) As in Fig. 3.1a, except vorticity is averaged over the 750–550-hPa layer and heights and winds are at the 650-hPa level at 0000 UTC 4 June 2000. (b) As in Fig. 3.1b, except radar observations are from the Dallas–Fort Worth, Texas radar at 0759 UTC and surface observations and analysis are from 0800 UTC 4 June 2000.

The flash flooding caused two fatalities and over \$100M in damage.

### 3.3.4 3–4 June 2000

Similar to the extreme rain events on 5–7 May 2000, the synoptic pattern leading up to the 3–4 June 2000 event involved a midlevel low that moved slowly eastward, helped to initiate convection each day, and was intensified and organized by that convection. This low moved from Mexico into west Texas on 1 June 2000 (not shown) and slowly drifted northeast such that it was located over north Texas as a positively tilted trough at 0000 UTC 4 June 2000 (Fig. 3.4a). Unlike the previously-discussed cases, the midlevel circulation was not an MCV *per se*, and it had much weaker vorticity compared with those events. Nonetheless, deep convection initiated within the circulation around 0000 UTC 4 June, and organized within a few hours to an extreme-rain-producing back-building MCS. By 0800 UTC (Fig. 3.4b), the convective line was located just to the south of the Dallas–Fort Worth metroplex. Surface observations revealed generally moist conditions with a pressure trough oriented from southwest to northeast. Winds were southerly to the south of the trough, and they switched to southeasterly and easterly on the north side of the trough.

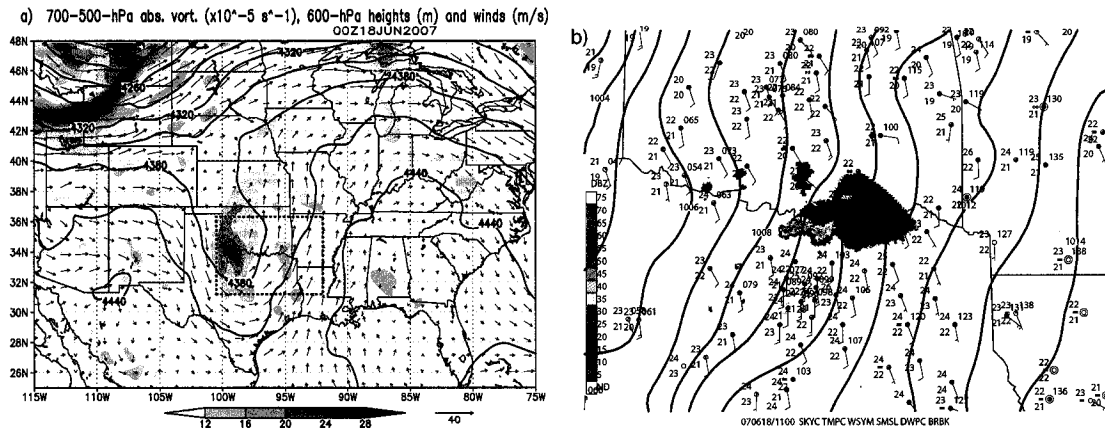


Figure 3.5: (a) As in Fig. 3.1a, except for 0000 UTC 18 June 2007. (b) As in Fig. 3.1b, except radar observations are from the Dallas–Fort Worth, Texas radar at 1056 UTC and surface observations and analysis are from 1100 UTC 18 June 2007.

A mesolow was present to the south of the convective line, but it is unclear whether it was convectively generated. The quasi-stationary convective line produced heavy rain over parts of north Texas, with a maximum rainfall total of 281 mm (11.08 in) at Cresson, just to the southwest of Fort Worth. Four people were killed and over 100 homes were damaged in the resulting flooding (USA Today 2000)<sup>2</sup>.

### 3.3.5 18 June 2007

The 18 June 2007 extreme-rain-producing MCS also occurred in association with a convectively-reinforced cutoff low over the southern Great Plains. This low cut off from the main branch of upper-level flow on 13 June 2007 over the Rocky Mountains, and slowly moved toward the southeast over next several days. By 0000 UTC 18 June, the circulation was a hybrid between the synoptic cutoff low and an MCV located over north Texas and southern Oklahoma (Fig. 3.5a). The surface flow was southerly with no discernible boundaries prior to convection initiation at around 0400 UTC. After this time, scattered convection developed over north Texas, and it organized into a quasi-stationary convective system over the next few hours. This convective system was much smaller than those

<sup>2</sup> Media reports are cited where the NCDC storm reports are incomplete or unavailable.

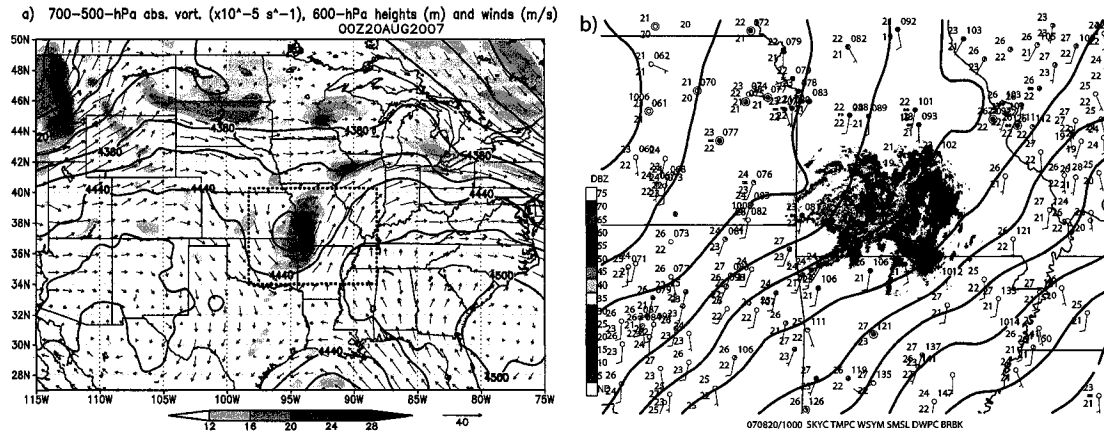


Figure 3.6: (a) As in Fig. 3.1a, except for 0000 UTC 20 August 2007. (b) As in Fig. 3.1b, except radar observations are from the Springfield, Missouri radar at 0959 UTC and surface observations and analysis are from 1000 UTC 20 August 2007.

previously discussed (Fig. 3.5b), with the convective line throughout most of its life cycle being shorter than the 100-km threshold for MCSs proposed by Parker and Johnson (2000). Nonetheless, the convective line was responsible for localized extreme rainfall, with a maximum rainfall amount of 203 mm (7.99 in) at Gainesville, Texas. This area had received well-above-normal rainfall in the months leading up to this event, and as a result the cities of Gainesville and Sherman suffered significant flooding. Six fatalities and over 500 flooded homes were reported in this event (MSNBC 2007).

### 3.3.6 20 August 2007

The origin of the midlevel circulation in the 20 August 2007 case was different from those previously discussed: it was the remnants of Tropical Storm Erin, which made landfall in south Texas on 16 August, turned northward and then traversed eastward across Oklahoma and Missouri. It was classified as a tropical depression as late as 2100 UTC on 19 August while over land, but the surface low soon dissipated and the circulation was primarily confined to midlevels with a structure similar to an MCV. At 0000 UTC 20 August 2007, the vortex was located over southwestern Missouri (Fig. 3.6a), and deep convection initiated in that region around 0600 UTC. Again, no surface boundaries were apparent

prior to the convection. By 1000 UTC (Fig. 3.6b), a weak pressure trough was present to the west of the deep convection, but analyses at other times did not show this feature. A weak north-south temperature gradient also existed at this time, due to the presence of a cold dome beneath the vortex and warm advection from the south. The convection organized into a west-to-east oriented back-building MCS (Fig. 3.6b) that remained nearly stationary through approximately 1500 UTC. This MCS produced a maximum of 266 mm (10.5 in) of rain in the town of Miller, Missouri. The resulting flooding affected primarily rural areas, and caused nearly \$1M of damage to roads (Springfield News-Leader 2007).

### 3.4 Similarities between the cases

There were several prominent similarities between the aforementioned extreme rain events:

- All of the events were nocturnal, with the heaviest rainfall generally falling between 0700–1100 UTC (0200–0600 local time).
- The heavy rainfall was produced by organized convective systems, which were on the small side of the MCS spectrum. All of the convective systems fit the “back-building/quasi-stationary” pattern described by Schumacher and Johnson (2005) for at least a portion of their life cycle.
- The rainfall in each event led to significant flash flooding.
- Each convective system developed in close proximity to a midlevel circulation. These circulations included mesoscale convective vortices, cutoff lows, and tropical cyclone remnants.
- In at least three of the cases, there was a surface mesolow on the upstream side of the convective system. However, none of the convective systems formed along a front or other strong surface boundary.

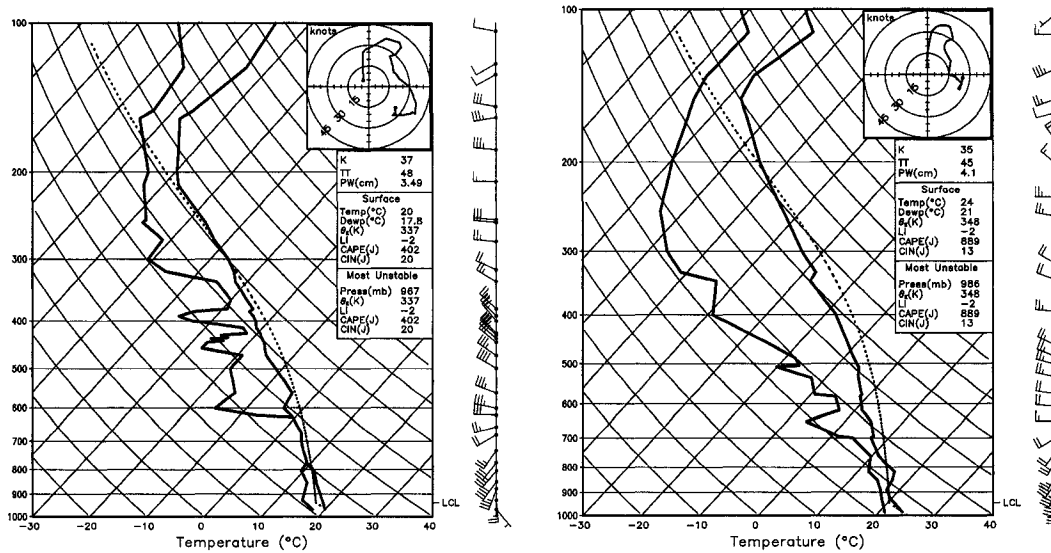
In the interest of space, additional synoptic and mesoscale conditions associated with the individual events have not been shown. Furthermore, as discussed previously, radiosonde observations that are truly representative of the environment were not always available. However, three soundings that were deemed reasonably representative are shown in Fig. 3.7. These observed soundings and investigation of RUC analyses for each case reveal several additional similarities:

- Each convective system developed in association with an LLJ and relatively weak midlevel flow. As a result, the wind shear vector reversed direction sharply with height; this shear reversal is illustrated by the “hairpin” shape in the hodographs.
- The lower troposphere exhibited high values of precipitable water and RH in the region of convective development.
- According to the soundings as well as RUC analyses of convective inhibition, the area beneath the midlevel circulation had been significantly destabilized relative to surrounding areas.

These features will be further illustrated in the next section using composite analysis.

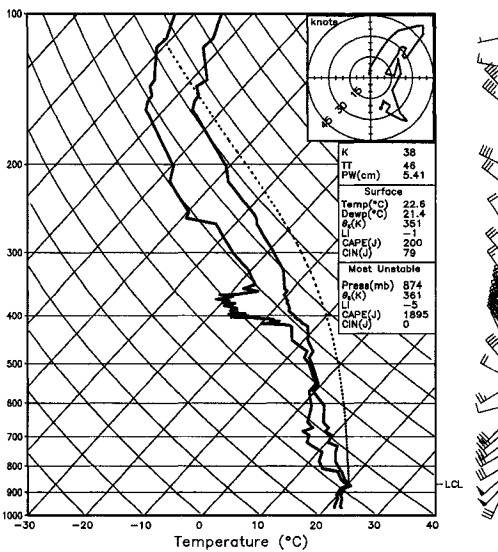
### **3.5 Composite analysis of synoptic and mesoscale conditions**

As in the individual cases, the composite of the six events shows a midlevel cyclonic vorticity maximum and height minimum located slightly to the north of the location of the heaviest rainfall (Fig. 3.8). The primary kinematic feature responsible for the development of deep convection are this circulation and a nocturnally-enhanced LLJ. In the hours leading up to the extreme rainfall, the circulation moved eastward and interacted with increasing southerly low-level winds (Fig. 3.9a–b). By the time of the heavy rainfall, the nose of the LLJ with wind speeds exceeding  $15 \text{ m s}^{-1}$  was almost directly below the vortex (Fig. 3.9c), and both of these features were very near the extreme rainfall location. In the six hours following the heaviest rainfall, the composite LLJ weakened as morning arrived, while the



(a) KSGF, 0000 UTC 7 May 2000

(b) KFWD, 1200 UTC 18 June 2007



(c) KSGF, 1200 UTC 20 August 2007

Figure 3.7: Skew- $T$  log  $p$  diagrams of three soundings representative of the inflow environments of extreme-rain-producing convective systems. (a) Springfield, MO at 0000 UTC 7 May 2000; (b) Dallas-Fort Worth, Texas at 1200 UTC 18 June 2007; (c) Springfield, MO at 1200 UTC 20 August 2007. Parcel paths for the parcels with the highest  $\theta_e$  in the lowest 3 km are shown by the dotted lines.

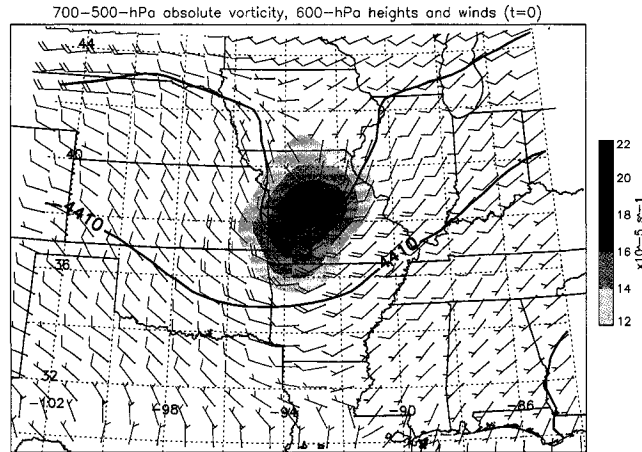


Figure 3.8: Composite of absolute vorticity averaged over the 700–500-hPa layer ( $\times 10^{-5} \text{ s}^{-1}$ , shaded every  $2 \times 10^{-5} \text{ s}^{-1}$  for values above  $12 \times 10^{-5} \text{ s}^{-1}$ ), 600-hPa heights (thick lines contoured every 30 m), and winds (short barb =  $2.5 \text{ m s}^{-1}$ , long barb =  $5 \text{ m s}^{-1}$ ) for the six extreme rain events at the peak rainfall time. For visual reference, the composite has been projected onto a map of the central United States, centered near Springfield, Missouri. The square at the center of the figure indicates the location of the highest rainfall report.

vortex intensified somewhat, reflecting the latent heating effects of the convective system (Fig. 3.9d). The observed hodographs previously shown in Fig. 3.7 had a “hairpin” shape, and the composite analysis of vertical shear shows a similar pattern. With northwesterly midlevel winds above the strong south-southwesterly LLJ, convection developing in this area would be interacting with vertical shear that changed directions sharply with height (Fig. 3.10).

The vertical structure of the composite vorticity maximum shows a deep, generally upright circulation (Fig. 3.11). In the twelve hours prior to the heaviest rainfall, the composite vortex was maximized at approximately 500 hPa, with cyclonic vorticity extending through a deep layer (Fig. 3.11a–b). Twelve hours prior to the peak rainfall, there was a cold, moist dome beneath the circulation, with a well-mixed boundary layer away from the circulation where skies were clear (Fig. 3.11a). After this time, nocturnal radiational cooling led to the stabilization of the boundary layer outside of the circulation, and this in turn decreased the temperature gradient associated with the cold dome. Moisture advection associated with the LLJ as well as radiational cooling increased the ambient low-level RH

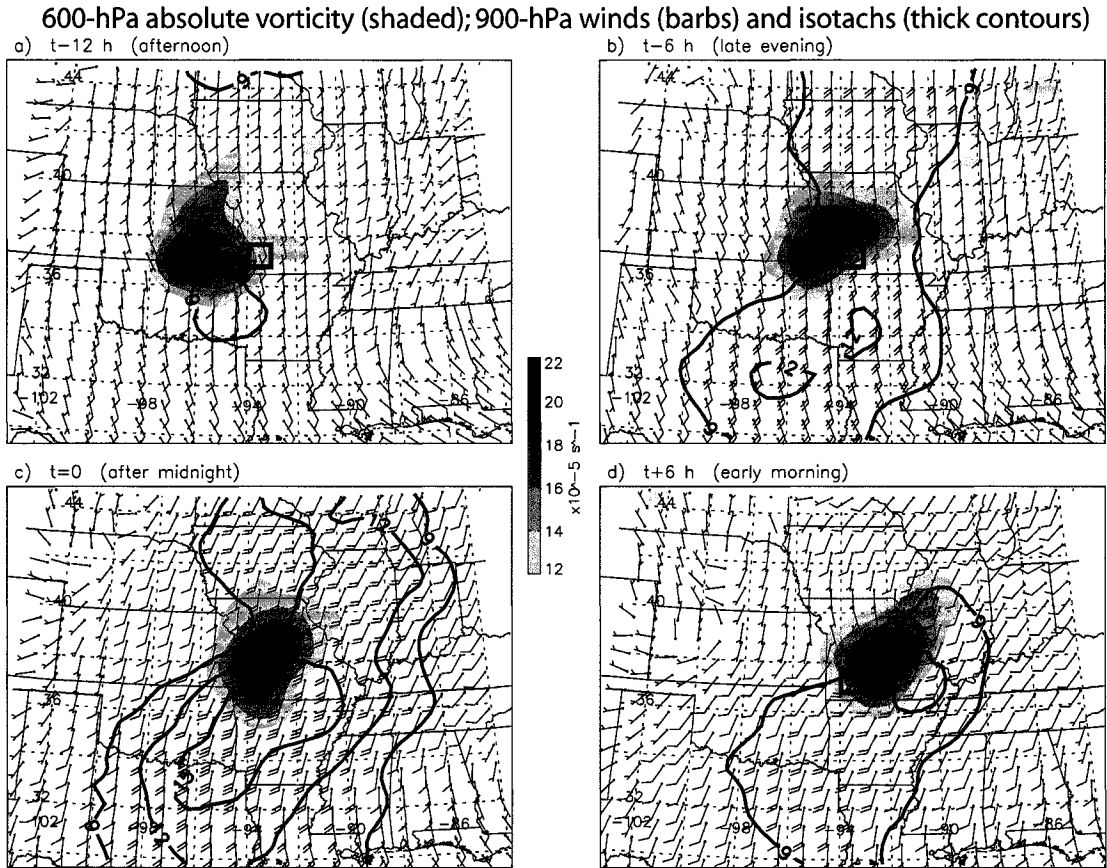


Figure 3.9: Composite of 600-hPa absolute vorticity ( $\times 10^{-5} \text{ s}^{-1}$ , shaded every  $2 \times 10^{-5} \text{ s}^{-1}$  for values above  $12 \times 10^{-5} \text{ s}^{-1}$ ), 900-hPa winds (short barb =  $2.5 \text{ m s}^{-1}$ , long barb =  $5 \text{ m s}^{-1}$ ) and isotachs (thick contours every  $3 \text{ m s}^{-1}$  above  $9 \text{ m s}^{-1}$ ) at (a) 12 h prior to peak rainfall; (b) 6 h prior to peak rainfall; (c) peak rainfall time; (d) 6 h after peak rainfall.

near the vortex. By the peak rainfall time (Fig. 3.11c), the surface temperature gradient associated with the daytime cold dome was no longer present, and a large area with  $\text{RH} > 90\%$  was in place. Six hours after the peak rainfall time, the cyclonic circulation had intensified significantly at midlevels and had weakened aloft (Fig. 3.11d), consistent with the diabatic redistribution of potential vorticity described by Haynes and McIntyre (1987).

Isentropic lifting resulting from the vortex's interaction with vertical wind shear can also be inferred from Figs. 3.11 and 3.12. Determining a single direction for the ambient shear (i.e., the shear the *vortex* is experiencing, as opposed to that affecting the *convection*) is not straightforward when the shear vector is turning sharply with height, and therefore

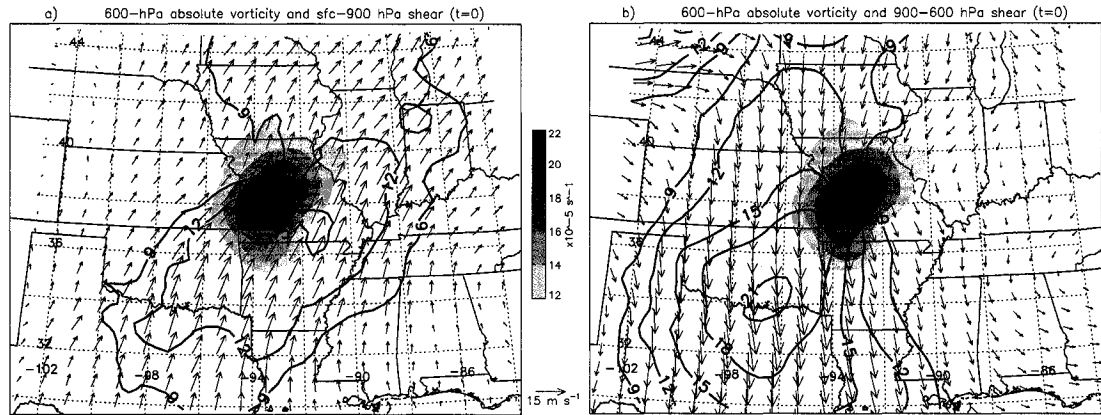


Figure 3.10: (a) Composite of 600-hPa absolute vorticity, surface-to-900-hPa wind shear vectors (scale shown at bottom) and shear magnitude over the depth of this layer (thick contours every  $3 \text{ m s}^{-1}$  above  $9 \text{ m s}^{-1}$ ) at the peak rainfall time. (b) As in (a), except for 900–600-hPa shear vectors and shear magnitude.

determining the “downshear” and “upshear” directions is also difficult (e.g., Knievel and Johnson 2002). In the composite, low-level (between approx. 950–700 hPa) air was generally approaching the vortex from the southwest (i.e., from the left in Fig. 3.11 and Fig. 3.12a) and was rising along upward-sloping isentropes. There was also an area of downward motion on the north side of the vortex (Fig. 3.12b). This couplet of ascent and descent is consistent with the findings of Raymond and Jiang (1990) and Trier and Davis (2007) for a vortex in northerly midlevel shear. In addition to the lifting on the southwest side of the vortex, there was additional upward motion provided by convergence at the nose of the strengthening LLJ (Figs. 3.9, 3.12b, and 3.13). Leading up to the heavy rainfall time, there was a persistent convergence maximum between around 950 and 800 hPa, which increased in magnitude with time as the LLJ strengthened (Fig. 3.13a–b). At the peak rainfall time, the composite shows a large area of ascent (part of which may be a reflection of deep convection in the RUC analyses) near the vortex center above a broad convergence maximum, with a maximum of divergence in the upper troposphere (Fig. 3.13c). This ascent continues for several hours after the peak rainfall (Fig. 3.13d). The combined lifting from the vortex in shear and from low-level convergence was also contributing to the aforementioned increase in low-level RH (e.g., Trier et al. 2000a). These factors made the region near the center

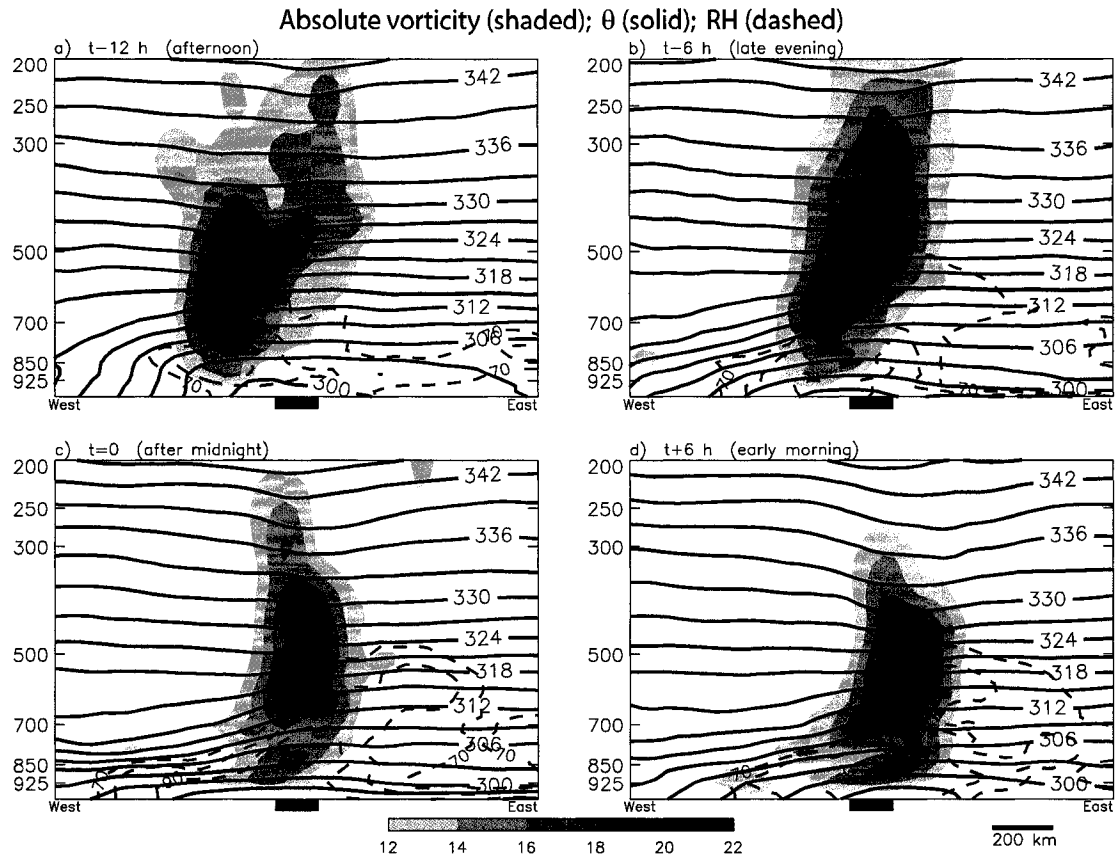


Figure 3.11: Composite west-to-east vertical cross-sections through the vorticity maximum. Shown are absolute vorticity (shaded every  $2 \times 10^{-5} \text{ s}^{-1}$  for values above  $12 \times 10^{-5} \text{ s}^{-1}$ ), potential temperature (thick contours every 2 K), and relative humidity (dashed contours every 10% above 70%) at (a) 12 h prior to peak rainfall; (b) 6 h prior to peak rainfall; (c) peak rainfall time; (d) 6 h after peak rainfall. The location of the heavy rainfall is shown by the thick black box at the bottom.

of the circulation increasingly favorable for the development of the deep convection that was observed in the individual cases. The effect on convection of this lifting and the strong reversal of shear with height will be examined in the idealized simulations to be presented in chapter 6.

As discussed above, the vertical cross-sections reveal minimal surface temperature gradients leading up to the time of peak rainfall, and composites of surface virtual potential temperature  $\theta_v$  bear this out (Fig. 3.14). Six hours prior to the heaviest rainfall, the daytime cold dome is still apparent near the location of the midlevel circulation, but there

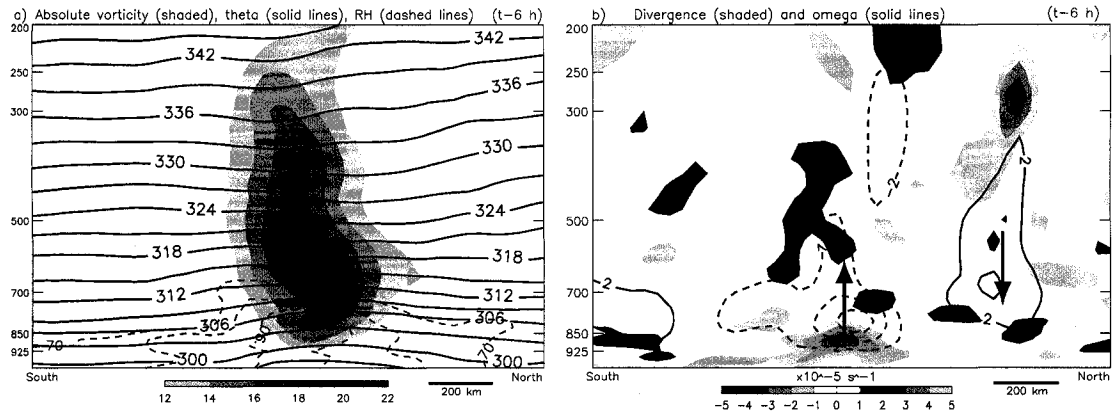


Figure 3.12: (a) As in Fig. 3.11, except for a south-to-north vertical cross section 6 h prior to peak rainfall time. (b) Composite south-to-north vertical cross section showing divergence ( $\times 10^{-5} \text{ s}^{-1}$ , shaded as shown) and pressure vertical velocity (contours every  $2 \times 10^{-3} \text{ hPa s}^{-1}$  with negative contours dashed and zero contour omitted;  $\omega < 0$  indicates ascent) 6 h prior to peak rainfall.

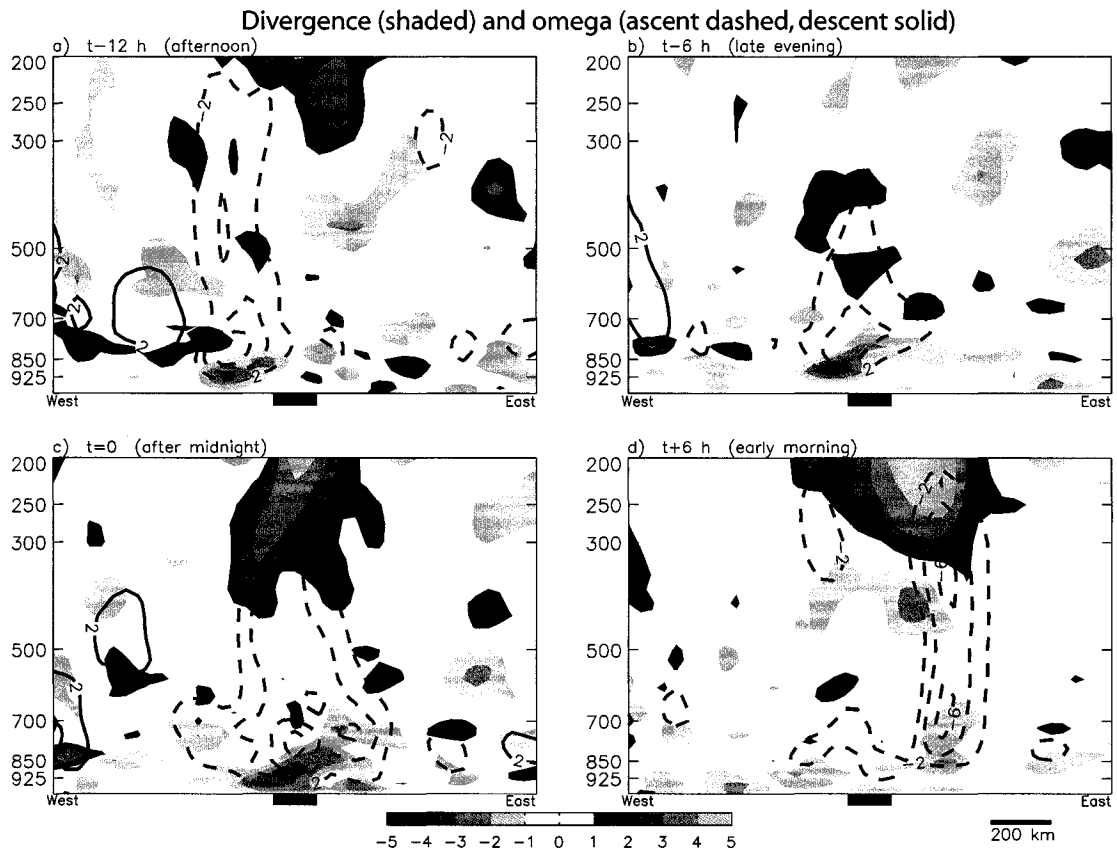


Figure 3.13: As in Fig. 3.12b, except for west-to-east vertical cross sections at (a) 12 h prior to peak rainfall; (b) 6 h prior to peak rainfall; (c) peak rainfall time; (d) 6 h after peak rainfall.

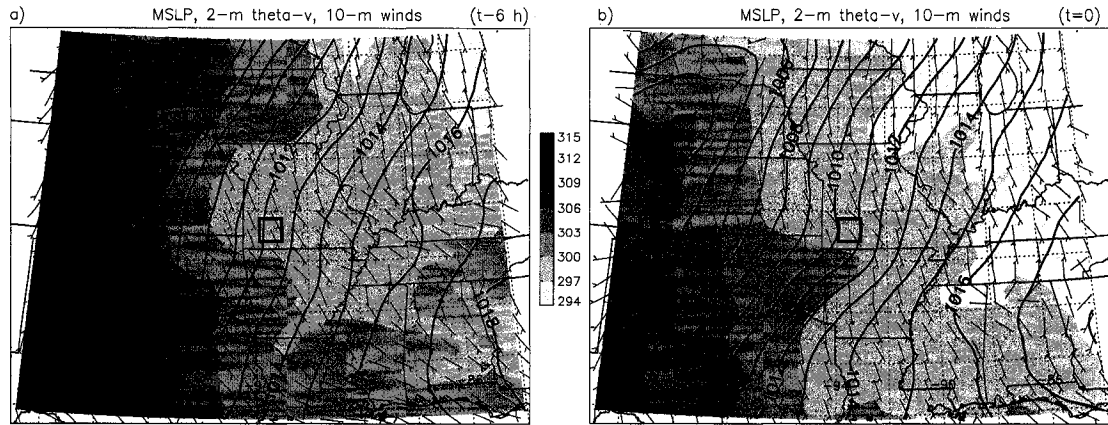


Figure 3.14: Composite of 2-m virtual potential temperature (shaded every 3 K), sea-level pressure (thick contours every 1 hPa) and 10-m winds at (a) 6 h prior to peak rainfall and (b) the peak rainfall time.

are no additional thermal boundaries (Fig. 3.14a). By the time of peak rainfall there is a localized temperature gradient near the heavy rainfall location, which is located near a weak pressure trough and wind shift (Fig. 3.14b). This composite boundary is consistent with the observation of mesolows in some of the individual cases (Figs. 3.1, 3.3, 3.4). Nonetheless, the temperature gradient across it is relatively weak, and its scale is quite small.

At the level of the LLJ, there were no notable features in this area 6 h prior to the peak rainfall (Fig. 3.15a). However, by the peak rainfall time (Fig. 3.15b) there is a band of strong advection of  $\theta_e$ , which is indicative of destabilization and has been cited as an important factor in previous studies of heavy rain events (e.g., Junker et al. 1999; Moore et al. 2003; Schumacher and Johnson 2005). The significant differences between panels (a) and (b) of Fig. 3.15 emphasize the important changes that take place in the 6 h leading up to the heavy rainfall, most of which are attributable to the nocturnal enhancement of the LLJ.

The evolution of the thermodynamic structure near the circulation (Fig. 3.16) emphasizes the effects of the destabilization caused by a vortex in shear. In the afternoon prior to the heavy rainfall (Fig. 3.16a), the most-unstable convective available potential energy (MUCAPE) near the circulation is relatively limited ( $<1000 \text{ J kg}^{-1}$ ), and there is

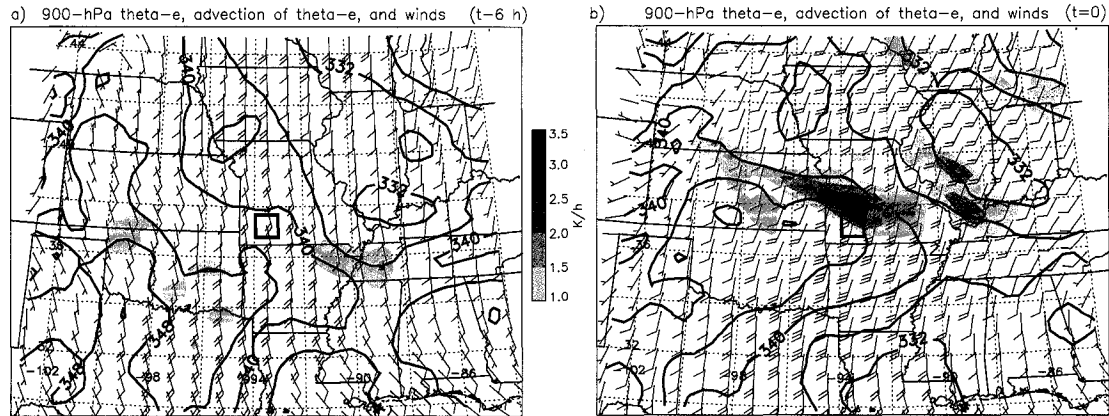


Figure 3.15: Composite of 900-hPa equivalent potential temperature (thick contours every 4 K), equivalent potential temperature advection ( $\text{K h}^{-1}$ ; shaded as shown), and winds at (a) 6 h prior to peak rainfall and (b) the peak rainfall time.

also substantial convective inhibition (CIN). However, as the evening progresses, the CIN beneath the vorticity maximum decreases significantly, with all of the CIN eroded by the time of peak rainfall (Fig. 3.16b–c). Though there may be some effect of deep convection in the RUC analyses used to make this composite, this minimum in CIN beneath the circulation is quite striking and is consistent with the findings of Trier et al. (2000a; see Fig. 2.10). At the same time, the MUCAPE has increased to over  $1500 \text{ J kg}^{-1}$  in this region, as a result of vortex-related destabilization (Trier et al. 2000a) and positive  $\theta_e$  advection by the LLJ (Fig. 3.14b). By six hours after the peak rainfall time, a minimum in CIN under the vortex remains, though the values have increased somewhat, and there are smaller values of CAPE in this region at this time (Fig. 3.16d).

The thermodynamic environment and wind profile in which the extreme-rain-producing convective systems develop is summarized in the composite sounding shown in Fig. 3.17. This sounding was calculated by averaging the RUC conditions at the grid point and analysis time nearest the heaviest rainfall for the six events.<sup>3</sup> The composite sounding has similar characteristics to the three observed soundings in Fig. 3.7, and is also

<sup>3</sup> To create the composite sounding, pressure-level temperature, relative humidity, and zonal and meridional wind components from the RUC analyses were simply averaged together. Since there was relatively little variation in elevation at the locations of the six events, this method provided reasonable results, and the composite sounding compares favorably to observed soundings and to the composite CAPE and CIN.

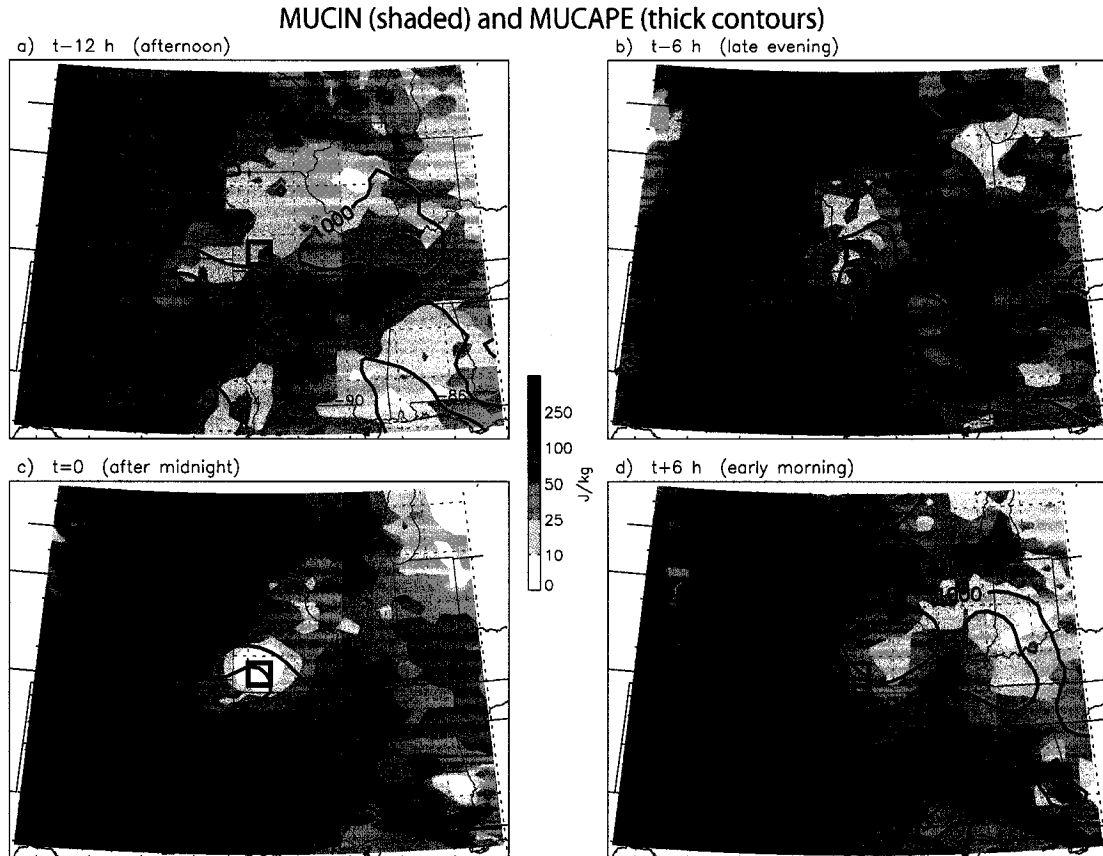


Figure 3.16: Composite of most-unstable convective available potential energy (MUCAPE; thick contours every  $500 \text{ J kg}^{-1}$  above  $1000 \text{ J kg}^{-1}$ ) and convective inhibition (MUCIN; shaded as shown) at (a) 12 h prior to peak rainfall; (b) 6 h prior to peak rainfall; (c) peak rainfall time; (d) 6 h after peak rainfall. In the RUC analyses, the MUCAPE is the CAPE of the parcel with the largest buoyancy in the lowest 300 hPa of the model atmosphere; the MUCIN is the convective inhibition for that same parcel.

similar to the immediate inflow sounding shown in the simulations that will be presented in chapter 4 (see Fig. 4.16). It also bears resemblance to the flash-flood sounding discussed by Davis (2001; his Fig. 12.20). It is nearly saturated over a layer approximately 100 hPa deep, has relatively high RH throughout the column, and has precipitable water of 49 mm (1.92 in). For parcels lifted from near the surface there is substantial CIN, but elevated parcels have CAPE exceeding  $1000 \text{ J kg}^{-1}$  and no CIN. The “hairpin” hodograph is also evident, with a  $15 \text{ m s}^{-1}$  LLJ. This composite sounding will be used as the basic-state environment in the idealized simulations to be presented in chapters 4, 5 and 6.

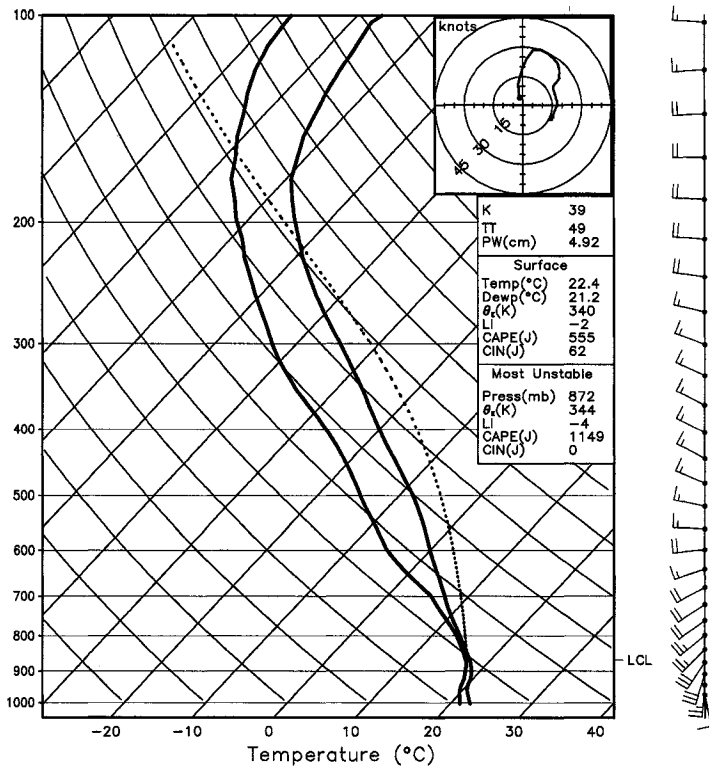


Figure 3.17: Composite skew- $T$  log  $p$  diagram for the extreme rainfall environment. The parcel path for the parcel with the highest  $\theta_e$  in the lowest 3 km is shown in the dotted line.

### 3.6 Summary

In this chapter, six extreme rain events that were associated with MCVs or other midlevel circulations were discussed, and composite analysis was performed to identify the characteristics of the environments in which they formed. In each of the six events, deep convection was organized into back-building lines or clusters that remained nearly stationary. These convective systems produced locally excessive rainfall and led to flash flooding.

In each of the six cases, a strong low-level jet interacted with a midlevel vorticity maximum, which provided the lifting required to initiate and maintain deep convection. Composite analysis showed that the thermodynamic environment near the convection was

characterized by very high relative humidity at low levels, moderate convective available potential energy (CAPE), and very little convective inhibition (CIN).

One of the events discussed briefly above (6–7 May 2000) will be analyzed in detail in the next chapter using observations and numerical simulations. This investigation, along with the additional idealized simulations that follow, is aimed at understanding the processes that are responsible for initiating, organizing, and maintaining quasi-linear, back-building convective systems that produce extreme rainfall.

## Chapter 4

### OBSERVATIONS AND NUMERICAL SIMULATIONS OF THE 6–7 MAY 2000 EASTERN MISSOURI FLASH-FLOOD-PRODUCING MESOSCALE CONVECTIVE SYSTEM

The 6–7 May 2000 BB MCS, introduced previously, will be the focus of this chapter. In this event, a cluster of quasi-stationary convection produced over 300 mm ( $\approx 12$  in.) of rain in 9 h (Fig. 4.1) and led to flash flooding that caused two fatalities and over \$100M in damage. In addition to the obvious societal impact of the flooding, this event is of meteorological interest because it occurred in an environment that provided few clues to indicate that such a large amount of rain would fall. Consistent with past analyses of heavy rain environments (e.g., Maddox et al. 1979), there were high values of precipitable water and relative humidity in east-central Missouri as well as a  $20 \text{ m s}^{-1}$  LLJ from the southwest. However, in contrast to other observed extreme rainfall environments, there was relatively little conditional instability and no surface boundaries were apparent prior to the onset of deep convection. The only midtropospheric feature evident was a mesoscale convective vortex (MCV) that developed in association with convection the previous night in Oklahoma.

#### 4.1 Description of the event

In this section, observations and analyses from several sources will be presented, including surface observations, analyses from the RUC, WSI NOWrad radar composites, and atmospheric soundings. The RUC analyses used herein, which are available hourly,

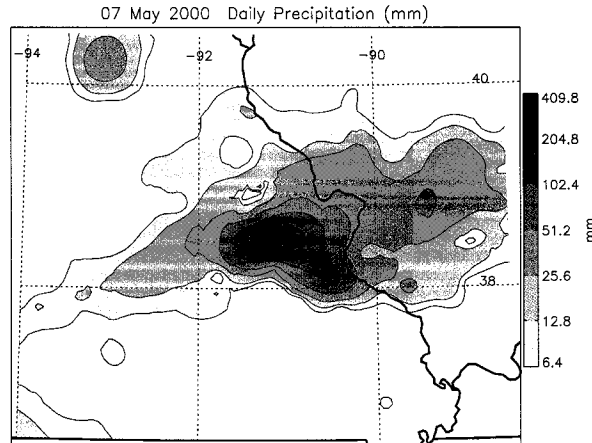


Figure 4.1: Objective analysis of National Weather Service/Cooperative rain gauge observations (mm) for the period 1200 UTC 6 May–1200 UTC 7 May 2000. The Missouri–Illinois border is shown with a bold line. The maximum observed total in this dataset was 309 mm (12.16 in); its location is marked with a black dot.

have horizontal grid spacing of approximately 40 km and 40 vertical levels using a hybrid isentropic-sigma coordinate. The NOWrad data have 2-km horizontal and 15-min temporal resolution. The reader is also directed to the observational case study of this event by Glass et al. (2001), in which additional radar data and other observations are summarized.

#### 4.1.1 *The mesoscale convective vortex*

As mentioned above, the primary midtropospheric feature in place during this event was an MCV. This MCV began its life cycle several days earlier as a cutoff low beneath a large-scale blocking pattern over the southern Plains (Fig. 4.2). This position relative to an upper-level ridge is similar to that of several of the MCVs identified in the climatology of Bartels and Maddox (1991). Each afternoon and evening, new convection developed in association with the circulation, which then helped reintensify and contract the vortex overnight (e.g., Trier et al. 2000b). On 5 May 2000 (Fig. 4.2c), the vortex helped to initiate deep, heavy-rain-producing convection over eastern Oklahoma, which continued through the early morning of 6 May 2000 and intensified the vortex in that area (Fig. 4.2d). The MCV then drifted eastward through the day on 6 May where it set the stage for the event

### 500-hPa heights, winds, and absolute vorticity

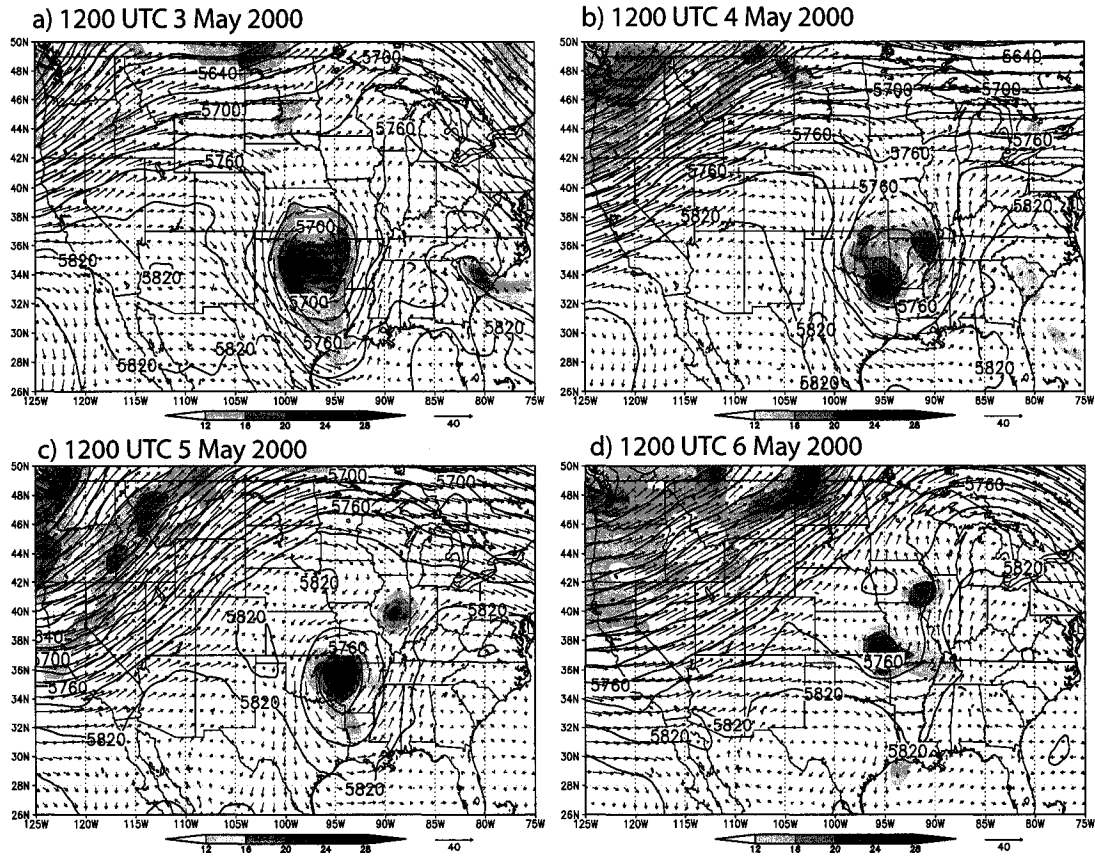


Figure 4.2: 500-hPa heights (thick lines contoured every 30 m), winds (vectors,  $\text{m s}^{-1}$ , with vector length scale indicated at bottom), and absolute vorticity ( $\times 10^{-5} \text{ s}^{-1}$ , shaded every  $4 \times 10^{-5} \text{ s}^{-1}$  for values above  $12 \times 10^{-5} \text{ s}^{-1}$ ), from RUC analyses. Plots shown are for 1200 UTC (a) 3 May 2000, (b) 4 May 2000, (c) 5 May 2000, (d) 6 May 2000.

being considered in this study. Visible and infrared satellite images (not shown) show distinct cyclonic rotation in the midlevel cloud field as the vortex moved eastward, along with anticyclonically-rotating cirrus outflow.

By 0000 UTC 7 May 2000, a few hours prior to convection initiation, the MCV was located over central Missouri (Fig. 4.3a). Its vertical structure (Fig. 4.3b) shows a potential vorticity (PV) anomaly (and absolute vorticity maximum, not shown) above approximately 700 hPa and the upward-sloping isentropes at low- and midlevels that are characteristic of such an anomaly (Haynes and McIntyre 1987; Raymond and Jiang 1990). The maximum PV was located at approximately 600 hPa, whereas the maximum in absolute vorticity was

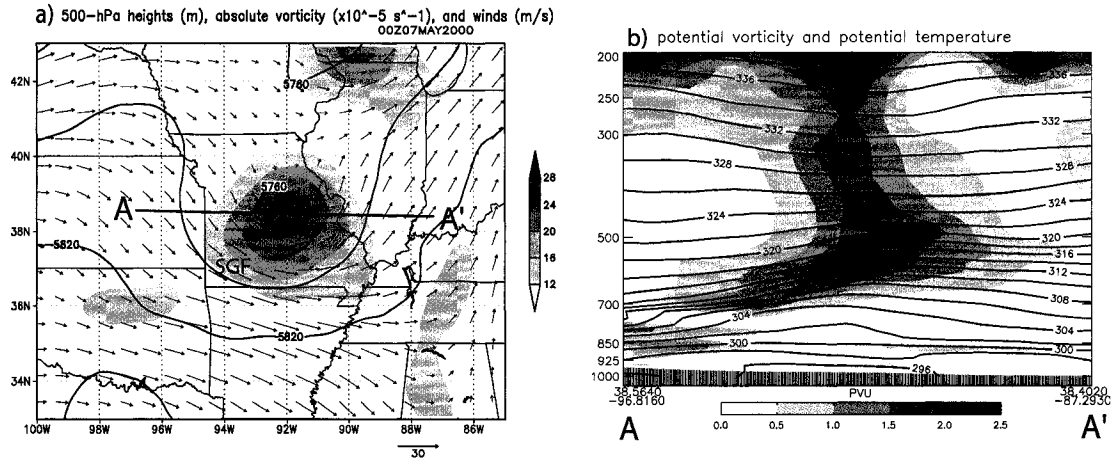


Figure 4.3: (a) As in Fig. 4.2, except for 0000 UTC 7 May 2000 and shown for a smaller area to emphasize the MCV. “SGF” denotes the location where the Springfield, MO sounding (shown in Fig. 3.7a) was taken. (b) West-east vertical cross-section (location shown by line A–A’ in panel (a)) of potential vorticity (PVU, shaded) and potential temperature (thick contours every 2 K).

slightly higher, at around 450 hPa. Air at low- and mid-levels was approaching the PV anomaly from the left in the sense of Fig. 4.3b and rose along the upward-sloping isentropes, just as in the case studied by Fritsch et al. (1994). Additionally, because the air to the south and west of the vortex was very moist, not much lifting was required for parcels in this region to reach saturation. The sounding from Springfield, Missouri (KSGF; shown previously in Fig. 3.7a) at 0000 UTC reflects this environment, as a deep MAUL is apparent in the observed sounding from approximately 775–625 hPa. Low-level cloudiness and some stratiform precipitation were also observed at this time in satellite and radar imagery (not shown). The KSGF sounding also shows the  $20 \text{ m s}^{-1}$  southwesterly LLJ and a “hairpin”-shaped hodograph reflecting the sharp reversal of shear with height. Though the 0000 UTC sounding from KSGF shows minimal CAPE, RUC analyses show the advection of higher  $\theta_e$  air from the southwest, which increased the most-unstable CAPE to over  $1000 \text{ J kg}^{-1}$  in west-central Missouri by 0600 UTC (Fig. 4.4). Through the overnight hours, the southwesterly LLJ provided a source of warm, moist air to the convection, and also contributed to continued isentropic lifting as it interacted with the MCV.

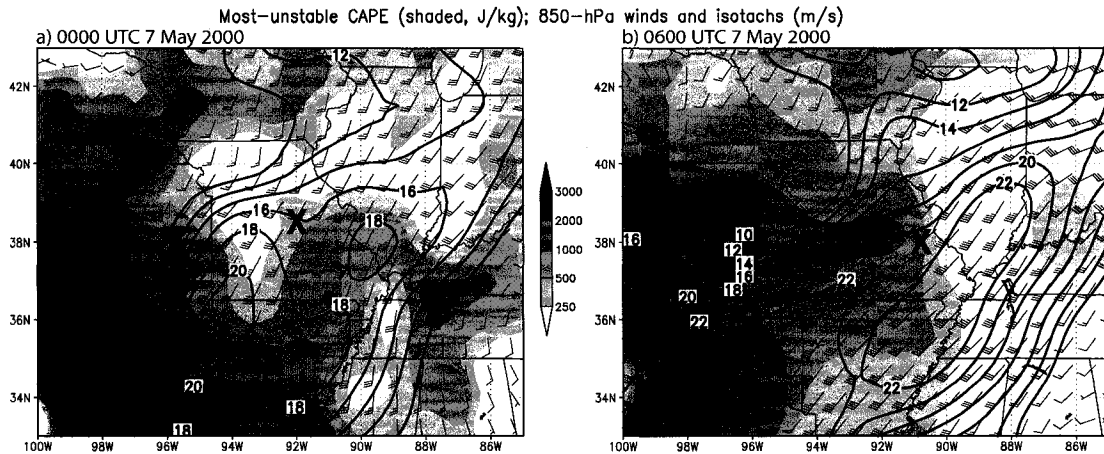


Figure 4.4: Most unstable CAPE ( $\text{J kg}^{-1}$ , shaded) and 850-hPa winds (short barb =  $2.5 \text{ m s}^{-1}$ , long barb =  $5 \text{ m s}^{-1}$ ) and isotachs ( $\text{m s}^{-1}$ , contoured every  $2 \text{ m s}^{-1}$  for values greater than  $10 \text{ m s}^{-1}$ ) from RUC analyses at (a) 0000 UTC and (b) 0600 UTC. The location of the maximum midlevel vorticity associated with the MCV is also shown with an “X.” In the RUC analyses, the most unstable CAPE is the CAPE of the parcel with the largest buoyancy in the lowest 300 hPa of the model atmosphere.

#### 4.1.2 Radar observations

Around 0300 UTC, radar observations showed the initiation of deep convection from within the region of stratiform rain near the center of the MCV. This convection grew into a larger, quasi-linear MCS over the next few hours, with the system as a whole remaining nearly stationary. By 0630 UTC (Fig. 4.5a), when the MCS has reached what might be considered its mature stage, there is a region of relatively high ( $>40 \text{ dBZ}$ ) reflectivity that is perhaps 100 km in length with a larger region of stratiform precipitation to its east. In this MCS, the decaying convective cells moved generally toward the east, with new cells developing on the west (upstream) side. One of the notable features in the observed reflectivity (Fig. 4.5a) is that the developing convective cells are apparent far upstream (in some cases nearly 100 km) of the cluster of high reflectivity. Animations of the reflectivity data show these small cells move toward the east and then eventually merge with the nearly stationary cluster. Some of these cells existed for 90–120 minutes from the time of their first echo until the time they merged with the larger system. This behavior is consistent

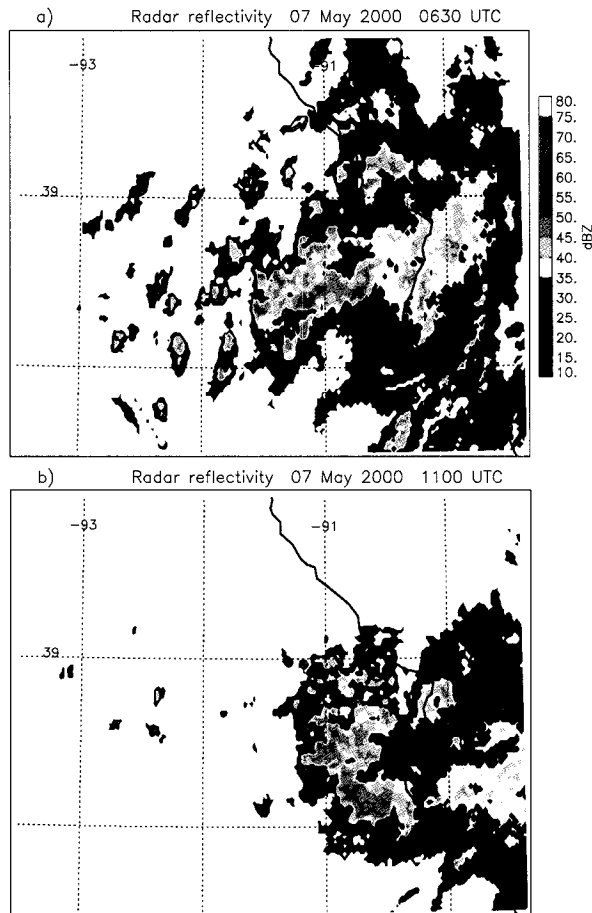


Figure 4.5: Observed composite radar reflectivity (dBZ) at (a) 0630 UTC and (b) 1100 UTC 7 May 2000.

with the idea that inflowing air is not being lifted by a strong surface outflow boundary; the new cells pop up in what appears to be nearly random fashion in the area upstream of the ongoing convection.

By 1100 UTC (Fig. 4.5b), the MCS was in nearly the same location as it was 4.5 h earlier. However, the convective line was oriented in a more north-to-south fashion at this time, and there were fewer incipient cells upstream. The convection began to move southeastward shortly after this time and then generally dissipated by 1500 UTC. However, over this approximately 9-h period, over 300 mm of rain had fallen in some locations (Fig. 4.1), which resulted in devastating flash flooding.

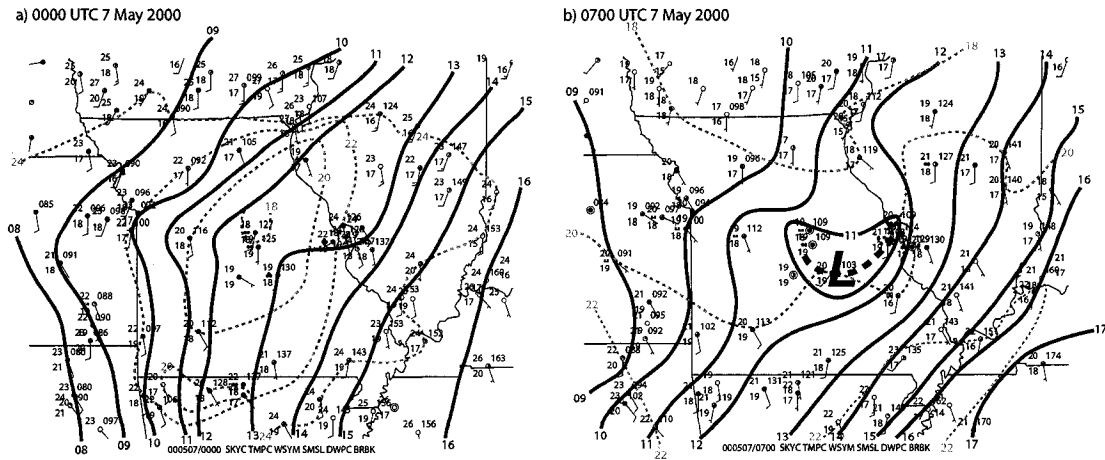


Figure 4.6: Subjective analysis of surface observations at (a) 0000 UTC and (b) 0700 UTC 7 May 2000. Analyzed is pressure adjusted to sea level (thick lines every 1 hPa) and surface temperature (dashed lines every 2°C). The sea-level pressure observation at Jefferson City, MO was found to be consistently approximately 1 hPa lower than surrounding stations on the days before and after this event; as a result the pressure value at this station was adjusted upward in the plots shown. Even with this adjustment, this station fell within the mesolow shown in (b).

#### 4.1.3 Surface observations

Though surface observing stations in central Missouri are relatively sparse, the surface data from this case reveal a pattern that is different from the cold pool and mesohigh that are usually observed beneath midlatitude squall lines and heavy rainstorms (e.g., Maddox et al. 1979; Johnson 2001). At 0000 UTC (1900 local time), prior to the onset of deep convection, the surface pattern over Missouri was rather nondescript, with isobars oriented from south to north and a weak cold dome and pressure ridge due to MCV-related cloudiness during the day (Fig. 4.6a). Surface dew point depressions beneath this cold dome were 0–2°C. As the deep convection developed and intensified, a mesoscale low pressure center and pressure trough began to appear at the surface; their structure was most pronounced at the 0700 UTC observing time (Fig. 4.6b). Market et al. (2001) showed an additional surface observation that confirmed the presence of a cyclonic circulation with this mesolow. Though the lack of temperature observations directly beneath the deep convection precludes a definitive statement about the lack of a surface cold pool,

temperatures at stations surrounding the MCS generally stayed steady or rose over this time period in spite of the effects of radiational cooling. Given the deep layer of high relative humidity in this area (Fig. 3.7a), cooling from the evaporation of raindrops—a major factor in cold-pool production—was likely very limited, as also noted by Glass et al. (2001) and Market et al. (2001). In the following sections, these observations will be supplemented by simulations of the MCS to explore the processes responsible for its maintenance and evolution.

## 4.2 Model configuration and experimental design

Version 2.2 of the Advanced Research version of the Weather Research and Forecasting model (WRF-ARW; Klemp et al. 2007; Skamarock et al. 2007) was run at convection-permitting resolutions to simulate the 6–7 May 2000 event. A series of simulations was carried out for the 24-h period 0000 UTC 7 May to 0000 UTC 8 May 2000. The model was initialized and used lateral boundary conditions from Eta model analyses with 40-km horizontal grid spacing. All simulations used 48 vertical levels with a stretched grid such that it has its finest grid spacing (approx. 125 m) in the boundary layer and coarser grid spacing aloft (the maximum grid spacing is approx. 2 km near the model top between 17–19 km.) The simulations presented herein take advantage of a two-way nested grid setup and include runs with two and three grids (Fig. 4.7). The parameterization schemes used and other details of the model configuration are shown in Table 4.1. The model is configured to use sixth-order monotonic numerical diffusion (Kniewel et al. 2007) and a positive-definite advection scheme such that moisture and scalar quantities are approximately conserved. The configuration is similar to that used for real-time forecasts at the National Center for Atmospheric Research in the summers of 2003–2006 (Done et al. 2004).

A simulation initialized at 1200 UTC 6 May 2000 (12 h earlier than the run discussed above) was also performed. This simulation produced heavy rainfall (suggesting that it may have been useful for forecasting applications), but the timing, location, and organization

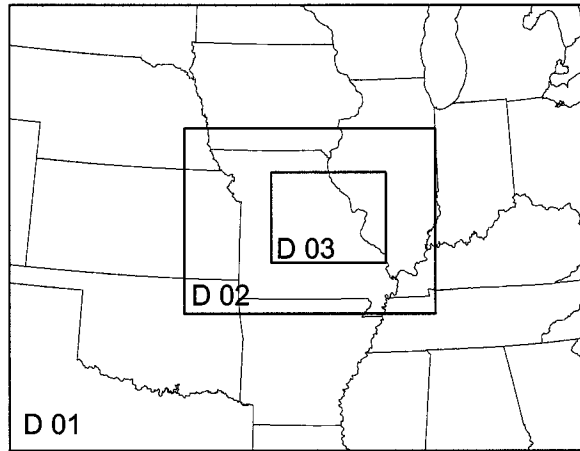


Figure 4.7: Location of model domains. The horizontal grid spacing is 9 km on domain 1, 3 km on domain 2, and 1 km on domain 3.

Table 4.1: Design of WRF-ARW version 2.2 numerical model experiments. Multiple entries indicate different configurations for domains 1, 2, and 3. See Fig. 4.7 for domain locations. Technical descriptions of the parameterizations are available in Skamarock et al. (2007).

Horizontal grid spacing	9.0 km, 3.0 km, 1.0 km
Vertical levels	48, 48, 48
Time step	54 s, 18 s, 6 s
Initial conditions	40-km Eta
Boundary conditions	40-km Eta (updated every 12 h)
Cumulus convection	Kain-Fritsch, explicit, explicit
Boundary layer	Yonsei University
Surface layer	Monin-Obukhov
Microphysics	Purdue Lin
Land surface	Noah
Turbulence	2D Smagorinsky
Shortwave radiation	Dudhia
Longwave radiation	Rapid radiative transfer

of the convection were much less accurate than the simulation initialized at 0000 UTC 7 May. Since this study is primarily concerned with understanding the processes that were important in this event, the 0000 UTC 7 May initialization is used here.

In the following sections, all discussion of small-scale convective structures will refer to the run with 1-km horizontal grid spacing. This grid spacing is not completely sufficient to resolve convective cells (e.g., Bryan et al. 2003; Skamarock 2004); however, it was not feasible to run the model including multiple physics parameterizations at higher resolution. As will be shown, the simulated convective system reproduces many of the observed features. Additionally, idealized simulations at convection-resolving grid spacing will be shown to illustrate that the primary features of interest are present in both cloud-resolving simulations and those that explicitly predict but do not truly resolve convective processes.

It will also be shown that the mesoscale structure of the simulated system when using 3-km grid spacing (i.e., without domain 3) is generally similar to that at 1-km grid spacing. Because of this similarity, a few sensitivity experiments will be presented that use this setup, which is significantly less computationally expensive. Also, given the larger size of the 3-km grid, some synoptic and larger mesoscale features will be analyzed on this domain. The primary run with  $\Delta x = \Delta y = 1$  km will be referred to as “1KM” and that with  $\Delta x = \Delta y = 3$  km will be referred to as “3KM.” The sensitivity runs, which are variations of 3KM, will be referred to as “NOLATENT,” in which phase changes of water are allowed in the model but no latent heat is released; and “NOEVAP,” in which the evaporation of raindrops is removed from the microphysics scheme.

Finally, some idealized simulations will be shown that use version 1.11 of the cloud model described by Bryan and Fritsch (2002). In these, the model is initialized with a horizontally-homogeneous base state that is representative of the environment in this and other extreme-rain-producing MCS events. Of note is that the vertical wind profile does not vary horizontally, but it does include a low-level jet in the vertical; therefore, the simulated convection is subject to the reversal of vertical shear inherent in a LLJ, but not

the horizontal variations. In these simulations, convection is initiated with a thermal and moisture perturbation<sup>1</sup>. The “bubble” has a maximum potential temperature perturbation of 2 K, a horizontal radius of 6 km and a vertical radius of 1.5 km with its center at 1.5 km above the surface. The moisture perturbation simply makes the relative humidity within the “bubble” the same as the relative humidity of the outside environment, which increases the bubble’s buoyancy compared with a temperature-only perturbation. The primary simulation used horizontal grid spacing of 125 m and a stretched vertical grid with grid spacing increasing from 100 m near the surface to 500 m at the model top. The domain size was 100 × 100 × 18.5 km. The results of interest in the simulation with grid spacing of 125 m were similar to those at coarser (e.g.,  $\Delta x=1$  km) resolution; therefore, several sensitivity simulations examining the effects of shear and the thermodynamic environment were run at  $\Delta x=\Delta y=1$  km. This model has free-slip upper and lower boundaries, with a Rayleigh damping layer above 14 km. It includes parameterized ice microphysics as described in Braun and Tao (2000), which is very similar to the Purdue Lin scheme used in the WRF simulations described above; both are based on the work of Lin et al. (1983).

### 4.3 Results

#### 4.3.1 *Overall structure of convection and precipitation in convection-permitting simulations*

Operational model forecasts and coarser-resolution WRF runs with parameterized convection significantly underpredicted the observed precipitation in this event, with maximum rainfall totals nearly an order of magnitude too small (Fig. 4.8). However, in simulation 1KM, the model successfully produces a back-building/quasi-stationary MCS which replicates many of the features of the observed system (Fig. 4.9a–b, cf. Fig. 4.5). The model also succeeds in producing a region of extreme rainfall amounts, the location and

---

<sup>1</sup> The convection that develops in these idealized simulations is not subject to the mesoscale lifting provided by the MCV in the real case; here we merely seek to understand a few particular processes associated with deep convection in this type of thermodynamic and kinematic environment. Results of more complex simulations that include background lifting will be presented in chapter 6.

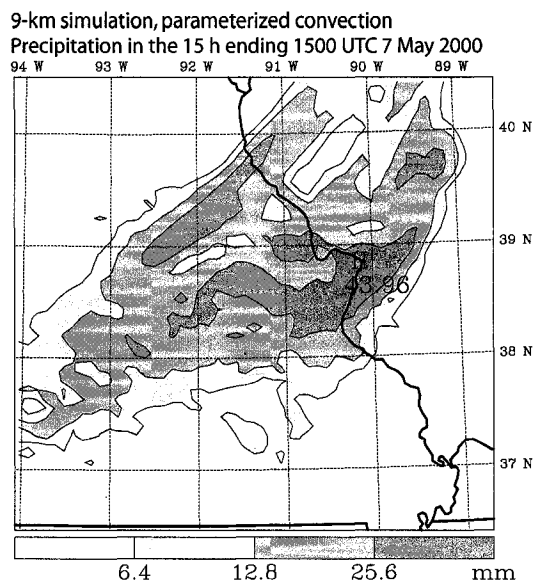


Figure 4.8: Model accumulated precipitation (mm) for the 15-h period ending at 1500 UTC 7 May 2000 from the run with 9-km grid spacing and Kain-Fritsch convection. The portion of the domain shown and the color scale is the same as that used in Fig. 4.1. The largest point rainfall total in this run was only 44 mm, compared with the observed maximum of 309 mm.

distribution of which are remarkably similar to the observations (cf. Figs. 4.10 and 4.1). The model underestimates the maximum rainfall amount: the maximum predicted rainfall is 261 mm, which is somewhat less than the observed maximum of 309 mm. However, given the challenges of predicting ground-accumulated rainfall when using microphysical parameterizations (e.g., Gilmore et al. 2004) and the large amount of rain that fell in this event, this can probably be considered a successful result.

The MCS's evolution begins slightly later and the system develops slightly to the west in the simulation compared with the observed system. Though the convective region of the MCS is well represented in the simulation, the model does not create the large region of stratiform rain (with embedded convection) that extends eastward into Illinois in the observations (cf. Figs. 4.5 and 4.9). The underprediction of stratiform rain in MCSs is a common problem in convection-allowing forecasts and simulations (e.g., Done et al. 2004). Consistent with the observed system, the simulated MCS generally dissipates after 1500

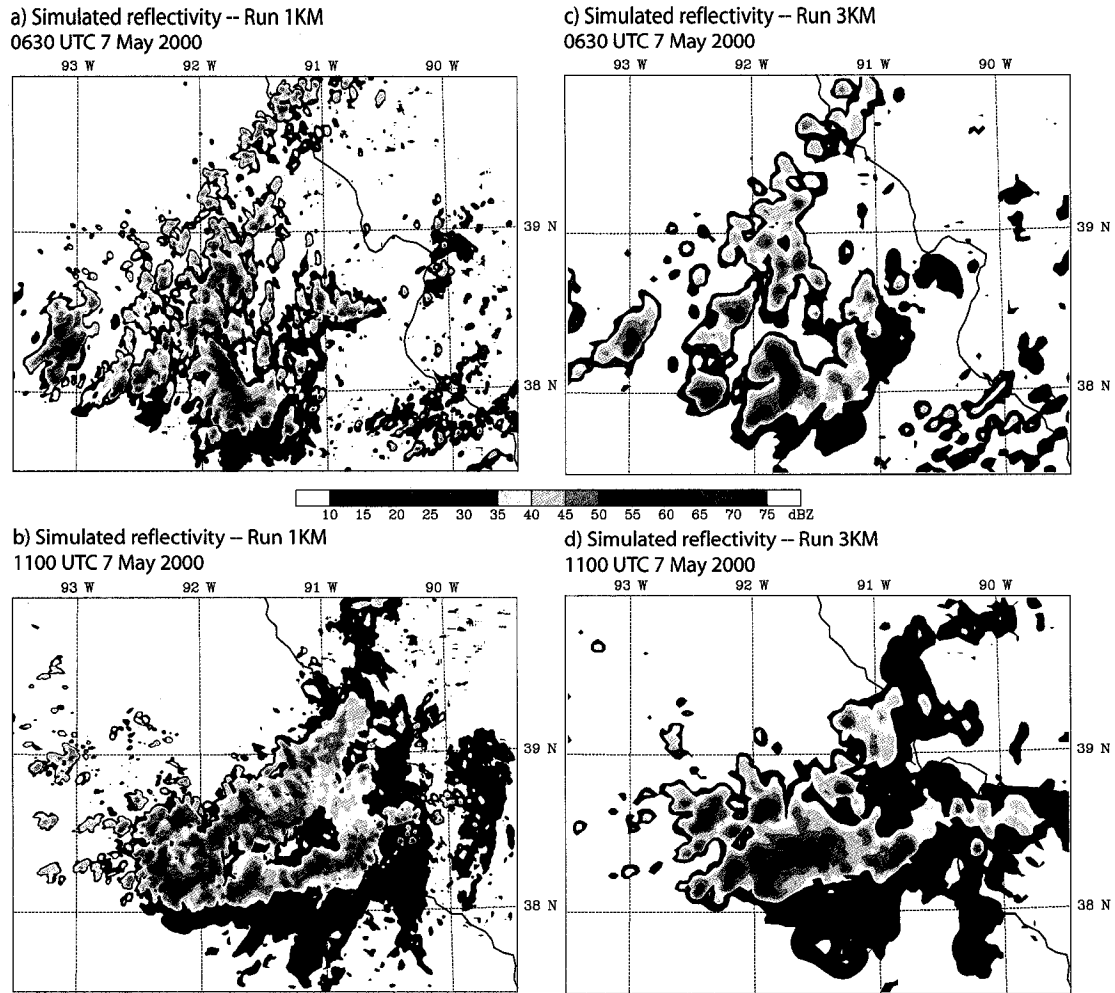


Figure 4.9: Simulated composite reflectivity (dBZ) at 0630 and 1100 7 May 2000 for (a–b) domain 3 in run 1KM and (c–d) domain 2 in run 3KM. The areas shown are the same as those in Fig. 4.5 for comparison.

UTC as the nocturnal LLJ weakens in the morning.

Since the 3KM run will also be used to describe the simulated mesoscale environment of the MCS, simulated reflectivity images for that run are also included in Fig. 4.9c–d. The location, timing, overall structure, and rainfall amounts for that run are similar to the higher-resolution run, though of course the updraft-scale details are not resolved nearly as well (e.g., Weisman et al. 1997).

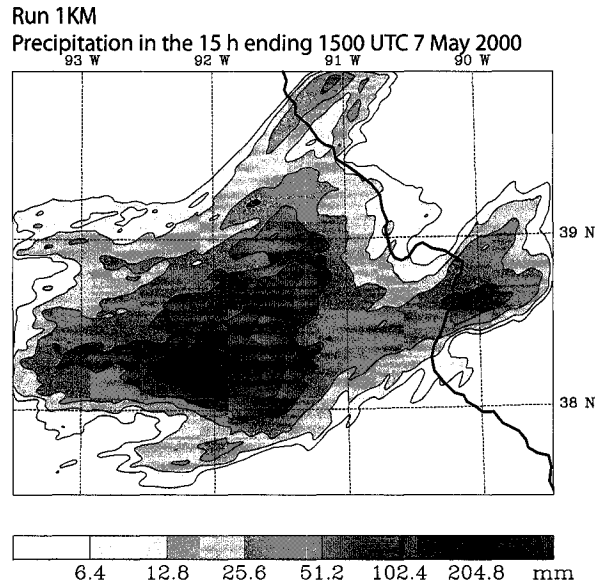


Figure 4.10: Model accumulated precipitation (mm) on domain 3 in run 1KM for the 15-h period ending at 1500 UTC 7 May 2000.

#### 4.3.2 *Initiation of convection*

In the Eta model analysis used to initialize this simulation, the MCV was initialized accurately over central Missouri, which surely contributed to the success of the simulation. As in the observations, the presence of a strong southwesterly LLJ and weak winds at upper levels created a reversal of shear with height; there was southerly shear near the surface (below the LLJ) which reversed to approximately northerly above the LLJ (Fig. 4.11a). Lifting in the layer above the LLJ was important in this case, with average vertical motions in the region to the south and southwest of the MCV on the order of a few  $\text{cm s}^{-1}$  (not shown). Such vertical velocities are relatively weak, but over several hours air can be displaced upward by hundreds of meters (e.g., Trier et al. 2000a). Assuming the MCV is nearly steady-state prior to the initiation of deep convection, this isentropic lifting can be visualized by looking at cross-isobaric flow on an isentropic surface: where winds are blowing from higher to lower pressure, there is isentropic upglide. At 0100 UTC (one hour into the

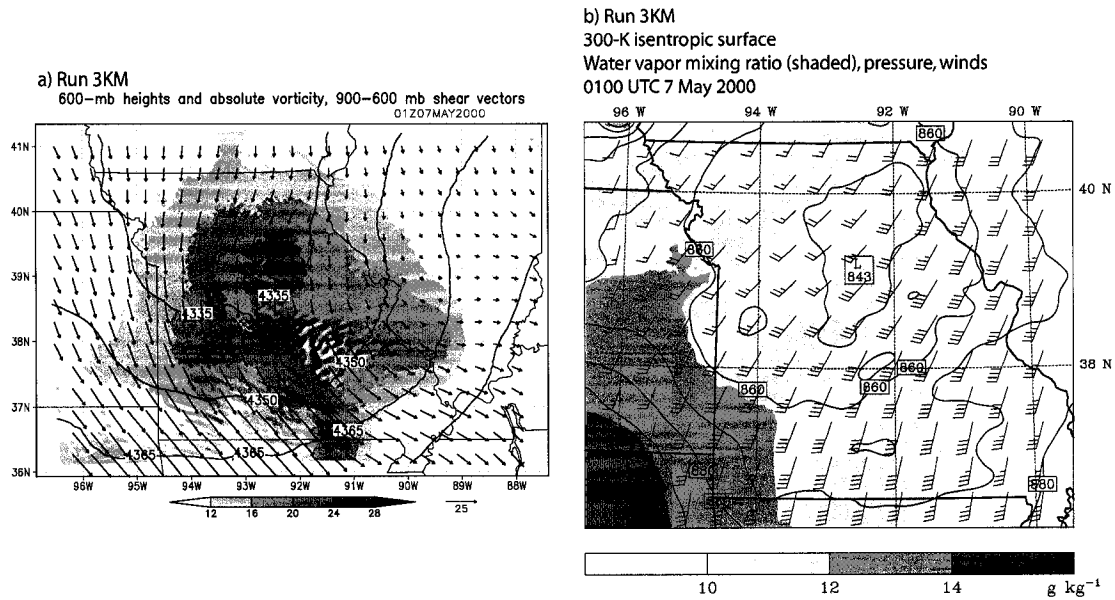


Figure 4.11: (a) 600-hPa geopotential height (contoured every 15 m) and absolute vorticity (shaded every  $4 \times 10^{-5} \text{ s}^{-1}$  for values greater than  $12 \times 10^{-5} \text{ s}^{-1}$ ), and 900–600 hPa shear vectors ( $25 \text{ m s}^{-1}$  reference vector shown at bottom) and (b) pressure (contoured every 10 hPa), water vapor mixing ratio (shaded every  $2 \text{ g kg}^{-1}$  above  $10 \text{ g kg}^{-1}$ ) and winds (conventional, every 15th grid point) on the 300-K isentropic surface on domain 2 of run 3KM at 0100 UTC 7 May 2000.

model integration<sup>2</sup>) there is pronounced low- and midlevel isentropic lift and moisture advection in southwestern Missouri toward the center of the MCV (Fig. 4.11b). This lifting on the downshear side of the MCV was instrumental in initiating and maintaining convection in this region, consistent with the ideas of Raymond and Jiang (1990).

As discussed in chapter 2, an additional effect of MCV-related lifting is that layers of air can be lifted to saturation, leading to moist absolutely-unstable layers (MAULs). The KSGF sounding (Fig. 3.7a) exhibited a MAUL, and deep, widespread MAULs are present in the model simulation as well (Fig. 4.12). It was within these layers of moist instability (or near-neutrality) that scattered convection developed, both in the radar observations and the simulation. This convection eventually organized into the heavy-rain-producing

<sup>2</sup> This time is still within the model's "spin-up" period, but from examining the output from this run, the relatively large-scale process of isentropic upglide appears to be robust, and it compares favorably with RUC analyses from the same time. On the other hand, convection-scale processes have not "spun up" until a few hours into the simulation.

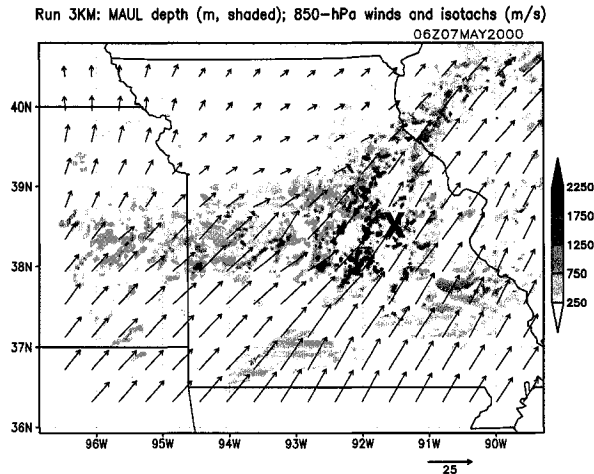


Figure 4.12: Depth of moist absolutely-unstable layers (m, shaded) at 0600 UTC on domain 2 of run 3KM. A MAUL is defined as a vertically continuous region where the moist Brunt-Väisälä frequency is negative and cloud liquid water content is greater than  $0.01 \text{ g kg}^{-1}$  (e.g., Bryan and Fritsch 2000; Kirshbaum and Durran 2004). Also shown are 850-hPa winds (vectors every 50th grid point) to show the location of the LLJ, and the “X” denotes the location of the maximum midlevel vorticity at this time.

MCS. In the first 2–3 hours of the simulation, some convection forms within the MAUL that appears to be a result of spurious gravity waves during the model “spin-up” period. However, this spurious convection quickly dissipates and the more organized, physically realistic convective system develops.

Even after the MCS matured, scattered convective cells continued to form upstream and eventually merged with the larger system (some of these cells can be seen in observations in Fig. 4.5a and from the model in Fig. 4.9). The duration of these scattered convective cells was unusual: many of the cells persisted for over 2 hours and traveled 50–75 km before merging with the larger MCS. Note the long corridor of moist absolute instability in western Missouri and eastern Kansas in Fig. 4.12; the MAUL is not horizontally continuous because convection has removed it in some areas, but the region where new convection is developing is being fed from the west with moist absolutely unstable air. Within the MAUL, any small perturbation can initiate a convective cell. However, there is also dry, subsiding air at midlevels being advected southward along the western side of the MCV in

western Missouri. As a result, parcels from within the MAUL that are perturbed do not immediately accelerate upward; instead, they continue to be lifted and fed with saturated air at low levels so that there is minimal evaporation and the updrafts can survive for extended periods of time. Eventually, they enter the slightly more favorable environment near the ongoing convection and they intensify and merge with the mature system.

#### 4.3.3 *Organization and maintenance of convective line*

In the 0500-1200 UTC time period, the simulated convection continues to intensify and organize into a quasi-stationary MCS. Both radar observations and simulations suggest two different mechanisms for the initiation of upstream convection: a “long distance” mechanism discussed above by which upstream parcels are lifted to their level of free convection (LFC) by MCV-related lifting and then slowly approach the ongoing deep convection, and a second process where new cells are initiated much more quickly in close proximity to the mature convective system. These two mechanisms often work in concert with one another, as shown in the series of vertical sections in Fig. 4.13. At 0945 UTC, two of the shallow, “long distance” cells are apparent in this west-east section at approximately  $x = 19$  and  $x = 38$ , with a deeper cell above  $x = 65$  (Fig. 4.13a). Fifteen minutes later (1000 UTC, Fig. 4.13b), these cells have moved eastward, with the one formerly at  $x = 38$  having become a deep convective cell now at  $x = 50$ . The westernmost cell is still relatively weak, with just a  $1 \text{ m s}^{-1}$  updraft confined to midlevels. Thirty minutes after this (1030 UTC, Fig. 4.13c), that cell is finally beginning its intensification above  $x = 52$  with no new development behind it in the plane of this cross-section. After another 15 min (1045 UTC, Fig. 4.13d), this is now an intense cell, which then apparently helps to initiate two new cells immediately upstream of it by 1100 UTC (Fig. 4.13e). These two processes of backward propagation owing to relatively slow MCV-related lifting and a more sudden convective-scale process can be observed at many different times throughout the simulation. The mechanism for the close-range back-building will be explored further with

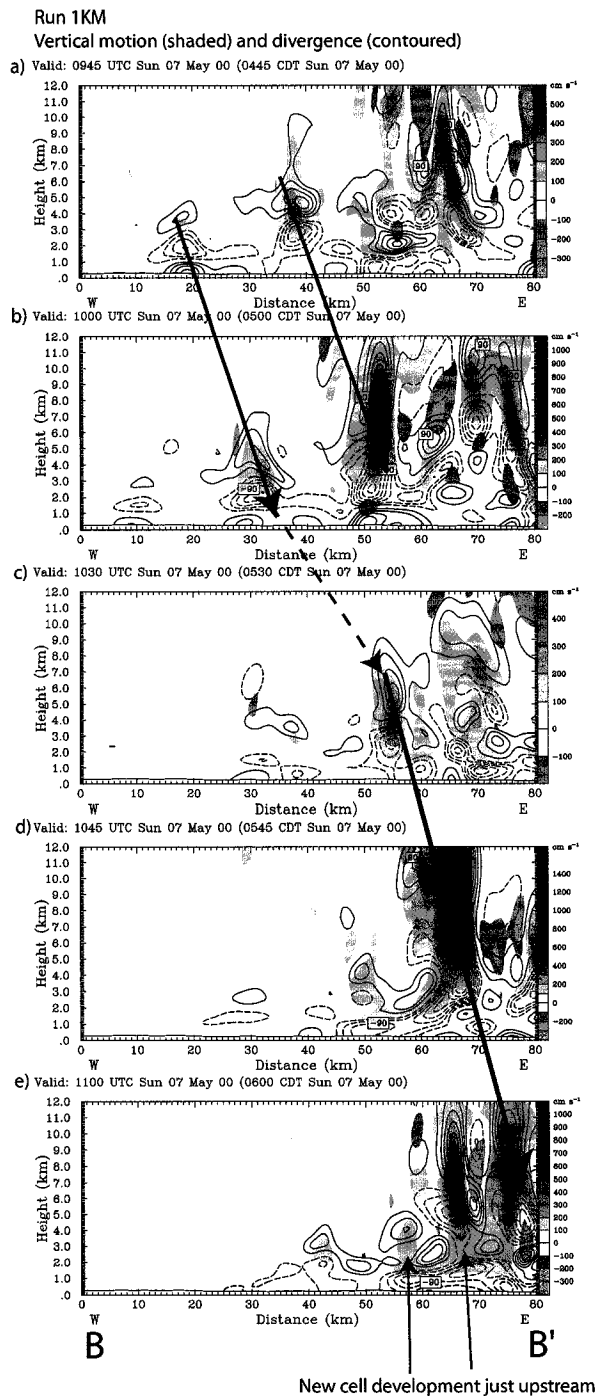


Figure 4.13: Approximately W-to-E section through development of several convective cells in run 1KM. Fields shown are vertical motion (color contours every  $1 \text{ m s}^{-1}$ ) and divergence (contours every  $30 \times 10^{-5} \text{ s}^{-1}$ , negative contours dashed) at (a) 0945 UTC, (b) 1000 UTC, (c) 1030 UTC, (d) 1045 UTC, and (e) 1100 UTC. Location of vertical section in the horizontal plane and reflectivity at 1000 UTC are shown by line B–B' in Fig. 4.15a. Values shown have been averaged over an area 3 grid points (3 km) in either direction of this line. The arrows superimposed on the plot follow individual convective cells through time; the dashed arrow between panels (b) and (c) reflects the 30-min interval between those two panels compared with 15 min for the other panels.

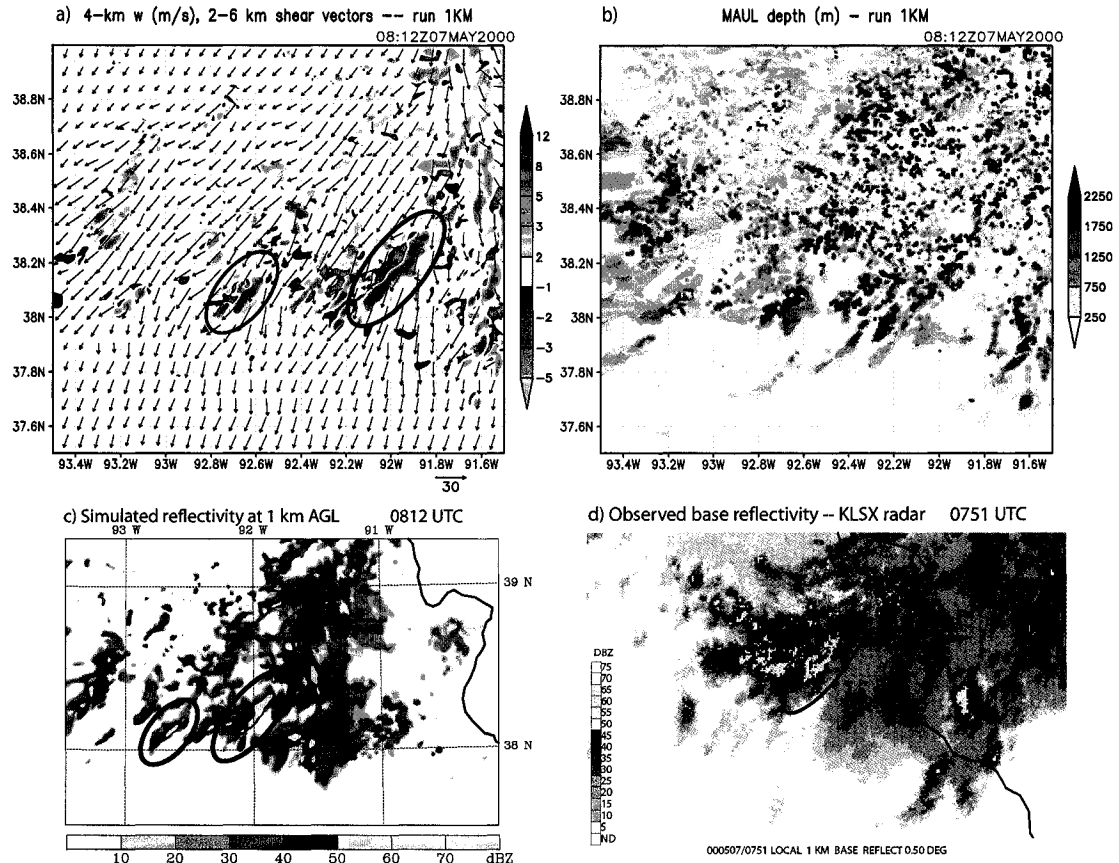


Figure 4.14: (a) 4-km vertical velocity ( $\text{m s}^{-1}$ , shaded as shown) and shear vectors in the 2–6-km layer ( $\text{m s}^{-1}$ ) at 0812 UTC on a portion of the domain in run 1KM. The primary roll-like structures are circled. (b) Depth of moist absolutely-unstable layers (m, shaded) at 0812 UTC on domain 3 of run 1KM. (c) Simulated radar reflectivity at 1 km AMSL at 0812 UTC showing the location of the rolls outlined in panel (a). (d) Observed base radar reflectivity from the St. Louis, MO radar (KLSX) at 0751 UTC. A possible roll is circled.

idealized simulations in the next subsection.

Another interesting aspect of the convective system is the appearance of roll-like convective circulations at midlevels that align themselves along the shear (Fig. 4.14a). At the time shown in Fig. 4.14, the 2–6-km shear vectors point toward the south-southwest and have ambient magnitudes around  $15 \text{ m s}^{-1}$  over the depth of this layer, with some much stronger values within the MCS. The rolls arise out of deep MAULs (Fig. 4.14b), which suggests that they are similar structures to the shear-parallel rolls within squall lines identified by Bryan et al. (2007). In the present simulations, the roll-like circulation

exists between about 2 and 5 km, with the convection above this level (where the shear is weaker) appearing cellular rather than banded (not shown). Though we cannot determine definitively that the structures are the same, bands of higher reflectivity with similar motion characteristics appear in radar observations of the MCS (Figs. 4.14c–d). As such, this may provide observational evidence for the simulated rolls that Bryan et al. (2007) showed in a more idealized environment, and also evidence that they occur in moist absolutely-unstable environments outside of the leading line/trailing stratiform squall line archetype.

There is a large spectrum of convective motions at work in this MCS, making it difficult to distinguish between a “convective” and “stratiform” region. However, the primary organizational mode is an approximately west-east quasi-linear convective system, especially in its mature stage. Simulations show that the mechanism responsible for the linear organization is not a surface cold pool. This being the case, we seek to determine what is organizing the system in this way, and why nearly all of the weak scattered cells discussed above seem to intensify in essentially the same place. These questions are key to understanding why the system remains quasi-stationary.

At 1000 UTC, when the convection is generally organized linearly (Fig. 4.15a), the surface virtual potential temperature ( $\theta_v$ ; a measure of density) difference across the region of developing deep convection was less than 1 K (Fig. 4.15b). However, when looking somewhat above the surface, things are much different: a narrow east-west band of cool air is present, and a narrow band of warmer air exists just to its north at 0.9 km AMSL (approx. 0.7 km AGL) (Fig. 4.15c). A vertical section across this feature reveals that this is a low-level internal gravity wave and that air encountering it from the south is lifted sharply (Fig. 4.16a). Since the air near the surface is within a nocturnal stable layer and has small CAPE and large CIN (Fig. 4.16), it does not accelerate upward in deep convective cells; rather, it is lifted over the cool branch of the gravity wave and then sinks along downward-sloped isentropes on the other side (Fig. 4.17a–b). This low-level flow pattern is reminiscent of the “up-down” downdraft described by Knupp (1987, 1988),

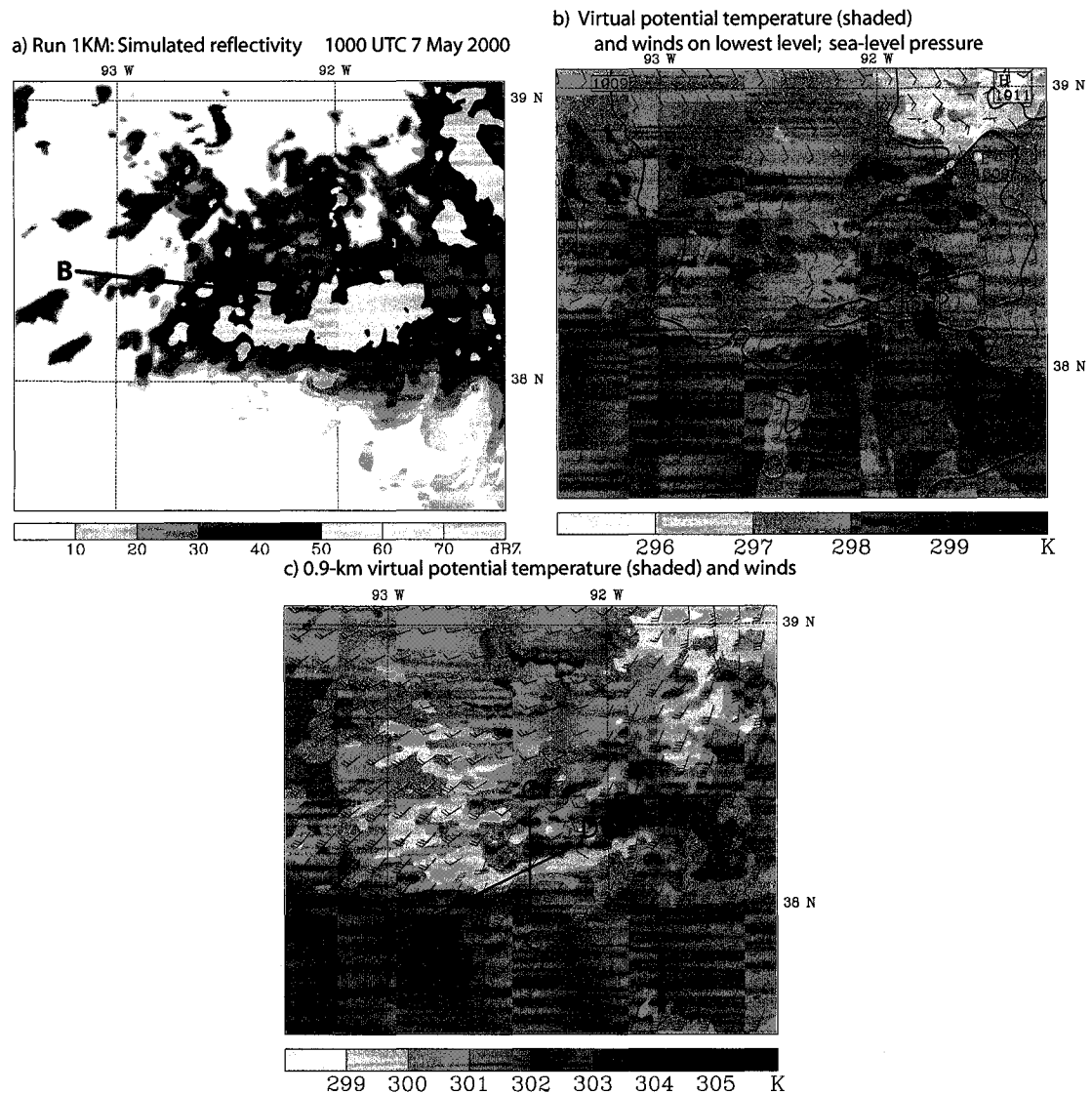


Figure 4.15: (a) Simulated composite radar reflectivity at 1000 UTC on a portion of domain 3 of run 1KM. (b–c) Virtual potential temperature (shaded every 1 K) and winds at 1000 UTC for (b) the lowest model level and (c) 0.9 km AMSL (approximately 0.7 km AGL). Pressure adjusted to sea level, contoured every 1 hPa, is also shown in panel (b). The portion of the domain shown is the same for all three panels. Wind barbs are shown at every tenth model grid point. Lines C–C' and D–D' in panel (c) show the locations of vertical sections to be shown in Figs. 4.16 and 4.17.

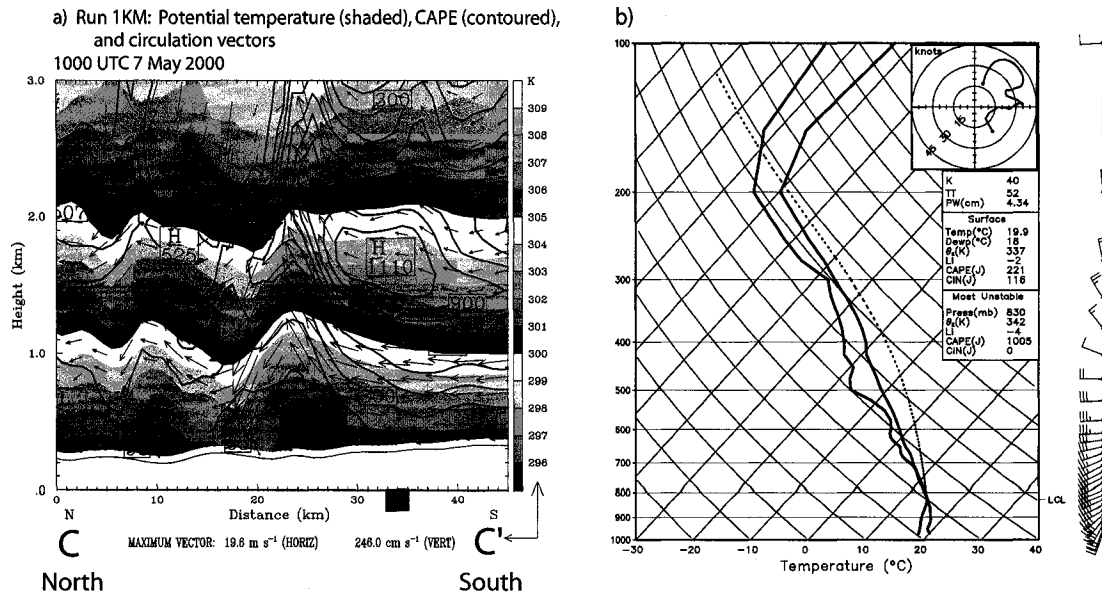


Figure 4.16: (a) North-south low-level vertical cross-section of potential temperature (shaded every 1 K), CAPE for parcels lifted from each level (contoured every 100 J kg<sup>-1</sup>), and flow vectors in the plane of the cross-section (length scale shown at bottom; the scales for horizontal and vertical velocities are different) through line C-C' shown on Fig. 4.15c at 1000 UTC on domain 3 of run 1KM. Note that only the lowest 3 km above sea level are shown. Values shown have been averaged over an area 5 km on either side of the line. (b) Average skew- $T$  log  $p$  diagram for the immediate inflow region. The grid points used for the average are shown by the thick black box at the bottom of panel (a). The parcel path shown with the dotted line is that for the parcel with the highest  $\theta_e$  in the lowest 3 km.

although he did not invoke gravity-wave dynamics as an explanation for such flow. Air farther aloft (from approximately 1.5–2 km AMSL), which has had the benefit of both strong moisture advection and MCV-related lifting, has much more CAPE and essentially zero CIN (Fig. 4.16). Parcels at this level also encounter the upward branch of the gravity wave and erupt into deep convection (Fig. 4.17a,c). Since the wind above approximately 1.5 km has a strong westerly component, the parcels' path over the west-east oriented wave is not such a sharp jump. The westerly upper-level flow results in the convective cells moving from west to east along the direction of the gravity wave and leads to the linearly-organized convective system. Thus, the strongly-turning wind shear vector (as illustrated in the hodograph in Fig. 4.16b) plays an important role in the organization of the system.

The importance of these gravity waves in organizing the convective system and the

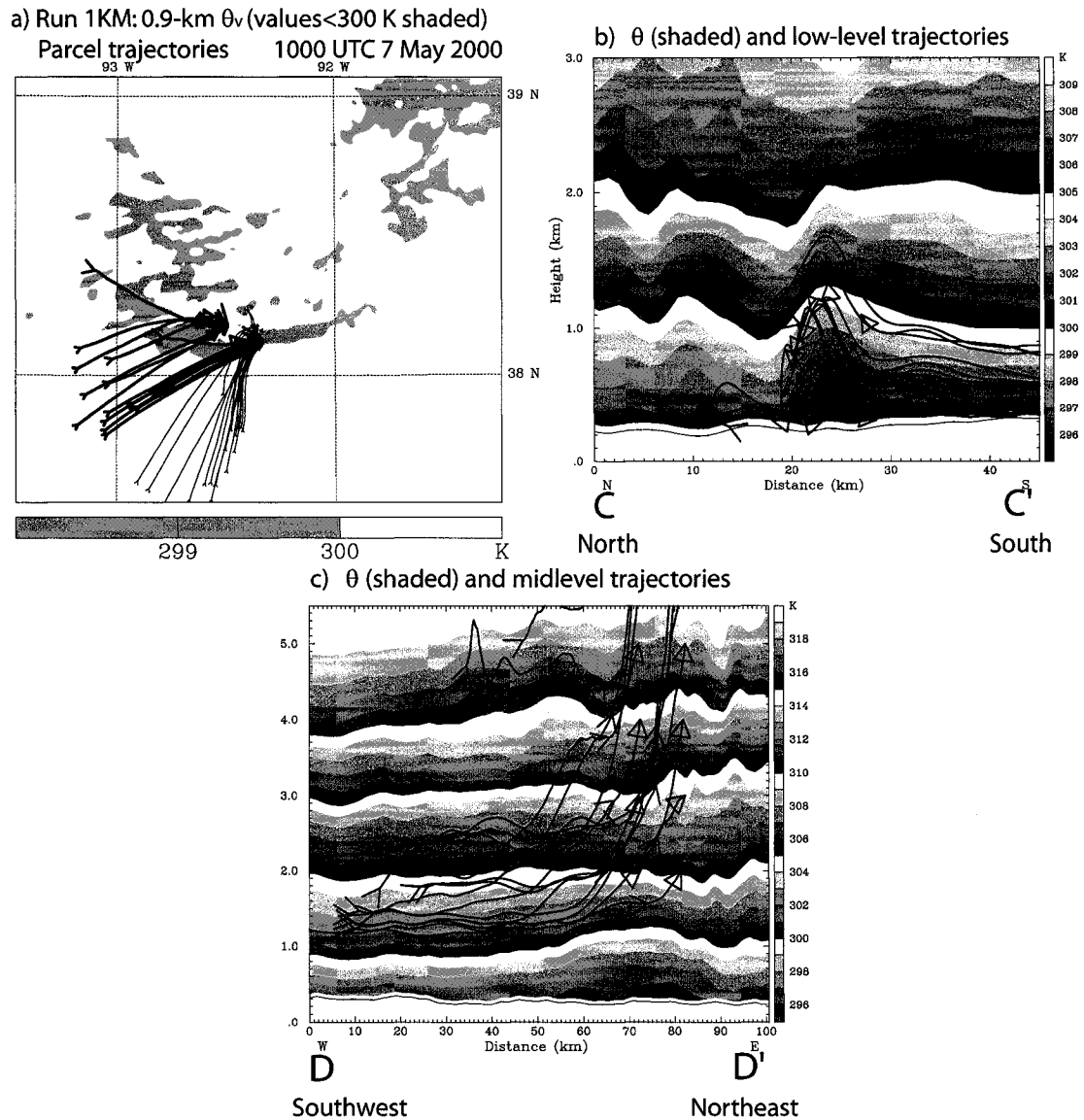


Figure 4.17: (a) As in Fig. 4.15c, except only values below 300 K are shaded. The narrow band of cool air represents the upward branch of the low-level gravity wave. Also shown are the the locations in the horizontal plane of the parcel trajectories shown in panels (b) and (c): the thin trajectories are the near-surface parcels shown in (b), and the thick trajectories are the elevated parcels shown in (c). (b-c) Vertical sections showing potential temperature (K, shaded) at 1000 UTC and representative parcel trajectories showing (b) airflow from south to north at low levels, rising and sinking over the gravity wave; and (c) air rising in deep updrafts. Panel (b) shows a south-to-north section (along line C-C' shown in Fig. 4.15b) and shows heights from 0–3 km. Panel (c) is a southwest-to-northeast section (along line D-D' shown in Fig. 4.15b) and shows heights from 0–5.5 km. The open triangles represent the endpoints of the trajectories.

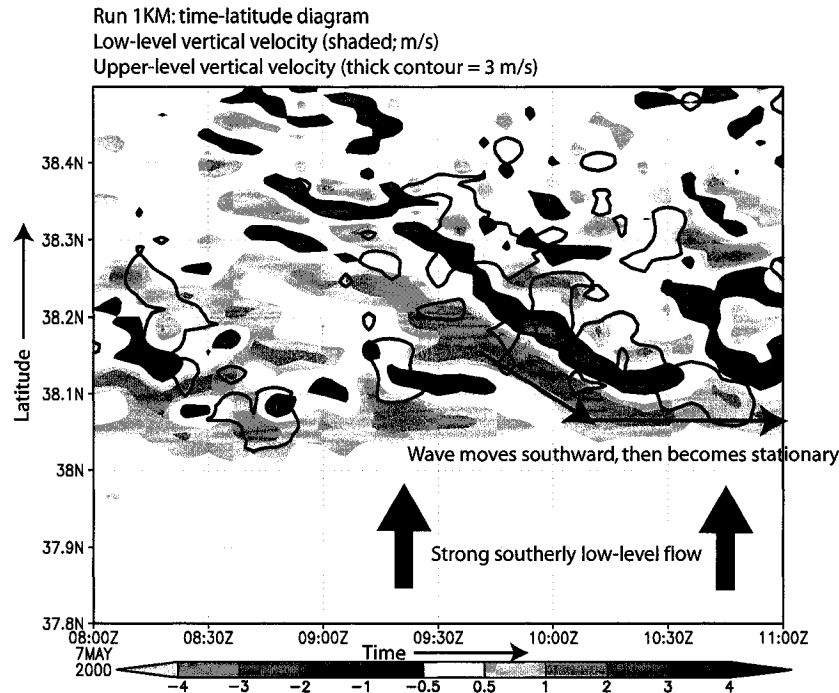


Figure 4.18: Time-latitude plot of vertical velocity showing the relationship between low-level gravity waves and deep convection. Vertical velocity from a model level at approximately 0.75 km AMSL has been averaged over longitudes  $93.5^{\circ}\text{W}$  to  $92.3^{\circ}\text{W}$  and is shaded. Vertical velocity from a model level at approximately 7 km has been averaged over longitudes  $93.1^{\circ}\text{W}$  to  $91.9^{\circ}\text{W}$ ; the  $3\text{ m s}^{-1}$  contour is shown to show locations with strong, deep updrafts. The difference in longitudes accounts for the fact that convection initiated at low levels does not reach upper levels until it travels some distance to the east.

waves' curious motion characteristics is illustrated in a time-latitude diagram of vertical velocity (Fig. 4.18). The low-level gravity waves have strong couplets of upward and downward motion, and in Fig. 4.18, the wave of primary interest is shown to move southward between approximately 0915–1030 UTC. Several other weaker waves can be seen at earlier times and in other locations. (One of these weaker waves was formed in association with the developing convective cells in Fig. 4.13, which was located just to the north of the strongest wave.) Fig. 4.18 also shows the strong relationship between the low-level vertical motion owing to the waves and strong upper-level vertical motion (i.e., deep convection) just to the north, especially along the strong southward-moving wave between 0930–1030 UTC. Also of interest is the fact that the primary wave moves southward at a ground-relative speed of

approximately  $9 \text{ m s}^{-1}$ , but when it reaches approximately  $38.05^\circ\text{N}$  latitude, it essentially stops. To the south of this point, the low-level winds are generally undisturbed by convection, and as such the wave slows when it propagates into this region of strong low-level flow. At earlier times, there is also no significant wave activity south of this latitude; these motion characteristics are crucial factors in the stationarity of the MCS.

Further evidence that these are indeed gravity waves is shown in Fig. 4.19. As the primary couplet of convergence and divergence passes through a given location (for instance, the point shown in Fig. 4.19a at 0945 UTC), the surface pressure and the wind in the direction of wave propagation vary exactly in phase (Fig. 4.19b). This behavior is consistent with that of a gravity wave (Fig. 2.14). Additionally, Fig. 4.19a shows that the surface pressure trough, which is similar to the observed trough shown in Fig. 4.6b, is  $90^\circ$  out of phase with the maximum convergence. This is also consistent with the expected behavior of a gravity wave.

That these waves are distinct from a cold pool is confirmed by the results of a simulation where the evaporation of raindrops is not allowed (run NOEVAP). In NOEVAP, the structure and evolution of the resulting MCS is nearly indistinguishable from run 3KM, which includes all microphysics processes, and the strength of the system is comparable (cf. Figs. 4.20a and 4.15a). The structure of the low-level gravity wave in NOEVAP is also nearly identical (cf. Figs. 4.20b and 4.15c), which shows that the wave is not a result of low-level cooling from evaporation. It will be shown in the next subsection that the formation of these waves is a response to latent *heating* rather than cooling.

#### 4.3.4 *Illustration of low-level waves in idealized simulations*

By employing simpler simulations in which a single convective burst is initiated through the use of a buoyant perturbation (see section 4.2 for details), it becomes clear that these low-level waves are a response to diabatic heating from the formation of clouds near the lifting condensation level. In these simulations, the composite thermodynamic

a) Run 1KM: Divergence (shaded) and winds on lowest level  
Sea-level pressure 0945 UTC 7 May 2000

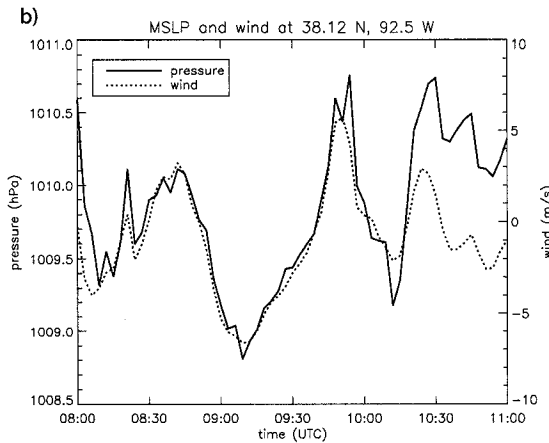
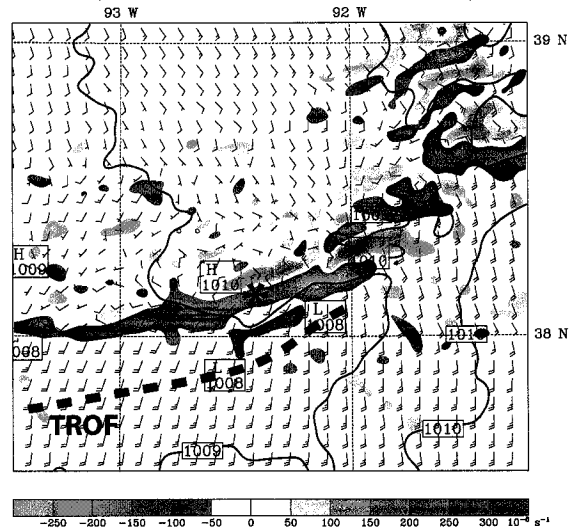


Figure 4.19: (a) Divergence (shaded) and winds on the lowest model level and pressure adjusted to sea level (thick contours every 1 hPa) on a portion of domain 3 of run 1KM at 0945 UTC. (b) Time series from 0800–1100 UTC showing pressure adjusted to sea level (hPa, solid line) and wind speed in the direction of wave propagation ( $\text{m s}^{-1}$ , dotted line) in run 1KM at the point shown by the asterisk in panel (a). The wind was calculated using Equation 1 of Koch and Golus (1988), using  $330^\circ$  as the direction from which the wave was propagating (measured clockwise from north).

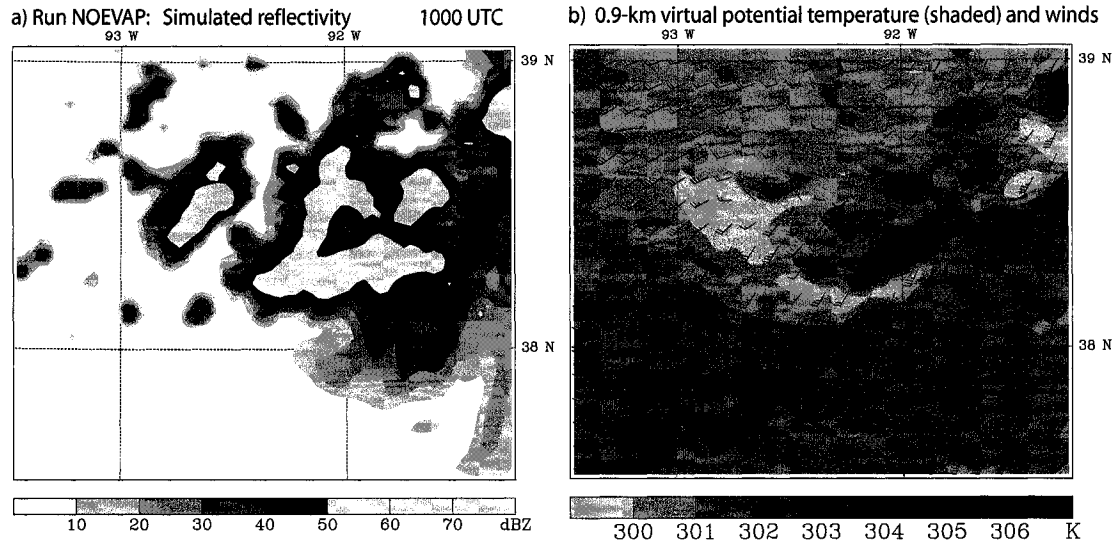


Figure 4.20: (a) As in Fig. 4.15a, but for run NOEVAP. (b) As in Fig. 4.15c, but for run NOEVAP.

sounding from the six extreme rain events presented in chapter 3 (Fig. 4.21) is used to construct a horizontally-homogeneous environment. This sounding closely resembles the inflow environment in the 6–7 May 2000 case (cf. Figs. 4.21 and 4.16). The initial wind profile used in these simulations is slightly different from the composite profile; it is a smoothed version of an average wind profile in the vicinity of the convective system at 0600 UTC in the case-study simulation discussed in the previous subsections. It includes strong reversal of shear at low levels and the hodograph has a “hairpin” shape, similar to the composite profile. For this simulation, the model domain was translated to attempt to keep the primary convective cell at the center of the domain. A full investigation of the behavior of convection in varying wind profiles is beyond the scope of this particular chapter and will be presented in chapter 5; however, two simulations will be shown here which illustrate the development of the low-level waves in this environment.

First, we show the results from a simulation where a buoyant bubble is released in the thermodynamic environment shown in Fig. 4.21 but with zero initial wind. In this simulation, the bubble rises and accelerates past the LFC directly above where it was released. At  $t = 30$  min, there is a strong updraft with the signature of gravity wave

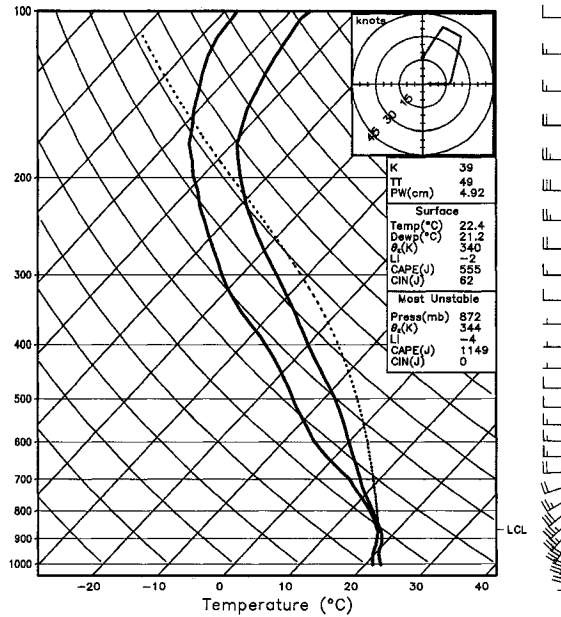


Figure 4.21: Skew- $T$  log  $p$  diagram showing the thermodynamic and wind profile used in horizontally-homogeneous idealized simulations. The thermodynamic profile is identical to the composite sounding shown in Fig. 3.17, and the wind profile is an averaged, smoothed profile from the vicinity of the convective system at 0600 UTC in the 6–7 May 2000 case study simulation. The parcel path shown with the dotted line is that for the parcel with the highest  $\theta_e$  in the lowest 3 km.

propagation flanking it (Fig. 4.22a). At midlevels, there is a gravity wave mode with a depth of approximately 3.5 km, and another mode at upper levels. Of primary interest here is the wave below about 1.5 km, which appears as cool perturbations propagating away in Fig. 4.22a. This wave is located near the simulated cloud base and appears to be very similar to the low-level waves shown in the no-shear case of Schmidt and Cotton (1990; see Fig. 2.13a).

When the same buoyant bubble is released within the complex reverse-shear wind profile, the result is quite different. Again, the bubble accelerates above its LFC, but the updraft is now affected by the changing wind with height (Fig. 4.22b). At low levels, rather than a wave propagating away in all directions, there is a single slow-moving wave that has amplified considerably (Fig. 4.22b). A closer look at low levels (Fig. 4.22c) reveals that this structure is very similar to the low-level waves that were prominent in the case-study

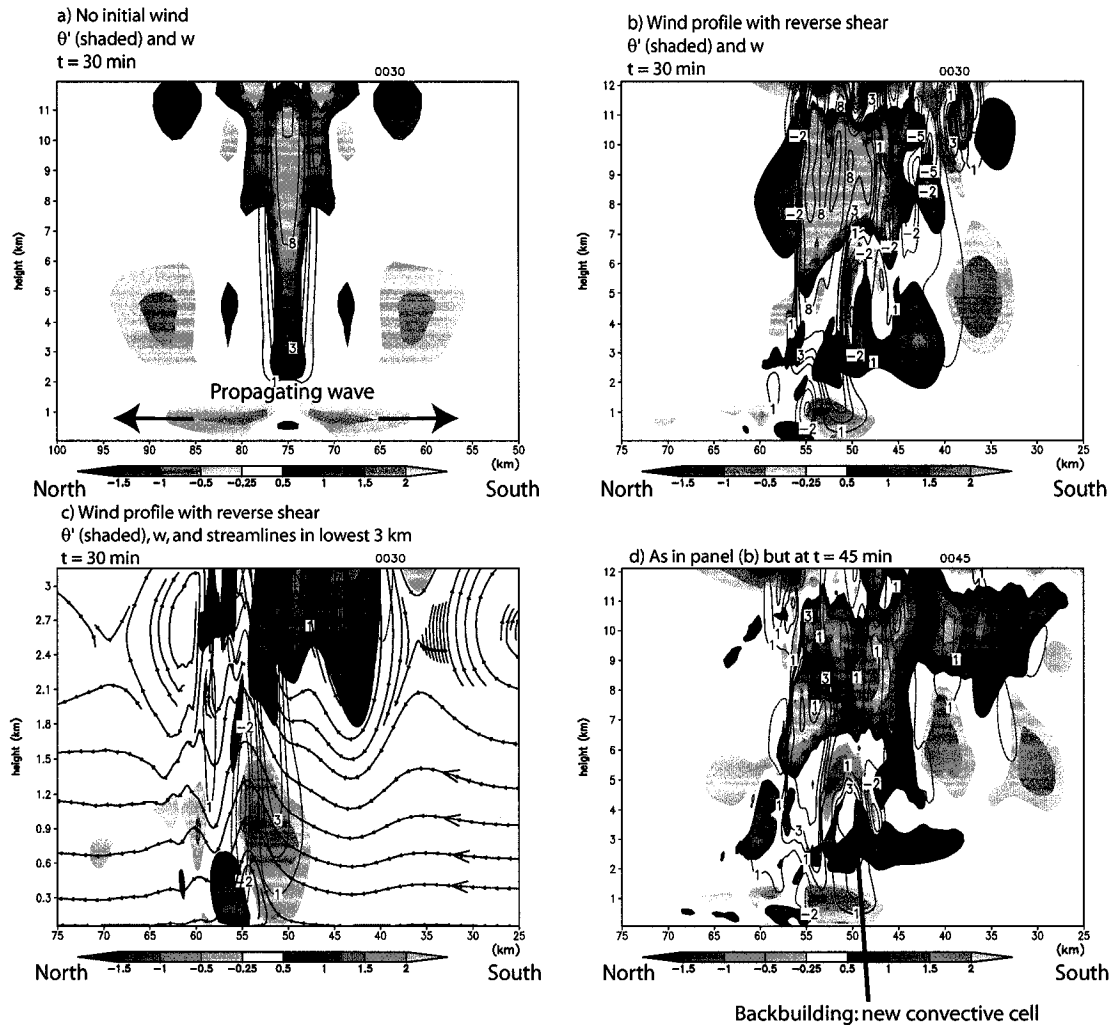


Figure 4.22: North-south vertical cross sections of potential temperature perturbation (K, shaded, see color bar for scaling) and vertical velocity (contours at  $-4$ ,  $-2$ ,  $-1$ ,  $1$ ,  $2$ ,  $3$ ,  $5$ ,  $8$ , and  $12 \text{ m s}^{-1}$ , with negative contours dashed) for (a) simulation with no initial wind at  $t = 30$  min; (b) simulation with wind profile shown in Fig. 4.21 at  $t = 30$  min; (c) as in panel (b), but showing only the lowest 3 km and including streamlines; (d) as in panel (b) but at  $t = 45$  min. The values shown in the cross-sections have been averaged over an area 3 km on either side of a line through the deep convection.

simulation (cf. Fig. 4.16). Air flowing toward the updraft from the south is lifted over the cool branch of the wave and then quickly descends on the other side, with even a hint of a rotor circulation beneath the wave near the surface. At some level above the surface, air is lifted to its LFC and accelerates upward, just as in the simulated MCS in the 6–7 May 2000 case. The flow pattern at this time is similar to the schematic of a “gravity wave with stagnation” shown by Crook and Moncrieff (1988; see Fig. 2.12). This low-level wave, which remains very near its source, is also responsible for the initiation of new discrete cells in the idealized simulation: by  $t = 45$  min, the back-building process has begun with a new cell initiating at approximately  $y = 50$  in Fig. 4.22d. This high-resolution simulation was only run out to 45 min, but in coarser-resolution simulations, the back-building process is observed to continue, with several discrete cells developing. This appears to be the same process as the “short distance” method of back-building discussed in section 4.3.3, and it is a different mechanism from that found by Parker (2007a), which involved the upshear acceleration of downdrafts. A simulation in which all latent cooling processes were removed from the model produces the same low-level wave feature (Fig. 4.23); as such it can be concluded that it is a response to the latent *heating*. Such waves also develop in simulations with different thermodynamic soundings, though they quickly disappear in drier environments as they are overwhelmed by the production of a cold pool. These waves will be investigated further in chapter 5, and understanding their dynamics will be a subject of future work.

#### 4.3.5 *Development of surface low pressure and re-intensification of MCV*

Recall that the primary feature in the surface weather observations during the MCS’s lifetime was a mesoscale region of low pressure (Fig. 4.6). The presence and location of this mesolow near the region of upstream convective development raises the possibility that convergence associated with the mesolow assisted in maintaining the heavy-rain-producing MCS. Past studies of quasi-stationary convection in Japan by Kato (1998) and Kato and

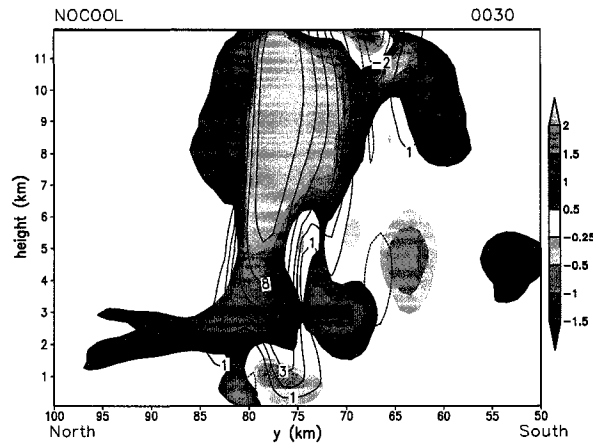
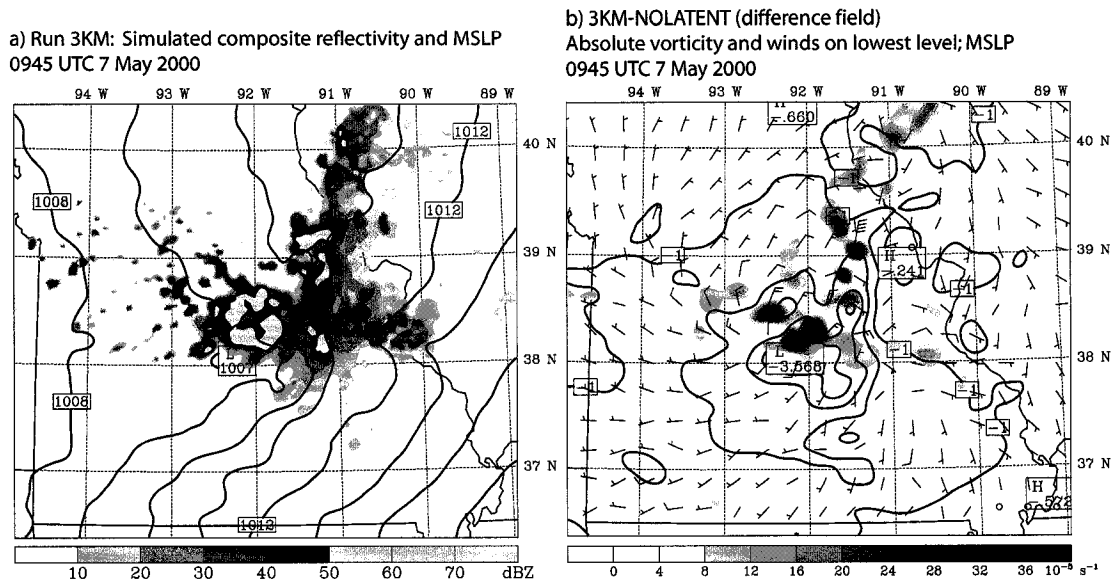


Figure 4.23: As in Fig. 4.22b, except for a run with all latent cooling processes removed at  $t = 30$  min. The horizontal grid spacing of this simulation is 1 km.

Goda (2001) have suggested that such a mechanism was important in the cases they investigated.

In simulations 3KM and 1KM, as scattered convection develops in the first several hours, a surface pressure trough forms and becomes stronger with time. It becomes oriented from west to east with the mesolow located on the upstream side of the MCS, consistent with the observed surface pressure pattern (Fig. 4.24a, cf. Fig. 4.6b). Fields showing the difference between runs 3KM and NOLATENT show that the MCS is generating the surface low pressure (i.e., it is not simply a manifestation of the initial midlevel PV anomaly at lower levels; Fig. 4.24b). There is strong cyclonic vorticity at the surface near the deep convection as well as a broader circulation that reaches far from the MCS. Although the pressure gradient associated with the surface low is likely playing a role in providing additional mesoscale uplift for new convective initiation and sustenance, it appears that the low-level gravity wave discussed previously is the primary organizing mechanism for the convective line. Fig. 4.19a showed that the strongest low-level convergence was out of phase with the lowest pressure, which suggests that the convergence associated with the gravity wave, rather than the latent-heating-driven pressure trough, was most responsible for the linear organization of the convection.



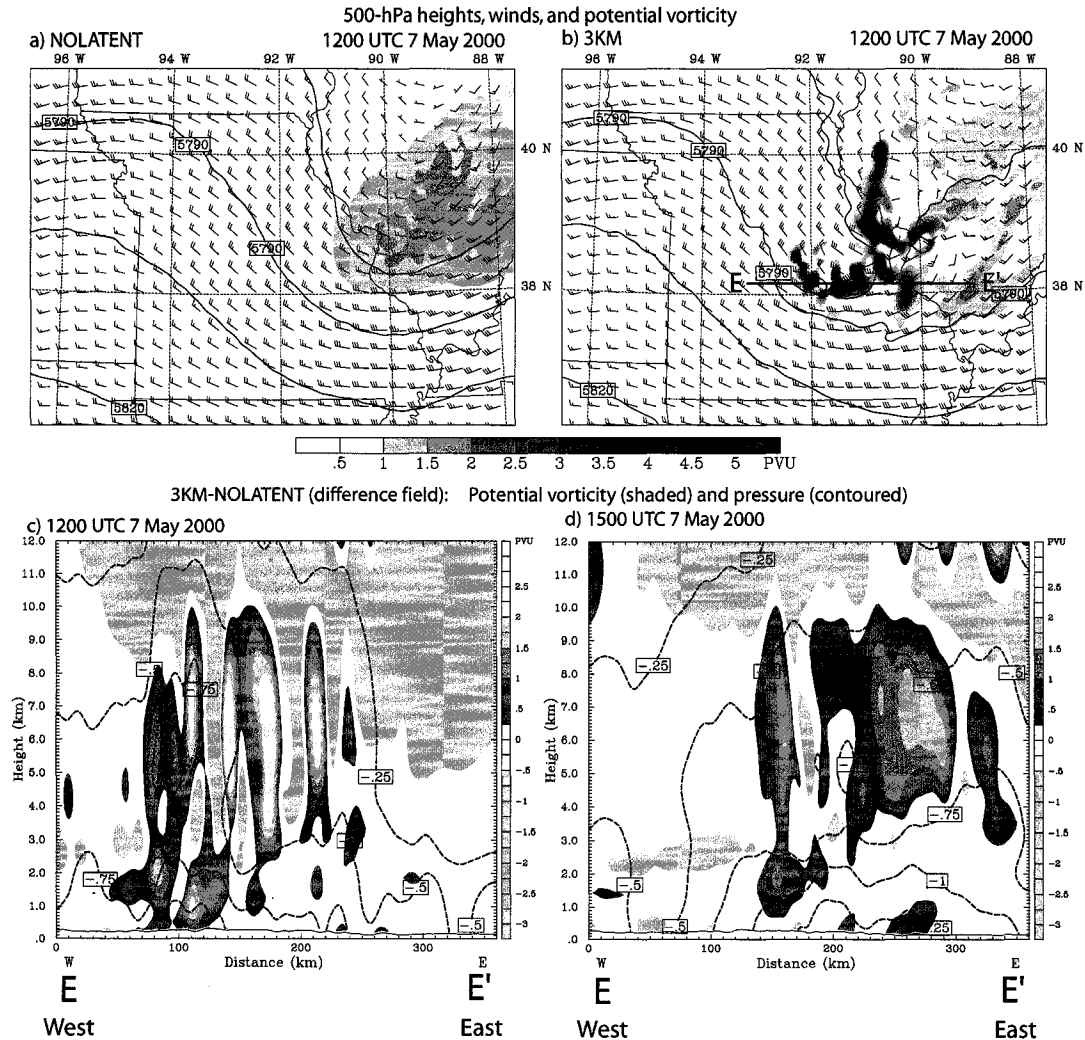


Figure 4.25: (Top row) 500-hPa potential vorticity (shaded), geopotential height (contoured every 15 m) and winds at 1200 UTC 7 May 2000 in (a) NOLATENT and (b) 3KM. Wind barbs are shown at every tenth model grid point. (Bottom row) West-to-east sections showing difference fields between 3KM and NOLATENT at (c) 1200 UTC and (d) 1500 UTC. Shown are potential vorticity (shaded as shown) and pressure (contoured every 0.25 hPa). The location of the vertical section is shown by line E-E' in panel (b). The values shown have been averaged over an area 45 km on either side of line E-E'.

surface has disappeared, but an organized midlevel PV anomaly is now apparent between about 5.5–8 km AMSL (Fig. 4.25d). This is the reintensified MCV, which then continues eastward during the day. This evolution is generally similar to that in the case studied by Davis and Trier (2002), and it suggests important roles for both deep convection (as in the “vortical hot tower” idea of Montgomery et al. (2006)) and stratiform rainfall (as in Hertenstein and Schubert (1991)) in the development of circulations at the surface and midlevels. A more thorough investigation of these processes will be a part of future research. The process by which tropical cyclones develop from midlevel vortices has been a topic of interest in the literature recently (e.g., Rogers and Fritsch 2001; Montgomery et al. 2006; Sippel et al. 2006; Tory et al. 2006), and the lack of a cold pool, the development of the surface mesolow, and the very moist conditions that existed in the 6–7 May 2000 event may make it a suitable case to study in this context.

#### 4.4 Summary and conclusions

This chapter presents observations and convection-permitting simulations of a significant heavy rain and flash flood event that occurred in Missouri on 6–7 May 2000. The primary findings are as follows:

- Prior to the event, a long-lived mesoscale convective vortex meandered through the southern Plains for several days. Mesoscale lifting resulting from the interaction of a strong low-level jet with this MCV led to the initiation of scattered convection, which intensified and became more organized with time. The resulting MCS remained quasi-stationary for over 8 h, and produced rainfall totals exceeding 300 mm.
- The WRF-ARW model, with horizontal grid spacings of 3 km and 1 km and explicitly predicted convection, is able to successfully simulate the organization and extreme rainfall totals of this MCS. Operational models and coarser-resolution runs

with parameterized convection did not provide any evidence of extreme rain in their output.

- The primary organizing mechanism for the convective system was not a surface cold pool; instead, a series of nearly-stationary low-level gravity waves gave the MCS its quasi-linear organization. Stable near-surface air approached the waves from the south, rose along the upward-sloping isentropes of the wave, and then fell on the other side. Slightly farther aloft, less stable, nearly saturated air was also lifted over the wave and accelerated upward as deep convective cells. Because the southward propagation of the waves was counteracted by the strong southerly flow, the MCS as a whole also moved very slowly, which contributed to the excessive local rainfall totals.
- Idealized simulations show that the low-level gravity wave is a response to latent heating in deep convection. The wind profile with a strong reversal of wind shear with height leads to the amplification and slowing of the wave.
- Observed and simulated surface pressure fields reveal a mesolow beneath the MCS. The deep convection also acts to reintensify and contract the initial midlevel vortex.

The primary mechanisms supporting the heavy rain production in this MCS are summarized in Fig. 4.26.

In the following chapters, further simulations will be performed to clarify the importance of low-level gravity waves in organizing extreme-rain-producing MCSs. In chapter 6, a series of idealized simulations will be presented in which many of the results of this case study will be shown to be generally applicable to quasi-stationary convective systems that form near a meso- or synoptic-scale lifting mechanism.

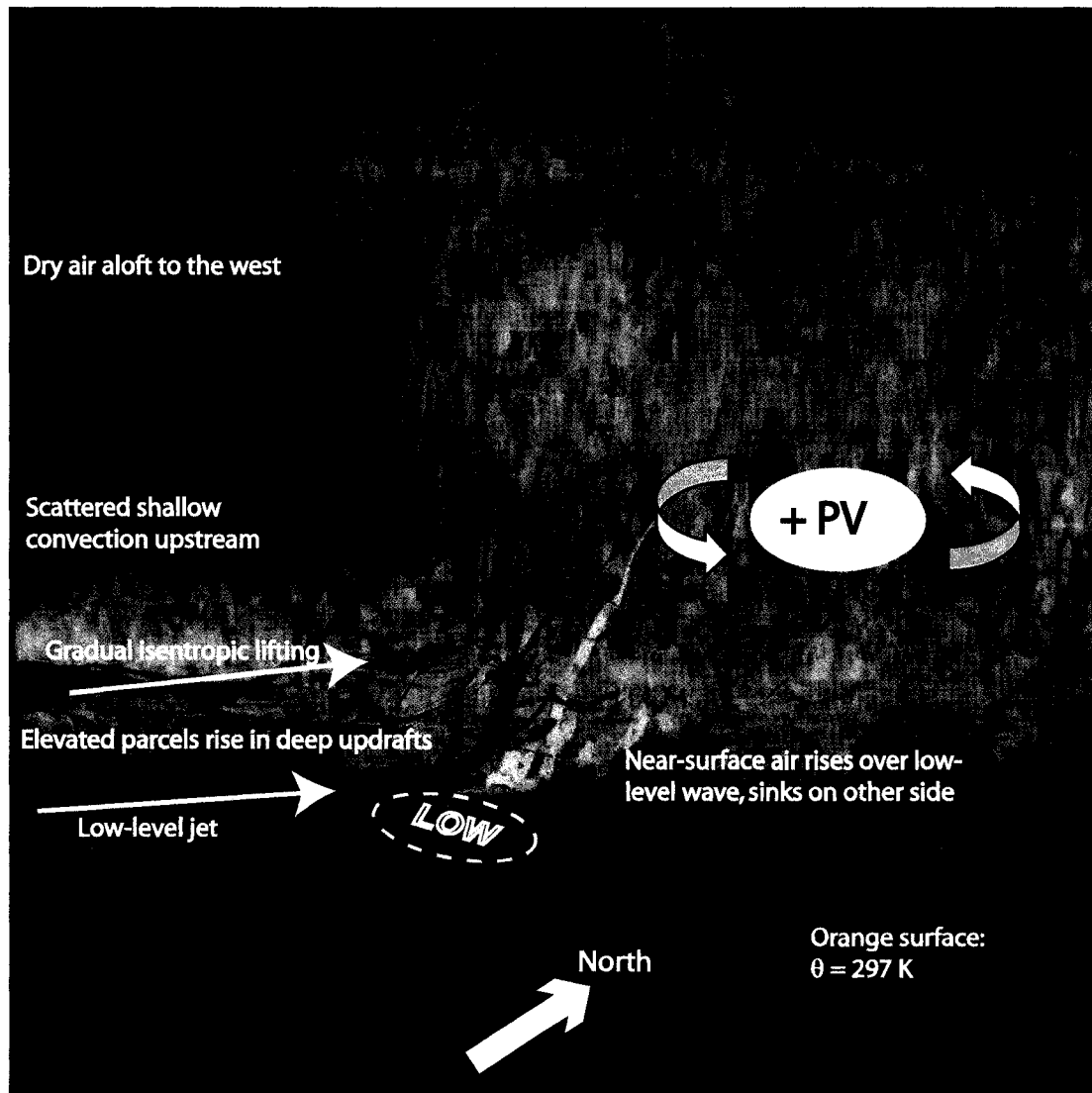


Figure 4.26: Three-dimensional picture highlighting the primary processes at work in the 6–7 May 2000 extreme-rain-producing MCS. In this figure, the viewer is looking at the system from the south-southeast. The MCV and its associated potential vorticity anomaly is shown by “+PV;” the curved arrows indicate the associated midlevel circulation. The orange isosurface at the bottom represents the 297 K isentropic surface; the low-level gravity wave activity can be seen under the convective system. The colored “ribbons” represent parcel trajectories originating at different levels: yellow at 0.4 km AMSL; blue at 0.8 km; green at 1.5 km; red at 2.1 km. The trajectories in yellow and blue show near-surface air that generally rises over the gravity waves but passes underneath the deep convection, whereas the parcels shown in green and red are approaching from the southwest and rise in deep updrafts. “LOW” signifies the surface mesolow.

## Chapter 5

# IDEALIZED SIMULATIONS OF CONVECTIVE UPDRAFTS IN VARYING THERMODYNAMIC AND KINEMATIC ENVIRONMENTS

In the previous chapter, idealized simulations in which convection was initiated with a single warm, moist “bubble” were used to illustrate the development and movement of convectively-generated low-level gravity waves that can help to initiate and organize quasi-stationary convective lines (Fig. 4.22). In an attempt to further understand the characteristics of these waves, further simulations in various thermodynamic and wind profiles will be presented in this chapter. These experiments will provide a lead-in to the more complex simulations to be presented in chapter 6.

### 5.1 Experimental design

As with the idealized simulations shown in chapter 4, these simulations use the Bryan and Fritsch (2002) cloud model. Once again, convection is initiated with a thermal and moisture perturbation, which has a maximum potential temperature perturbation of 2 K, a horizontal radius of 6 km and a vertical radius of 1.5 km with its center at 1.5 km above the model surface. As will be discussed in chapter 6, a “bubble” may not be the most realistic method for initiating convection, especially in the thermodynamic environments considered here. However, the goal of these “bubble” simulations is simply to understand how the immediate environment is affected by deep convective updrafts. Using a single bubble is appropriate for this task, and a more physically realistic method for initiating

Table 5.1: Description of the simulations. “Sounding” refers to the thermodynamic profile, and for most simulations, the composite sounding (abbreviated as “Comp.”) shown in Figs. 3.17 and 4.21 is used. For simulation WK, the analytic sounding of Weisman and Klemp (1982), referred to as WK82, is used. “Wind” refers to the vertical wind profile, which will be shown within the analysis of each simulation.

Name	Sounding	Wind	Other changes
NOWIND	Comp.	Zero initial wind	
FULL	Comp.	Full reverse-shear profile	
NOCOOL	Comp.	Full reverse-shear profile	All latent cooling removed
WK	WK82	Full reverse-shear profile	
NOULSHEAR	Comp.	No shear above LLJ	
NOLLSHEAR	Comp.	No shear below 2 km	
NOLLSHEAR+5	Comp.	No shear below 2 km	$v$ increased by $5 \text{ m s}^{-1}$
NOLLSHEAR1KM	Comp.	No shear below 1 km	
HALFSHEAR	Comp.	Shear reduced by half	
NOULJET	Comp.	No upper-level jet	

convection will be left for the more complex simulations in the next chapter.

All of the simulations to be presented in this chapter use horizontal grid spacing of 1 km and the same stretched vertical grid described in section 4.2. This relatively coarse resolution was used given the number of simulations to be presented and the large computational requirements for true cloud-resolving simulations. As will be shown below, the primary features of interest are present in both cloud-resolving simulations and those that explicitly predict but do not truly resolve convective processes. The domain size is  $144 \times 144 \times 18.5 \text{ km}$ , and the large model timestep is 5 s. Each simulation was integrated for 2 h. Other details of the model were described in section 4.2 and 4.3.4.

A summary of the simulations in this chapter is given in Table 5.1, and further details will be given along with the results of each simulation. Unless otherwise noted, the simulations use a horizontally-homogeneous base state with the composite thermodynamic profile shown in Figs. 3.17 and 4.21.

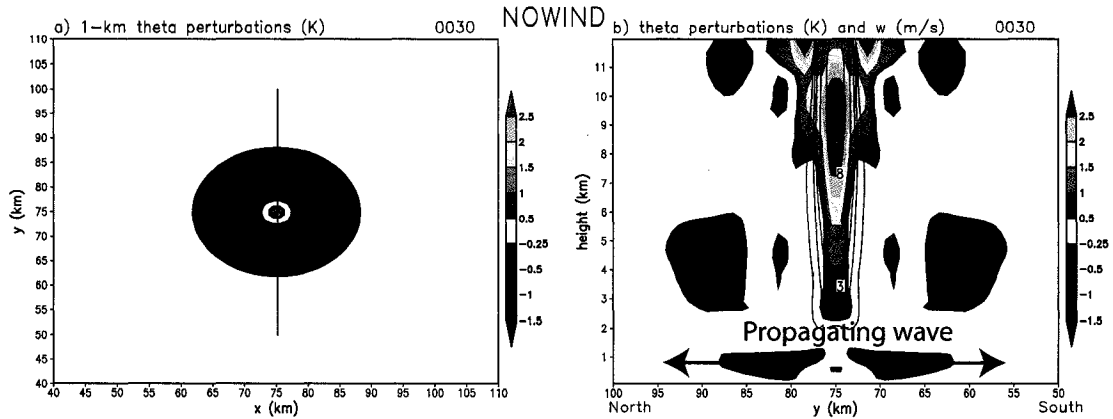


Figure 5.1: (a) Potential temperature perturbations (K, shaded) at 1 km AGL for simulation NOWIND at  $t=30$  min. (b) North–south vertical cross section through the convective cell. Its location is shown by the line in panel (a), and values have been averaged over a 3-km area on either side of this line. Shown are potential temperature perturbation (K, shaded) and vertical velocity (contours at  $-4$ ,  $-2$ ,  $-1$ ,  $1$ ,  $2$ ,  $3$ ,  $5$ ,  $8$ , and  $12$   $\text{m s}^{-1}$ , with negative contours dashed) for simulation NOWIND at  $t=30$  min.

## 5.2 Results

### 5.2.1 NOWIND

The first simulation, NOWIND, uses the composite thermodynamic sounding, but zero initial wind. The results of this simulation were discussed in section 4.3.4, but they are repeated here for the sake of completeness. In this simulation, the warm, moist bubble rises and accelerates past the LFC directly above where it was released, and a gravity wave develops below about 1.5 km AGL (Fig. 5.1). The crest of the wave is shown by the cool perturbations in Fig. 5.1, which signify areas where isentropes have been displaced upward. This wave propagates away in all directions, and the initial updraft dissipates completely after approximately  $t=1$  h. There is no convective organization, and there is no further deep convection after the initial updraft dissipates in the same location where it developed. This simulation is instructive in that it shows that low-level gravity waves are a fundamental response to deep convection in this thermodynamic environment.

### 5.2.2 FULL

A version of the FULL simulation, which used horizontal grid spacing of 125 m, was presented in section 4.3.4. Here, an otherwise identical simulation with  $\Delta x = 1$  km will be shown. This will illustrate that the results are generally similar between the higher- and lower-resolution simulations, and it will also allow for direct comparisons between FULL and the other simulations to be presented later. The model domain was translated with a speed of  $u = 8.5 \text{ m s}^{-1}$  and  $v = 6 \text{ m s}^{-1}$  to attempt to keep the primary convective cell at the center of the domain. However, given the complex motion characteristics of the resultant convection (including splitting cells), the convection does not remain exactly at the center.

As convection develops in FULL, a deep updraft develops, and some cell splitting (e.g., Rotunno and Klemp 1982) takes place (Fig. 5.2b). In several of these “bubble” simulations, supercell-type convection appears to take place. Although the wind profile with a strongly-turning hodograph is supportive of supercells, they are not typically observed in nature in these types of environments. This is probably because large, undilute thermals, such as the one inserted here, are also rare in these conditions. In any case, supercell dynamics are not the focus of this study, but these simulations still provide valuable insights into how convection behaves in this type of environment.

At low levels, rather than a low-level wave propagating away in all directions, there is a single slow-moving wave that has steepened and strengthened considerably (Fig. 5.2c–d). Air flowing toward the updraft from the south is lifted over the cool branch of the wave and then quickly descends on the other side. At some level above the surface, air is lifted to its LFC and accelerates upward. This low-level wave is also responsible for the initiation of new discrete cells upstream. By  $t=1$  h, this back-building process has started to take place with a new updraft to the south of the initial cell (Fig. 5.3a). A cross-section reveals that this new cell, which can be seen at approximately  $x = 75$  in Fig. 5.3b, has initiated along the low-level gravity wave. Backbuilding continues along the gravity wave in this area, with

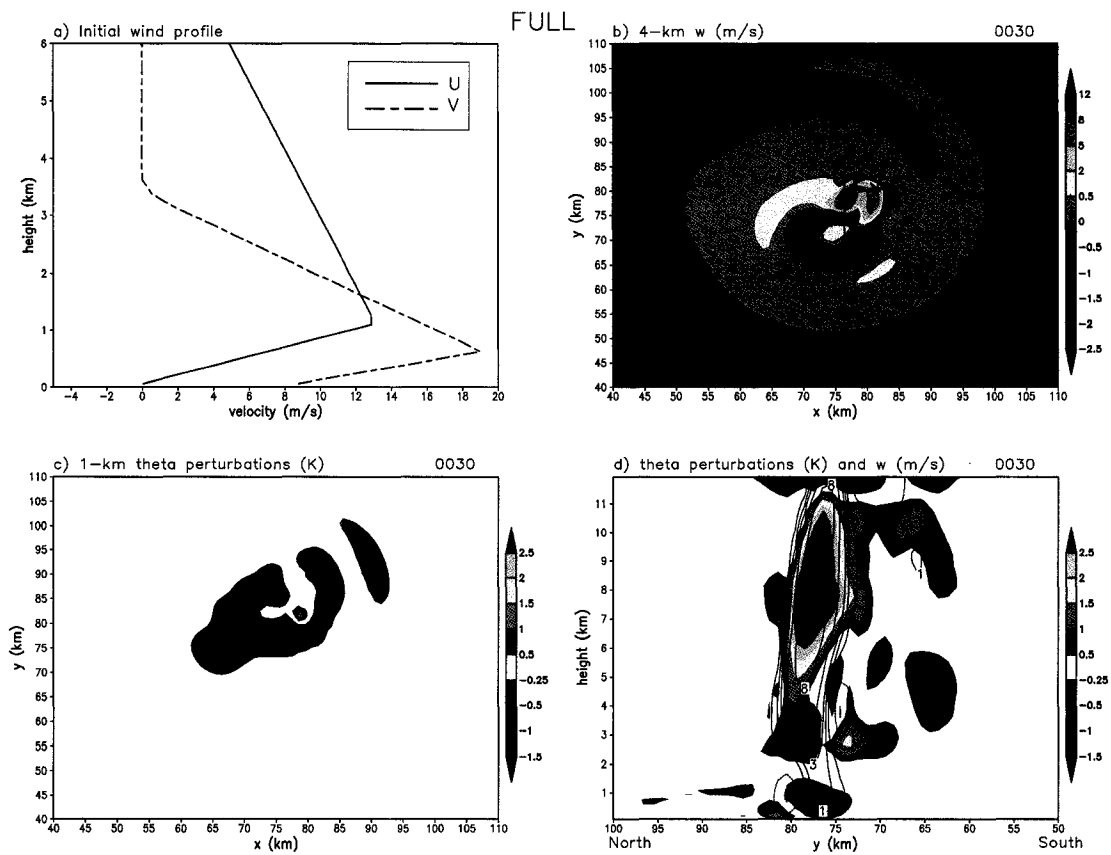


Figure 5.2: (a) Initial wind profile in the lowest 6 km for simulation FULL. The zonal wind ( $u$ ) is shown by the solid line, and the meridional wind ( $v$ ) by the dashed line. (b) Vertical velocity ( $\text{m s}^{-1}$ ) at 4 km AGL at  $t=30$  min in FULL. (c) Potential temperature perturbations (K) at 1 km AGL at  $t=30$  min in FULL. (d) North-south vertical cross section through the convective cell. Its location is shown by the line in panel (a), and values have been averaged over a 3-km area on either side of this line. Shown are potential temperature perturbation (K, shaded) and vertical velocity (contours at -4, -2, -1, 1, 2, 3, 5, 8, and  $12 \text{ m s}^{-1}$ , with negative contours dashed) for simulation FULL at  $t=30$  min.

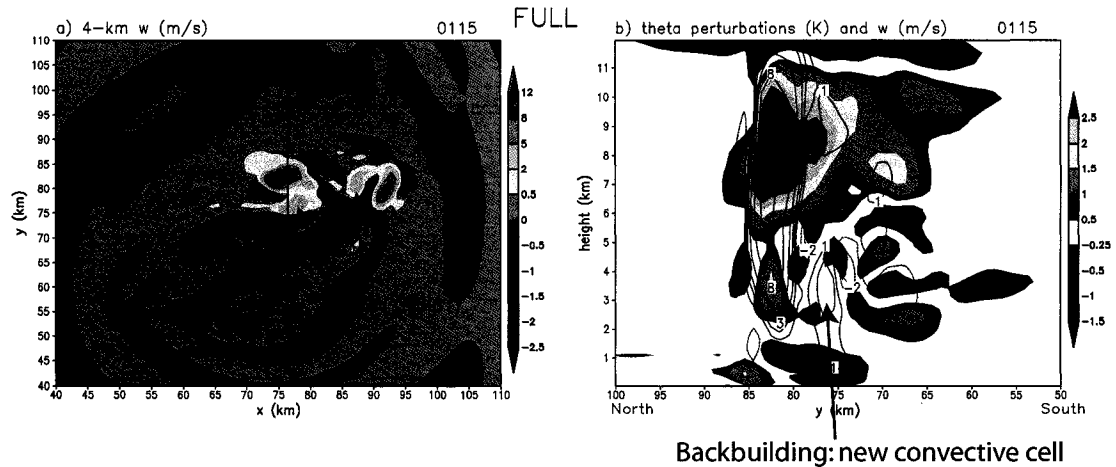


Figure 5.3: (a) As in Fig. 5.2b, except for  $t=1.25$  h. (b) As in Fig. 5.2d, except for  $t=1.25$  h.

three additional cells developing upstream of their predecessors in this area through  $t=2$  h (not shown). Farther to the east, the right-moving cell from the split has also initiated a new cell to its west.

It has been shown here that when a single warm, moist bubble is released in a wind profile with a strong reversal of shear with height, a combination of supercell and multicell processes take place. The favored location for new cell development is to the south and west of existing deep convection along a convectively-generated low-level gravity wave. These processes are similar to those responsible for “echo training” in quasi-stationary convective systems. As will be demonstrated below, a shear profile of this type is particularly favorable for back-building convection.

### 5.2.3 NOCOOL

One obvious question about the low-level gravity waves discussed above is what causes them to form. Some past studies (e.g., Raymond and Rotunno 1989, Haertel et al. 2001) have addressed the response of a stable atmosphere to low-level cooling (such as that from evaporation in a thunderstorm outflow) and shown that the result is a gravity wave, or a combination between a gravity wave and gravity current. To test whether these waves

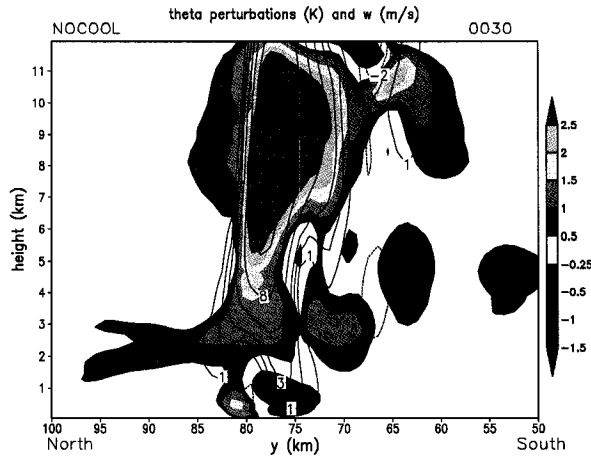


Figure 5.4: As in Fig. 5.2d, except for simulation NOCOOL at  $t=30$  min.

are generated by latent cooling processes, simulation NOCOOL, in which all latent cooling processes are removed from the microphysics scheme, was designed. The results of this run were shown in section 4.3.4 and are repeated here for the sake of completeness and to allow for comparison with the other runs in this chapter.

As convection develops in NOCOOL, the low-level gravity wave seen before is indeed present (Fig. 5.4). In fact, its amplitude is slightly stronger than that in FULL, particularly in the downward branch. This demonstrates that the wave is a response to latent *heating* rather than cooling. The convective updraft that develops in NOCOOL is significantly stronger than that in FULL, likely owing to the lack of detrimental processes such as dry-air entrainment in the microphysics scheme.

#### 5.2.4 WK

Another possible explanation for these gravity waves is that they develop only in this specific thermodynamic environment and are thus not widely applicable to other cases. To test this, the analytic thermodynamic sounding from Weisman and Klemp (1982), which has been widely used in modeling studies of convective storms, is used to initialize the horizontally-homogeneous base state. This simulation will be referred to as WK. This thermodynamic environment has much more CAPE than the composite sounding (2297 J

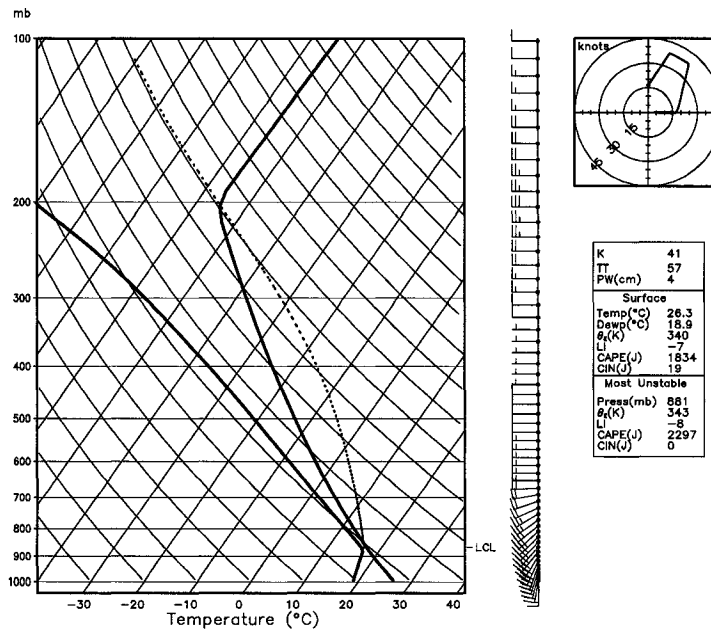


Figure 5.5: Skew- $T$  log  $p$  diagram showing the analytic thermodynamic sounding from Weisman and Klemp (1982). This is the sounding used in simulation WK.

$\text{kg}^{-1}$  compared with  $1149 \text{ J kg}^{-1}$  for the parcel with the highest  $\theta_e$  in the lowest 3 km), but it is much drier at low levels. This sounding is shown in Fig. 5.5. The initial wind profile used in WK is the same as that used in FULL.

The results of the WK simulation show that deep convection in a more “typical” midlatitude environment also produces a low-level gravity wave in approximately the same location (Fig. 5.6). From this, it can be concluded that these gravity waves are a fundamental response to deep convection in a conditionally unstable environment, not simply an oddity of the composite sounding. However, after approximately  $t=30$  min of simulation WK, a surface cold pool begins to develop. The signature of the gravity wave is still somewhat evident at  $t=1.25$  h (Fig. 5.7), but the cold pool quickly becomes the predominant low-level forcing mechanism for convection. These results reveal why such low-level gravity waves likely have not been a primary focus of past research: in relatively dry environments, a surface-based cold pool will quickly develop and dominate the evolution of convective systems, overwhelming any effects of the gravity waves.

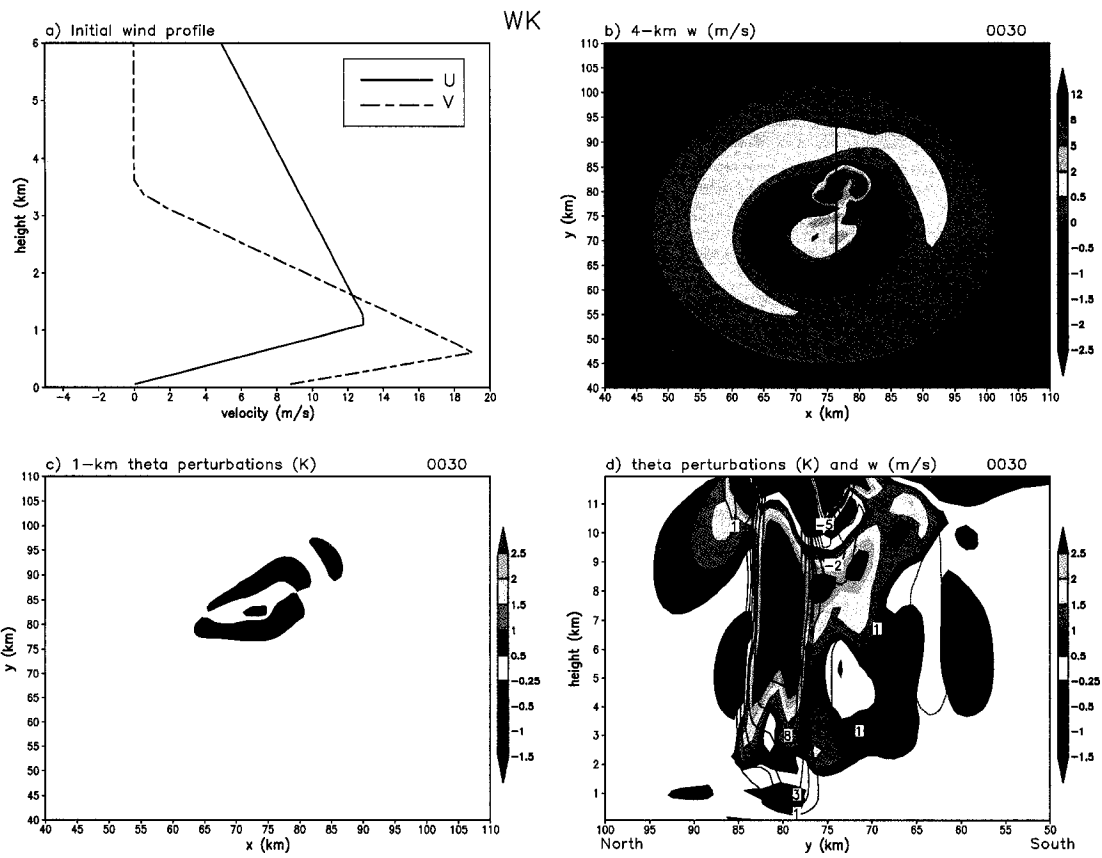


Figure 5.6: As in Fig. 5.2, except for simulation WK.

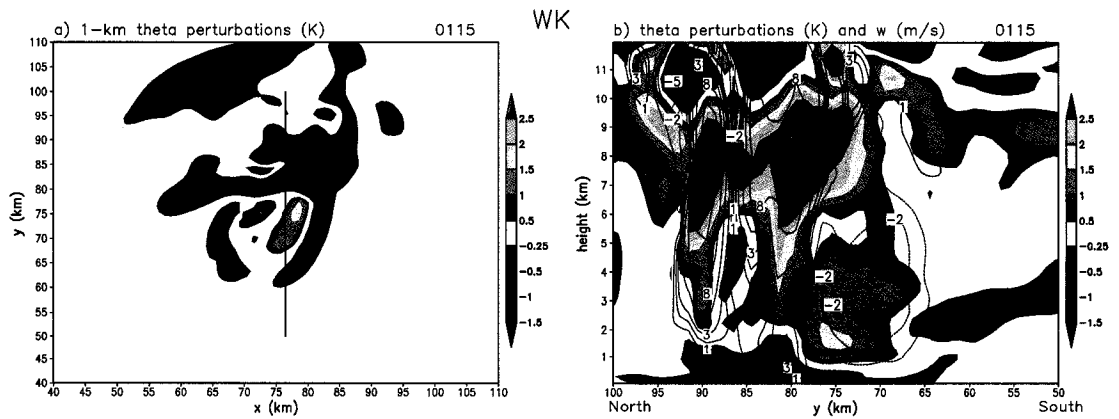


Figure 5.7: As in Fig. 5.1, except for t=1.25 h in simulation WK.

The WK simulation also assists in understanding the location of the wave in the vertical. The composite thermodynamic sounding is much more stable at low levels than is the WK sounding, though both are statically stable. Despite the significant differences at low levels, the wave's maximum amplitude is at approximately 1 km AGL in both cases. However, both thermodynamic soundings show a lifting condensation level (LCL) at approximately 1 km AGL, and the height of the cloud base in both simulations is near this level. Given that the wave is produced by latent heating rather than cooling (Fig. 5.4), it appears that the *lowest* level where such heating occurs is where the wave appears. In additional simulations where the placement of the initial bubble is varied (not shown), the wave also has its strongest signal at 1 km AGL. The wave also appears at 1 km in the simulations to be presented in chapter 6, in which convection is initiated by a completely different method. These results provide further evidence that the wave's location is related to the LCL height rather than the particular choice of sounding or initiation mechanism. It is beyond the scope of this study to conclusively prove that the wave's height is directly determined by the cloud-base height, but the available evidence suggests that this is the case.

### 5.2.5 *NOULSHEAR*

Now that the development of the waves and their relationship to thermodynamics has been established, let us turn attention to the importance of the vertical wind profile. Of particular interest is the magnitude of the shear and its reversal with height. In the first of a series of simulations with the composite sounding and varying wind profiles, the shear above the level of the LLJ has been removed. This experiment, named NOULSHEAR, begins to examine the effect of the reverse-shear profile by eliminating one of the shear layers.

As the initial "bubble" is released in this simulation, a deep convective updraft develops that closely resembles the updraft in NOWIND. The updraft remains essentially

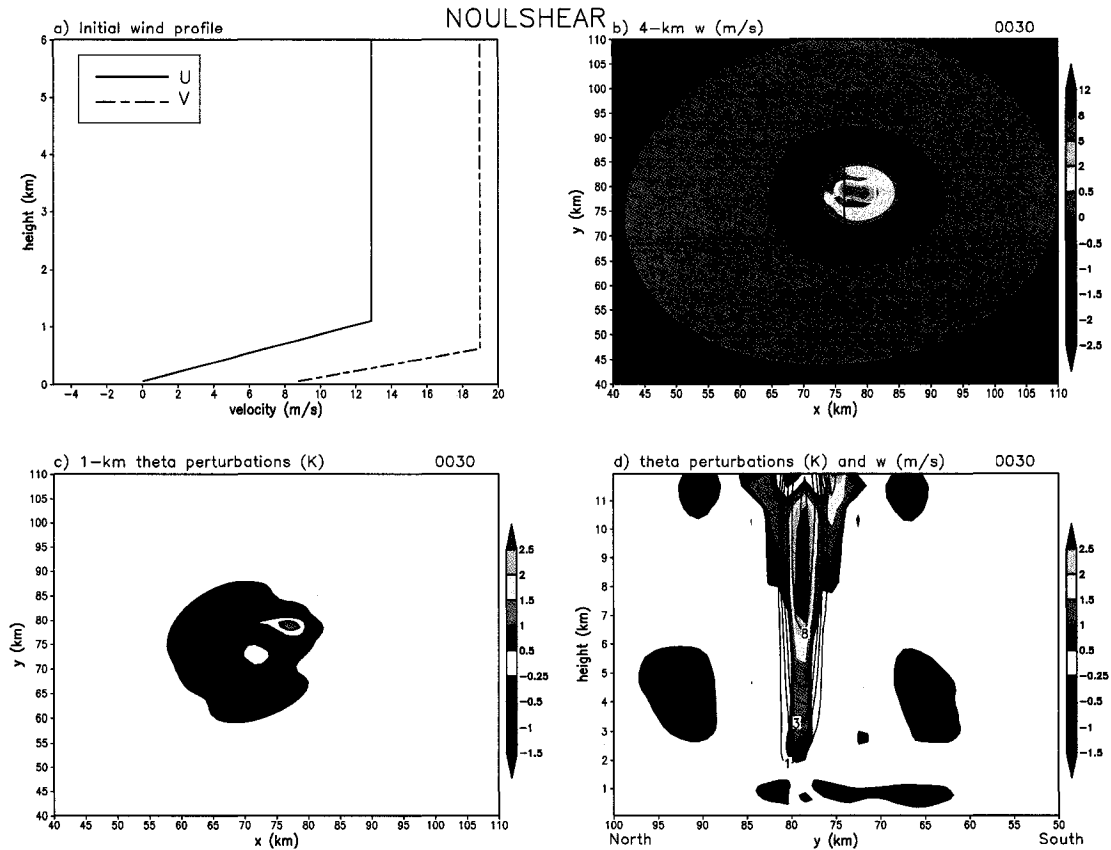


Figure 5.8: As in Fig. 5.2, except for simulation NOULSHEAR.

vertical with no shear above approximately 1 km, and there is no convective organization (Fig. 5.8). The initial cell splits after approximately 1 h, but then these two resulting cells quickly dissipate, and no deep convection remains after 1.25 h. This is in stark contrast to FULL, which includes mid- and upper-level shear, and in which vigorous deep convection continued through the end of the simulations at  $t=2$  h. The strong low-level shear appears to affect the propagation of the low-level gravity waves (Fig. 5.8c), as the wave signal is not completely symmetric as it was in NOWIND. However, without any midlevel shear, no new cell development occurs.

This simulation is interesting in light of recent debates in the literature regarding the importance of upper-level shear in the controlling the longevity of squall lines (e.g., Coniglio and Stensrud 2001, Weisman and Rotunno 2004, Stensrud et al. 2005, Weisman

and Rotunno 2005). These studies, which focus on cold-pool-driven convective systems, differ significantly on the importance of upper-level shear. Weisman and Rotunno find that the low-level shear (specifically the shear over the depth of the cold pool) is most important, whereas Coniglio, Stensrud, and colleagues find that upper-level shear plays a very important role in observed systems. In NOULSHEAR, in which there is strong low-level shear but no upper-level shear and in which a cold pool does not develop, convection is unable to organize and it quickly dissipates. However, in FULL, the convection is able to persist. Of course, the differences between the present simulations and those in the cited studies are many; for instance, in NOULSHEAR the shear is only in the lowest  $\sim 1$  km, but Weisman and Rotunno generally consider shear in the lowest 3 km. Furthermore, the full shear profile appears to be more favorable for supercells than does the profile with only low-level shear, which also affects the interpretation of the results. Nonetheless, the lack of convective organization in NOULSHEAR is worth noting in the context of these other studies.

### 5.2.6 *NOLLSHEAR*

The next several simulations experiment with different ways of removing the low-level shear to determine how it affects the deep convection and the low-level gravity wave. The first such experiment, NOLLSHEAR, has an initial wind profile in which the shear below 2 km AGL is removed. To construct this profile, the  $u$  and  $v$  velocities below 2 km AGL were simply made equal to their values at 2 km (Fig. 5.9a). At  $t=30$  min in this simulation, the wave is yet again present, and the southward-propagating part of the wave has again been amplified and it remains near its source (Fig. 5.9). However, the northward-propagating portion of the wave is much stronger here than it was in FULL (cf. Figs. 5.9c and 5.2c). Additionally, the strong downward branch of the wave that was present in FULL is absent here (cf. Figs. 5.9d and 5.2d). The differences between the runs with and without low-level shear become even more apparent later in the simulation. In FULL, we saw that

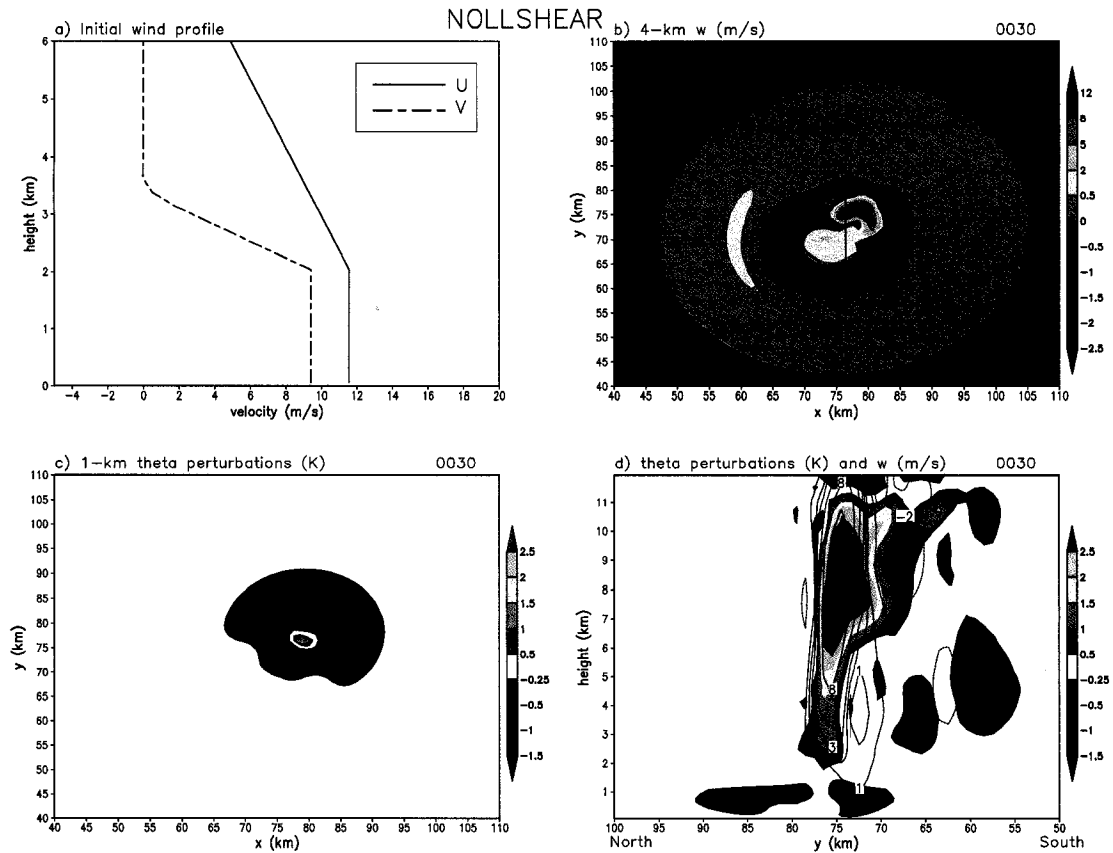


Figure 5.9: As in Fig. 5.2, except for simulation NOLLSHEAR.

several new cells initiated to the south and west of their predecessors by  $t=1.25$  h. This is not the case in NOLLSHEAR: elevated supercell-type convection continues, though the updrafts are considerably smaller and weaker than those in FULL, and no back-building takes place (Fig. 5.10). Nearly all evidence of the low-level gravity wave is gone by this time; animations show that the wave has dispersed and moved southward away from the deep convection. Without the wave as a source of lifting, no new discrete cells are able to form.

### 5.2.7 *NOLLSHEAR+5*

The next simulation is identical to NOLLSHEAR, except that the  $v$  component of the wind below 2 km has been increased by  $5 \text{ m s}^{-1}$ . This brings the magnitude of the low-

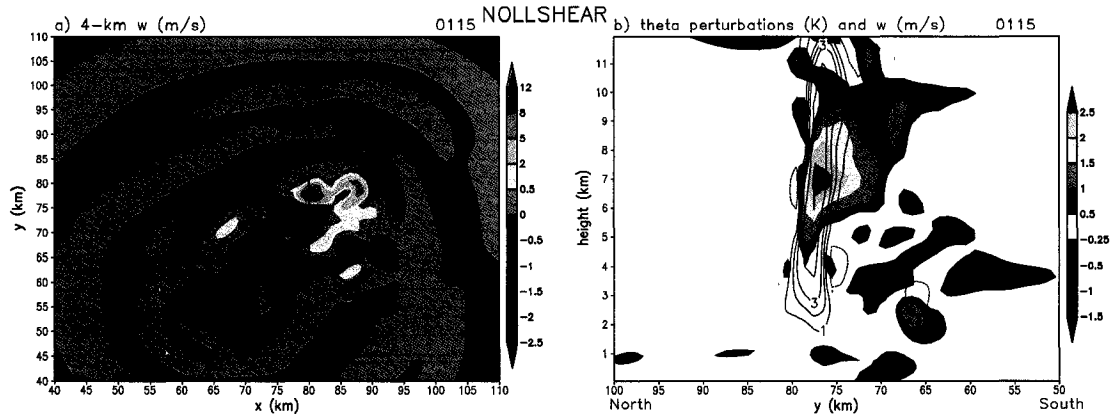


Figure 5.10: (a) As in Fig. 5.3, except for  $t=1.25$  h in simulation NOLLSHEAR.

level meridional wind closer to the value within the LLJ, but there is still no shear below 2 km. This increase in the low-level wind does also increase the midlevel shear somewhat compared with NOLLSHEAR (Fig. 5.11a, cf. Fig. 5.9a).

The simulated convection in NOLLSHEAR+5 is generally similar to that in NOLLSHEAR through the first 30 min (Fig. 5.11). However, the results of the two simulations diverge after this point. The primary difference for the purposes of this study is that the process of back-building along the low-level gravity wave takes place in NOLLSHEAR+5. The initiation of new cells occurs slightly later than it did in FULL, but by  $t=1.5$  h, a discrete, intense cell is developing to the southwest of the left-moving portion of the initial updraft (Fig. 5.12). The supercell-type convective updrafts are also generally stronger in this run than in NOLLSHEAR, though this may be related to the increase in midlevel shear that was an artifact of increasing the low-level wind speed.

The impact of the increased low-level wind speed on the movement and strength of the low-level gravity wave is illustrated in Fig. 5.13. After 1.5 h of simulation NOLLSHEAR (Fig. 5.13a), most of the gravity wave energy (signified by the 1-km negative potential temperature perturbations) has moved southward and dispersed and, as discussed above, there was no additional initiation of new convective cells. In NOLLSHEAR+5, on the other hand, the wave energy is confined much closer to its source and the  $\theta$  perturbations

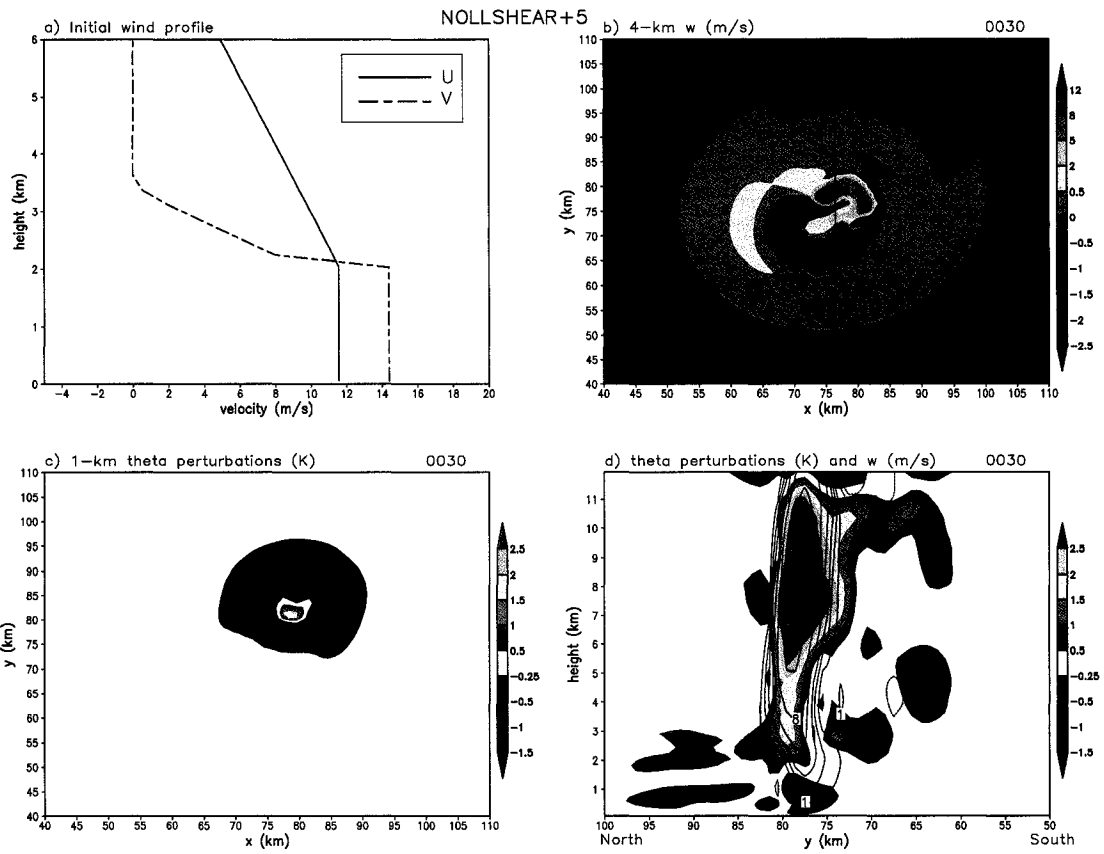


Figure 5.11: As in Fig. 5.2, except for simulation NOLLSHEAR+5.

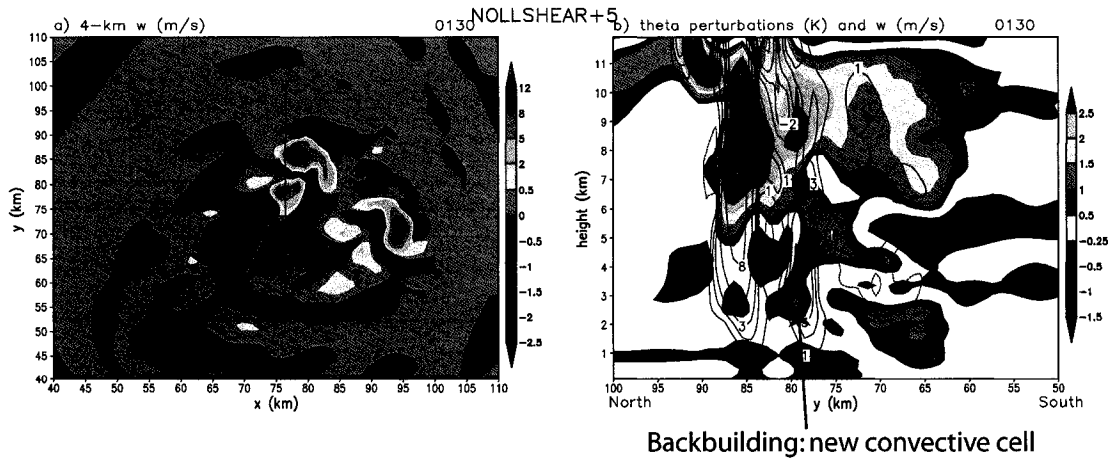


Figure 5.12: (a) As in Fig. 5.3, except for  $t=1.5$  h in simulation NOLLSHEAR+5.

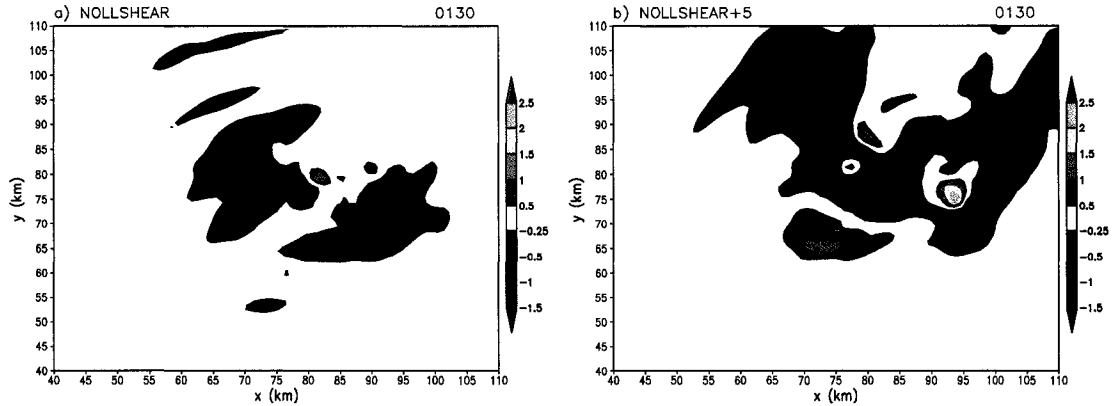


Figure 5.13: Potential temperature perturbations (K) at 1 km AGL at  $t=1.5$  h in (a) NOLLSHEAR and (b) NOLLSHEAR+5.

are much larger (Fig. 5.13b). As a result, the southwesterly inflow is lifted over the waves and parcels are able to attain their LFC. This leads to the back-building process seen in Fig. 5.12.

From the wind shear sensitivity simulations shown thus far, it can be concluded that:

- When convection (initiated with a single undilute thermal) develops in the full wind profile that includes a strong reversal of shear with height, a combination of supercellular and multicellular convection takes place. When new convective cells form, they appear on the southwest side of established cells (i.e., the upshear side relative to the midlevel shear).
- The shear layer above the LLJ is necessary for convective organization in this thermodynamic environment. Without midlevel shear, convection dissipates relatively quickly.
- The lower shear layer is not necessary for backward propagation to occur. However, without shear, the wind speed in the lower layer must be sufficiently strong to keep the low-level gravity wave near its source if back-building is to occur.

Dynamical interpretation of these results will be a subject of future work.

### 5.2.8 *NOLLSHEAR1KM*

The previous two simulations involved two different methods for removing the shear below 2 km. Here, in *NOLLSHEAR1KM*, the shear below 1 km is removed. This simulation closely resembles *NOLLSHEAR+5* through 30 min, with splitting cells and a low-level gravity wave that is amplified to the south of the convection (Fig. 5.14, cf. Fig. 5.11). However, in *NOLLSHEAR1KM*, the convection remains only supercellular, with no discrete multicell behavior. By  $t=1.5$  h, there are several intense supercells that have undergone the splitting process, but no freshly-initiated cells (Fig. 5.15). Animations of the vertical motion field show that the cells in the domain throughout the simulation result from splitting rather than discrete propagation. The intense supercells remain near-surface-based throughout their lifetimes, and their low-level updrafts are collocated with the nearly-stationary low-level gravity wave (Fig. 5.15b). The results of *NOLLSHEAR1KM* are somewhat difficult to interpret in the context of observed back-building convective systems, since supercells are not typically observed in these environments and because a wind profile of this type (Fig. 5.14a) is probably rarely observed. However, the results are included here for the sake of completeness, and to once again illustrate the large effect that small changes in the wind profile can bring about.

### 5.2.9 *HALFSHEAR*

In the next sensitivity simulation, a reverse-shear profile is still used, but the magnitude of the shear in both layers has been reduced by approximately half (Fig. 5.16a). In other words, there is still the vertical structure of a low-level jet, but it is a much weaker jet than that represented in the *FULL* profile.

In the first 30 min of *HALFSHEAR*, the results are very similar to those in *FULL*: the initial updraft splits and the low-level wave is present and has been steepened and slowed to the south of the convection. (Fig. 5.16, cf. Fig. 5.2). Even later in the simulation, the structure of the low-level gravity wave is almost the same as that in *FULL* (Fig. 5.17).

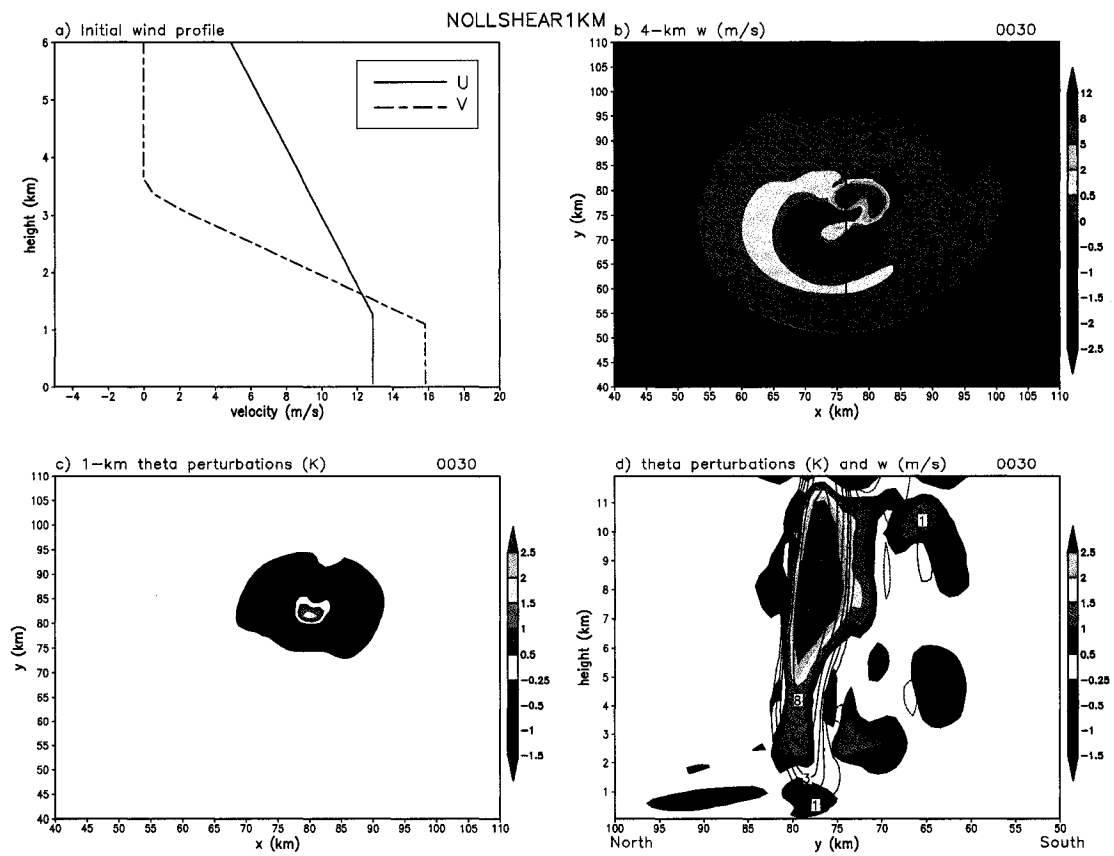


Figure 5.14: As in Fig. 5.2, except for simulation NOLLSHEAR1KM.

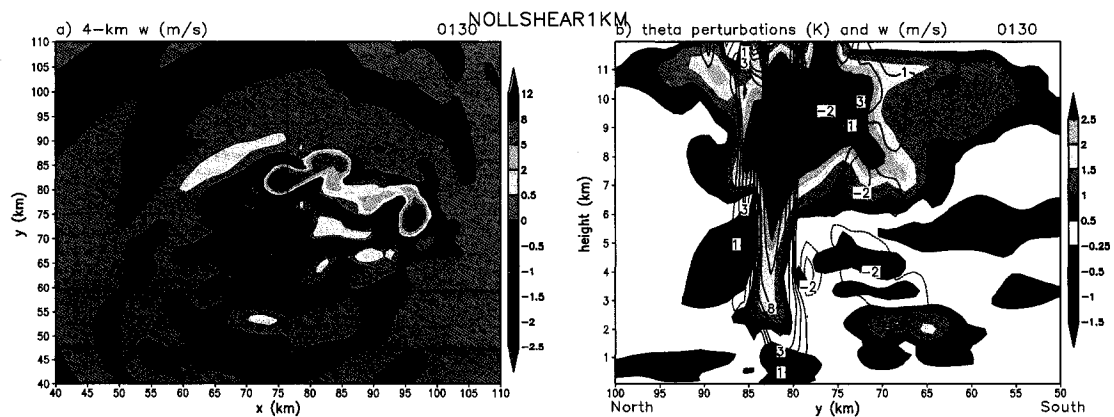


Figure 5.15: (a) As in Fig. 5.3, except for  $t=1.5$  h in simulation NOLLSHEAR1KM.

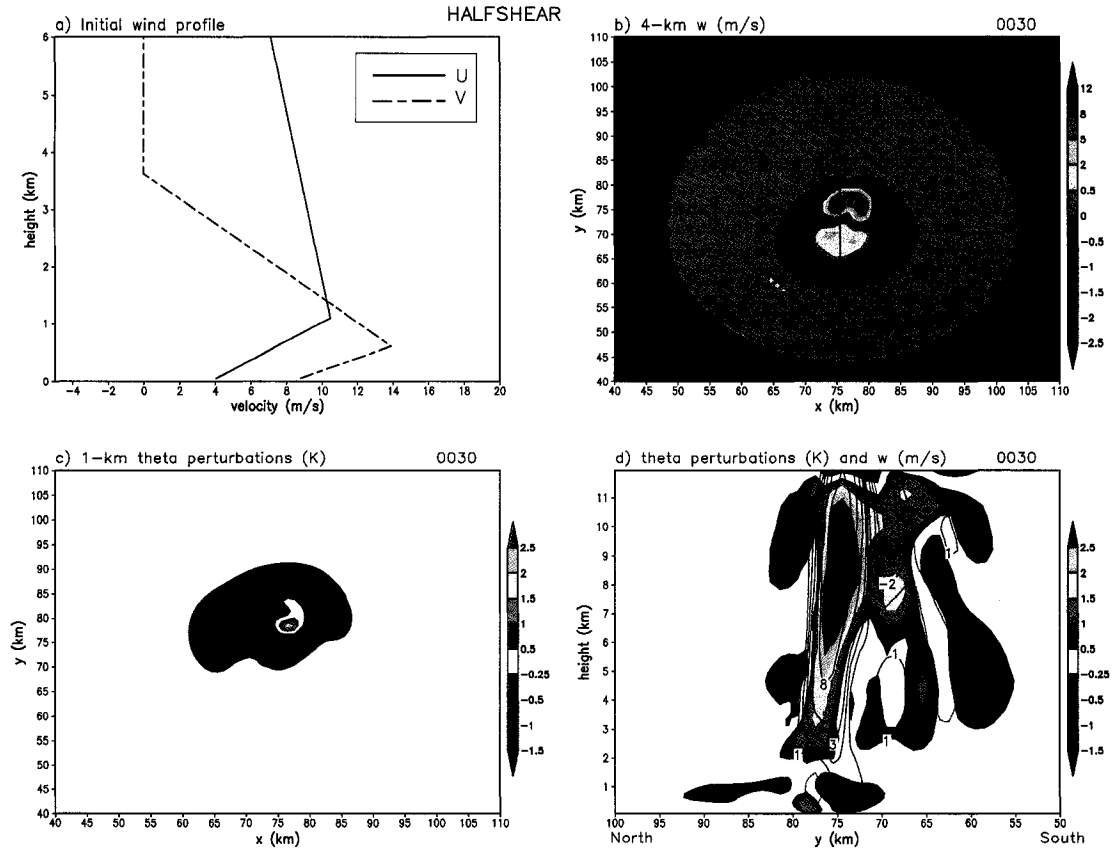


Figure 5.16: As in Fig. 5.2, except for simulation HALFSHEAR.

However, in HALFSHEAR, no new convective cells develop. Instead, only the two cells that split from the initial updraft remain, and they weaken somewhat with time. The reason for this difference is not entirely clear, though it appears that it must be related to the strength of the low-level inflow. Whatever the reason, the weaker reverse-shear profile in HALFSHEAR is apparently less favorable for discrete back-building convection than is the FULL profile. This result, combined with the differences between NOLLSHEAR and NOLLSHEAR+5, suggest that both a reversal of shear *and* the strength of the low-level winds are important factors in determining whether backward propagation can occur.

Of course, not every possible wind profile has been explored here. But from the evidence provided by the series of sensitivity simulations presented in this chapter, it appears that the wind profiles associated with strong midlatitude low-level jets are conducive to

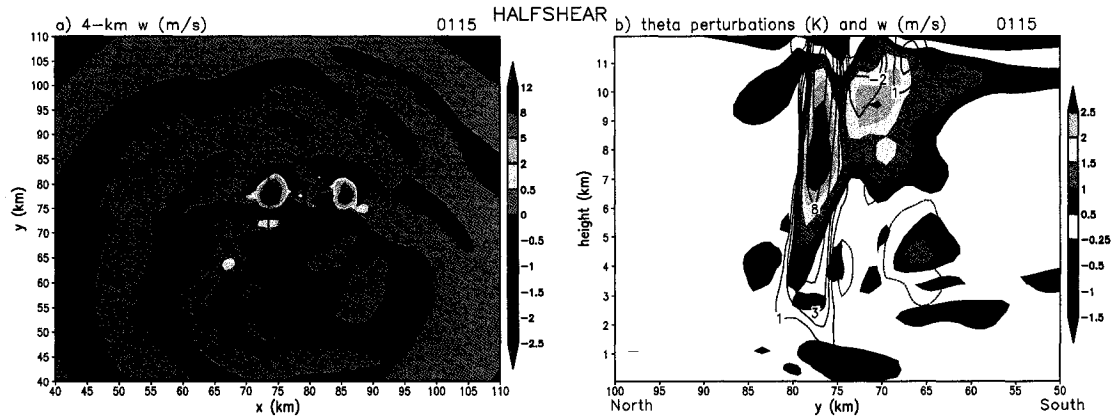


Figure 5.17: (a) As in Fig. 5.3, except for  $t=1.5$  h in simulation HALFSHEAR.

back-building, quasi-stationary convection on their own, even without any of the additional enhancements that LLJs often provide.

#### 5.2.10 NOULJET

One final simulation is presented here that is relevant to the results in the next chapter. In the full wind profile used for the simulations in this chapter and in the more complex simulations in chapter 6, the zonal winds between 10–14 km AGL reflect an upper-level jet streak (Fig. 5.18). This jet streak was present in the 6–7 May 2000 event, but was less prominent in the composite. Simulation NOULJET, in which this upper-level jet structure is removed, is designed to test whether this feature significantly affects the convection that develops.

A comparison of the vertical velocity field in FULL and NOULJET at  $t=2$  h (the end of the model integration) shows little difference in the convective structure between the two simulations (Fig. 5.19). Animations of vertical velocity and other fields show that although the evolution of the convection is not exactly the same in the two simulations, the simulations are nearly indistinguishable in terms of relevant characteristics such as storm motion and initiation of upstream convective cells. Although it is possible that the upper-level wind field could have more of an effect in the more complex, longer-term simulations

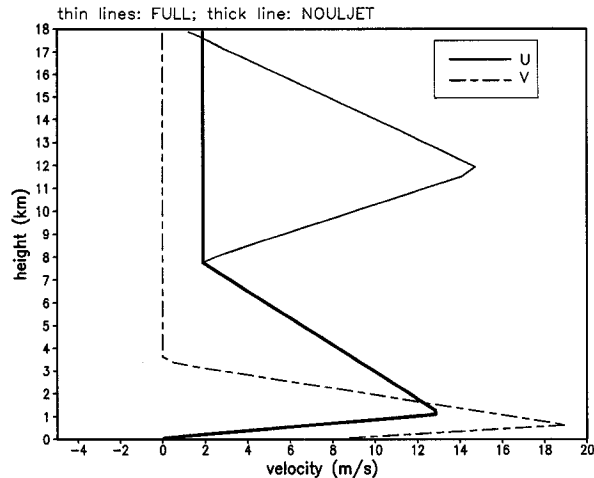


Figure 5.18: Comparison of initial wind profiles for simulations FULL and NOULJET. The thin line shows the FULL wind profile, and the thick line shows the  $u$  profile for NOULJET, in which the upper-level jet has been removed. The  $v$  profile is the same for both simulations.

shown in chapter 6, the results of this idealized simulation suggests that, for the features of interest in this study, the upper-level jet has a minimal impact.

### 5.3 Summary and conclusions

The idealized simulations in this chapter were designed to illustrate some of the important processes and sensitivities associated with deep convection in a variety of environments, before moving on to the more complex simulations to be presented in chapter 6. The set of simulations performed here is obviously not comprehensive, but the simulations do provide insight into several key factors that are relevant to this study. The primary results of these simulations are as follows:

- When deep convection develops in a conditionally unstable (but statically stable) environment, the associated latent heating produces a low-level gravity wave that has its peak amplitude at approximately the lifting condensation level.
- The ambient wind profile strongly affects the characteristics of this low-level wave. When there is no background wind, the wave simply propagates away. However, in

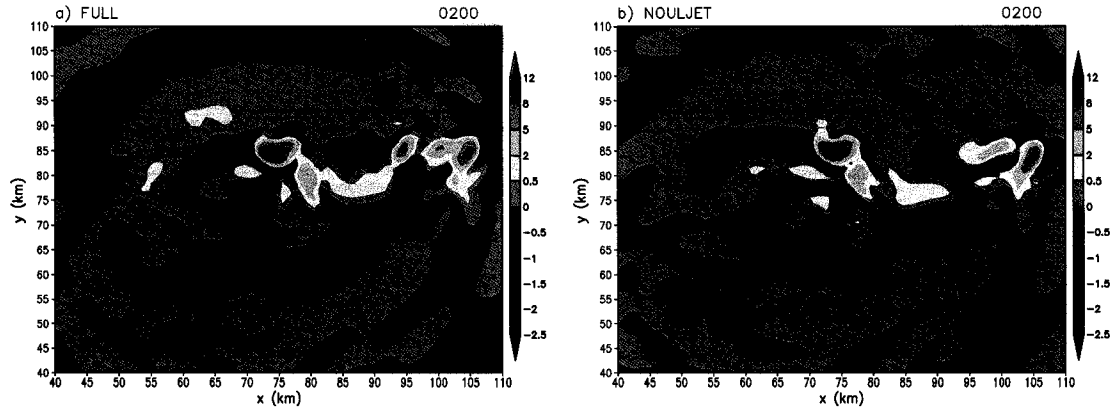


Figure 5.19: Vertical velocity ( $\text{m s}^{-1}$ ) at 4 km AGL at  $t=2$  h in (a) FULL and (b) NOULJET.

a wind profile with the vertical representation of a strong southwesterly low-level jet, the wave is amplified on the south side of the deep convection and it remains nearly stationary relative to its source. When this occurs, inflowing air is lifted over the wave and can attain its LFC, resulting in additional deep convective cells. These cells develop to the south and west of existing convection, resembling the back-building process that is commonly observed in mesoscale convective systems.

- In such a wind profile, which has a strong reversal of the wind shear with height, the shear layer above the LLJ is crucial for convective organization. Without this upper shear layer, convection does not organize and it dissipates relatively quickly.
- Apparently, it is not strictly necessary to have *shear* in the lower layer for back-building convection to occur, but it is necessary to have strong winds in this layer. In the midlatitude, nocturnal, warm-season environments that are the focus of this study, low-level shear is almost always present when the winds below 2 km are strong, so it can be safely concluded that *a reverse-shear profile is particularly conducive to back-building convection.*
- When the magnitude of the shear is reduced by half, back-building does not take place. This suggests that the shear must not only reverse with height, but it must

reverse *sharply* if a back-building, quasi-stationary convective system is to develop.

- A sharp reversal of the shear with height is by itself conducive to back-building convection. There are other reasons why observed LLJs are often associated with such convective systems: they are typically responsible for advecting warm, moist air into a region, and they also have frontogenetical ascent at the “nose” of the jet. However, these effects are neglected in the simulations presented in this chapter, and yet the convection is maintained and discrete propagation of convective cells is in the opposite direction of the cell motion.

These “bubble” simulations assist in understanding the processes that lead to back-building convection in a relatively simple framework. However, these simulations also exhibit several dissimilarities to the observed events that are the primary focus of this study. First, as shown above, the relatively large bubbles used here to initiate convection tend to produce supercell-type convective updrafts, which are rarely observed in the actual events. Second, although deep convection is maintained through the 2 h integration time of these simulations, it is not organized in the same way as in the observed MCSs. Here, it is primarily the supercells that persist, even though new discrete cells develop in some cases. Finally, when smaller bubbles with less intense thermal perturbations are used, the resulting deep convection is not supercellular, but it is also not long-lived. In light of these dissimilarities, a series of simulations that are still relatively idealized, but are intended to be more realistic than those in this chapter, will be presented in chapter 6.

## Chapter 6

# IDEALIZED SIMULATIONS OF QUASI-STATIONARY CONVECTIVE SYSTEMS

### 6.1 Description of the numerical model and experimental design

In this chapter, idealized simulations of MCSs forming in an environment with mesoscale lifting will be presented. For these simulations, version 1.11 of the nonhydrostatic cloud model described by Bryan and Fritsch (2002) was used once again. These three-dimensional simulations used the composite thermodynamic sounding from the six cases discussed in chapter 3, which is repeated here in Fig. 6.1, to create a horizontally-homogeneous base state. The wind profile used in the model was very similar to the composite profile, but the surface winds are slightly stronger, as are the zonal winds between 10–14 km; these fields are averaged, smoothed wind fields from the case-study simulation presented in chapter 4 (Fig. 6.2). A slight upper-level jet streak was present in that case, which was less prominent in the composite. The sensitivity to this feature was tested and found to not cause any significant differences in the results to be presented (see section 5.2.10). This wind profile was used because near-surface RUC analyses underestimated the observed surface winds in MCS inflow regions in some cases. The primary feature of this wind profile is the strong reversal of shear associated with the LLJ. In these simulations, this LLJ only exists in the vertical; there is no initial horizontal variation in the wind, except for that associated with the forcing described below.

Instead of the “warm bubble” (e.g., Klemp and Wilhelmson 1978) or “cold box”

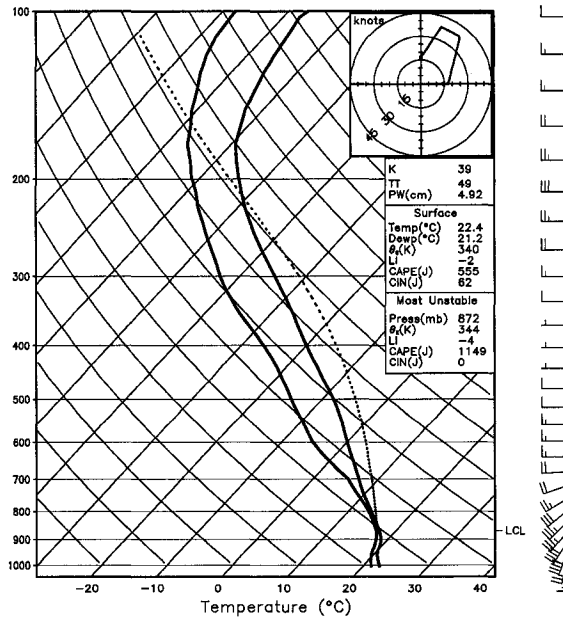


Figure 6.1: Composite skew- $T$  log  $p$  diagram for the extreme rainfall environment. The parcel path for the parcel with the highest  $\theta_e$  in the lowest 3 km is shown in gray.

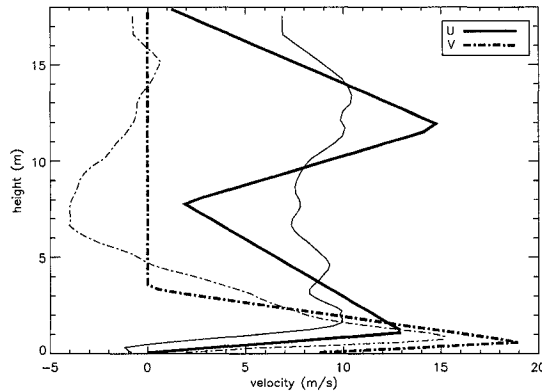


Figure 6.2: Vertical wind profile used for the horizontally-homogeneous initial state in the idealized simulations (thick lines). This is an averaged, smoothed wind profile from 0600 UTC in the case-study simulation presented in chapter 4. The wind profile from the RUC composite is shown in the thin lines for comparison.

(e.g., Weisman et al. 1997) methods that are often used to initiate deep moist convection, a momentum forcing based on that developed by Loftus et al. (2008, hereafter LWD08) is used. An initiation method of this type has been chosen for several reasons: (1) MCSs forming near midlevel circulations typically are affected by mesoscale convergence and lifting (chapter 3); (2) in the horizontally-homogeneous environment used here, which is very moist and has relatively little CAPE in comparison with the soundings typically used for simulating midlatitude convective systems, the “warm bubble” method is insufficient for creating an organized MCS on its own; (3) such systems do not typically form in association with strong cold pools, so the “cold box” method would not be appropriate; (4) creating a balanced initial state which includes a vortex and a strong low-level jet is difficult within simple balance constraints, such as gradient and thermal wind balance; (5) we wish to simulate the meso- to synoptic-scale lifting that takes place with MCVs and other midlevel circulations in shear; but (6) we wish to avoid the complexities of vortex dynamics for investigating the structure, evolution, and maintenance mechanisms of the simulated convective systems. Examining the interactions between midlevel vortices and strong low-level shear is an avenue of potential future research, but the primary focus of this study is on the workings of the MCSs. The discussion to follow will demonstrate that a momentum forcing is a reasonable method for simulating the lifting that occurs with midlevel circulations in shear, and for initiating simulated convective systems that resemble the observed MCSs shown in chapter 3.

A full description of the momentum forcing can be found in LWD08, but an overview is given here, as are a few important modifications made for this study. In this method for initiating convection, a convergence field is prescribed and added to the basic state wind. The horizontal wind perturbations used to create the convergence field are given by:

$$u' = -\frac{2A(x - x_c)}{\lambda_x^2} e^{-\left(\frac{x-x_c}{\lambda_x}\right)^2} e^{-\left(\frac{y-y_c}{\lambda_y}\right)^2} f(z) \quad (6.1)$$

and

$$v' = -\frac{2A(y - y_c)}{\lambda_y^2} e^{-\left(\frac{x-x_c}{\lambda_x}\right)^2} e^{-\left(\frac{y-y_c}{\lambda_y}\right)^2} f(z) \quad (6.2)$$

where  $x_c$  and  $y_c$  are the centerpoints of the forcing in the  $x$  and  $y$  directions, respectively, and  $\lambda_x$  and  $\lambda_y$  are shape control parameters which define the eccentricity of the convergence region. When  $\lambda_x = \lambda_y$ , it is circular in the horizontal plane.  $A$  is a constant that is related to the maximum divergence  $D_{max}$  according to:

$$A = \frac{-D_{max}}{2} \left( \frac{1}{\lambda_x^2} + \frac{1}{\lambda_y^2} \right)^{-1} \quad (6.3)$$

and  $f(z)$  defines the vertical structure of the convergence field. LWD08 used a linear function with convergence maximized at the surface, but the convection in the observed MCSs shown in chapter 3 typically develops within elevated convergence and lifting (Fig. 3.13). As such, the vertical structure is defined here as a sine wave with an elevated convergence maximum:

$$f(z) = \cos^2 \left( \frac{1}{2} \pi \beta \right)$$

where

$$\beta = \left| \frac{z - z_c}{z_r} \right|,$$

$z_c$  is the height of the center of the imposed convergence field, and  $z_r$  is its vertical radius.

The other significant difference from the method used in LWD08 is in the time-dependent application of the wind perturbations. LWD08 calculated the wind perturbations required to create a desired convergence field, and then applied those same calculated perturbations at each model timestep. Thus, their convergence was held constant, and any convectively-generated effects on the wind field were neglected. For their investigation of the development of isolated multicellular convection over short periods of time, this was appropriate. However, the goal of the numerical simulations in this study is to examine the important processes in organized mesoscale convective systems, and the feedbacks between organized convection and the larger environment cannot be ignored. Therefore, rather than applying a constant convergence, we allow the convergence to increase in time. This

Table 6.1: Parameters chosen for the convergence forcing in the idealized numerical simulations.

Domain size	$400 \times 400 \times 18.3$ km
$x_c, y_c$	200 km
$\lambda_x, \lambda_y$	140 km
$z_c$	1.4 km
$z_r$	1.0 km
$D_{max}$	$-1 \times 10^{-4} \text{ s}^{-1}$

amounts to a momentum forcing, similar to the approach used by CM88.<sup>1</sup> To create the forcing, a value for  $D_{max}$  is chosen and the associated values of  $u'$  and  $v'$  are calculated using (6.1) and (6.2), but then only a *fraction* of those perturbations is added to the wind field at each timestep. This allows the convergence field, and subsequent vertical motions, to gradually develop, while also allowing the circulations that develop to feed back on the horizontal wind field. In all of the simulations presented herein, the wind perturbations were centered at the center of the model domain. Then, the model domain was translated with a speed of  $u = 7.5 \text{ m s}^{-1}$  and  $v = 2.5 \text{ m s}^{-1}$ , which was similar to the translation speed of the composite vortex shown in Fig. 3.9, and also to the approximate speed of convective cells in this wind profile. Thus, this method is essentially simulating a moving low-level forcing (such as an MCV), and how convection behaves when it develops within this forcing.

The values of the parameters chosen for the convergence forcing are shown in Table 6.1. Appropriate values for the fraction of the wind perturbations to apply at each timestep were found using trial and error in dry simulations before applying them to simulations with moisture. These fractions had to be adjusted when changes to the model grid spacing or time step were made. To illustrate the structure of the forcing, some results from a dry simulation are shown in Fig. 6.3. This simulation used 1-km horizontal grid spacing

<sup>1</sup> As will be shown later in section 6.3.2, continued forcing after the initiation of convection is not necessary to maintain a long-lived convective system.

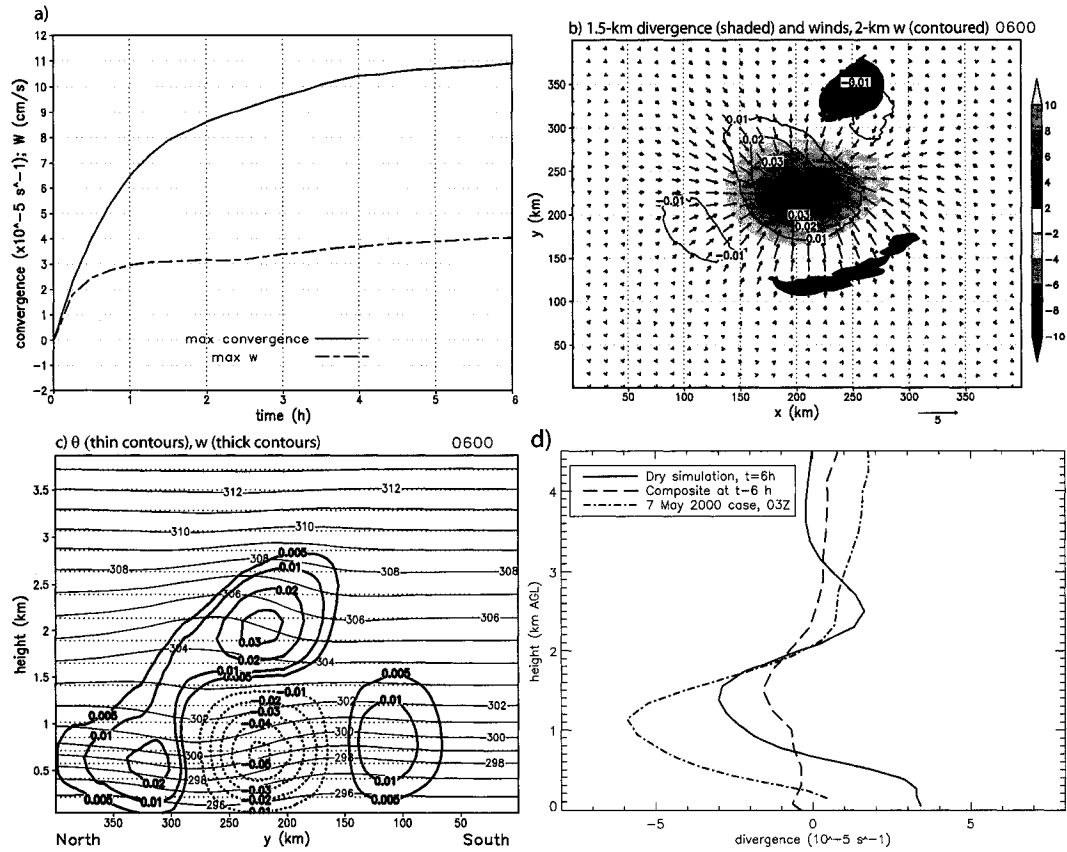


Figure 6.3: (a) Time series showing the maximum convergence (solid line) and maximum upward vertical velocity (dashed line) in a dry simulations using the momentum forcing described in the text. For convergence, the units are  $\times 10^{-5} \text{ s}^{-1}$  and for vertical velocity they are  $\times 10^{-2} \text{ m s}^{-1}$ ; both are plotted on the same axis. (b) Divergence (shaded every  $2 \times 10^{-5} \text{ s}^{-1}$ ) and wind perturbations ( $\text{m s}^{-1}$ , reference vector at bottom) at 1.5 km above the surface and vertical velocity (line contours every  $0.01 \text{ m s}^{-1}$ ) at 2 km above the surface at  $t=6 \text{ h}$  in the dry simulation. (c) North-south vertical section of potential temperature and vertical velocity in the lowest 4 km of the dry simulation. The section is taken through the center of the domain, and values have been averaged over an area 20 km on either side of this line. The thin solid contours represent potential temperature at  $t=6 \text{ h}$ , the thin dashed contours show the potential temperature of the base state. Thick contours represent vertical velocity ( $\text{m s}^{-1}$ ) with negative values dashed. (d) Vertical profiles of divergence, averaged over a  $150 \text{ km} \times 150 \text{ km}$  box centered on the maximum convergence. The solid line is the divergence in the dry simulation after 6 h; the dashed line is from the RUC composites at six hours before the heaviest rainfall; the dash-dot line is from the 1-km simulation of the 6–7 May 2000 case described in chapter 4.

and a stretched vertical grid with grid spacing increasing from 100 m near the surface to 500 m at the model top. Fig. 6.3a shows that the convergence and associated vertical motions increase fairly quickly in the first two hours of the simulation, and then level off beyond that time. After six hours, an approximately circular convergence field exists at the center of the domain (Fig. 6.3b). The vertical structure shows the response to the elevated convergence, with a region of descent near the surface and ascent above (Fig. 6.3c). In addition to these weak vertical motions, the applied lifting also affects the potential temperature field. There is a slight cool perturbation near the surface on the south side of the forcing, and a stronger cool perturbation above and to the north of the forcing. Thus, there is a slight upward slope to the isentropes for parcels approaching from the south in the 1.5–2.5 km AGL layer, which is where the most unstable air is located when moisture is added. This lifting resembles the isentropic upglide in a midlevel positive PV anomaly discussed by Raymond and Jiang (1990). Though the vertical velocities are relatively weak and the change in the slope of the isentropes is also relatively minor, parcels within the southwesterly low-level flow at around 2 km AGL are displaced upward by approximately 250 m over 6 h. An averaged vertical profile of the imposed convergence is compared with a similar profile from the composite analysis, and with a profile from the case-study simulation in chapter 4 (Fig. 6.3d). The shape of the profile is similar in all three instances, with the maximum convergence occurring between 1 and 1.5 km AGL. Note that the profile for the dry simulation partially includes the simulated response to the momentum forcing, which explains the divergence above and below the maximum convergence. The divergence and descent near the surface are relatively strong, but as will be shown, this does not prevent the initiation of deep convection in moist simulations.

The forcing applied in these simulations is slightly weaker than those used in similar past studies. The maximum vertical velocity here is just over  $0.04 \text{ m s}^{-1}$ , which is similar to the  $0.05 \text{ m s}^{-1}$  value in the idealized MCV simulation of Trier et al. (2000a, cf. their Fig. 5). The upward motion in CM88 approached  $0.1 \text{ m s}^{-1}$  (cf. their Fig. 4). Trier et al.

(2000a) reported upward displacements of over 800 m in 8 h, and the displacements shown in CM88 were approximately 300 m in 3 h, both of which are stronger than the 250 m in 6 h using the method described above. In this context, it appears to be a justifiable method for initiating and maintaining a convective system that is similar to those observed to occur beneath midlevel circulations, without adding the complexities of the circulation itself.

The primary simulation to be presented below used horizontal grid spacing of 1 km and the same vertical grid spacing as the dry simulation. This grid spacing is not fully sufficient to resolve individual convective cells, but convective systems are well resolved (e.g., Weisman et al. 1997; Bryan et al. 2003; Skamarock 2004). To better resolve the convection, an additional simulation with horizontal grid spacing of 500 m was run. However, given the computing resources required for the 500-m simulation on such a large domain, it was only run for 5 h, whereas the 1-km simulation was run for 11.5 h, and several sensitivity tests were run at  $\Delta x=1$  km for 9 h. (The momentum forcing was adjusted so that it was essentially identical in the 500-m and 1 km runs.) Additionally, to speed up the initiation of convection in the 500-m run so unnecessary model integration time could be avoided, a spectrum of random potential temperature perturbations with maximum magnitude of 2 K were applied at the initial time using the method of Bryan et al. (2007). In the 1-km simulation, the convection was allowed to initiate “naturally” through the lifting process. Though the convection organizes more quickly in the 500-m run owing to the initial random convection, the organization and evolution of the systems in the simulations were otherwise very similar. Results from both simulations will be presented where appropriate.

In the simulations presented below, the model has free-slip upper and lower boundaries, with a Rayleigh damping layer above 14 km. For the simulations with  $\Delta x = 500$  m, the large timestep is 3 s; for  $\Delta x = 1$  km,  $\Delta t= 5$  s. The model is configured to use sixth-order monotonic numerical diffusion (Knievel et al. 2007) and a positive-definite advection scheme such that moisture and scalar quantities are approximately conserved. It uses open-radiative lateral boundaries as formulated in Durran and Klemp (1983), and it

restricts the outward flux of mass so that it does not exceed the total inward mass flux. The model includes parameterized ice microphysics based on the scheme of Lin et al. (1983) and modified as described in Braun and Tao (2000). One feature of the model is the ability to examine parcel trajectories by inserting passive, massless air parcels which are advected by the gridscale winds. Such parcels were inserted at various levels and their trajectories will be illustrated in the following section. In the primary simulation to be discussed below, the Coriolis force was neglected. However, since the MCSs we wish to simulate occurred in midlatitudes, and because Coriolis accelerations can have significant effects on MCSs (e.g., Skamarock et al. 1994; Liu and Moncrieff 2004), a sensitivity simulation where the Coriolis force acted upon perturbations from the base-state wind will be discussed and presented in section 6.3.

## 6.2 Results

### 6.2.1 *Development and organization of convective system*

As the lifting builds over the first few hours of the 1-km simulation, air near the center of the convergence zone is lifted to saturation, yielding a layer of cloudiness and moist absolute instability (Fig. 6.4a). The first deep convective cells appear in this region approximately 2.75 h into the simulation. As these cells develop, they create a low-level gravity wave signature similar to that shown in the idealized simulations in chapter 4 (Fig. 6.4b, cf. Fig. 4.22). It was shown in chapters 4 and 5 that these waves are a response to latent heating in convection, and that the wind profile with a reversal of shear with height keeps the waves near their source rather than propagating away.

Unlike the large, undilute thermals that were shown in chapter 5, the convection that develops within the background lifting is not supercellular. In time, this initially scattered deep convection (Fig. 6.5a) organizes into a quasi-linear arrangement, with new convection developing on the southwest flank (within the region of lifting) and deep convective cells moving from southwest to northeast along the line (Fig. 6.5b–c). The system attains this

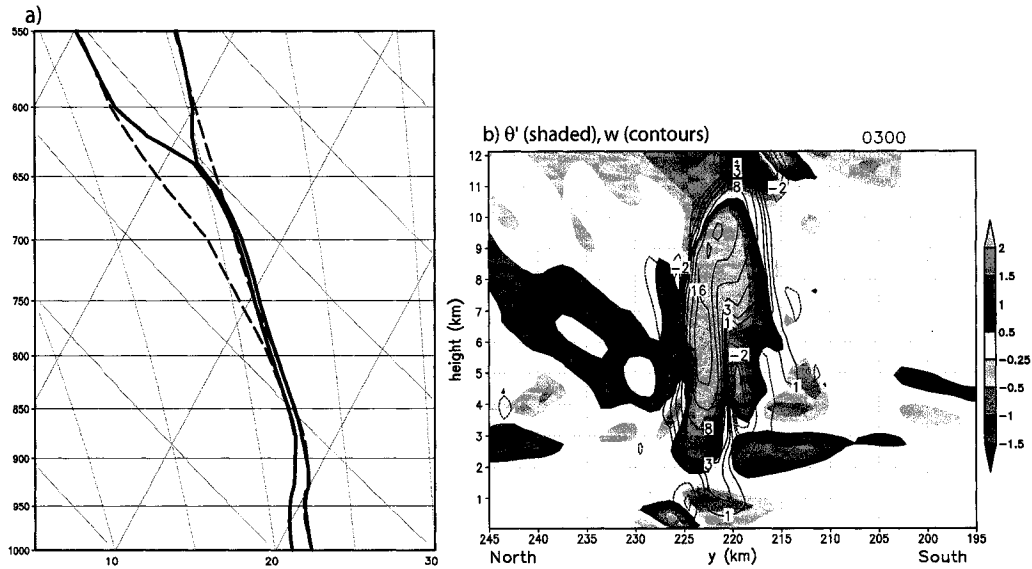


Figure 6.4: (a) Skew- $T$  log  $p$  diagram showing the effect of the lifting on the environment. The initial thermodynamic profile is shown with the dashed lines, and the solid lines show the profile at  $t=1.75$  h at the center of the convergence zone. (b) North-south vertical cross section through one of the first deep convective cells at  $t=3$  h. Shown are potential temperature perturbations (K, shaded, see color bar for scaling) and vertical velocity (contours at  $-4, -2, -1, 1, 2, 3, 5, 8, 12,$  and  $16$   $\text{m s}^{-1}$ , with negative contours dashed).

linear organization by  $t=3.5$  h in the 500-m simulation, and by  $t=5.5$  h in the 1-km simulation. In its early stages, the convective line was organized *parallel* to the average deep-layer shear, but then evolved such that the line had components both along and across the deep-layer shear vector. This orientation is generally similar to some of the simulations shown in Robe and Emanuel (2001), particularly their Fig. 12b. The organization and motion characteristics of this simulated system are very similar to those in observed extreme-rain-producing convective systems, and are consistent with the back-building/quasi-stationary pattern discussed by Schumacher and Johnson (2005). After approximately  $t=7.5$  h in the 1-km simulation, the convective line begins to surge southward (Fig. 6.5d-e), and the processes that lead to this southward surge at later times will be discussed in the next subsection.

An investigation of the low-level potential temperature fields shows that the initial linear organization is not caused by a cold pool. At  $t=5$  h in the 500-m simulation, the

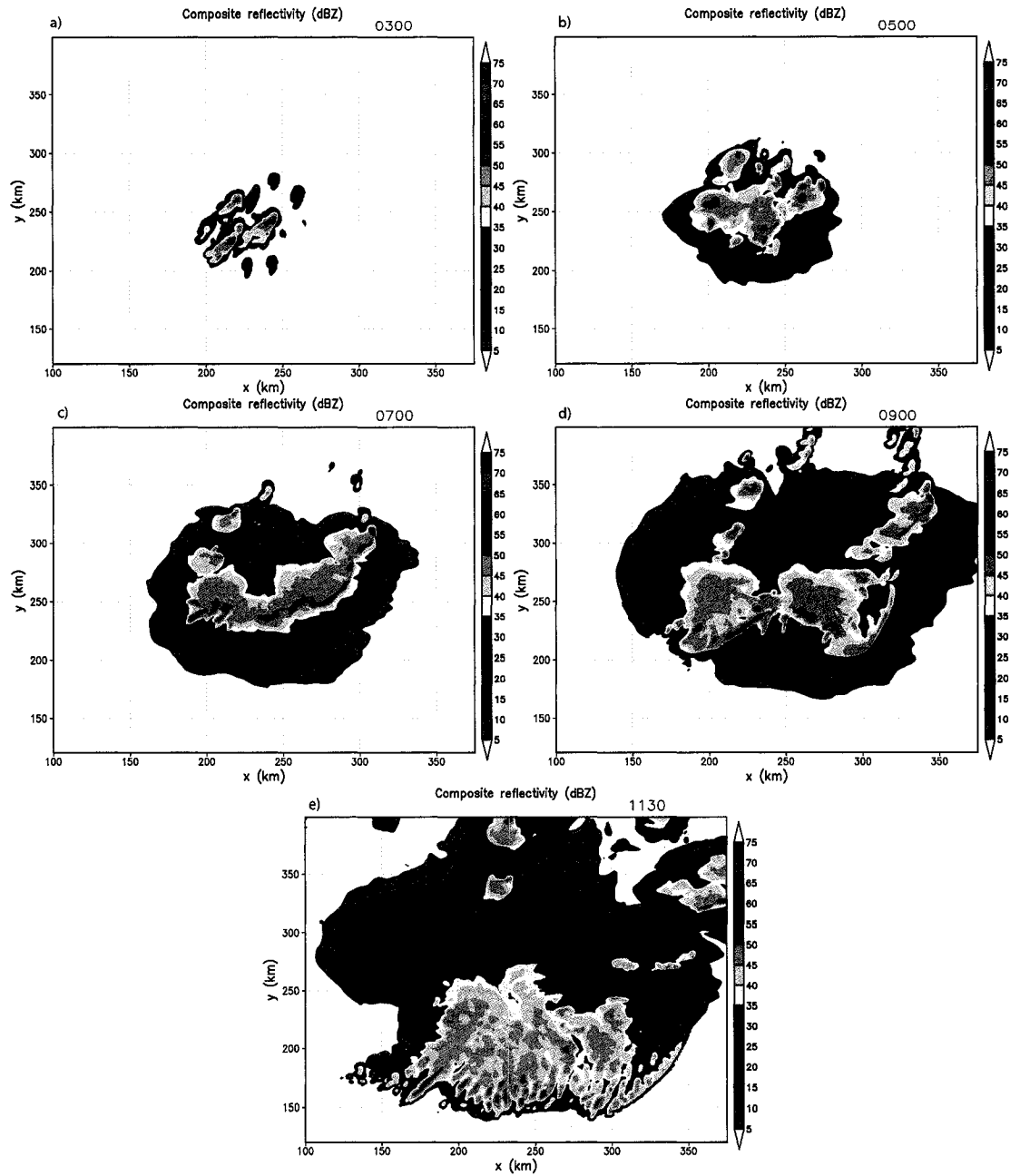


Figure 6.5: Simulated composite radar reflectivity (dBZ) from the 1-km simulation at (a)  $t=3$  h, (b)  $t=5$  h, (c)  $t=7$  h, (d)  $t=9$  h, and (e)  $t=11.5$  h. The portion of the domain shown is the same in all panels; however, recall that the domain is being translated toward the east-northeast as discussed in the text.

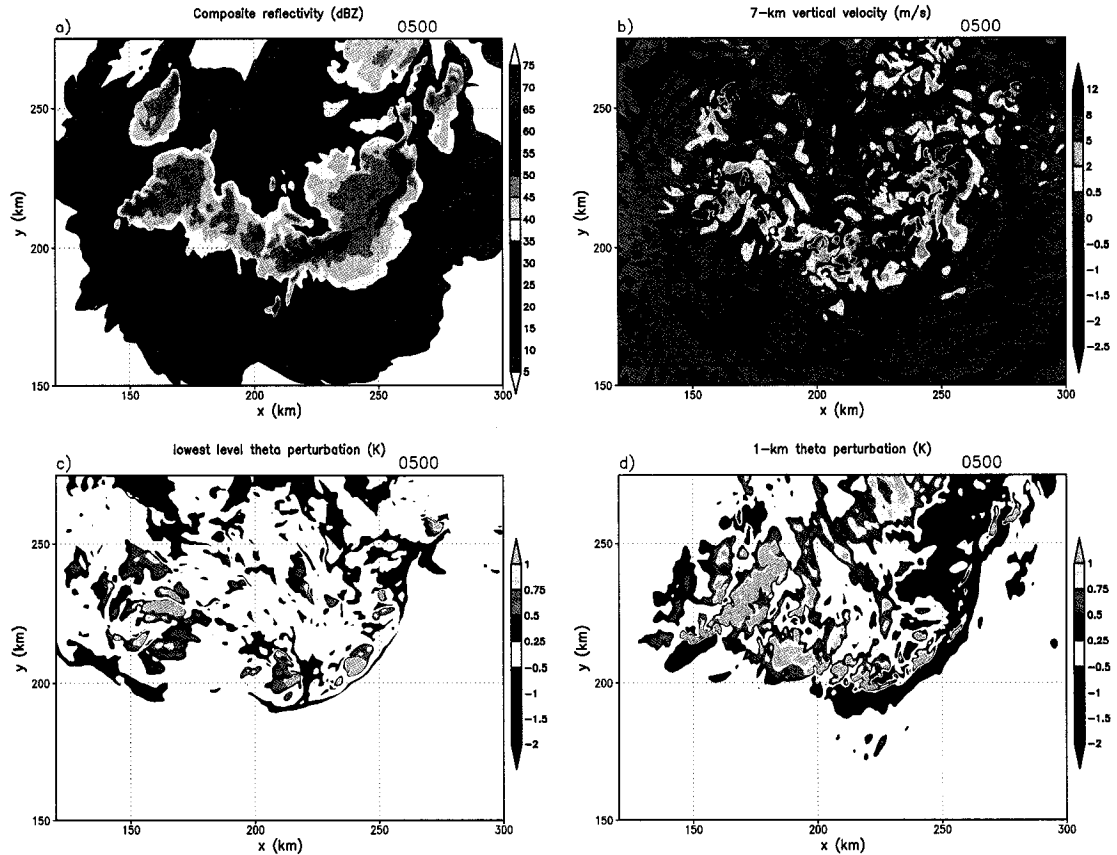


Figure 6.6: (a) As in Fig. 6.5, but for the 500-m simulation at  $t=5$  h. (b) Vertical velocity ( $\text{m s}^{-1}$ ) at 7 km AGL at  $t=5$  h in the 500-m simulation. (c) Potential temperature perturbations (K) on the lowest model level at the same time. (d) Potential temperature perturbations at 1 km AGL.

primary area of convection is organized in a line from southwest to northeast, with a smaller region of developing convection to its west (Fig. 6.6a,b). (The convective system in the 500-m simulation at this time is very similar to that in the 1-km simulation at  $t=7$  h.) At the surface, potential temperature perturbations ( $\theta'$ , calculated relative to the initial state) are generally weak (Fig. 6.6c). However, at 1 km AGL there is a strong signal of a gravity wave, with narrow bands of warm and cool air existing beneath the two primary regions of deep convection (Fig. 6.6d). Where  $\theta'$  is negative (positive), isentropes have been displaced upward (downward) from their initial state, and the narrow couplet seen in Fig. 6.6d illustrates the presence of a wave pattern in the isentropes. Thus, rather than

the low-level structure being defined by a density current as is the case with most linear convective systems, it is defined by a nearly stationary gravity wave with its maximum amplitude about 1 km above the surface.

Because it was necessary to choose a size for the imposed region of lifting, the size of the resulting MCS is somewhat pre-ordained by the size of the forcing. However, nothing about the momentum forcing favors linear organization for the resulting convection. The lack of a cold pool is to be expected, given that the nearly saturated low-level conditions inhibit the evaporation of raindrops. However, the tendency for the convection to organize itself linearly *without* a cold pool is somewhat surprising. The interaction between the deep convection, a low-level gravity wave, and the vertical wind shear appears to be the organizing factor for this convective system.

The vertical structure of the convective system (Fig. 6.7a) reveals many similarities to those found in past observational and modeling studies (e.g., Houze et al. 1989; Fovell 2002). There is strong low-level inflow into a deep, nearly upright convective line, and an overturning circulation aloft (e.g., Thorpe et al. 1982). Here, the maximum inflow is about 1 km above the surface owing to the representation of the LLJ in the initial wind profile. There is a broad region aloft that has been warmed, which is a gravity wave response to the convective system's latent heating (e.g., Nicholls et al. 1991). The cool, moist tongue of air described by Fovell (2002) is also present on the south side of the convective line from approximately 4–6 km AGL.

However, there are several important differences between this system and most previously simulated MCSs, most notably the lack of a cold pool near the surface. For the purpose of comparison, a similar figure from a typical simulation of a cold-pool-driven squall line (Fovell and Tan 1998, their Fig. 1a) is included in Fig. 6.7b. In their simulation, there is strong low-level vertical motion along the edge of a cold pool with  $\Delta\theta \approx -10$  K. They show that as air is lifted at the edge of the density current, new convective cells form periodically. The present simulation (Fig. 6.7a) also shows an updraft at low levels with

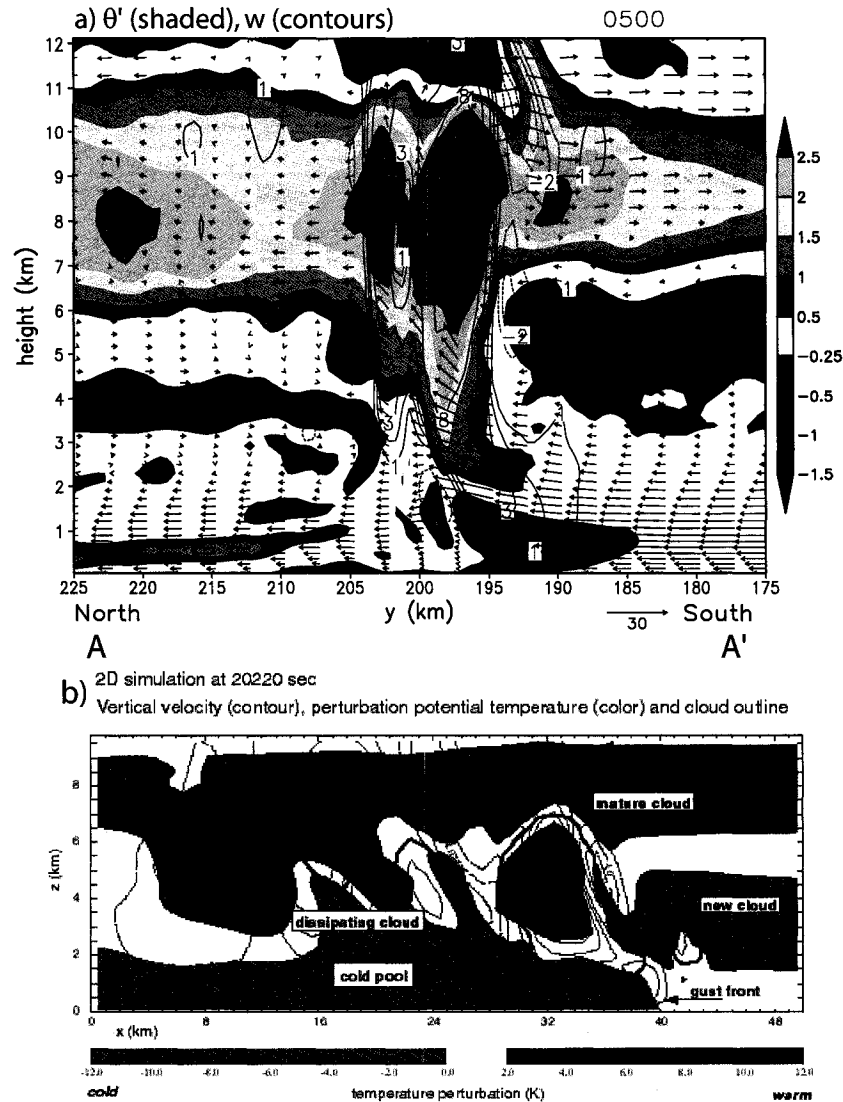


Figure 6.7: (a) North–south vertical section through the convective line at  $t=5$  h in the 500-m simulation. The location of the cross-section is shown by line A–A' in Fig. 6.6b, and values have been averaged over an area 5 km on either side of this line. Shown are potential temperature perturbations (K, shaded), vertical velocity ( $\text{m s}^{-1}$ , contoured), and system-relative, line-perpendicular flow vectors (shown at every fifth horizontal grid point). (b) A similar figure from Fovell and Tan (1998), showing a simulation of a cold-pool-driven squall line for comparison. The thin dashed contours near the surface are potential temperature perturbations, contoured every 2 K; note that these perturbations are significantly larger than those shown in panel (a).

periodic initiation of new cells, but the temperature structure is markedly different. There is no cold air near the surface on the north side of the updraft; instead, there is an elevated cool perturbation almost directly below the updraft (e.g., at  $z=1$  km above  $y=190-197$  in Fig. 6.7a). Just to the north of the cool perturbation and updraft, there is a downdraft, and this couplet is the vertical representation of the low-level gravity wave described above and shown in Fig. 6.6d.

Trajectories of air parcels originating at two different levels illustrate the effect of this gravity wave on the air that encounters it (Fig. 6.8a). Subsaturated air originating near the surface (i.e., in the lowest 500 m) approaches the wave from the south-southeast and is lifted sharply over the crest of the wave, and then just as quickly sinks on the other side. In contrast, parcels from within the elevated southwesterly inflow, which have already been destabilized by the large-scale lifting, are lifted over the wave, attain their level of free convection, and rise in deep updrafts.

A closer look at the structure of the low-level wave reveals a distinct crest and trough in the isentropes (Fig. 6.8b). As near-surface parcels are lifted along the upward-sloping isentropes, they reach their lifting condensation level, clouds form, and the parcels continue to rise (Fig. 6.8b). However, the parcels then move into the downward branch of the gravity wave and they sink and become subsaturated once again.

It was shown in chapters 4 and 5 how a stationary low-level gravity wave in an environment with a strong reversal of the wind shear with height can contribute to the back-building behavior (i.e., propagation in the opposite direction of the cell motion) of a convective system (e.g., Fig. 4.22). Additionally, meso-to-synoptic scale lifting can bring parcels to their LFC on its own, which provides another mechanism for back-building when the lifting is upstream of the ongoing convection. These two processes also appear to be at work in this idealized simulation.

The back-building process is ubiquitous in the regions of deep convection in this simulation, and one location where it is very clearly illustrated is along the newly-developing

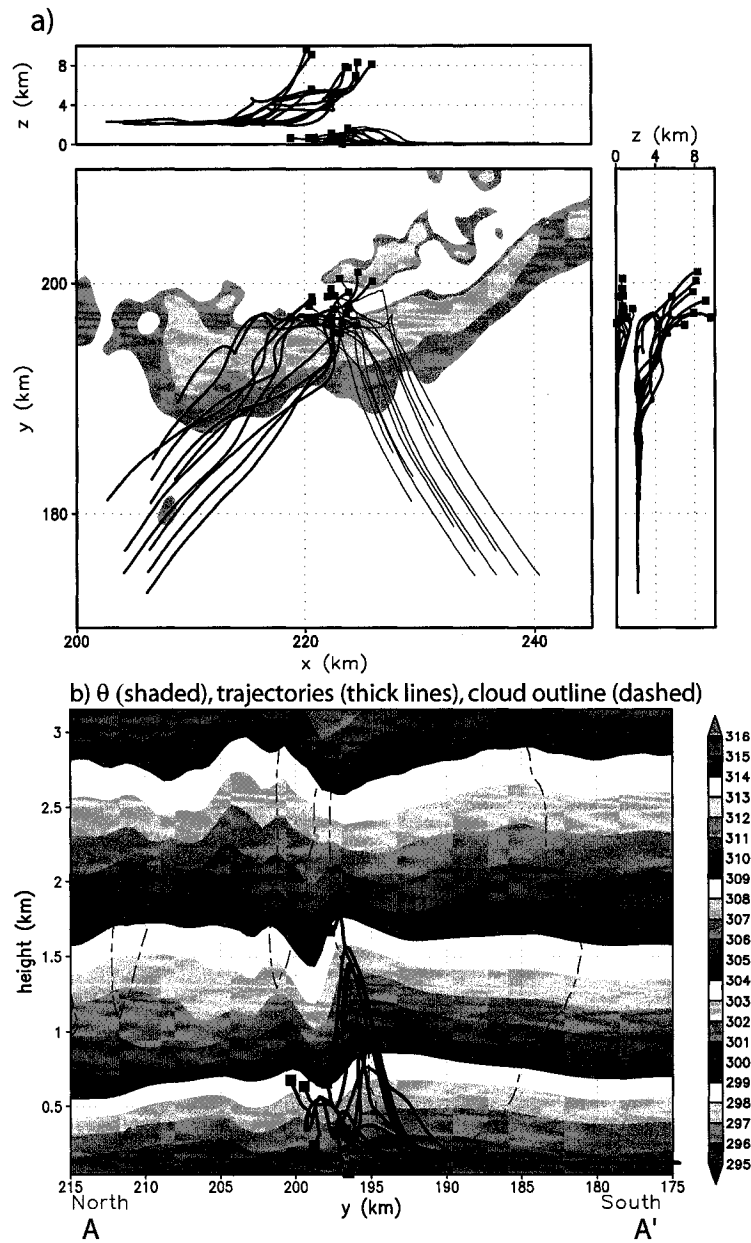


Figure 6.8: (a) Projection of selected 3-dimensional air parcel trajectories onto Cartesian planes. The trajectories are shown from  $t=4$  h to  $t=5$  h and the end of each trajectory is marked with a square. The thin trajectories originated at approximately 0.125 km above the surface, and the thick trajectories originated at approximately 2.1 km. In the  $x$ - $y$  plane, the  $\theta'=-0.5$  and  $-1$  K contours at  $t=5$  h are shaded to show the location of the low-level gravity wave. (b) North-south vertical section showing potential temperature (shaded every 1 K), cloud outline (thin dashed line), and the low-level trajectories from panel (a) in the lowest 3 km to emphasize the low-level structure. The location of the cross-section and the averaging is the same as in Fig. 6.7a.

convective cluster to the west of the primary convective line (see line B–B' in Fig. 6.6b). Fig. 6.9 shows discrete cells forming upstream of their predecessors and developing into deep updrafts as they move northeastward, while the cluster as a whole is propagating toward the southwest. It also reveals the role of the low-level gravity wave in maintaining and focusing the deep convection. At  $t=4.5$  h (Fig. 6.9a), a progression of convective cells is apparent: two deep, strong updrafts on the right (northeast) side of the figure, one strengthening cell to their southwest, and one relatively new updraft (referred to as cell number 1). Over the next twenty minutes (Fig. 6.9b–c), cell 1 develops into an intense updraft, and we see the initiation of cells 2 and 3 upstream. Cell 2 follows in the path of cell 1 and also becomes a deep updraft by  $t=5$  h (Fig. 6.9d), when another new cell (number 4) begins to appear. A similar multicellular back-building process is common to quasi-stationary convective systems (see, e.g., the schematic from Doswell et al. (1996) shown in Fig. 2.2), but here the low-level mechanism responsible for initiating new deep convective cells is not a “traditional” outflow boundary. Instead, as the developing shallow updrafts encounter the low-level gravity wave, they are lifted and erupt into deep convective cells. (The wave is shown by the cool perturbations centered at approximately 1 km AGL in Fig. 6.9; the plane of the vertical section is parallel to the wave, so the wave appears as a long band of  $\theta' < 0$ .) Over the 30-minute period shown in Fig. 6.9, the gravity wave and associated convection has also moved toward the southwest, i.e., it has propagated in the opposite direction of cell motion.

As shown previously, the wave is produced by the latent heating from the developing convective cells and its motion is altered by the reverse-shear wind profile at low levels. Additionally, the convection has become oriented from southwest to northeast, aligned approximately parallel to the low level shear (Fig. 6.6c). These two mechanisms contribute to a self-perpetuating system whereby convection is initiated, producing a low-level gravity wave, which in turn assists in initiating additional convection along a southwest-to-northeast line that develops parallel to the shear vector. When convection back-builds

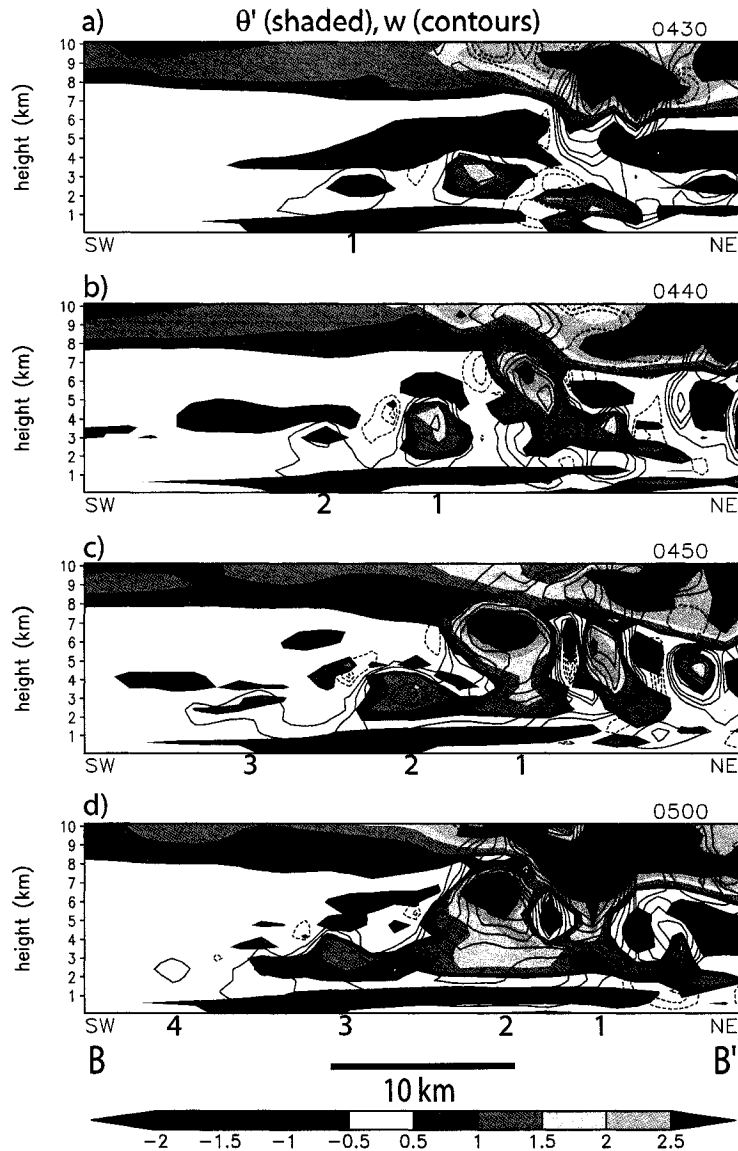


Figure 6.9: Series of southwest-to-northeast sections showing the development of several convective cells in the 500-m simulation. The location of the sections is shown by line B–B' in Fig. 6.7a. Shown are potential temperature perturbations (K, shaded as shown) and vertical velocity (line contours at  $\pm 1, 2, 3, 5, 7, 9, 11, 13,$  and  $15 \text{ m s}^{-1}$ , with negative contours dashed). The numbers 1–4 denote specific cells discussed in the text. Times shown are (a) 4.5 h (4 h 30 min), (b) 4.67 h, (c) 4.83 h, and (d) 5 h.

and becomes linearly organized in this way, it creates an optimal configuration for locally excessive rainfall amounts.

Though the discussion in the previous two paragraphs focused mainly on the imme-

diate vicinity of the convection, the importance of the background lifting should not be neglected: it is what gets this process started initially, and it also aids in the initiation of the shallow cells upstream. In the case studied in chapter 4, the shallow cells formed much farther upstream than they do in this simulation, but this was likely a result of inhomogeneities in the thermodynamic environment in that case that are not present here.

Most past research on linear convective systems has focused on the cold pool as a maintenance mechanism, because the environments in which most MCSs form have dry air at some level, which promotes evaporative cooling and cold-pool production. In this context, the above findings represent a much different mechanism for MCS organization and maintenance, though they are not entirely unique. The idea of low-level gravity waves or bores as maintenance mechanisms for mesoscale convective systems has been put forth by Dudhia et al. (1987), CM88, Schmidt and Cotton (1990), and Parker (2008), and the parcel trajectories in this simulation are very similar to the “underflow” regime discovered in the “DEEP-unlim” simulation of Parker (2008, his Fig. 8). However, Dudhia et al. (1987), CM88 and Schmidt and Cotton (1990) used two-dimensional simulations, and it is shown here that, at least for environments in which quasi-stationary MCSs develop, three-dimensional effects are important. Unlike Parker’s simulation, which transitions from a cold-pool-driven squall-line to one with a low-level gravity wave, the gravity wave is the initial structure here. (This difference likely comes about because the initial thermodynamic environment here is stable at low levels, whereas he increased the stability over time by adding low-level cooling.) Based on the results of the “real-data” simulation in chapter 4 and in the idealized simulation shown here, we conclude that low-level gravity waves are a fundamental, though often overlooked, mechanism for the organization and maintenance of linear convective systems, especially in very moist environments that are not supportive of strong cold pools.

### 6.2.2 *Observational evidence for low-level gravity waves*

Considering the relatively coarse resolution of the surface observing network in the central United States and the relatively small size of some of the observed MCSs, observations of the low-level gravity waves discussed above are few. However, in one of the events discussed previously, the 20 August 2007 case in Missouri (section 3.3.6), the convective line passed over two automated surface stations that reported data every minute. At 0745 UTC (Fig. 6.10a), the MCS is developing over southwest Missouri with a linear band of convection oriented from southwest to northeast. As this convective line passes over the Joplin, Missouri observing station (denoted by “JLN” in Fig. 6.10a) between approximately 0735–0815 UTC, one-minute surface observations show several undulations in the pressure field, with the wind field varying in phase with the pressure (Fig. 6.10b). This behavior is consistent with that of a gravity wave. Also of note at this time are the large rainfall rates associated with the convective line: 1-min rainfall totals reach 2 mm, which converts to an instantaneous rainfall rate of  $120 \text{ mm h}^{-1}$  ( $4.8 \text{ in h}^{-1}$ ).

Somewhat later, at 0930 UTC, the convective line passes over the Springfield, Missouri observing station (denoted by “SGF” in Fig. 6.10c). Although the phase relationship between pressure and wind during the convection’s passage at this station is not quite as clear, these two fields do vary in phase between approximately 0920 and 0945 UTC during a period of convective rainfall (Fig. 6.10d). Furthermore, over the time periods shown in Figs. 6.10b and d, the surface temperature changed by no more than  $1^\circ\text{F}$  ( $0.56^\circ\text{C}$ ), with the temperature actually rising by  $1^\circ\text{F}$  at Joplin (not shown). This minimal temperature change suggests that the convection is not being organized and maintained by a surface cold pool/density current. Although the observations shown in Fig. 6.10 are limited, they provide some evidence for the idea that low-level waves are assisting in the organization of these extreme-rain-producing convective systems. Further observations of such MCSs with a denser observing network (such as the Oklahoma Mesonet) could provide more substantial information about their surface features.

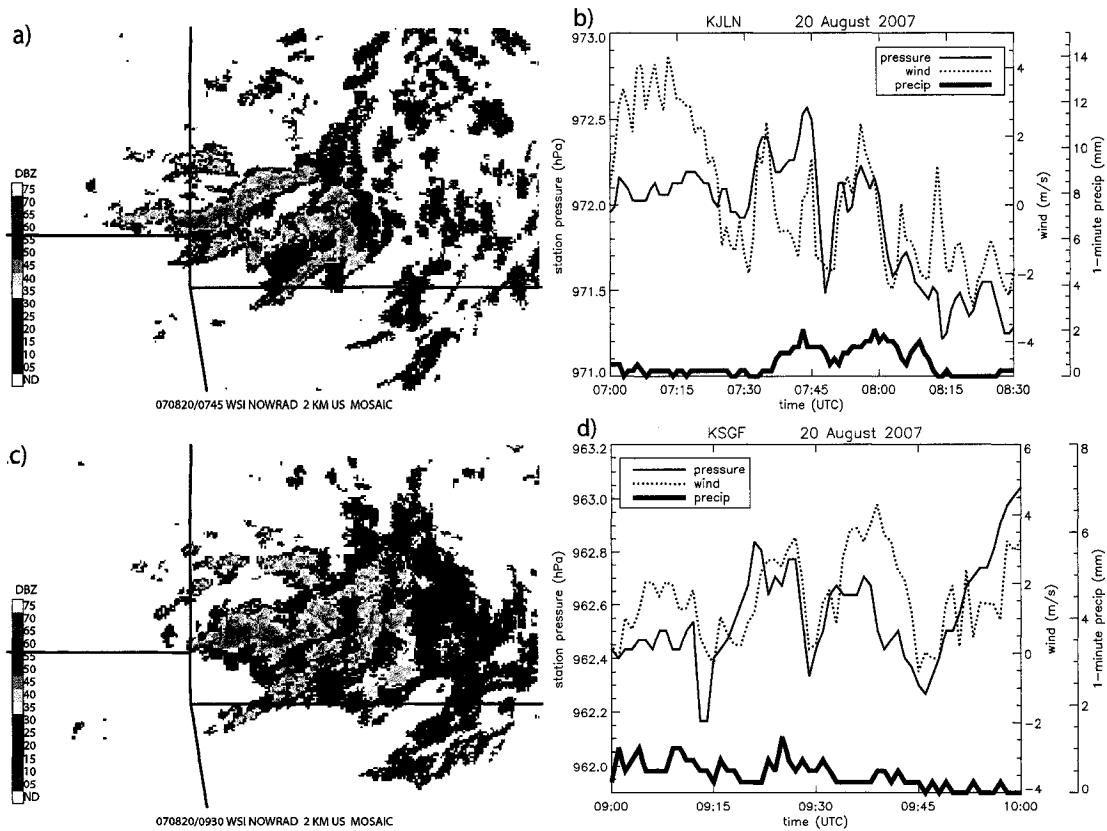


Figure 6.10: (a,c) Observed composite radar reflectivity at (a) 0745 and (b) 0930 UTC 20 August 2007. Also shown are the locations of surface observing stations at Joplin (JLN) and Springfield (SGF), Missouri. (b,d) Time series showing station pressure (hPa; solid line) and wind speed in the direction of (possible) wave propagation ( $\text{m s}^{-1}$ ; dotted line) on 20 August 2007. Panel (b) shows station JLN from 0700–0830 UTC and panel (d) shows station SGF from 0900–1000 UTC. Also shown in the thick solid lines is precipitation accumulated in the previous minute (mm). The winds were calculated using Equation 1 of Koch and Golus (1988), using  $270^\circ$  as the direction from which the wave was propagating (measured clockwise from north) for the earlier time shown in panels (a–b), and  $290^\circ$  for the later time shown in panels (c–d).

### 6.2.3 *Evolution of simulated convective system at later times*

As discussed above, in the 1-km simulation, the integration was carried out beyond the 5 h of the 500-m simulation. The convective system at later times exhibits some characteristics that contrast with how it initially became organized (Fig. 6.5). The gravity wave discussed above was the primary low-level structure through approximately  $t=7$  h, but after this time a cold pool began to develop and quickly altered the convective organization (Fig. 6.11). At  $t=7$  h (Fig. 6.11a), the first signs of a cold pool are appearing, but the deep convective lines are still associated with the low-level gravity wave, which is only barely visible at the surface but is strongest at  $\sim 1$  km AGL (cf. Fig. 6.6). But by  $t=9$  h (Fig. 6.11c), the cold pool has become much stronger and has spread toward the south. There is still deep convection at this time, but it has become somewhat less organized and does not have the distinctly linear pattern that existed earlier. Additionally, the deep convection is not located at the leading edge of the cold pool, but it is displaced 20–30 km behind the gust front. By the end of the simulation ( $t=11.5$  h; Fig. 6.11d), the deep convection has weakened even further, and by this time an extensive region of stratiform rainfall has developed behind the dissipating convective line (Fig. 6.5e). This evolution is consistent with Parker (2007b), who found that simulated MCSs with parallel stratiform precipitation undergo a “seemingly inexorable march toward [trailing stratiform] structure.”

The vertical cross-section in Fig. 6.12 shows an example of some of the processes involved when the convection undergoes the transition between the gravity wave and cold-pool-driven stages of the convective system. At  $t=8$  h (Fig. 6.12a; a plan view at the same time is shown in Fig. 6.11b) the low levels still show some signs of the gravity wave, but the near-surface cold pool is also intensifying and is beginning to spread southward. There is a weak updraft at the leading edge of the cold pool (above approx.  $y = 227$ ), but the deep convection is located farther to the north. The convection is still vigorous at this time, but it is becoming tilted toward the north (upshear relative to the deep-layer shear). As the cold pool spreads southward, the convection becomes more tilted, and the deep

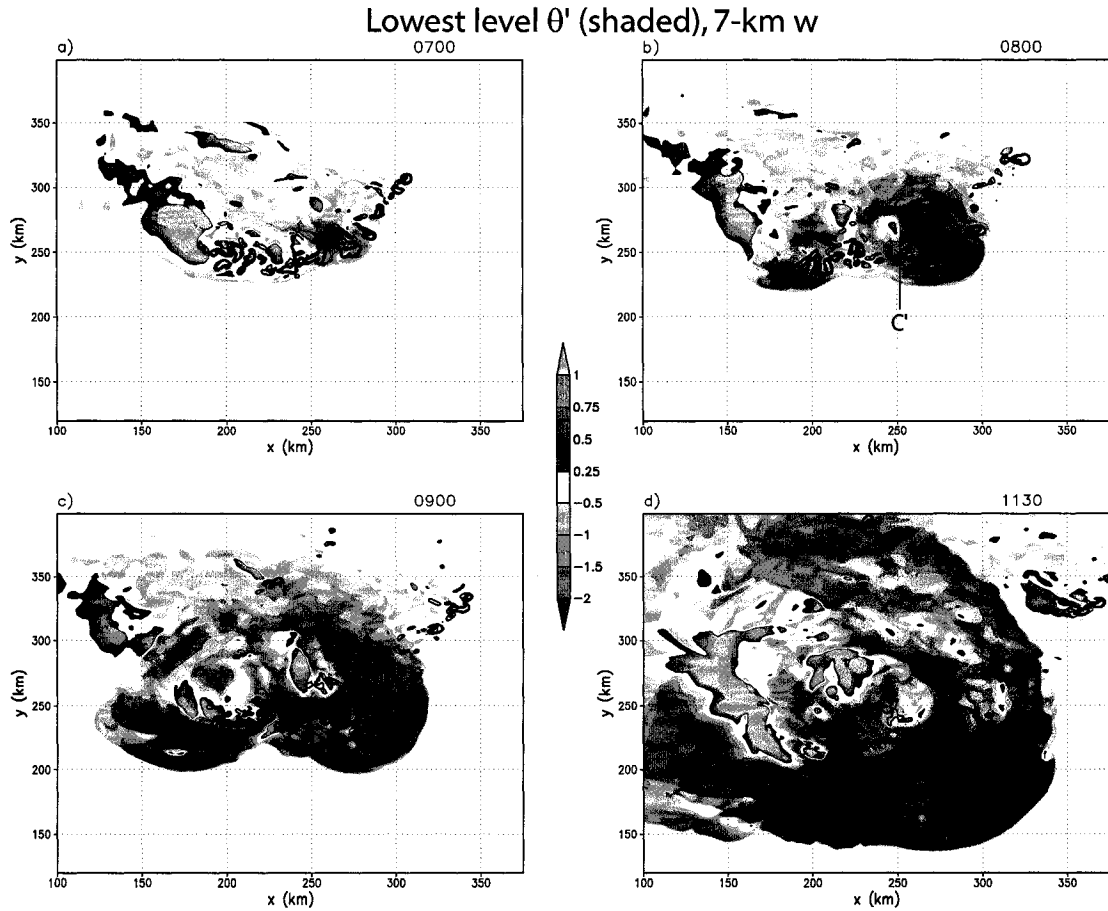


Figure 6.11: Potential temperature perturbations (K, shaded) on the lowest model level and vertical velocity at 7 km AGL (contoured every  $2 \text{ m s}^{-1}$  above  $2 \text{ m s}^{-1}$ ) at  $t =$  (a) 7 h, (b) 8 h, (c) 9 h, and (d) 11.5 h of the 1-km simulation.

convection becomes farther removed from the cold pool edge. At  $t = 8.58 \text{ h}$ , however, a pocket of cold air, with associated inflow from the rear of the system, appears and causes the deep convective cells to become upright once again (Fig. 6.12b). This cool perturbation, which is located at approximately 3–4.5 km AGL above  $y = 245\text{--}250$ , resembles the elevated rear-inflow jets discussed by Weisman (1992), which he argued could assist in keeping a convective line upright when the horizontal vorticity from the cold pool overwhelms that from the ambient shear. In animations of the cross-sections shown in Fig. 6.12, the cool perturbation appears to “push” the convective line from its tilted position toward a more upright orientation. These elevated cool pockets also apparently contribute to the fact that

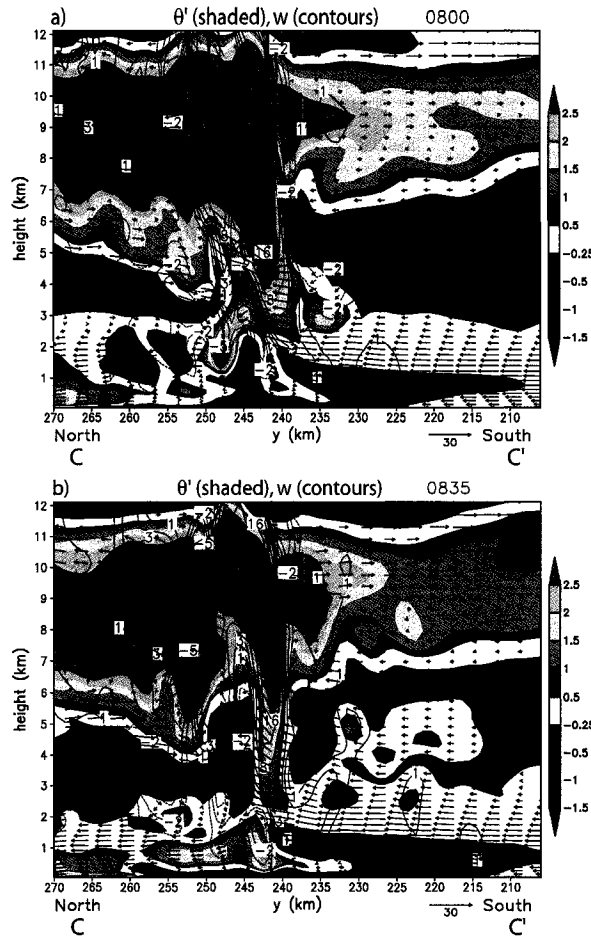


Figure 6.12: As in Fig. 6.7, except for the cross-section location shown by line C–C' in Fig. 6.11b at (a)  $t=8$  h and (b)  $t=8.58$  h of the 1-km simulation.

the deep convective activity is essentially stationary (above  $y = 240\text{--}245$ ) in the 35-min period shown here, even though the surface cold pool has surged southward substantially to  $y = 215$ . These perturbations are generally located near the melting level, and as will be illustrated later by a sensitivity simulation, their development is directly related to cooling from the melting of hydrometeors.

The transition from a gravity-wave-driven to cold-pool-driven convective line is similar to that in the two-dimensional simulations of CM88 and Lafore and Moncrieff (1989). However, the tendency of the convection to become *less* organized after the development of a strong cold pool is quite different from most past studies of convective systems. In this

simulation, it takes a long time for a cold pool to develop owing to the nearly saturated midlevels, and the cold pool that does develop is very shallow because the subsaturated layer near the surface is also very shallow. The cold pool spreads southward in an environment that is very suboptimal in terms of the theory of Rotunno et al. (1988), because the horizontal vorticity at the edge of the cold pool is of the same sign as that of the ambient shear in the lowest 1 km. However, the reversal of the shear above the cold pool allows moist, conditionally unstable air to continue to flow into the system from the south, and the background lifting and the melting-induced cold pockets assist in maintaining some deep convection even though the surface cold pool has “undercut” the system. This evolution bears at least some similarity to a few of the observed extreme-rain-producing convective systems as well, particularly the 5–6 May (Fig. 3.2) and 3–4 June 2000 (Fig. 3.4) events. In both of these cases, the primary convective lines remained quasi-stationary for several hours, after which there were southward “surges” of convection consistent with the spreading of a cold pool. And even after these surges took place, other clusters of convection within these MCSs continued to back-build and move slowly.

Although accumulated rainfall is not one of the best-performing output fields for cloud models (Gilmore et al. 2004), the purpose of these simulations is to understand convective systems that produce locally extreme rainfall that has the potential to cause flash flooding. If the simulated rainfall amounts are not consistent with observations, it would be a dubious claim that these were faithful simulations of extreme-rain-producing MCSs. For the purposes of comparing the simulated rainfall with an actual event, the rainfall field (translated to account for the moving domain) has been projected onto a map and is shown next to accumulations from the simulation of the 6–7 May 2000 case presented in chapter 4 (Fig. 6.13).<sup>2</sup> Through 11 h, the accumulated rainfall from the idealized simulation compares favorably with the 6–7 May 2000 case, though the rainfall was

---

<sup>2</sup> Data from the case study simulation is used here instead of rain gauge observations so that a particular 11-h period can be compared. Chapter 4 showed that it was a very accurate simulation of the 6–7 May 2000 case, and selecting particular hours was not possible with the sparse hourly rain gauge network.

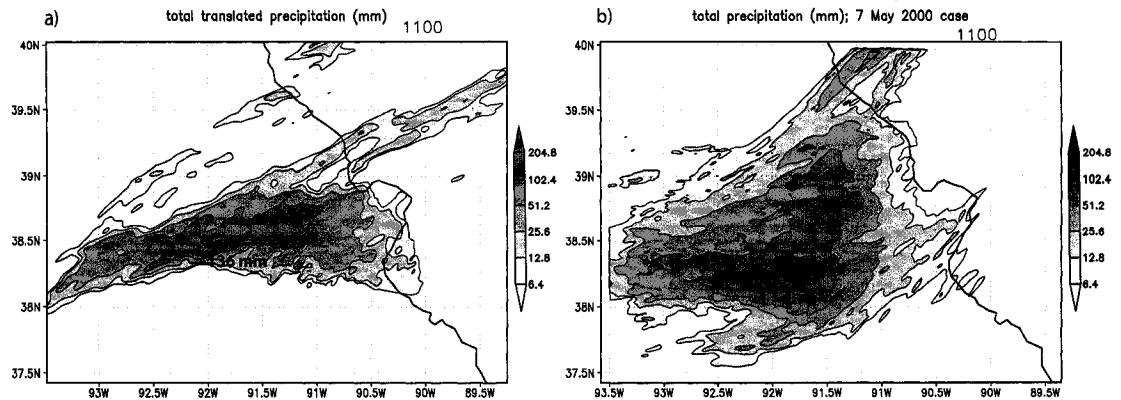


Figure 6.13: Comparison of accumulated rainfall between the idealized simulation and an accurate simulation of a real event. (a) Accumulated rainfall through  $t=11$  h in the 1-km idealized simulation. (b) Accumulated rainfall from 0000–1100 UTC 7 May 2000, from the simulation presented in chapter 4. The rainfall data in (a) have been translated to remove the effects of the moving model domain, and they have been projected onto the same map that is shown in (b) for purposes of visual comparison.

more widespread in that event. The maximum rainfall in the idealized simulation through 11 h was 136 mm (5.35 in), whereas it was 172 mm (6.77 in) in the case-study simulation. In the 6–7 May event, the heavy rainfall continued for several hours beyond the time shown here, but in the idealized simulation the heaviest rain has likely ended by  $t=11$  h because of the cold-pool-induced weakening of the convective line. A strong cold pool never formed in the 6–7 May 2000 event, which allowed it to continue producing locally heavy rainfall for a longer period of time. In the region of maximum rainfall amounts in the idealized simulations, most of the rain fell in about a 4 h period from  $t=5$  to 9 h. Given these local rainfall totals in excess of  $25 \text{ mm h}^{-1}$  for several hours and the accurate representation of the back-building, quasi-stationary characteristics of observed systems, and considering the uncertainties in model-predicted rainfall, it appears that this is generally a faithful idealized simulation of an extreme-rain-producing MCS.

### 6.3 Sensitivity experiments

Several numerical experiments were carried out to test the sensitivity of the simulated convective systems to various processes. These sensitivity experiments are summarized in

Table 6.2: Descriptions of the sensitivity experiments. Additional details are given in the text.

CTRL	Primary 1-km simulation discussed in section 6.2
NOEVAP	No latent cooling from evaporation of raindrops
NOMELT	No latent cooling from melting or sublimation of graupel and snow
STOPFORCE	Momentum forcing is removed after 2 h
CORIOLIS	Coriolis force included, with $f = 8.882 \times 10^{-5} \text{ s}^{-1}$

Table 6.2. Other than the changes listed in Table 6.2 and discussed in this paragraph, these simulations are identical to the primary 1-km simulation presented above. The primary simulation will be referred to as “CTRL” in the discussion to follow. For the microphysical sensitivities (NOEVAP and NOMELT), the code of the microphysics scheme was modified so that phase changes occur as usual, but no latent cooling occurs when the respective phase changes take place. In NOEVAP, the cooling is only removed for the evaporation of rainwater; evaporation of cloud water is unchanged. In STOPFORCE, the momentum forcing is applied for the first 2 h of the simulation and is then removed. This provides the lifting necessary to initiate convection initially, and then tests whether the deep convection can be maintained without additional forcing. After the forcing is removed, the associated convergence and vertical motion weaken quickly, but some lifting does remain for several hours (Fig. 6.14). This is similar to an experiment in CM88. They also ran an additional simulation where they stopped the forcing and then re-initialized the model without any residual convergence, but such an experiment has not been performed here. Finally, the CORIOLIS experiment was designed to test the effects of planetary rotation on the simulated convection. In this run, the Coriolis force is only applied to perturbations from the basic-state wind. However, this means that Coriolis accelerations are also acting upon the imposed forcing, the physical meaning of which is not entirely clear since the forcing is applied artificially. Nonetheless, a dry simulation shows that the resulting flow fields in CORIOLIS are broadly similar to that in CTRL, though the upward vertical

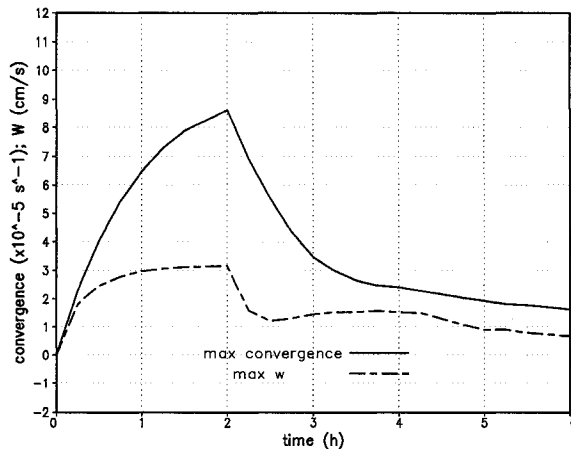


Figure 6.14: As in Fig. 6.3a, except for STOPFORCE (in a dry simulation), where the momentum forcing is turned off after 2 h of integration.

motion owing to the forcing is slightly weaker (Fig. 6.15, cf. 6.3b) and the stronger wind perturbations have experienced a noticeable deflection due to Coriolis accelerations. As such, CORIOLIS and CTRL are not exactly comparable, because the imposed forcing is not identical between the two runs. However, the primary effects of planetary rotation can still be examined. In this run, the value of the Coriolis parameter, which is constant across the domain (i.e., an  $f$ -plane) was chosen to correspond to the latitude of Springfield, MO (37.25°N).

### 6.3.1 *Microphysical processes*

The first two sensitivity experiments were designed to test the importance of specific microphysical processes on the simulated convection. CM88 removed evaporation of rain in their simulations and found that in an environment with large-scale lifting, a cold pool (produced by evaporative cooling) was not necessary for maintaining a squall line. Since the convective system discussed in section 6.2 initially became organized despite the lack of a cold pool, a similar simulation is employed here to understand the role of latent cooling in organizing and maintaining the convection.

Somewhat counterintuitively, the simulation here without cooling from evaporation

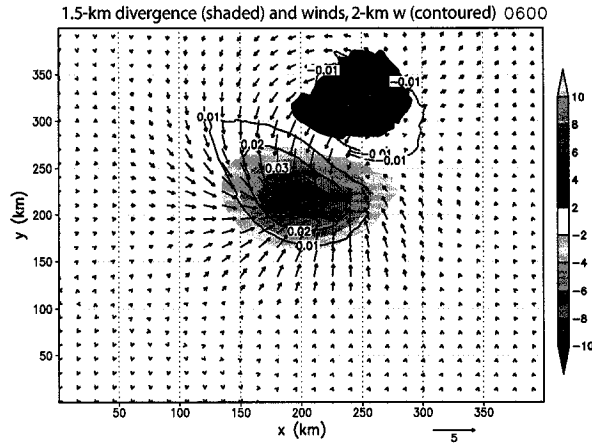


Figure 6.15: As in Fig. 6.3b, except for CORIOLIS (in a dry simulation).

of rainwater (NOEVAP) has consistently stronger convection than in the control run or any of the other sensitivity tests (Fig. 6.16). Through the first 4 h of NOEVAP, the convection initiates and evolves similarly to CTRL (not shown). There are indications of linear organization and back-building along the same low-level gravity waves discussed previously. However, in the later stages of NOEVAP, two clusters of convection separate from each other: the strongest convection moves quickly toward the northeast, while a smaller cluster remains near the center of the domain within the convergence region (Figs. 6.17b and 6.18b). By  $t=9$  h, a loosely-organized line of intense convective cells was located in the northeast part of the domain (Fig. 6.18b), signifying that the most intense convection has actually moved away from the forcing. Furthermore, it has propagated in this direction without any contribution from a low-level density current; the maximum surface potential temperature deficit is less than 1 K.

The convective system in NOMELT is organized more like CTRL than NOEVAP. It has a back-building southwest-northeast oriented convective line in a similar location (Figs. 6.17c and 6.18c). Although the maximum vertical velocities in NOMELT are comparable to those in CTRL (Fig. 6.16), the distribution of deep convection differs. In NOMELT, there are just a few intense convective cores, which are mainly located near the momentum forcing. However, there is a large region of weaker, less-organized convection throughout

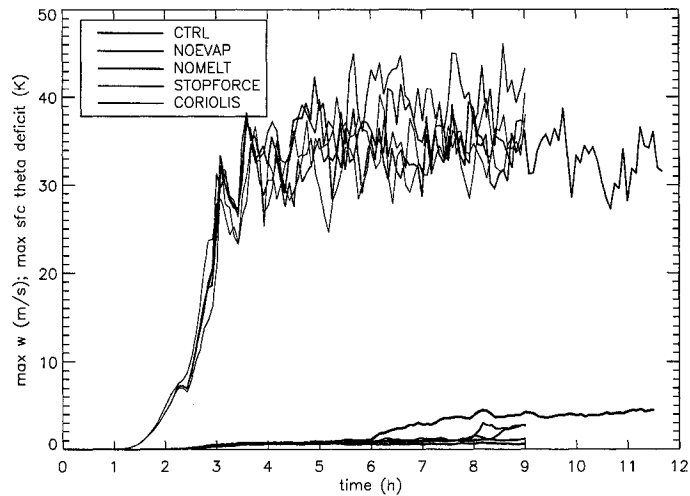


Figure 6.16: Time series comparing the sensitivity simulations. The traces at top show the maximum vertical velocity ( $\text{m s}^{-1}$ ), and those at the bottom show the maximum  $\theta$  deficit (K) on the lowest model level. Recall the the control run was integrated for 11.5 h, whereas the other runs were only integrated for 9 h.

much of the domain. This contrasts with the more focused convective line in CTRL. As alluded to previously, one reason for this difference may be related to the development of a rear-inflow jet. In CTRL (Fig. 6.12), a pocket of cold air located at about 4 km AGL assists in keeping the deep convection upright. However, cross-sections through the deep convection show that no such jets are present in NOMELT. One such cross-section is presented in Fig. 6.19, which shows an upshear-tilted convective line. Even at this late time in the simulation, the convection is still being organized by the low-level gravity wave, as a cold pool has not formed. An examination of the temperature tendency owing to microphysical latent heating and cooling in relation to the location of frozen hydrometeors reveals that the elevated cool perturbations and rear inflow in CTRL are collocated with the level where snow and graupel are melting (Fig. 6.20a), similar to the findings of Szeto et al. (1988). Since melting processes are neglected in NOMELT, the elevated microphysical cooling does not occur, the rear inflow does not develop, and the convective line generally remains tilted and less organized than that in CTRL (Fig. 6.20b). Additionally, Fig. 6.20 shows that the strength of evaporative cooling (located below about 2.5 km AGL) is roughly comparable

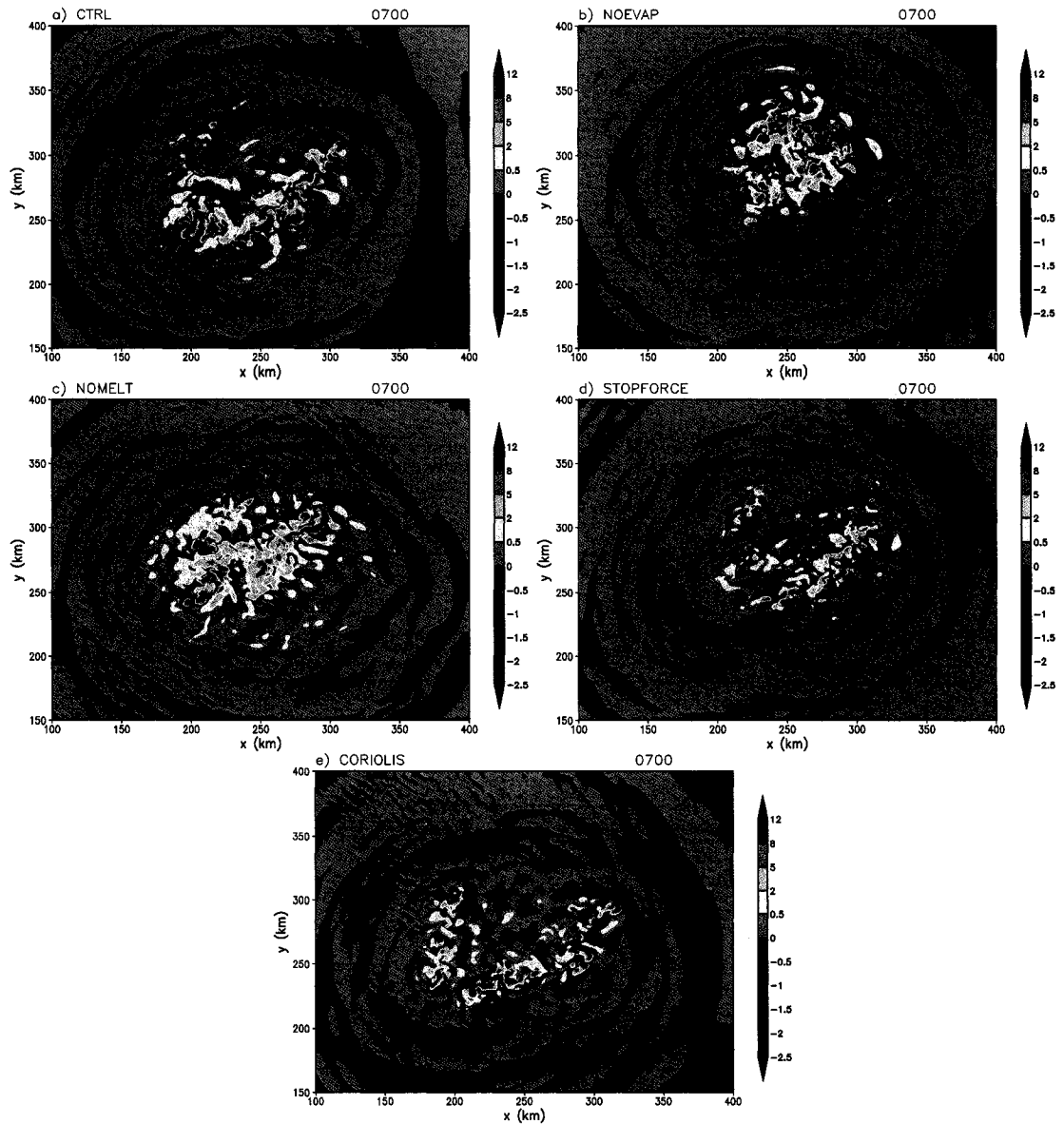


Figure 6.17: Vertical velocity ( $\text{m s}^{-1}$ ) at 7 km AGL for (a) CTRL, (b) NOEVAP, (c) NOMELT, (d) STOPFORCE, and (e) CORIOLIS at  $t=7$  h. Also shown by a thick black line, where applicable, is the  $\theta = -1$  K contour on the lowest model level to denote the cold pool outline. The same portion of the model domain is shown in all panels.

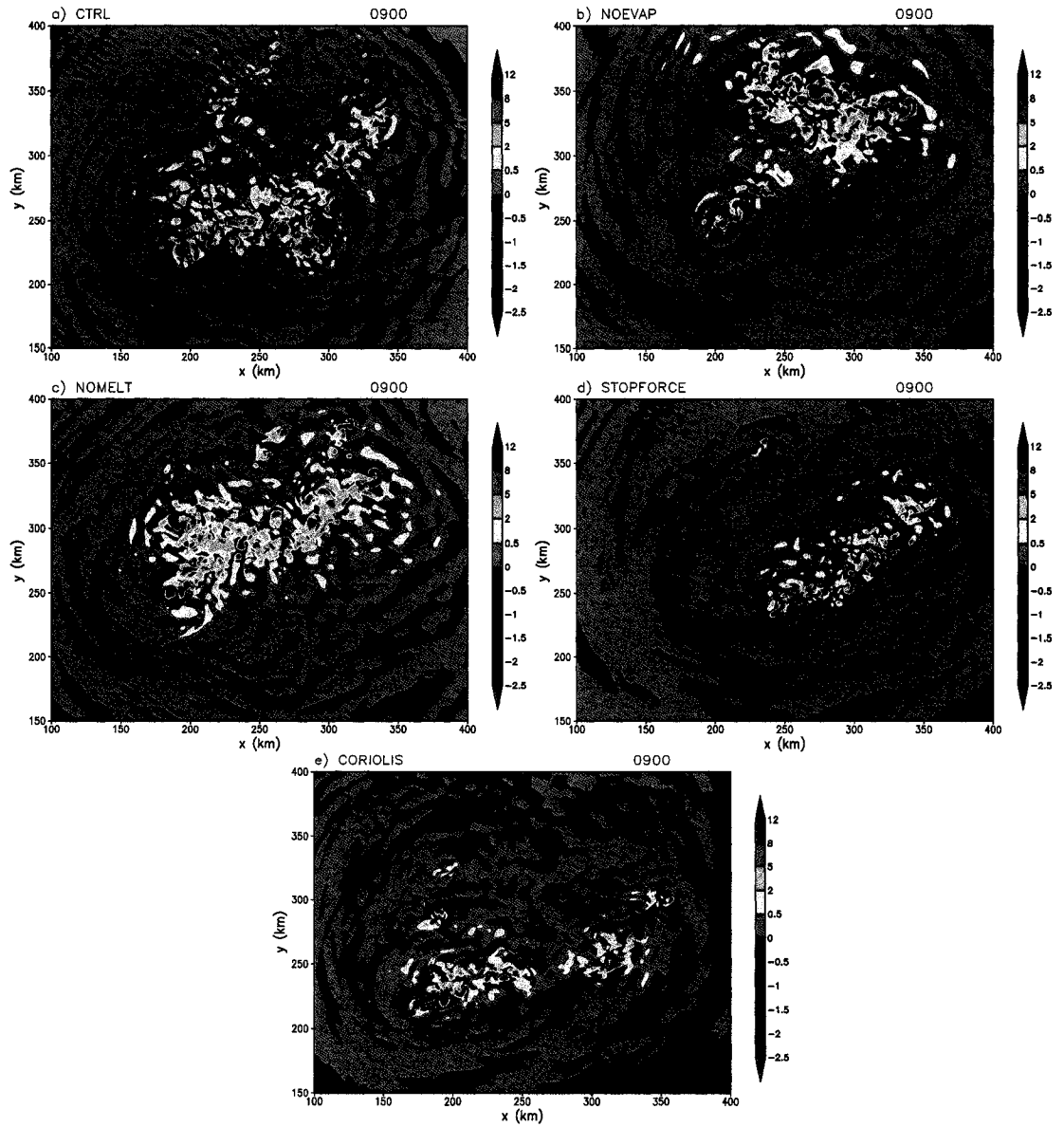


Figure 6.18: As in Fig. 6.17, except at t=9 h.

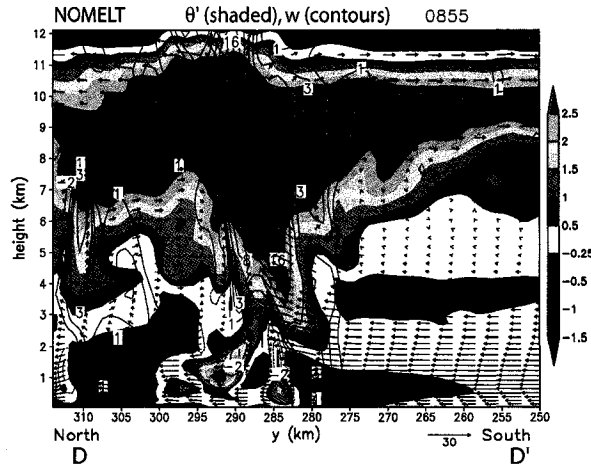


Figure 6.19: As in Fig. 6.12, except for run NOMELT at  $t=8.92$  h. The location of the cross-section is shown by line D–D' in Fig. 6.18c.

between the two runs, but a surface cold pool never forms in the 9 h of integration of NOMELT. This suggests that melting effects were very important in the development of the cold pool that formed in the later stages of CTRL, as discussed by Atlas et al. (1969) and others.

The differing organization and motion of the convection in NOEVAP compared with CTRL and NOMELT suggests at least two important ways that the evaporation of rain-water can have an impact other than through the development of a cold pool. First, considering that the convection in NOEVAP is the strongest of any of the runs, it appears that latent cooling owing to evaporation of raindrops actually *weakens* the convective system overall. This is likely a result of the detrimental effects of dry-air entrainment: though these effects are weak in CTRL owing to the moist environment, they are not present at all in NOEVAP. Second, although it was shown previously that a latent-heating-related gravity wave, rather than a cold pool, was the organizing mechanism in the first several hours of the simulations, evaporative cooling apparently still plays an important role in keeping the convective system quasi-stationary. In both CTRL and NOMELT (Fig. 6.18a and c), the convection was organized from southwest to northeast and exhibited significant back-building behavior. In NOEVAP (Fig. 6.18b), on the other hand, the convection raced

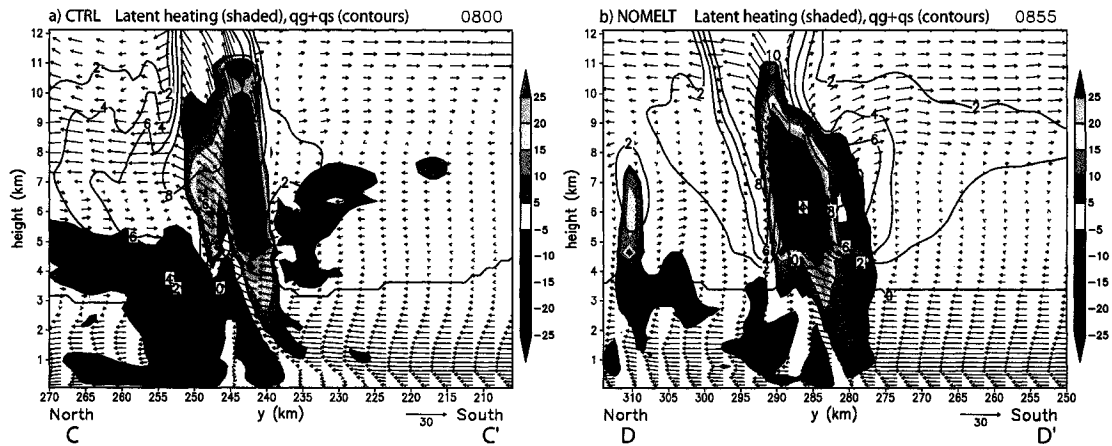


Figure 6.20: Cross-sections showing instantaneous potential temperature tendency owing to microphysical effects ( $\text{K h}^{-1}$ , shaded), mixing ratio of graupel and snow ( $\text{g kg}^{-1}$ , contoured every  $2 \text{ g kg}^{-1}$ ), and system-relative, line-perpendicular flow vectors (shown at every fifth horizontal grid point). Panel (a) shows CTRL at  $t=8 \text{ h}$  for the same cross section as that in Fig. 6.12a, and panel (b) shows NOMELT at  $t=8.92 \text{ h}$  for the same cross section as that in Fig. 6.19.

toward the northeast and was organized very differently. Thus, processes resulting from evaporative cooling are evidently responsible for pushing the convective line southward, although it is not entirely clear how these processes come about when the potential temperature has only been cooled by a fraction of a degree. This is a potential avenue for future research.

### 6.3.2 STOPFORCE

The next sensitivity experiment, STOPFORCE, identifies the role of the imposed forcing and tests whether a strong convective system can be maintained even after this forcing has been removed. Of particular interest in designing this simulation is this finding of CM88: “if the environmental air is lifted to its level of saturation over a wide region before the initiation of convection, then the lifting at the cold pool is no longer critical in maintaining the convective system.” Simulation STOPFORCE will test this assertion in a more sophisticated model.

Although the convective system that develops in STOPFORCE is not quite as strong

as that in CTRL, it is nonetheless organized very similarly and shows no signs of weakening through the 9 h of the simulation (Fig. 6.17d and 6.18d). Furthermore, the convective line is organized linearly and maintained *without forcing or a cold pool* through most of the simulation; only after approximately 8 h does a surface cold pool begin to appear (Fig. 6.16). The low-level mechanism responsible for organizing the system through  $t=8$  h of STOPFORCE is the same low-level gravity wave discussed previously (not shown). The “short-distance” mechanism for back-building along the low-level wave illustrated in Fig. 6.9 is also at work in this simulation. This demonstrates that even though the background convergence can lift parcels to their LFC (and it does so to initiate the very first convective cells), once a large region of saturation has been attained and deep convection has been initiated, in this shear profile the convection will organize into a back-building line on its own.

### 6.3.3 CORIOLIS

The final sensitivity experiment, CORIOLIS, considers the effect of planetary rotation on the simulated convective systems. Because the Rossby radius of deformation decreases with increasing latitude (e.g., Holton 2004), the distance that gravity waves can propagate away from their source is shorter in midlatitudes than in the tropics. Mapes (1993) and Liu and Moncrieff (2004) found that adiabatic displacements associated with convectively-generated gravity waves can make the nearby environment more favorable for convection, and that the ability for waves to propagate longer distances at lower latitudes makes “clustering” of convection more prominent there. Planetary rotation can have other effects on midlatitude convection, such as favoring the evolution of squall lines toward an asymmetric structure (e.g., Skamarock et al. 1994). Finally, the midlevel circulations (such as MCVs) that help to initiate the convective systems that motivate this study are generally balanced vortices that are strongly affected by planetary rotation (e.g., Davis and Weisman 1994). Since the observed MCSs of interest are midlatitude phenomena, it is important to

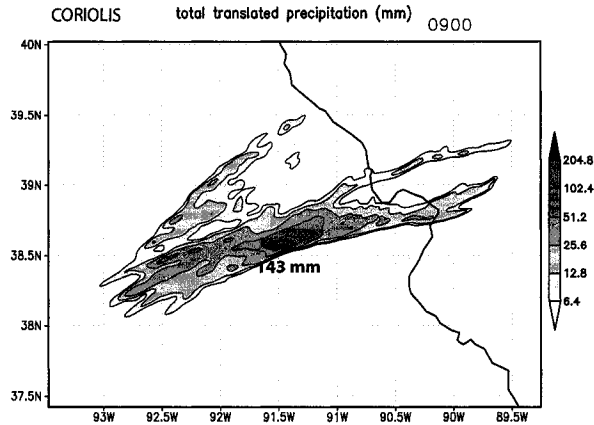


Figure 6.21: As in Fig. 6.13, except for simulation CORIOLIS through  $t=9$  h.

test whether the previously-presented simulations, which had  $f=0$ , are still representative of the observed system when  $f$  is nonzero.

Through the first 5 h of CORIOLIS, convection initiates and evolves almost identically to the CTRL run (Fig. 6.16). However, after this time, some differences begin to emerge. (Recall also that the background forcing is being altered by the Coriolis force so that it also differs slightly from that in CTRL.) The convection in CORIOLIS does not organize and strengthen quite as quickly as in CTRL, but it still organizes into a southwest-to-northeast back-building line by  $t=7$  h. The length of the line is similar to that in CTRL, but it is not as intense (Fig. 6.17e). Again, the low-level organizing mechanism is a gravity wave (not shown). The simulations diverge after  $t=7$  h: the cold pool develops and dominates the evolution of the system in CTRL, whereas in CORIOLIS a cold pool fails to develop but the length of the convective line decreases. By  $t=9$  h, the line in CORIOLIS is much smaller than that in CTRL (Fig. 6.18e), but it is still quite intense. It has also moved toward the southwest relative to the forcing, and this led to a very long period of “echo training” in that region. In fact, the maximum point rainfall total through 9 h in CORIOLIS is larger than that through 11 h in CTRL, even though the convective system is smaller in size (Fig. 6.21, cf. Fig. 6.13a).

That a convective system subjected to planetary rotation would be smaller than

one with  $f=0$  is to be expected based on the theory and observations of the above-cited studies. Nonetheless, the primary results presented in the previous sections (except for the evolution of the system after the cold pool formed) are generally similar in CTRL and CORIOLIS, especially the organization of the convection by the low-level gravity wave. The lack of cold pool production in CORIOLIS is curious, though it may stem from the fact that the convection was not quite as strong, and thus the cooling from evaporation and melting was also weaker. The motion characteristics of the convection in CORIOLIS, particularly its tendency to propagate strongly toward the southwest, are deserving of further study. Determining the cause of this behavior is beyond the scope of this study. However, these results suggest that it may be possible that, all else being equal, midlatitude convective systems are dynamically more likely than their tropical cousins to become quasi-stationary and produce very large point rainfall totals.

#### 6.4 Summary and Conclusions

In this chapter, a series of idealized simulations of quasi-stationary convective systems was presented. The simulations were designed to understand the workings of convection that forms and organizes within an environment of meso- to synoptic-scale lifting, such as is provided by an MCV or other midlevel circulation. The thermodynamic and kinematic profile used was a composite from several extreme rainfall events. The thermodynamic profile was nearly saturated at midlevels, and the wind profile included a strong reversal of wind shear with height associated with a low-level jet. To initiate convection, a momentum forcing was applied, which created an elevated convergence layer that lifted layers of air to saturation and initiated deep moist convection after a few hours. This forcing allows for a realistic examination of convective systems that develop near midlevel vortices without the additional complications of the vortices themselves.

The primary conclusions drawn from these simulations are as follows:

- Within 2-3 hours of initiation, the convection organizes into a back-building line

that has similar characteristics to observed extreme-rain-producing convective systems. New convection forms on the southwest end of the line and moves northeast along the line, which leads to large rainfall accumulations at points along the line.

- The initial low-level mechanism for organizing and maintaining the convective line is not a cold pool but a gravity wave with a maximum amplitude at approximately 1 km above the surface. Near-surface air rises over this wave and sinks on the other side, but more-unstable air above the surface is lifted over the wave, attains its level of free convection, and erupts into deep updrafts.
- In the later stages of the simulated convective system, a surface cold pool does form. However, it tends to cause the convective line to be less organized, and the continuing deep convection is far separated from the leading edge of the cold pool.
- Sensitivity tests reveal that in an environment with background lifting, an intense convective system can be maintained without the benefit of lifting from a latent-cooling-driven cold pool. However, latent cooling from evaporation and melting does affect the system in other ways. When evaporative cooling is removed, the convective system moves more quickly toward the northeast. A rear-inflow jet associated with cooling from melting assists in keeping the convective line upright and intense.
- When the background forcing is removed after convection initiates, the resulting convective system is still strong, long-lived, and quasi-stationary. This suggests that the organization, motion, and maintenance of the system is primarily controlled by the interaction between the shear and the development of the low-level gravity wave, rather than by the shape and strength of the imposed convergence field.

Although an imposed momentum forcing has been used here, there are surely other justifiable methods that could be used for simulating convection occurring within an environment of large-scale lifting. However, the method used here succeeded in producing

physically realistic simulations of quasi-stationary convective systems. Furthermore, the generality of the method used here (and originally developed by CM88 and LWD08) means that it is not limited to the application of MCVs and other midlevel circulations. With appropriate adjustments, it could be used to simulate other situations in which large-scale convergence and lifting occurs.

## Chapter 7

### CONCLUSIONS AND FUTURE WORK

#### 7.1 Conclusions

In this dissertation, observations and numerical simulations were used to investigate the atmospheric processes responsible for initiating, organizing, and maintaining quasi-stationary mesoscale convective systems (MCSs) that produce extreme amounts of rainfall. Of particular interest were MCSs that formed in association with midlevel mesoscale convective vortices or cutoff lows. Six of these MCSs were examined, each of which remained nearly stationary for 6-12 hours and produced excessive rainfall that led to significant flash flooding. Composite analysis revealed several characteristics that were common to these events:

- Convection was initiated and maintained in part by lifting associated with the interaction between a strong low-level jet (LLJ) and the midlevel cyclonic circulation.
- The presence of the LLJ and generally weak midlevel winds led to a strong reversal of the vertical wind shear with height. This type of wind profile appears as a “hairpin” shape on a wind hodograph.
- The thermodynamic environment near the deep convection was characterized by very high relative humidity at low levels, moderate convective available potential energy (CAPE), and very little convective inhibition (CIN).

One of these six events, which occurred on 6–7 May 2000 in eastern Missouri, was examined in more detail using both observations and numerical simulations. This back-building/quasi-stationary MCS produced over 300 mm of rain to the southwest of St. Louis and led to a flash flood that caused two fatalities and over \$100M in damage. The primary conclusions of this case study were:

- Prior to the event, a long-lived mesoscale convective vortex meandered through the southern Plains for several days. Mesoscale lifting resulting from the interaction of a strong low-level jet with this MCV led to the initiation of scattered convection within a deep moist absolutely-unstable layer, which intensified and became more organized with time.
- Operational model forecasts and simulations using a convective parameterization scheme failed to produce the observed rainfall totals for this event. However, convection-permitting simulations using the Weather Research and Forecasting (WRF) model were successful in reproducing the quasi-stationary organization and evolution of this MCS. In both observations and simulations, scattered elevated convective cells were repeatedly initiated 50–75 km upstream before merging into the mature MCS and contributing to the heavy rainfall.
- The primary organizing mechanism for the convective system was not a surface cold pool; instead, a series of nearly-stationary low-level gravity waves gave the MCS its quasi-linear organization. Because the southward propagation of the waves was counteracted by the strong southerly flow, the MCS as a whole also moved very slowly, which contributed to the excessive local rainfall totals.
- Observed and simulated surface pressure fields revealed a mesolow beneath the MCS. The deep convection also acted to reintensify and contract the initial midlevel vortex.

To further understand the low-level gravity waves that were identified in the case-study simulation, a series of idealized numerical experiments was performed. These simulations, which used a “bubble” to initiate deep convection, were designed to examine the development and propagation of these waves in differing thermodynamic and kinematic environments. Several conclusions were reached from these simulations:

- When deep convection develops in a conditionally unstable (but statically stable) environment, the associated latent heating produces a low-level gravity wave that has its peak amplitude at approximately the lifting condensation level.
- The ambient wind profile strongly affects the characteristics of this low-level wave. When there is no background wind, the wave simply propagates away. However, in a wind profile with the vertical representation of a strong southwesterly low-level jet, the wave is amplified on the south side of the deep convection and it remains nearly stationary relative to its source. When this occurs, inflowing air is lifted over the wave and can attain its level of free convection (LFC), resulting in additional deep convective cells. These cells develop to the south and west of existing convection, resembling the back-building process that is commonly observed in mesoscale convective systems.
- When the magnitude of the shear is reduced by half, back-building does not take place. This suggests that the shear must not only reverse with height, but it must reverse *sharply* if a back-building, quasi-stationary convective system is to develop.

Although the relatively simple “bubble” experiments offered some insight into the processes involved in back-building convection, they did not include the synoptic- to mesoscale lifting that occurred in association with the midlevel circulations in the observed events. To simulate this lifting without the additional complications of the circulation itself, a low-level momentum forcing was applied in another series of numerical experiments. These simulations proved to be realistic representations of the observed convective systems.

The primary results of these simulations were:

- Within 2-3 hours after the initiation of deep convection, the convection organizes into a back-building line that has similar characteristics to observed extreme-rain-producing convective systems. New convection forms on the southwest end of the line and moves northeast along the line, which leads to large rainfall accumulations at points along the line.
- In an environment with background lifting, an intense convective system can be maintained without the benefit of lifting from a latent-cooling-driven cold pool. This confirms the results of Crook and Moncrieff (1988) using much more complex, three-dimensional simulations.
- The initial low-level mechanism for organizing and maintaining the convective line is not a cold pool but a gravity wave with a maximum amplitude at approximately 1 km above the surface. Near-surface air rises over this wave and sinks on the other side, but more-unstable air above the surface is lifted over the wave, attains its LFC, and rises in deep updrafts.
- When the background forcing is removed after convection initiates, the resulting convective system is still strong, long-lived, and quasi-stationary. This suggests that the organization, motion, and maintenance of the system is primarily controlled by the interaction between the shear and the development of the low-level gravity wave, rather than by the shape and strength of the imposed convergence field.

## 7.2 Future Work

The results described above also suggest several possibilities for potential future investigations. The first avenue for further numerical experiments would be to actually simulate the interaction between an MCV or other midlevel circulation and strong low-level wind shear in an idealized environment. Although it has been shown here that it is possible to

simulate quasi-stationary convective systems by using an artificial lifting mechanism rather than an actual vortex, MCSs in the real atmosphere are also affected by the vortex and its associated dynamics. Care would need to be taken when designing such experiments, as it would be necessary to include both a balanced vortex and a strong LLJ, which is by definition highly ageostrophic. However, these simulations could be very fruitful, revealing the processes by which the LLJ interacts with the vortex to initiate convection and potentially leading to the discovery of an “optimal” configuration of the MCV and LLJ for producing heavy local rainfall.

These experiments could also provide insights into possible connections between mid-latitude and tropical MCVs, as briefly suggested in chapter 4. Compared with most tropical MCVs and MCSs, midlatitude systems are relatively well observed. The lack of a cold pool and the development of a surface low pressure center in the 6–7 May 2000 MCS suggests that it may be an interesting case to study in the context of recent work on the genesis of tropical cyclones from MCVs. Further study of that case as well as the idealized experiments discussed above could yield information about whether surface cyclogenesis associated with midlatitude MCVs is similar to the process of tropical cyclogenesis.

The results of the “bubble” simulations in chapter 5 could be extended to include a dynamical analysis of convective heating in complex wind profiles. The roles of buoyant and dynamic pressure perturbations (e.g., Rotunno and Klemp (1982)) in the development (or non-development) of back-building convection should be quantified, as should the specific role of the reversal of shear with height. Simulations that use an average idealized latent heating profile (rather than the rapidly-changing profile that occurs when simulating convection explicitly) may also provide information about the origin and evolution of the low-level gravity waves discussed previously. All of these experiments would yield insights into the dynamics of discretely propagating convection.

Additional observations of extreme-rain-producing MCSs would certainly add to the understanding of their workings. A field study dedicated to extreme rain events would

be logistically difficult to execute since such events are relatively rare and often isolated. However, including extreme-rain-producing MCSs into a wider-ranging field program that includes a dense network of soundings, radars, surface observations, and rain gauges could provide the necessary data if a significant event was heavily observed. The low-level gravity waves that were discussed at length in this study may be difficult to observe, since they occur on small scales and may not be very common. However, if an event were sampled by a dense observing network such as the Oklahoma Mesonet, the observations could be examined to identify and confirm the characteristics of these waves. Mesonet data could also be used to further understand the properties of surface mesolows that form near MCSs. The 5–6 May 2000 event would be a good candidate for study since it occurred over the Oklahoma Mesonet, was long lived, and had complex organization and motion characteristics.

Another aspect of extreme rainfall that has been only considered briefly in this study is the important role of cloud microphysics. Sensitivity simulations of the 6–7 May 2000 case and other extreme rain events using different microphysical parameterizations show that even though the model may correctly simulate the organization and motion of an MCS, the ground-accumulated rainfall can vary significantly. These findings will likely be part of a future manuscript. Furthermore, building on the work of Gilmore et al. (2004), the composite thermodynamic environment identified in this study could be used to initialize a series of sensitivity tests that identify the microphysical processes that are most important for the production of heavy rainfall. For application to flash-flood forecasting and hydrological prediction, the amount and distribution of rainfall at the ground are crucial variables, and the studies suggested above could improve confidence (or quantify uncertainty) in quantitative precipitation forecasts.

Finally, this study has primarily focused on a subset of extreme-rain-producing MCSs that are associated with midlevel circulations: those that generally fit the back-building/quasi-stationary pattern proposed by Schumacher and Johnson (2005). Other MCSs that occur in association with MCVs are organized differently but still produce

heavy rainfall. This dissertation included two events from the summer of 2007, but numerous other extreme rain events occurred during this anomalously wet summer in the southern Plains of the U. S. One of the primary mesoscale features during the summer of 2007 was a persistent midlevel circulation that was reinforced each day by deep convection, similar to that in the events described herein. This unusual flow pattern provided plenty of possible case studies that could be analyzed to learn about the processes that contribute to extreme rainfall as well as those involved in the feedback between midlevel vorticity and latent heating. As was shown in 2007, these small-scale processes can alter the local weather over the course of weeks and months, which suggests that they may need to be considered in climate analysis and prediction as well.

## REFERENCES

- Atlas, D., R. Tatehira, R. C. Srivastava, W. Marker, and R. E. Carbone, 1969: Precipitation-induced mesoscale wind perturbations in the melting layer. *Quart. J. Roy. Meteor. Soc.*, **95**, 544–560.
- Augustine, J. A., and F. Caracena, 1994: Lower-tropospheric precursors to nocturnal MCS development over the central United States. *Wea. Forecasting*, **9**, 116–135.
- Bartels, D. L., and R. A. Maddox, 1991: Midlevel cyclonic vortices generated by mesoscale convective systems. *Mon. Wea. Rev.*, **119**, 104–118.
- Benjamin, S. G., and Coauthors, 2004: An hourly assimilation-forecast cycle: The RUC. *Mon. Wea. Rev.*, **132**, 495–518.
- Bosart, L. F., and F. Sanders, 1981: The Johnstown flood of July 1977: A long-lived convective system. *J. Atmos. Sci.*, **38**, 1616–1642.
- Braun, S. A., and W.-K. Tao, 2000: Sensitivity of high-resolution simulations of Hurricane Bob (1991) to planetary boundary layer parameterizations. *Mon. Wea. Rev.*, **128**, 3941–3961.
- Bryan, G. H., and J. M. Fritsch, 2000: Moist absolute instability: The sixth static stability state. *Bull. Amer. Meteor. Soc.*, **81**, 1207–1230.
- Bryan, G. H., and J. M. Fritsch, 2002: A benchmark simulation for moist nonhydrostatic numerical models. *Mon. Wea. Rev.*, **130**, 2917–2928.

- Bryan, G. H., R. Rotunno, and J. M. Fritsch, 2007: Roll circulations in the convective region of a simulated squall line. *J. Atmos. Sci.*, **64**, 1249–1266.
- Bryan, G. H., J. C. Wyngaard, and J. M. Fritsch, 2003: Resolution requirements for the simulation of deep moist convection. *Mon. Wea. Rev.*, **131**, 2394–2416.
- Chappell, C. F., 1986: Quasi-stationary convective events. *Mesoscale Meteorology and Forecasting*, P. S. Ray, Ed., Amer. Meteor. Soc., 289–309.
- Coniglio, M. C., and D. J. Stensrud, 2001: Simulation of a progressive derecho using composite initial conditions. *Mon. Wea. Rev.*, **129**, 1593–1616.
- Conzemius, R. J., R. W. Moore, M. T. Montgomery, and C. A. Davis, 2007: Mesoscale convective vortex formation in a weakly sheared moist neutral environment. *J. Atmos. Sci.*, **64**, 1443–1466.
- Corfidi, S. F., 2003: Cold pools and MCS propagation: Forecasting the motion of downwind-developing MCSs. *Wea. Forecasting*, **18**, 997–1017.
- Crook, N. A., and M. W. Moncrieff, 1988: The effect of large-scale convergence on the generation and maintenance of deep moist convection. *J. Atmos. Sci.*, **45**, 3606–3624.
- Davis, C. A., D. A. Ahijevych, and S. B. Trier, 2002: Detection and prediction of warm season midtropospheric vortices by the Rapid Update Cycle. *Mon. Wea. Rev.*, **130**, 24–42.
- Davis, C. A., and S. B. Trier, 2002: Cloud-resolving simulations of mesoscale vortex intensification and its effect on a serial mesoscale convective system. *Mon. Wea. Rev.*, **130**, 2839–2858.
- Davis, C. A., and S. B. Trier, 2007: Mesoscale convective vortices observed during BAMEX. Part I: Kinematic and thermodynamic structure. *Mon. Wea. Rev.*, **135**, 2029–2049.

- Davis, C. A., and M. L. Weisman, 1994: Balanced dynamics of mesoscale vortices produced in simulated convective systems. *J. Atmos. Sci.*, **51**, 2005–2030.
- Davis, R. S., 2001: Flash flood forecast and detection methods. *Severe Convective Storms, Meteor. Monogr.*, No. 50, Amer. Meteor. Soc., 481–525.
- Done, J., C. A. Davis, and M. Weisman, 2004: The next generation of NWP: Explicit forecasts of convection using the Weather Research and Forecasting (WRF) model. *Atmos. Sci. Lett.*, **5**, 110–117.
- Doswell, C. A., III, H. E. Brooks, and R. A. Maddox, 1996: Flash flood forecasting: An ingredients-based methodology. *Wea. Forecasting*, **11**, 560–581.
- Dudhia, J., and M. W. Moncrieff, 1987: A numerical simulation of quasi-stationary tropical convective bands. *Quart. J. Roy. Meteor. Soc.*, **113**, 929–967.
- Dudhia, J., M. W. Moncrieff, and D. W. K. So, 1987: The two-dimensional dynamics of West African squall lines. *Quart. J. Roy. Meteor. Soc.*, **113**, 121–146.
- Durrán, D. R., and J. B. Klemp, 1983: A compressible model for the simulation of moist mountain waves. *Mon. Wea. Rev.*, **111**, 2341–2361.
- Fovell, R. G., 2002: Upstream influence of numerically simulated squall-line storms. *Quart. J. Roy. Meteor. Soc.*, **128**, 893–912.
- Fovell, R. G., and P.-H. Tan, 1998: The temporal behavior of numerically simulated multicell-type storms. Part II: The convective cell life cycle and cell regeneration. *Mon. Wea. Rev.*, **126**, 551–577.
- Fritsch, J. M., and R. E. Carbone, 2004: Improving quantitative precipitation forecasts in the warm season: A USWRP research and development strategy. *Bull. Amer. Meteor. Soc.*, **85**, 955–965.

- Fritsch, J. M., J. D. Murphy, and J. S. Kain, 1994: Warm-core vortex amplification over land. *J. Atmos. Sci.*, **51**, 1780–1807.
- Gilmore, M. S., J. M. Straka, and E. N. Rasmussen, 2004: Precipitation uncertainty due to variations in precipitation particle parameters within a simple microphysics scheme. *Mon. Wea. Rev.*, **132**, 2610–2627.
- Glass, F. H., D. L. Ferry, J. T. Moore, and S. M. Nolan, 1995: Characteristics of heavy convective rainfall events across the Mid-Mississippi valley during the warm season: Meteorological conditions and a conceptual model. Preprints, *14th Conference on Weather Analysis and Forecasting*, Dallas, TX, Amer. Meteor. Soc., 34–41.
- Glass, F. H., J. P. Gagan, and J. T. Moore, 2001: The extreme east-central Missouri flash flood of 6–7 May 2000. Preprints, *Symposium on Precipitation Extremes: Prediction, Impacts, and Responses*, Albuquerque, NM, Amer. Meteor. Soc., 174–179.
- Haertel, P. T., R. H. Johnson, and S. N. Tulich, 2001: Some simple simulations of thunderstorm outflows. *J. Atmos. Sci.*, **58**, 504–516.
- Haynes, P. H., and M. E. McIntyre, 1987: On the evolution of vorticity and potential vorticity in the presence of diabatic heating and frictional or other forces. *J. Atmos. Sci.*, **44**, 828–841.
- Hertenstein, R. F. A., and W. H. Schubert, 1991: Potential vorticity anomalies associated with squall lines. *Mon. Wea. Rev.*, **119**, 1663–1672.
- Holton, J. R., 2004: *An Introduction to Dynamic Meteorology*. 4th edition. Academic Press, 535 pp.
- Hoskins, B. J., M. E. McIntyre, and A. W. Robertson, 1985: On the use and significance of isentropic potential vorticity maps. *Quart. J. Roy. Meteor. Soc.*, **111**, 877–946.
- Houze, R. A., Jr., S. A. Rutledge, M. I. Biggerstaff, and B. F. Smull, 1989: Interpretation

- of Doppler weather radar displays of midlatitude mesoscale convective systems. *Bull. Amer. Meteor. Soc.*, **70**, 608–619.
- Jewett, B. F., and R. B. Wilhelmson, 2006: The role of forcing in cell morphology and evolution within midlatitude squall lines. *Mon. Wea. Rev.*, **134**, 3714–3734.
- Johnson, R. H., 2001: Surface mesohighs and mesolows. *Bull. Amer. Meteor. Soc.*, **82**, 13–31.
- Junker, N. W., R. S. Schneider, and S. L. Fauver, 1999: A study of heavy rainfall events during the Great Midwest Flood of 1993. *Wea. Forecasting*, **14**, 701–712.
- Kato, T., 1998: Numerical simulation of the band-shaped torrential rain observed over southern Kyushu, Japan on 1 August 1993. *J. Meteor. Soc. Japan*, **76**, 97–128.
- Kato, T., and H. Goda, 2001: Formation and maintenance processes of a stationary band-shaped heavy rainfall observed in Niigata on 4 August 1998. *J. Meteor. Soc. Japan*, **79**, 899–924.
- Kirshbaum, D. J., and D. R. Durran, 2004: Factors governing cellular convection in orographic precipitation. *J. Atmos. Sci.*, **61**, 682–698.
- Klemp, J. B., W. C. Skamarock, and J. Dudhia, 2007: Conservative split-explicit time integration methods for the compressible nonhydrostatic equations. *Mon. Wea. Rev.*, **135**, 2897–2913.
- Klemp, J. B., and R. B. Wilhelmson, 1978: The simulation of three-dimensional convective storm dynamics. *J. Atmos. Sci.*, **35**, 1070–1096.
- Knievel, J. C., G. H. Bryan, and J. P. Hacker, 2007: Explicit numerical diffusion in the WRF model. *Mon. Wea. Rev.*, **135**, 3803–3824.
- Knievel, J. C., and R. H. Johnson, 2002: The kinematics of a midlatitude, continental mesoscale convective system and its mesoscale vortex. *Mon. Wea. Rev.*, **130**, 1749–1770.

- Knupp, K. R., 1987: Downdrafts within high plains cumulonimbi. Part I: General kinematic structure. *J. Atmos. Sci.*, **44**, 987–1008.
- Knupp, K. R., 1988: Downdrafts within high plains cumulonimbi. Part II: Dynamics and thermodynamics. *J. Atmos. Sci.*, **45**, 3965–3982.
- Koch, S. E., and R. E. Golus, 1988: A mesoscale gravity wave event observed during CCOPE. Part I: Multiscale statistical analysis of wave characteristics. *Mon. Wea. Rev.*, **116**, 2527–2544.
- Lafore, J.-P., and M. W. Moncrieff, 1989: A numerical investigation of the organization and interaction of the convective and stratiform regions of tropical squall lines. *J. Atmos. Sci.*, **46**, 521–544.
- Lin, Y.-L., R. D. Farley, and H. D. Orville, 1983: Bulk parameterization of the snow field in a cloud model. *J. Climate Appl. Meteor.*, **22**, 1065–1092.
- Liu, C., and M. W. Moncrieff, 2004: Effects of convectively generated gravity waves and rotation on the organization of convection. *J. Atmos. Sci.*, **61**, 2218–2227.
- Loftus, A. M., D. B. Weber, and C. A. Doswell, III, 2008: Parameterized mesoscale forcing mechanisms for initiating numerically-simulated isolated multicellular convection. *Mon. Wea. Rev.*, in press.
- Maddox, R. A., C. F. Chappell, and L. R. Hoxit, 1979: Synoptic and meso- $\alpha$  scale aspects of flash flood events. *Bull. Amer. Meteor. Soc.*, **60**, 115–123.
- Mapes, B. E., 1993: Gregarious tropical convection. *J. Atmos. Sci.*, **50**, 2026–2037.
- Market, P. S., A. R. Lupo, C. E. Halcomb, F. A. Akyüz, and P. Guinan, 2001: Overview of the 7 May 2000 extreme rain event in Missouri. Preprints, *Symposium on Precipitation Extremes: Prediction, Impacts, and Responses*, Albuquerque, NM, Amer. Meteor. Soc., 162–165.

- Montgomery, M. T., M. E. Nicholls, T. A. Cram, and A. B. Saunders, 2006: A vortical hot tower route to tropical cyclogenesis. *J. Atmos. Sci.*, **63**, 355–386.
- Moore, J. T., F. H. Glass, C. E. Graves, S. M. Rochette, and M. J. Singer, 2003: The environment of warm-season elevated thunderstorms associated with heavy rainfall over the central United States. *Wea. Forecasting*, **18**, 861–878.
- MSNBC, cited 2007: Death toll in Texas floods reaches six. [Available online at: <http://www.msnbc.msn.com/id/19288697/>].
- Nicholls, M. E., R. A. Pielke, and W. R. Cotton, 1991: Thermally forced gravity waves in an atmosphere at rest. *J. Atmos. Sci.*, **48**, 1869–1884.
- Nielsen-Gammon, J. W., F. Zhang, A. M. Odins, and B. Myoung, 2005: Extreme rainfall in Texas: Patterns and predictability. *Phys. Geogr.*, **26**, 340–364.
- NOAA, cited 2008: Natural hazard statistics. [Available online at <http://www.nws.noaa.gov/om/hazstats.shtml>].
- Parker, M. D., 2007a: Simulated convective lines with parallel stratiform precipitation. Part I: An archetype for convection in along-line shear. *J. Atmos. Sci.*, **64**, 267–288.
- Parker, M. D., 2007b: Simulated convective lines with parallel stratiform precipitation. Part II: Governing dynamics and associated sensitivities. *J. Atmos. Sci.*, **64**, 289–313.
- Parker, M. D., 2008: Response of simulated squall lines to low-level cooling. *J. Atmos. Sci.*, **65**, 1323–1341.
- Parker, M. D., and R. H. Johnson, 2000: Organizational modes of midlatitude mesoscale convective systems. *Mon. Wea. Rev.*, **128**, 3413–3436.
- Parker, M. D., and R. H. Johnson, 2004: Structures and dynamics of quasi-2D mesoscale convective systems. *J. Atmos. Sci.*, **61**, 545–567.

- Pontrelli, M. D., G. Bryan, and J. M. Fritsch, 1999: The Madison County, Virginia, flash flood of 27 June 1995. *Wea. Forecasting*, **14**, 384–404.
- Raymond, D. J., and H. Jiang, 1990: A theory for long-lived mesoscale convective systems. *J. Atmos. Sci.*, **47**, 3067–3077.
- Raymond, D. J., and R. Rotunno, 1989: Response of a stably stratified flow to cooling. *J. Atmos. Sci.*, **46**, 2830–2837.
- Robe, F. R., and K. A. Emanuel, 2001: The effect of vertical wind shear on radiative–convective equilibrium states. *J. Atmos. Sci.*, **58**, 1427–1445.
- Rogers, R. F., and J. M. Fritsch, 2001: Surface cyclogenesis from convectively driven amplification of midlevel mesoscale convective vortices. *Mon. Wea. Rev.*, **129**, 605–637.
- Rotunno, R., and J. B. Klemp, 1982: The influence of the shear–induced pressure gradient on thunderstorm motion. *Mon. Wea. Rev.*, **110**, 136–151.
- Rotunno, R., J. B. Klemp, and M. L. Weisman, 1988: A theory for strong, long-lived squall lines. *J. Atmos. Sci.*, **45**, 463–485.
- Sanders, F., 2000: Frontal focusing of a flooding rainstorm. *Mon. Wea. Rev.*, **128**, 4155–4159.
- Schmidt, J. M., and W. R. Cotton, 1990: Interactions between upper and lower tropospheric gravity waves on squall line structure and maintenance. *J. Atmos. Sci.*, **47**, 1205–1222.
- Schubert, W. H., J. J. Hack, P. L. Silva Dias, and S. R. Fulton, 1980: Geostrophic adjustment in an axisymmetric vortex. *J. Atmos. Sci.*, **37**, 1464–1484.
- Schumacher, R. S., and R. H. Johnson, 2005: Organization and environmental properties of extreme-rain-producing mesoscale convective systems. *Mon. Wea. Rev.*, **133**, 961–976.
- Schumacher, R. S., and R. H. Johnson, 2006: Characteristics of United States extreme rain events during 1999–2003. *Wea. Forecasting*, **21**, 69–85.

- Sippel, J. A., J. W. Nielsen-Gammon, and S. E. Allen, 2006: The multiple-vortex nature of tropical cyclogenesis. *Mon. Wea. Rev.*, **134**, 1796–1814.
- Skamarock, W. C., 2004: Evaluating mesoscale NWP models using kinetic energy spectra. *Mon. Wea. Rev.*, **132**, 3019–3032.
- Skamarock, W. C., J. B. Klemp, J. Dudhia, D. O. Gill, D. M. Barker, W. Wang, and J. G. Powers, cited 2007: A description of the Advanced Research WRF version 2. NCAR/TN-468+STR. [Available online at [http://www.mmm.ucar.edu/wrf/users/docs/arw\\_v2.pdf](http://www.mmm.ucar.edu/wrf/users/docs/arw_v2.pdf)]
- Skamarock, W. C., M. L. Weisman, and J. B. Klemp, 1994: Three-dimensional evolution of simulated long-lived squall lines. *J. Atmos. Sci.*, **51**, 2563–2584.
- Springfield News-Leader, cited 2007: Road crews still battling flood damage. [Available online at <http://www.news-leader.com/apps/pbcs.dll/article?AID=/20070920/NEWS01/7%09200397/1007/BREAKING03>].
- Stensrud, D. J., 1996: Effects of persistent, midlatitude mesoscale regions of convection on the large-scale environment during the warm season. *J. Atmos. Sci.*, **53**, 3503–3527.
- Stensrud, D. J., M. C. Coniglio, R. P. Davies-Jones, and J. S. Evans, 2005: Comments on “A theory for strong long-lived squall lines’ revisited”. *J. Atmos. Sci.*, **62**, 2989–2996.
- Stensrud, D. J., and J. M. Fritsch, 1993: Mesoscale convective systems in weakly forced large-scale environments. Part I: Observations. *Mon. Wea. Rev.*, **121**, 3326–3344.
- Szeto, K. K., R. E. Stewart, and C. A. Lin, 1988: Mesoscale circulations forced by melting snow. Part II: Application to meteorological features. *J. Atmos. Sci.*, **45**, 1642–1650.
- Thompson, R. L., R. Edwards, J. A. Hart, K. L. Elmore, and P. Markowski, 2003: Close proximity soundings within supercell environments obtained from the Rapid Update Cycle. *Wea. Forecasting*, **18**, 1243–1261.

- Thorpe, A. J., M. J. Miller, and M. W. Moncrieff, 1982: Two-dimensional convection in non-constant shear: A model of midlatitude squall lines. *Quart. J. Roy. Meteor. Soc.*, **108**, 739–762.
- Tory, K. J., M. T. Montgomery, and N. E. Davidson, 2006: Prediction and diagnosis of tropical cyclone formation in an NWP system. Part I: The critical role of vortex enhancement in deep convection. *J. Atmos. Sci.*, **63**, 3077–3090.
- Trier, S. B., and C. A. Davis, 2002: Influence of balanced motions on heavy precipitation within a long-lived convectively generated vortex. *Mon. Wea. Rev.*, **130**, 877–899.
- Trier, S. B., and C. A. Davis, 2007: Mesoscale convective vortices observed during BAMEX. Part II: Influences on secondary deep convection. *Mon. Wea. Rev.*, **135**, 2051–2075.
- Trier, S. B., C. A. Davis, and W. C. Skamarock, 2000a: Long-lived mesoconvective vortices and their environment. Part II: Induced thermodynamic destabilization in idealized simulations. *Mon. Wea. Rev.*, **128**, 3396–3412.
- Trier, S. B., C. A. Davis, and J. D. Tuttle, 2000b: Long-lived mesoconvective vortices and their environment. Part I: Observations from the central United States during the 1998 warm season. *Mon. Wea. Rev.*, **128**, 3376–3395.
- Trier, S. B., and D. B. Parsons, 1993: Evolution of environmental conditions preceding the development of a nocturnal mesoscale convective complex. *Mon. Wea. Rev.*, **121**, 1078–1098.
- Trier, S. B., W. C. Skamarock, M. A. LeMone, D. B. Parsons, and D. P. Jorgensen, 1996: Structure and evolution of the 22 February 1993 TOGA COARE squall line: Numerical simulations. *J. Atmos. Sci.*, **53**, 2861–2886.
- USA Today, cited 2000: At least 4 killed in Texas floods. [Available online at <http://www.usatoday.com/weather/news/2000/wtxfld605.htm>].

- Weisman, M. L., 1992: The role of convectively generated rear-inflow jets in the evolution of long-lived mesoconvective systems. *J. Atmos. Sci.*, **49**, 1826–1847.
- Weisman, M. L., and J. B. Klemp, 1982: The dependence of numerically simulated convective storms on vertical wind shear and buoyancy. *Mon. Wea. Rev.*, **110**, 504–520.
- Weisman, M. L., and R. Rotunno, 2004: “A theory for strong long-lived squall lines” revisited. *J. Atmos. Sci.*, **61**, 361–382.
- Weisman, M. L., and R. Rotunno, 2005: Reply. *J. Atmos. Sci.*, **62**, 2997–3002.
- Weisman, M. L., W. C. Skamarock, and J. B. Klemp, 1997: The resolution dependence of explicitly modeled convective systems. *Mon. Wea. Rev.*, **125**, 527–548.
- Xin, L., and G. W. Reuter, 1996: Numerical simulation of the effects of mesoscale convergence on convective rain showers. *Mon. Wea. Rev.*, **124**, 2828–2842.